INTEGRATED STRATIGRAPHY OF THE CRYOGENIAN AND THE EDIACARAN–CAMBRIAN BOUNDARY: PERSPECTIVES FROM SOUTHWESTERN NORTH AMERICA AND SOUTHERN AFRICA

by
Lyle Lee Nelson

A dissertation submitted to Johns Hopkins University in conformity with the requirements for the degree of Doctor of Philosophy

Baltimore, Maryland
March 2022

ABSTRACT

This dissertation (1) examines sedimentary records of Cryogenian (717-635 million years ago [Ma]) glacial deposits to constrain records of carbon cycle perturbations and extreme climate change and (2) examines sedimentary records across the Ediacaran–Cambrian transition (c. 550–530 Ma) to test hypotheses regarding the tempo and drivers of biotic and geochemical changes during early animal evolution.

Chapters 2 and 3 are studies of Cryogenian strata preserved in California. In Chapter 2, I solidify chronostratrigraphic correlation to strata on other paleocontinents, supporting interpretation of two distinct Cryogenian snowball Earth glacial epochs and demonstrating that a Cryogenian nonglacial interval lasted for at least 9 m.y. In Chapter 3, I produce high-resolution multiproxy stable isotope records from Cryogenian nonglacial interlude carbonate platform strata to test the relationship between carbon isotope perturbations and climate variability. Based on these results, I suggest that these carbonate strata preserve records of local organic carbon production and remineralization that do not necessarily reflect coeval global carbon fluxes.

Chapters 4–6 are studies of strata deposited across the Ediacaran–Cambrian boundary preserved in California, Mexico, and South Africa. In Chapter 5, I document structures preserved in terminal Ediacaran siliciclastic rocks of California that resemble late Ediacaran body fossils but are instead interpreted as a rare type of peritidal microbially induced sedimentary structure, suggestive of unusual paleoenvironmental and paleoecological conditions at the Ediacaran–Cambrian boundary. In Chapter 6, I report integrated stratigraphic data sets from Sonora, Mexico, which (1) demonstrate a temporal relationship between the regional disappearance of Ediacaran fossils, a marine carbon isotope perturbation, and rift-related basalt volcanism, and (2) provide the

first radioisotopic age constraint on the Ediacaran–Cambrian boundary in North America. In Chapter 7, I report integrated stratigraphic data sets from northwestern South Africa that provide a precise age model for trace and body fossil biostratigraphy and carbon isotope chemostratigraphy in the terminal Ediacaran. These results indicate that the Ediacaran–Cambrian boundary carbon isotope excursion, the disappearance of Ediacaran-type body fossils, and the appearance of basal Cambrian trace fossils are all younger than previously recognized, suggesting a more condensed early Cambrian biological radiation.

Primary Reader and Advisor: Professor Emily F. Smith

Secondary Reader: Professor Daniel R. Viete

ACKNOWLEDGEMENTS

It takes a village to complete most Earth science dissertations, and so many individuals have contributed to this one. I will attempt to acknowledge some of them here.

Five people have, above others, contributed to the foundation and progression of my career in geology. First and foremost, I am grateful to Emmy Smith for supporting a wide range of research endeavors and taking me on as her first graduate student. She has been an exemplary mentor and exceedingly generous with her time and resources. Francis Macdonald introduced me to the time-traveling power of stratigraphy, generously included me in his lab group during my undergraduate years, and has provided an outstanding example of relentless curiosity for the natural world and ambition to reconstruct Earth history. Justin Strauss took me on as a novice field and lab assistant, patiently allowed me to watch, imitate, and fail for three years, and continues to be a generous mentor and colleague. Jenny Haywood and Betsy Friedlander introduced me to geoscience industry, kindly tolerated my occasional impudence, and taught me structural geology in a complex fold-and-thrust belt. I am indebted to each of you.

I have many other people to acknowledge for my development as a geoscientist through shared time on outcrops and/or in the lab, discussions, and correspondence—and I will undoubtedly accidently omit others: Anne-Sofie Ahm, John Almond, Eliel Antilla, Uyanga Bold, Nick Christie-Blick, Hannah Cothren, Grant Cox, Peter Crockford, Simon Darroch, Carol Dehler, Julie Dumoulin, Doug Erwin, Athena Eyster, Karol Faehnrich, Ryan Furey, Freya George, Emily Geyman, Maya Gomes, John Grotzinger, Galen Halverson, John Higgins, Paul Hoffman, Rob Holder, Ganqing Jiang, Dave Johnston, Dave Jones, Esther Kennedy, Kim Lau, Bill McClelland, Lexie Millikin, Hannah Mills, Li Murphy, Paul Myrow, Ryan Nel, Nizhoni O'Connell, Rustam Orozbaev, Terry Pavlis, Tanya Petach, Tony Prave, Sara Pruss, Judy Pu, Alan Rooney, Kirby Runyon, Jim Schiffbauer, Tara Selly, Darin Schwartz, Erik Sperling, Nick Swanson-Hysell, Roger Swart, Lidya Tarhan, Wendy Taylor, Will Thompson-Butler, Madison Turner, Felix Waechter, Lucy Webb, and Shuhai Xiao.

I am especially grateful to Jahan Ramezani, Jim Crowley, and Mark Schmitz for generously hosting me in their respective labs and patiently training me in the intricacies of U-Pb geochronology, and to Blake Hodgin for friendship and collaboration in the field and in the lab.

At Hopkins, I thank my other committee members: Daniel Viete and Dimitri Sverjensky for thoughtful mentorship and feedback, my labmate Mary Lonsdale for being a considerate and engaging colleague, and Dana Brenner for expertise and generosity in the labs.

Special thank you to Beck, who serendipitously arrived in my life as the result of emergency field vehicle repairs in Baker, California: he has been a wonderful companion, both as a field-dog and as a town-dog. Speaking of field vehicles: these endeavors would not have been possible without the reliability (and occasional fickleness) of Bucky, Kitty, Reggie, and Dik-dik. In the secluded corners of the Panamints, Sylvester the kangaroo rat and Bessie the burro provided indispensable companionship.

Thank you to my Baltimore family: the Vance-Vietes, the Wolff clan, and Freya for making this town a lovely home.

I am deeply grateful to my parents, Julie and Lee, for unwavering support of my education and of my curiosity and love for the natural world; and to my sister Michaeline Albright who has been an outstanding role model for my entire life.

The foundations of my passion for natural science were the marine environments off the coast of Cape Ann, where I spent countless hours exploring with cousins and childhood friends.

All flaws and inaccuracies in this dissertation are mine alone.

Epigraph

Thus, although we are mere sojourners on the surface of the planet, chained to a mere point in space, enduring but for a moment of time, the human mind is not only enabled to number worlds beyond the unassisted ken of mortal eye, but to trace the events of indefinite ages before the creation of our race, and is not even withheld from penetrating into the dark secrets of the ocean, or the interior of the solid globe; free, like the spirit which the poet described as animating the universe.

– Sir Charles Lyell, *Principles of Geology, Book I, Chapter XIII*, 1830

TABLE OF CONTENTS

LIST OF TABLES

LIST OF FIGURES

CHAPTER 1. INTRODUCTION

The late Neoproterozoic Era–early Cambrian Period (c. 810 to 520 million years ago) was a critical interval in Earth history for the evolution of modern surface environments, recording major fluctuations in biogeochemical cycles (e.g., Halverson et al., 2005), long-lived low-latitude glaciations (e.g., Hoffman et al., 2017), a rise in atmospheric oxygen (e.g., Canfield and Farquhar, 2009; Och and Shields-Zhou, 2012), the evolution and diversification of metazoans (e.g., Love et al., 2009; Erwin et al., 2011; Sperling and Stockey, 2018), and supercontinent reorganization (e.g., Li et al., 2013; Merdith et al., 2017) (Fig. 1.1). Sedimentary strata, that have been tectonically uplifted and preserved on continental margins, provide a fragmented record of these environmental and biological changes. This thesis probes this record by using methodologies built upon geologic mapping, which allows for reconstruction of primary stratigraphic relationships and basin geometries, and the measurement of stratigraphic sections, which allows for interpretation of temporal and spatially lateral changes in surface environment. Within the regional geologic context provided by field work, carbonate geochemistry and U-Pb isotope geochronology are applied to: 1) constrain changes in the aqueous geochemistry of these surface environments, and 2) temporally calibrate changes in surface environments and ecologies. Here, I focus these studies on two specific windows of the Neoproterozoic: the Cryogenian Period and the terminal Ediacaran Period.

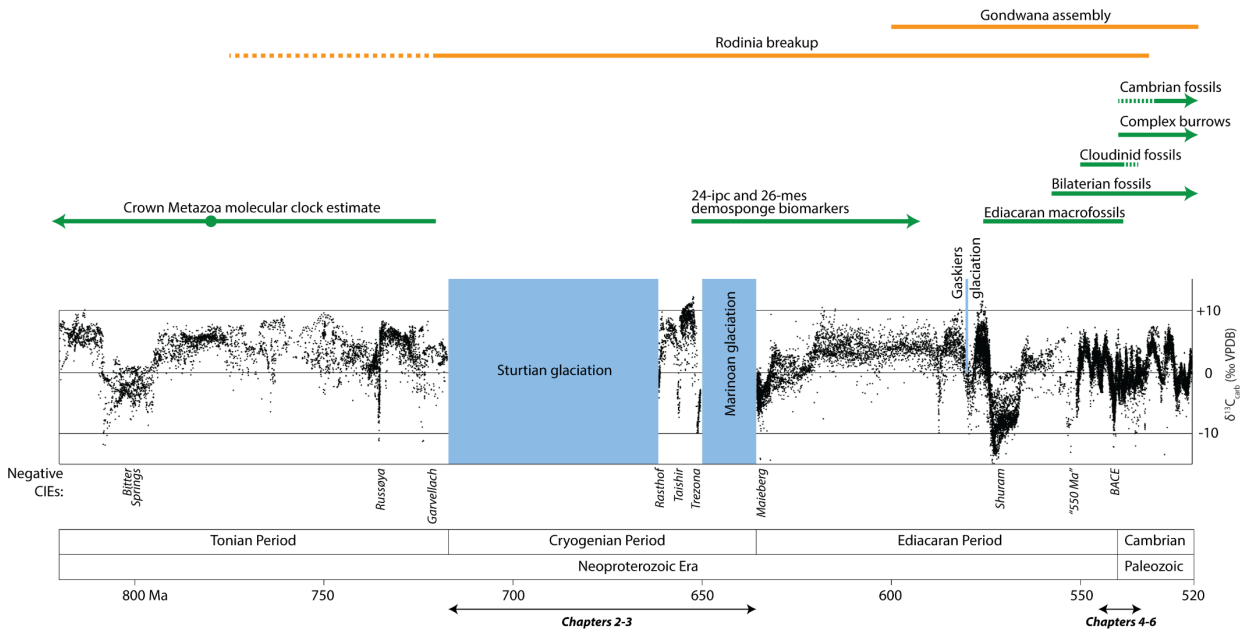

Figure 1.1. Earth-life changes in the late Neoproterozoic–early Cambrian including composite carbon isotope record of carbonate rocks, glacial intervals, major biological innovations, and supercontinent reorganization. Time intervals examined in this thesis indicated in bold. Data compiled from Love et al. (2009), Macdonald et al. (2010), Erwin et al. (2011), Pu et al. (2016), Rooney et al. (2020), Park et al. (2020), Nelson et al. (2020), Yang et al. (2021), Bowyer et al. (2022), and references within each of these publications. CIEs—carbon isotope excursions.

The Cryogenian Period (c. 717 Ma to 635 Ma) is stratigraphically defined by globally-widespread, low-latitude glacial deposits that are interpreted to have been deposited during Snowball Earth episodes that resulted from ice-albedo climate feedback (e.g., Hoffman et al., 2017, and references therein). Two discrete intervals of Cryogenian glaciation have been recognized, and designated as the Sturtian and Marinoan cryochrons, respectively (Fig. 1.1), derived from stratigraphic nomenclature in the Adelaide basin of South Australia (Mawson and Sprigg, 1950). The onset of the older Sturtian glaciation is estimated at c. 717 Ma based on U-Pb zircon dates of volcanic horizons intercalated with basal glacial diamictite deposits in Yukon, Canada (Macdonald et al., 2010) and below basal diamictite deposits in Ethiopia (MacLennan et al., 2018). The termination of the Sturtian glacial interval is estimated at c. 661 Ma, calibrated by a syn-glacial U-Pb date from an ash bed within upper glacial deposits of South Australia and by post-glacial U-Pb

dates from ash beds above glacial deposits in South China (Cox et al., 2018; Rooney et al., 2020), demonstrating an ~56 m.y. duration for the Sturtian cryochron. The onset and duration of the younger Marinoan glaciation are comparatively poorly calibrated. Astrochronology based on the cyclostratigraphic analysis of magnetic susceptibility measurements in post-Sturtian strata in South China suggests an ~9.8 m.y. duration for the nonglacial interlude, which would indicate a c. 651 Ma Marinoan initiation if there are no unconformities in this succession (Bao et al., 2018). A syn-glacial U-Pb date from an ash bed within Marinoan glacial deposits in northern Namibia confirms the Marinoan cryochron was ongoing by c. 639 Ma (Prave et al., 2016). The end of the Marinoan is well-calibrated at c. 635 Ma based on U-Pb ash bed dates within and above Marinoan glacial deposits in China, Namibia, and South Australia (Hoffmann et al., 2004; Condon et al., 2005; Calver et al., 2013; Prave et al, 2016; Zhou et al., 2019). Global synchroneity of both the Sturtian and Marinoan deglaciations are further supported by Re-Os dates from organic rich shale and carbonate overlying glacial deposits in North America, Mongolia, South China, and Svalbard (Rooney et al., 2014, 2015, 2020; Millikin et al. 2022).

Once a Snowball Earth glaciation is established from runaway ice sheet advance towards the equator, that climate state is maintained by ice albedo (e.g., Budyko, 1969; Kirschvink, 1992). Over millions of years, continuous outgassing from volcanic emissions, coupled with reduced silicate-weathering carbon sinks leads to increasing buildup of atmospheric CO_2 (e.g., Le Hir et al., 2008). The modeled deglaciation threshold of a hard Snowball Earth with thick tropical ice is predicted as at least 0.29 bar (660% of present atmospheric levels) of pCO_2 (Pierrehumbert, 2005). However, it is likely lower, in the range of 0.01-0.1 bar, when accounting for reduced albedo due to surface dust (Abbot and Pierrehumbert, 2010), which is more consistent with oxygen isotope anomalies preserved in Cryogenian and basal Ediacaran sulfate minerals (Bao et al., 2008, 2009).

Following initiation of deglaciation, the positive ice-albedo feedback of open water would lead to rapid ice line retreat to higher latitudes and complete deglaciation in <2,000 years (Hyde et al., 2000). The high pCO_2 and low planetary albedo of the ensuing ice-free Earth would result in extreme greenhouse conditions, within which low-density meltwater would form a stable freshwater lid of ~1 km with sea surface temperatures of 40° to 60°C that could be maintained for 10,000 to 100,000 years (Yang et al., 2017). The meltwater lid would be supersaturated with respect to $CaCO_3$, as a result of high alkalinity driven by equilibration with high pCO_2, combined with intensive carbonate and loess weathering, which would promote the deposition of cap carbonate sequences of the type that overlie Sturtian and Marinoan glacial sequences, globally (Higgins and Schrag, 2003; Hoffman, 2011).

Sturtian and Marinoan cap carbonate sequences are generally associated with sea level transgression related to deglaciation, but local sea level histories are complicated by the effects of gravitational interaction between ice sheets and oceans and isostatic adjustments of the solid Earth (Hoffman and Macdonald, 2011; Creveling and Mitrovica, 2014). The cap carbonate sequences preserve characteristic negative carbon isotope excursions that have been attributed to a shutdown in biological productivity that caused a shift towards mantle carbon isotope composition in the ocean-atmosphere system (Hoffman et al., 1998), combined with the effects of increasing temperature and the balance of carbonate and silicate weathering (Higgins and Schrag, 2003). Alternatively, destabilized methane hydrates (e.g., Jiang et al., 2003) or kinetic isotope effects (e.g., Ahm et al., 2019) during and following deglaciation may have contributed to generation of these excursions. Lateral gradients in these carbon isotopes excursions have been attributed to diachronous deposition (Hoffman et al., 2007) or to variability of early diagenetic dolomitization (Ahm et al., 2019; Hoffman and Lamothe, 2019). In the aftermath of Snowball Earth glaciation,

enhanced silicate weathering is thought to have been driven by greenhouse conditions interacting with large volumes of loess, glacial till, and fractured rock (e.g., Walker et al., 1981; Fabre et al., 2012). These processes would have stabilized CO_2 levels to pre-glacial levels in ~1 m.y. (Higgins and Schrag, 2003; Le Hir et al., 2009), although physical transport limitations could have reduced silicate weathering rates and protracted carbon cycle stabilization to ~10 m.y. (Mills et al., 2011).

The processes that initiated Cryogenian Snowball Earth glaciations remain ambiguous, but global paleogeography was certainly a contributing factor. The position of the Neoproterozoic supercontinent Rodinia at equatorial latitudes (Fig. 1.2; Li et al., 2013; Merdith et al., 2017) increased planetary albedo (Kirschvink, 1992) and enhanced silicate weathering due to considerable continental area in the hot and wet tropics (Walker et al., 1981; Marshall et al., 1988). Furthermore, large areas of rifted continental margins were generated during supercontinent break-up in the late Tonian and Cryogenian, possibly increasing continental runoff (Donnadieu et al., 2004) and shelf area for organic carbon burial (Hoffman et al., 1998). The absence of high-latitude continents could have inhibited the operation of the silicate weathering feedback, as the growth of polar ice sheets did not reduce continental weathering (Schrag et al., 2002).

Within this relatively cool background climate state in the Tonian, a more proximal trigger for initiation of the Sturtian glaciation could relate to emplacement of the rift-related Franklin Large Igneous Province (LIP) at low-latitudes, between c. 720 and 715 Ma (Denyszyn et al., 2009; Macdonald et al., 2010; Eyster et al., 2017). The emplacement of large volumes of fresh, weatherable basalt into the tropics would have enhanced silicate weathering and CO_2 consumption (Godderís et al., 2003), which is supported by Nd and Sr isotopic data that suggest a coeval influx of juvenile material into sedimentary basins (Cox et al., 2016). Associated phosphorous delivery could have further augmented CO_2 drawdown by promoting efficient organic carbon production

and burial, a model which is supported by relatively ^{13}C-enriched marine carbonates in the late Tonian (Horton, 2015). The Franklin LIP partially intruded evaporite basins, and many of its sills and dikes contain high sulfur concentrations as a result (Bedard et al., 2016). Therefore, in an alternative model, stratospheric sulfur aerosol injections from these eruptions could have increased albedo and initiated the Sturtian glaciation, particularly if the background climate state was relatively cool, lowering the tropopause height (Macdonald and Wordsworth, 2017). Arabian-Nubian arc accretion and exhumation in the tropics during the Tonian may have also enhanced weathering and CO_2 drawdown in the lead up to the Sturtian glaciation (Park et al., 2020). Proximal triggers for the onset of the Marinoan glaciation remain even more uncertain, although silicate weathering of glacial regolith developed during the Sturtian may have played a role (Mills et al., 2011). Following the Cryogenian Period, continued continental reconfiguration eventually led to a global paleogeography with high latitude continents less conducive to initiation of Snowball Earth glaciations (Fig. 1.2; Li et al., 2013).

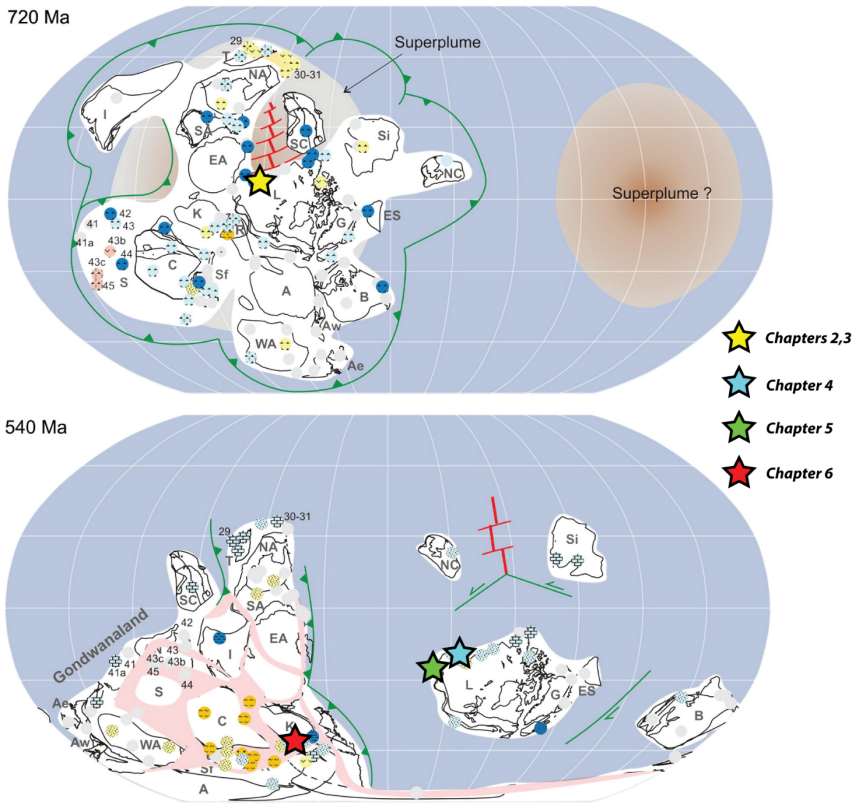

Figure 1.2. Paleogeographic reconstructions at the base of the Cryogenian Period (~720 Ma) and base of the Cambrian Period (~540 Ma) from Li et al. (2013), showing locations of study areas examined in this thesis.

The Ediacaran Period (c. 635-539 Ma), which followed the termination of the Marinoan glaciation, is characterized by the first major diversification of multicellular eukaryotes, predating the more-widely-celebrated Cambrian radiation of modern metazoan clades. The mechanistic relationships among surface environment changes and biotic extinction and evolution across the late Ediacaran and early Cambrian remain poorly understood. While molecular clock analyses predict metazoan origination in the Tonian or Cryogenian (e.g., Erwin et al., 2011), the oldest stratigraphic evidence for animals comes from 24-isopropylcholestane and 26-methylstigmastane biomarkers that occur in late Cryogenian and basal Ediacaran oils and are attributed to marine demosponges (Fig. 1.1; Love et al., 2009; Zumberge et al., 2018). The earliest radioisotopically

dated multicellular Ediacaran macrofossils occur in the late Ediacaran at c. 570 Ma (Pu et al., 2016). These soft-bodied organisms have been variably interpreted as a mixture of stem- and crown-group animals and extinct lineages (e.g., Xiao and Laflamme, 2009) or as extinct higher order clades (e.g., Budd and Jackson, 2016). Based on temporal distribution of different Ediacaran fossil morphoclades, they have been divided into three distinct biostratigraphic assemblages: the Avalon (c. 570-560 Ma), White Sea (c. 560-550 Ma), and Nama (c. 550-539 Ma) assemblages (Martin et al., 2000; Waggoner, 2003; Bowring et al., 2007; Xiao and Laflamme, 2009; Noble et al., 2015; Pu et al., 2016; Linnemann et al., 2019). Although a number of morphoclades and specific taxa occur within two or three of these assemblages, the assemblages may be partially explained by intra-Ediacaran extinction and biotic turnover (e.g., Darroch et al., 2018).

The Avalon assemblage comprises paleoecological communities that are environmentally restricted to offshore and slope environments below wave base, so it is difficult to make direct taxonomic comparisons to the White Sea and Nama assemblages, which have different ecologies (e.g., Boag et al., 2016; Muscente et al., 2019). However, the White Sea assemblage, which contains the highest diversity of Ediacaran body fossils, and the Nama assemblage both occupy shelf environments and have sufficiently divergent diversity to be considered as distinct biostratigraphic zones (Boag et al., 2016; Darroch et al., 2018; Muscente et al., 2019). The White Sea assemblage (c. 560-550 Ma) includes the first fossil evidence for bilaterian metazoans: occurrence of the body fossil *Kimberella*, which has some mollusk-like characteristics (Fedonkin and Waggoner, 1997; Martin et al., 2000), and stratigraphically lower occurrences of the trace fossil *Helminthoidichnites* (e.g., Gehling and Droser, 2012), which are potentially the trails of the meiobenthic organism *Ikaria* (Evans et al., 2020). While the terminal Ediacaran Nama assemblage (c. 550-539 Ma) includes lower overall fossil diversity than the White Sea assemblage, it hosts

significantly higher trace fossil diversity (e.g., Mangano and Buatois, 2014), a higher diversity of tubular organisms (cloudinomorphs) that are probable metazoans (e.g., Zhuravlev et al., 2015; Schiffbauer et al., 2016, 2020), and the earliest mineralized macrofossils (e.g., Germs, 1972; Grotzinger et al., 2000).

The ensuing Cambrian Period is characterized by the diversification of metazoans into the majority of extant animal phyla (e.g., Marshall, 2006; Erwin et al., 2011). The base of the Cambrian is defined by the Global Boundary Stratotype Section and Point at Fortune Head, Newfoundland and is intended to coincide with the first appearance of the trace fossil *Treptichnus pedum*, which was thought to be the first evidence of a bilaterian capable of creating complex burrows in both horizontal and vertical directions (Narbonne et al., 1987; Brasier et al., 1994; Landing, 1994). In sections lacking fossils of *Treptichnus pedum*, other secondary biostratigraphic markers that may constrain the Ediacaran–Cambrian boundary include the last occurrence of Ediacaran soft-bodied fossils such as erniettomorphs (e.g., Grotzinger et al., 1995), the last occurrence of tubular mineralized fossils belonging to taxa of cloudinomorphs (e.g., Grant, 1990), and the first occurrence of early Cambrian small shelly fossils that include *Anabarites* and *Protohertzina* (e.g., Qian et al., 2001).

Potential complications in the biostratigraphic utility of these fossils include the appearance of relatively complex bed-penetrative bilaterian burrows within the terminal Ediacaran prior to *Treptichnus pedum* (e.g., Jensen et al., 2000; Jensen and Runnegar, 2005; Buatois et al., 2018), potential stratigraphic overlap between cloudinomorph fossils and small shelly fossils of the *Anabarites trisulcatus-Protohertzina anabarica* assemblage zone (e.g. Zhu et al., 2017; Yang et al., 2020), and isolated occurrences of putative erniettomorphs within the Cambrian (e.g., Jensen et al., 1998; Hagadorn and Waggoner, 2000). Recognition of stratigraphic association between the

first appearance of *Treptichnus pedum* and a large negative carbon isotope excursion (Narbonne et al., 1994; Corsetti and Hagadorn, 2000), has led to the definition of the BAsal Cambrian carbon isotope Excursion (BACE) that, in some sections, also appears to post-date the last occurrences of cloudinomorphs and erniettomorphs (e.g., Corsetti and Hagadorn, 2003; Amthor et al., 2003; Smith et al., 2016, 2017). This carbon isotope excursion has been proposed as a formal marker for identifying the Ediacaran–Cambrian boundary (Zhu et al., 2019). Although this is an eon-scale stratigraphic boundary, the absolute ages and temporal correlations of these biostratigraphic and geochemical markers remain poorly defined, and hypothesized mechanistic links among carbon cycle instability, the extinction of Ediacaran clades, and the Cambrian radiation of metazoans are inconclusive and debated. The ability to test different hypotheses that have been proposed for coeval biotic and environmental change across this transition are limited by the precision with which disparate sections can be correlated.

The subsequent chapters of this thesis will contribute geological data to constrain surface environment and evolutionary changes across the Ediacaran–Cambrian boundary and variability in Cryogenian climate and geochemistry, through the lens of focused regional stratigraphic investigation. The integration of these types of regional stratigraphic data sets ultimately forms the backbone of the global record of Earth history (Fig. 1.1).

1.2. References

Abbot, D.S., and Pierrehumbert, R.T., 2010, Mudball: Surface dust and snowball Earth deglaciation: Journal of Geophysical Research: Atmospheres, v. 115, no. D03104, 11 p.

Ahm, A.S.C., Maloof, A.C., Macdonald, F.A., Hoffman, P.F., Bjerrum, C.J., Bold, U., Rose, C.V., Strauss, J.V., and Higgins, J.A., 2019, An early diagenetic deglacial origin for basal Ediacaran "cap dolostones": Earth and Planetary Science Letters, v. 506, p. 292–307.

Amthor, J.E., Grotzinger, J.P., Schröder, S., Bowring, S.A., Ramezani, J., Martin, M.W., and Matter, A., 2003, Extinction of Cloudina and Namacalathus at the Precambrian-Cambrian boundary in Oman: Geology, v. 31, p. 431–434. doi:10.1130/0091-7613(2003)031<0431:EOCANA>2.0.CO;2.

Bao, H., Fairchild, I.J., Wynn, P.M., and Spötl, C., 2009, Stretching the envelope of past surface environments: Neoproterozoic glacial lakes from Svalbard: Science, v. 323, no. 5910, p. 119–122.

Bao, H., Lyons, J.R., and Zhou, C., 2008, Triple oxygen isotope evidence for elevated CO_2 levels after a Neoproterozoic glaciation: Nature, v. 453, no. 7194, p. 504–506.

Bao, X., Zhang, S., Jiang, G., Wu, H., Li, H., Wang, X., An, Z., and Yang, T., 2018, Cyclostratigraphic constraints on the duration of the Datangpo Formation and the onset age of the Nantuo (Marinoan) glaciation in South China: Earth and Planetary Science Letters, v. 483, p. 52–63.

Bédard, J.H., Hayes, B., Hryciuk, M., Beard, C., Williamson, N., Dell'Oro, T.A., Rainbird, R.H., Prince, J., Baragar, W.R.A., Nabelek, P.I., and Weis, D., 2016, Geochemical database of Franklin sills, Natkusiak Basalts and Shaler Supergroup rocks, Victoria Island, Northwest Territories, and correlatives from Nunavut and the mainland: Geoligical Survey of Canada Open File, v. 8009, no. 1.

Boag, T.H., Darroch, S.A., and Laflamme, M., 2016, Ediacaran distributions in space and time: testing assemblage concepts of earliest macroscopic body fossils: Paleobiology, v. 42, no. 4, p. 574–594.

Bowring, S.A., Grotzinger, J.P., Condon, D.J., Ramezani, J., Newall, M.J. and Allen, P.A., 2007. Geochronologic constraints on the chronostratigraphic framework of the Neoproterozoic Huqf Supergroup, Sultanate of Oman. American Journal of Science, 307(10), pp.1097–1145.

Bowyer, F.T., Zhuravlev, A.Y., Wood, R., Shields, G.A., Zhou, Y., Curtis, A., Poulton, S.W., Condon, D.J., Yang, C., and Zhu, M., 2022, Calibrating the temporal and spatial dynamics of the Ediacaran–Cambrian radiation of animals: Earth-Science Reviews, v. 103913.

Brasier, M., Cowie, J., and Taylor, M., 1994, Decision on the Precambrian-Cambrian boundary stratotype: Episodes Journal of International Geoscience, v. 17, no. 1, p. 3–8.

Buatois, L. A., Almond, J., Mángano, M. G., Jensen, S., and Germs, G. J., 2018, Sediment disturbance by Ediacaran bulldozers and the roots of the Cambrian explosion: Scientific reports, v. 8, no. 1, p. 1–9.

Budd, G.E., and Jackson, I.S., 2016, Ecological innovations in the Cambrian and the origins of the crown group phyla: Philosophical Transactions of the Royal Society B: Biological Sciences, v. 371, no. 1685, p. 20150287.

Budyko, M.I., 1969, The effect of solar radiation variations on the climate of the Earth: Tellus, v. 21, no. 5, p. 611–619.

Calver, C.R., Crowley, J.L., Wingate, M.T.D., Evans, D.A.D., Raub, T.D., and Schmitz, M.D., 2013, Globally synchronous Marinoan deglaciation indicated by U-Pb geochronology of the Cottons Breccia, Tasmania, Australia: Geology, v. 41, no. 10, p. 1127–1130.

Canfield, D.E., and Farquhar, J., 2009, Animal evolution, bioturbation, and the sulfate concentration of the oceans: Proceedings of the National Academy of Sciences, v. 106, no. 20, p. 8123–8127.

Condon, D., Zhu, M., Bowring, S., Wang, W., Yang, A., and Jin, Y., 2005, U-Pb ages from the Neoproterozoic Doushantuo Formation, China: Science, v. 308, no. 5718, p. 95–98.

Corsetti, F.A., and Hagadorn, J.W., 2000, Precambrian-Cambrian transition: Death Valley, United States: Geology, v. 28, p. 299–302. doi:10.1130/0091-7613(2000)028<0299:PCTDVU>2.3.CO;2.

Corsetti, F.A., and Hagadorn, J.W., 2003, The Precambrian–Cambrian Transition in the Southern Great Basin: The Sedimentary Record, v. 1, p. 4–8. doi:10.2110/sedred.2003.1.4.

Cox, G.M., Halverson, G.P., Stevenson, R.K., Vokaty, M., Poirier, A., Kunzmann, M., Li, Z.X., Denyszyn, S.W., Strauss, J.V., and Macdonald, F.A., 2016, Continental flood basalt weathering as a trigger for Neoproterozoic Snowball Earth: Earth and Planetary Science Letters, v. 446, p.89–99.

Cox, G.M., Isakson, V., Hoffman, P.F., Gernon, T.M., Schmitz, M.D., Shahin, S., Collins, A.S., Preiss, W., Blades, M.L., Mitchell, R.N., and Nordsvan, A., 2018, South Australian U-Pb zircon (CA-ID-TIMS) age supports globally synchronous Sturtian deglaciation: Precambrian Research, v. 315, p. 257–263.

Creveling, J.R., and Mitrovica, J.X., 2014, The sea-level fingerprint of a Snowball Earth deglaciation: Earth and Planetary Science Letters, v. 399, p. 74–85.

Darroch, S. A., Smith, E. F., Laflamme, M., and Erwin, D. H., 2018, Ediacaran extinction and Cambrian explosion: Trends in ecology & evolution, v. 33, no. 9, p. 653–663.

Denyszyn, S.W., Halls, H.C., Davis, D.W., and Evans, D.A., 2009, Paleomagnetism and U–Pb geochronology of Franklin dykes in High Arctic Canada and Greenland: a revised age and paleomagnetic pole constraining block rotations in the Nares Strait region: Canadian Journal of Earth Sciences, v. 46, no. 9, p. 689–705.

Donnadieu, Y., Goddéris, Y., Ramstein, G., Nédélec, A., and Meert, J., 2004, A 'snowball Earth' climate triggered by continental break-up through changes in runoff: Nature, v. 428, no. 6980, p. 303–306.

Erwin, D.H., Laflamme, M., Tweedt, S.M., Sperling, E.A., Pisani, D., and Peterson, K.J., 2011, The Cambrian conundrum: early divergence and later ecological success in the early history of animals: Science, v. 334, no. 6059, p. 1091–1097.

Evans, S.D., Hughes, I.V., Gehling, J.G., and Droser, M.L., 2020, Discovery of the oldest bilaterian from the Ediacaran of South Australia: Proceedings of the National Academy of Sciences, v. 117, no. 14, p. 7845–7850.

Eyster, A.E., Fu, R.R., Strauss, J.V., Weiss, B.P., Roots, C.F., Halverson, G.P., Evans, D.A., and Macdonald, F.A., 2017, Paleomagnetic evidence for a large rotation of the Yukon block relative to Laurentia: Implications for a low-latitude Sturtian glaciation and the breakup of Rodinia: Geological Society of America Bulletin, v. 129, no 1-2, p. 38–58.

Fabre, S., and Berger, G., 2012, How tillite weathering during the snowball Earth aftermath induced cap carbonate deposition: Geology, v. 40, no. 11, p. 1027–1030.

Fedonkin, M.A., and Waggoner, B.M., 1997, The Late Precambrian fossil Kimberella is a mollusc-like bilaterian organism: Nature, v. 388, no. 6645, p. 868–871.

Gehling, J.G., and Droser, M.L., 2012, Ediacaran stratigraphy and the biota of the Adelaide Geosyncline, South Australia: Episodes, v. 35, no. 1, p. 236–246.

Germs, G.J., 1972, New shelly fossils from Nama Group, South West Africa: American Journal of Science, v. 272, no. 8, p. 752–761.

Goddéris, Y., Donnadieu, Y., Nédélec, A., Dupré, B., Dessert, C., Grard, A., Ramstein, G., and François, L.M., 2003, The Sturtian 'snowball'glaciation: fire and ice: Earth and Planetary Science Letters, v. 211, no. 1-2, p.1–12.

Grant, S.W., 1990, Shell structure and distribution of *Cloudina*, a potential index fossil for the terminal Proterozoic: American Journal of Science, v. 290, p .261–294.

Grotzinger, J. P., 2000, Facies and paleoenvironmental setting of thrombolite-stromatolite reefs, terminal Proterozoic Nama Group (ca. 550–543 Ma), central and southern Namibia: Communications of the Geological Survey of Namibia, v. 12, p. 221–233.

Grotzinger, J. P., Bowring, S. A., Saylor, B. Z., and Kaufman, A. J., 1995, Biostratigraphic and geochronologic constraints on early animal evolution: Science, v. 270, no. 5236, p. 598–604.

Hagadorn, J.W., and Waggoner, B., 2000, Ediacaran fossils from the southwestern Great Basin, United States: Journal of Paleontology, v. 74, no. 2, p. 349–359.

Halverson, G.P., Hoffman, P.F., Schrag, D.P., Maloof, A.C., and Rice, A.H.N., 2005, Toward a Neoproterozoic composite carbon-isotope record: GSA bulletin, v. 117, no. 9-10, p. 1181–1207.

Higgins, J.A., and Schrag, D.P., 2003, Aftermath of a snowball Earth: Geochemistry, Geophysics, Geosystems, v. 4, no. 3, p. 1028.

Hoffman, P.F., 2011, Strange bedfellows: glacial diamictite and cap carbonate from the Marinoan (635 Ma) glaciation in Namibia: Sedimentology, v. 58, no. 1, p. 57–119.

Hoffman, P.F., and Lamothe, K.G., 2019, Seawater-buffered diagenesis, destruction of carbon isotope excursions, and the composition of DIC in Neoproterozoic oceans: Proceedings of the National Academy of Sciences, v. 116, v. 38, p. 18874–18879.

Hoffman, P.F., and Macdonald, F.A., 2010, Sheet-crack cements and early regression in Marinoan (635 Ma) cap dolostones: regional benchmarks of vanishing ice-sheets?: Earth and Planetary Science Letters, v. 300, no. 3-4, p. 374–384.

Hoffman, P.F., et al., 2017, Snowball Earth climate dynamics and Cryogenian geology-geobiology: Science Advances, v. 3, p. e1600983.

Hoffman, P.F., Halverson, G.P., Domack, E.W., Husson, J.M., Higgins, J.A., and Schrag, D.P., 2007, Are basal Ediacaran (635 Ma) post-glacial “cap dolostones” diachronous?: Earth and Planetary Science Letters, v. 258, no. 1-2, p. 114–131.

Hoffman, P.F., Kaufman, A.J., Halverson, G.P., and Schrag, D.P., 1998, A Neoproterozoic snowball earth: *Science*, v. *281*, no. 5381, p. 1342–1346.

Hoffmann, K.H., Condon, D.J., Bowring, S.A., and Crowley, J.L., 2004, U-Pb zircon date from the Neoproterozoic Ghaub Formation, Namibia: constraints on Marinoan glaciation: Geology, v. 32, no. 9, p. 817–820.

Horton, F., 2015, Did phosphorus derived from the weathering of large igneous provinces fertilize the Neoproterozoic ocean?: Geochemistry, Geophysics, Geosystems, v. 16, no. 6, p. 1723–1738.

Hyde, W.T., Crowley, T.J., Baum, S.K., and Peltier, W.R., 2000, Neoproterozoic 'snowball Earth'simulations with a coupled climate/ice-sheet model: Nature, v. 405, no. 6785, p. 425–429.

Jensen, S., and Runnegar, B.N., 2005, A complex trace fossil from the Spitskop Member (terminal Ediacaran–? Lower Cambrian) of southern Namibia: Geological Magazine, v. 142, no. 5, p. 561–569.

Jensen, S., Gehling, J.G. and Droser, M.L., 1998. Ediacara-type fossils in Cambrian sediments. Nature, 393(6685), pp.567-569.

Jensen, S., Saylor, B.Z., Gehling, J.G. and Germs, G.J., 2000. Complex trace fossils from the terminal Proterozoic of Namibia. Geology, 28(2), pp.143-146.

Jiang, G., Kennedy, M.J. and Christie-Blick, N., 2003. Stable isotopic evidence for methane seeps in Neoproterozoic postglacial cap carbonates. Nature, 426(6968), pp.822-826.

Kirschvink, J.L., 1992, Late Proterozoic low-latitude global glaciation: the snowball Earth, *in* Schopf, J.W., and Klein, C., eds., The Proterozoic Biosphere: Cambridge University Press, New York, p. 51–52.

Kirschvink, J.L., 1992, Late Proterozoic low-latitude global glaciation: the snowball Earth, *in* The Proterozoic biosphere: a multidisciplinary study: Cambridge University Press , New York, p. 51-52.

Landing, E., 1994. Precambrian-Cambrian boundary global stratotype ratified and a new perspective of Cambrian time. Geology, 22(2), pp.179-182.

Le Hir, G., Donnadieu, Y., Goddéris, Y., Pierrehumbert, R.T., Halverson, G.P., Macouin, M., Nédélec, A. and Ramstein, G., 2009. The snowball Earth aftermath: Exploring the limits of continental weathering processes. Earth and Planetary Science Letters, 277(3-4), pp.453-463.

Le Hir, G., Ramstein, G., Donnadieu, Y. and Goddéris, Y., 2008. Scenario for the evolution of atmospheric p CO2 during a snowball Earth. Geology, 36(1), pp.47-50.

Li, Z.X., Evans, D.A. and Halverson, G.P., 2013. Neoproterozoic glaciations in a revised global palaeogeography from the breakup of Rodinia to the assembly of Gondwanaland. Sedimentary Geology, 294, pp.219-232.

Li, Z.X., Evans, D.A., and Halverson, G.P., 2013, Neoproterozoic glaciations in a revised global palaeogeography from the breakup of Rodinia to the assembly of Gondwanaland: Sedimentary Geology, v. 294, p. 219–232.

Linnemann, U., Ovtcharova, M., Schaltegger, U., Gärtner, A., Hautmann, M., Geyer, G., Vickers-Rich, P., Rich, T., Plessen, B., Hofmann, M. and Zieger, J., 2019. New high-resolution age

data from the Ediacaran–Cambrian boundary indicate rapid, ecologically driven onset of the Cambrian explosion. Terra Nova, 31(1), pp.49-58.

Love, G.D., Grosjean, E., Stalvies, C., Fike, D.A., Grotzinger, J.P., Bradley, A.S., Kelly, A.E., Bhatia, M., Meredith, W., Snape, C.E. and Bowring, S.A., 2009. Fossil steroids record the appearance of Demospongiae during the Cryogenian period. Nature, 457(7230), pp.718-721.

Macdonald, F.A. and Wordsworth, R., 2017. Initiation of Snowball Earth with volcanic sulfur aerosol emissions. Geophysical Research Letters, 44(4), pp.1938-1946.

Macdonald, F.A., and Wordsworth, R., 2017, Initiation of Snowball Earth with volcanic sulfur aerosol emissions: Geophysical Research Letters, v. 44, no. 4, p. 1938–1946.

Macdonald, F.A., Schmitz, M.D., Crowley, J.L., Roots, C.F., Jones, D.S., Maloof, A.C., Strauss, J.V., Cohen, P.A., Johnston, D.T., and Schrag, D.P., 2010, Calibrating the Cryogenian: Science, v. 327, no. 5970, p. 1241–1243.

Macdonald, F.A., Schmitz, M.D., Crowley, J.L., Roots, C.F., Jones, D.S., Maloof, A.C., Strauss, J.V., Cohen, P.A., Johnston, D.T. and Schrag, D.P., 2010. Calibrating the cryogenian. science, 327(5970), pp.1241-1243.

MacLennan, S., Park, Y., Swanson-Hysell, N., Maloof, A., Schoene, B., Gebreslassie, M., Antilla, E., Tesema, T., Alene, M., and Haileab, B., 2018, The arc of the Snowball: U-Pb dates constrain the Islay anomaly and the initiation of the Sturtian glaciation: Geology, v. 46, no. 6, p. 539–542.

MacLennan, S., Park, Y., Swanson-Hysell, N., Maloof, A., Schoene, B., Gebreslassie, M., Antilla, E., Tesema, T., Alene, M. and Haileab, B., 2018. The arc of the Snowball: U-Pb dates constrain the Islay anomaly and the initiation of the Sturtian glaciation. Geology, 46(6), pp.539-542.

Mángano, M.G. and Buatois, L.A., 2014. Decoupling of body-plan diversification and ecological structuring during the Ediacaran–Cambrian transition: evolutionary and geobiological feedbacks. Proceedings of the Royal Society B: Biological Sciences, 281(1780), p.20140038.

Marshall, C.R., 2006. Explaining the Cambrian "explosion" of animals. Annu. Rev. Earth Planet. Sci., 34, pp.355-384.

Marshall, H.G., Walker, J.C. and Kuhn, W.R., 1988. Long-term climate change and the geochemical cycle of carbon. Journal of Geophysical Research: Atmospheres, 93(D1), pp.791-801.

Martin, M.W., Grazhdankin, D.V., Bowring, S.A., Evans, D.A.D., Fedonkin, M.A. and Kirschvink, J.L., 2000. Age of Neoproterozoic bilatarian body and trace fossils, White Sea, Russia: Implications for metazoan evolution. Science, 288(5467), pp.841-845.

Mawson, D. and Sprigg, R.C., 1950. Subdivision of the Adelaide system. Australian Journal of Science, 13(3), pp.69-72.

Merdith, A.S., Williams, S.E., Müller, R.D. and Collins, A.S., 2017. Kinematic constraints on the Rodinia to Gondwana transition. Precambrian Research, 299, pp.132-150.

Millikin, A.E., Strauss, J.V., Halverson, G.P., Bergmann, K.D., Tosca, N.J. and Rooney, A.D., 2022. Calibrating the Russøya excursion in Svalbard, Norway, and implications for Neoproterozoic chronology. Geology, 50(4), pp.506-510.

Mills, B., Watson, A.J., Goldblatt, C., Boyle, R. and Lenton, T.M., 2011. Timing of Neoproterozoic glaciations linked to transport-limited global weathering. Nature geoscience, 4(12), pp.861-864.

Mills, B., Watson, A.J., Goldblatt, C., Boyle, R., and Lenton, T.M., 2011, Timing of Neoproterozoic glaciations linked to transport-limited global weathering: Nature Geoscience, v. 4, no. 12, p. 861–864.

Muscente, A.D., Bykova, N., Boag, T.H., Buatois, L.A., Mángano, M.G., Eleish, A., Prabhu, A., Pan, F., Meyer, M.B., Schiffbauer, J.D. and Fox, P., 2019. Ediacaran biozones identified with network analysis provide evidence for pulsed extinctions of early complex life. Nature communications, 10(1), pp.1-15.

Narbonne, G.M., Kaufman, A.J. and Knoll, A.H., 1994. Integrated chemostratigraphy and biostratigraphy of the Windermere Supergroup, northwestern Canada: Implications for Neoproterozoic correlations and the early evolution of animals. Geological Society of America Bulletin, 106(10), pp.1281-1292.

Narbonne, G.M., Myrow, P.M., Landing, E. and Anderson, M.M., 1987. A candidate stratotype for the Precambrian–Cambrian boundary, Fortune head, Burin Peninsula, southeastern Newfoundland. Canadian Journal of Earth Sciences, 24(7), pp.1277-1293.

Nelson, L.L., Smith, E.F., Hodgin, E.B., Crowley, J.L., Schmitz, M.D. and Macdonald, F.A., 2020. Geochronological constraints on Neoproterozoic rifting and onset of the Marinoan glaciation from the Kingston Peak Formation in Death Valley, California (USA). Geology, 48(11), pp.1083-1087.

Noble, S.R., Condon, D.J., Carney, J.N., Wilby, P.R., Pharaoh, T.C. and Ford, T.D., 2015. U-Pb geochronology and global context of the Charnian Supergroup, UK: constraints on the age of key Ediacaran fossil assemblages. Bulletin, 127(1-2), pp.250-265.

Och, L.M. and Shields-Zhou, G.A., 2012. The Neoproterozoic oxygenation event: Environmental perturbations and biogeochemical cycling. Earth-Science Reviews, 110(1-4), pp.26-57.

Park, Y., Swanson-Hysell, N.L., MacLennan, S.A., Maloof, A.C., Gebreslassie, M., Tremblay, M.M., Schoene, B., Alene, M., Anttila, E.S., Tesema, T., and Haileab, B., 2020, The lead-up

to the Sturtian Snowball Earth: Neoproterozoic chemostratigraphy time-calibrated by the Tambien Group of Ethiopia. Geological Society of America Bulletin, v. 132, no. 5–6, p. 1119–1149.

Park, Y., Swanson-Hysell, N.L., MacLennan, S.A., Maloof, A.C., Gebreslassie, M., Tremblay, M.M., Schoene, B., Alene, M., Anttila, E.S., Tesema, T. and Haileab, B., 2020. The lead-up to the Sturtian Snowball Earth: Neoproterozoic chemostratigraphy time-calibrated by the Tambien Group of Ethiopia. GSA Bulletin, 132(5-6), pp.1119-1149.

Pierrehumbert, R.T., 2005. Climate dynamics of a hard snowball Earth. Journal of Geophysical Research: Atmospheres, 110(D1).

Prave, A.R., Condon, D.J., Hoffmann, K.H., Tapster, S. and Fallick, A.E., 2016. Duration and nature of the end-Cryogenian (Marinoan) glaciation. Geology, 44(8), pp.631-634.

Prave, A.R., Condon, D.J., Hoffmann, K.H., Tapster, S., and Fallick, A.E., 2016, Duration and nature of the end-Cryogenian (Marinoan) glaciation: Geology, v. 44, no. 8, p. 631–634.

Pu, J.P., Bowring, S.A., Ramezani, J., Myrow, P., Raub, T.D., Landing, E., Mills, A., Hodgin, E. and Macdonald, F.A., 2016. Dodging snowballs: Geochronology of the Gaskiers glaciation and the first appearance of the Ediacaran biota. Geology, 44(11), pp.955-958.

Qian, Y., Li, G.X. and Zhu, M.Y., 2001. The Meishucunian Stage and its small shelly fossil sequence in China. Acta Palaeontologica Sinica, 40(SUPP), pp.54-62.

Rooney, A.D., Macdonald, F.A., Strauss, J.V., Dudás, F.Ö., Hallmann, C. and Selby, D., 2014. Re-Os geochronology and coupled Os-Sr isotope constraints on the Sturtian snowball Earth. Proceedings of the National Academy of Sciences, 111(1), pp.51-56.

Rooney, A.D., Strauss, J.V., Brandon, A.D. and Macdonald, F.A., 2015. A Cryogenian chronology: Two long-lasting synchronous Neoproterozoic glaciations. Geology, 43(5), pp.459-462.

Rooney, A.D., Yang, C., Condon, D.J., Zhu, M. and Macdonald, F.A., 2020. U-Pb and Re-Os geochronology tracks stratigraphic condensation in the Sturtian snowball Earth aftermath. Geology, 48(6), pp.625-629.

Rooney, A.D., Yang, C., Condon, D.J., Zhu, M., and Macdonald, F.A., 2020, U-Pb and Re-Os geochronology tracks stratigraphic condensation in the Sturtian Snowball aftermath: Geology, v. 48, no., 6, p. 625–629.

Schiffbauer, J.D., Huntley, J.W., O'Neil, G.R., Darroch, S.A., Laflamme, M. and Cai, Y., 2016. The latest Ediacaran wormworld fauna: setting the ecological stage for the Cambrian explosion.

Schiffbauer, J.D., Selly, T., Jacquet, S.M., Merz, R.A., Nelson, L.L., Strange, M.A., Cai, Y. and Smith, E.F., 2020. Discovery of bilaterian-type through-guts in cloudinomorphs from the terminal Ediacaran Period. Nature communications, 11(1), pp.1-12.

Schrag, D.P., Berner, R.A., Hoffman, P.F. and Halverson, G.P., 2002. On the initiation of a snowball Earth. Geochemistry, Geophysics, Geosystems, 3(6), pp.1-21.

Smith, E.F., Nelson, L.L., Strange, M.A., Eyster, A.E., Rowland, S.M., Schrag, D.P. and Macdonald, F.A., 2016. The end of the Ediacaran: Two new exceptionally preserved body fossil assemblages from Mount Dunfee, Nevada, USA. Geology, 44(11), pp.911-914.

Smith, E.F., Nelson, L.L., Tweedt, S.M., Zeng, H. and Workman, J.B., 2017. A cosmopolitan late Ediacaran biotic assemblage: new fossils from Nevada and Namibia support a global biostratigraphic link. Proceedings of the Royal Society B: Biological Sciences, 284(1858), p.20170934.

Sperling, E.A. and Stockey, R.G., 2018. The temporal and environmental context of early animal evolution: Considering all the ingredients of an "explosion". Integrative and Comparative Biology, 58(4), pp.605-622.

Waggoner, B., 2003. The Ediacaran biotas in space and time. Integrative and Comparative Biology, 43(1), pp.104-113.

Walker, J.C., Hays, P.B. and Kasting, J.F., 1981. A negative feedback mechanism for the long-term stabilization of Earth's surface temperature. Journal of Geophysical Research: Oceans, 86(C10), pp.9776-9782.

Xiao, S. and Laflamme, M., 2009. On the eve of animal radiation: phylogeny, ecology and evolution of the Ediacara biota. Trends in Ecology & Evolution, 24(1), pp.31-40.

Yang, B., Steiner, M., Schiffbauer, J.D., Selly, T., Wu, X., Zhang, C., and Liu, P., 2020, Ultrastructure of Ediacaran cloudinids suggests diverse taphonomic histories and affinities with non-biomineralized annelids: Scientific Reports, v. 8, p. 1–10. doi:10.1038/s41598-019-56317-x.

Yang, C., Rooney, A.D., Condon, D.J., Li, X.H., Grazhdankin, D.V., Bowyer, F.T., Hu, C., Macdonald, F.A. and Zhu, M., 2021. The tempo of Ediacaran evolution. Science advances, 7(45), p.eabi9643.

Yang, J., Jansen, M.F., Macdonald, F.A. and Abbot, D.S., 2017. Persistence of a freshwater surface ocean after a snowball Earth. Geology, 45(7), pp.615-618.

Zhou, C., Huyskens, M.H., Lang, X., Xiao, S. and Yin, Q.Z., 2019. Calibrating the terminations of Cryogenian global glaciations. Geology, 47(3), pp.251-254.

Zhou, C., Huyskens, M.H., Lang, X., Xiao, S., and Yin, Q.-Z., 2019, Calibrating the terminations of Cryogenian global glaciations: Geology, v. 47, no. 3, p. 251–254.

Zhu, M.Y., Zhuravlev, A.Y., Wood, R.A., Zhao, F. and Sukhov, S.S., 2017. A deep root for the Cambrian explosion: Implications of new bio-and chemostratigraphy from the Siberian Platform. Geology, 45(5), pp.459-462.

Zhu, M., Yang, A., Yuan, J., Li, G., Zhang, J., Zhao, F., Ahn, S.Y., and Miao, L., 2019, Cambrian integrative stratigraphy and timescale of China: Science China–Earth Sciences, v. 62, p. 25–60.

Zhuravlev, A.Y., Wood, R.A. and Penny, A.M., 2015. Ediacaran skeletal metazoan interpreted as a lophophorate. Proceedings of the Royal Society B: Biological Sciences, 282(1818), p.20151860.

Zumberge, J.A., Love, G.D., Cárdenas, P., Sperling, E.A., Gunasekera, S., Rohrssen, M., Grosjean, E., Grotzinger, J.P. and Summons, R.E., 2018. Demosponge steroid biomarker 26-methylstigmastane provides evidence for Neoproterozoic animals. Nature ecology & evolution, 2(11), pp.1709-1714.

CHAPTER 2. GEOCHRONOLOGICAL CONSTRAINTS ON NEOPROTEROZOIC RIFTING AND ONSET OF THE MARINOAN GLACIATION FROM THE KINGSTON PEAK FORMATION IN DEATH VALLEY, CALIFORNIA

A version of this chapter was published in:

[Nelson, L. L., Smith, E. F., Hodgin, E. B., Crowley J. L., Schmitz, M. D., & Macdonald, F. A. (2020). Geochronological constraints on Neoproterozoic rifting and onset of the Marinoan glaciation from the Kingston Peak Formation in Death Valley, California (USA). *Geology*, *48*, *11*, *1083-1087*.]

Abstract

Death Valley (California, USA) hosts iconic Cryogenian snowball Earth deposits, but the lack of direct geochronological constraints has permitted a variety of correlations and age models. Here, we report two precise zircon U-Pb isotope dilution–thermal ionization mass spectrometry dates for the Kingston Peak Formation: a volcanic eruptive age of 705.44 ± 0.28 Ma from the synglacial Limekiln Spring Member and a maximum depositional age of 651.69 ± 0.64 Ma from the nonglacial Thorndike submember, which is below the Wildrose diamictite. These dates confirm that the Limekiln Spring and Surprise members were deposited during the Sturtian glaciation, while the Wildrose submember is a Marinoan glacial deposit, and the overlying Sentinel Peak Member of the Noonday Formation is a Marinoan cap carbonate. Additionally, the age from the Thorndike submember supersedes existing radioisotopic ages from the Datangpo Formation in South China as the youngest constraint on the onset of the Marinoan glaciation, demonstrating that the Cryogenian nonglacial interlude lasted for at least 9 m.y. and the Marinoan glaciation was <17 m.y. long. Cryogenian glaciation in western Laurentia occurred against the backdrop of ~85 m.y.

of episodic rift-related subsidence and magmatism within laterally discontinuous, fault-bound basins.

2.1. Introduction

Along the western margin of Laurentia, the Neoproterozoic–early Cambrian Windermere Supergroup and its correlatives were deposited during basin formation associated with the protracted rifting of Rodinia (e.g., Stewart, 1972; Bond et al., 1985). However, the timing and dynamics of this ~ 250 m.y. interval of rift-related tectonism remain uncertain. Was rifting continuous throughout this time, or were there multiple discrete rifts? Was rifting diachronous with clear directionality along the margin, or were there synchronous pulses? Testing hypotheses related to rift dynamics of this supercontinent breakup requires age models for subsidence and volcanism, which rely on geochronological constraints.

Death Valley (California, USA) hosts a spectacular succession of Neoproterozoic strata within the Pahrump Group, and its uppermost unit, the Kingston Peak Formation, is well known for hosting glacial diamictite (Wright et al., 1976; Miller, 1985; Prave, 1999). Prior to this study, the only existing Neoproterozoic radioisotopic age constraints from this region were two maximum depositional ages: a 775 ± 18 Ma age (laser ablation–inductively coupled plasma mass spectrometry [LA-ICPMS] weighted mean) for the base of the Horse Thief Springs Formation (Mahon et al., 2014), and a 640.3 ± 0.1 Ma age (isotope dilution–thermal ionization mass spectrometry [ID-TIMS] from one zircon) for the Johnnie Formation (Verdel et al., 2011). Due to syn-rift stratigraphic variability and a lack of radioisotopic age constraints from the Pahrump Group and overlying units, correlations of the Death Valley glacial units to dated Cryogenian glaciations have remained contentious. Specifically, it has remained unclear whether the Kingston

Peak Formation was deposited entirely during the Sturtian glacial epoch with evidence of syn-Sturtian nonglacial conditions (Link et al., 2005; Le Heron et al., 2014; Yonkee et al., 2014), or whether the Kingston Peak Formation recorded both the Sturtian and Marinoan snowball Earth glaciations, and the overlying Noonday Formation is a basal Ediacaran cap carbonate (Prave, 1999; Petterson et al., 2011b; Macdonald et al., 2013).

Outside of Death Valley, two distinct Cryogenian (ca. 717-635 Ma) low-latitude glaciations, commonly referred to as snowball Earth events, have been distinguished on the basis of globally integrated stratigraphy, geochemistry, paleomagnetism, and geochronology (Hoffman et al., 2017, and references therein). The onset and termination of the former, the Sturtian glaciation, and the termination of the latter, the Marinoan glaciation, are well-constrained (Fig. 2.1; Condon et al., 2005; Macdonald et al., 2010; Prave et al., 2016; Rooney et al., 2020). However, the onset of the Marinoan glaciation—and, thus, its duration and that of the Cryogenian nonglacial interlude—remains poorly constrained, which has hindered evaluation of mechanisms for extreme climate change. Currently, the Marinoan glacial onset is bracketed by a U-Pb ID-TIMS age of 657.17 ± 0.27 Ma from the pre-glacial Datangpo Formation of South China (Rooney et al., 2020) and a U-Pb ID-TIMS age of 639.29 ± 0.26 Ma from the syn-glacial Ghaub Formation of Namibia (Prave et al., 2016). Here we present new age constraints that integrate the iconic Death Valley strata into global records of Cryogenian Earth history.

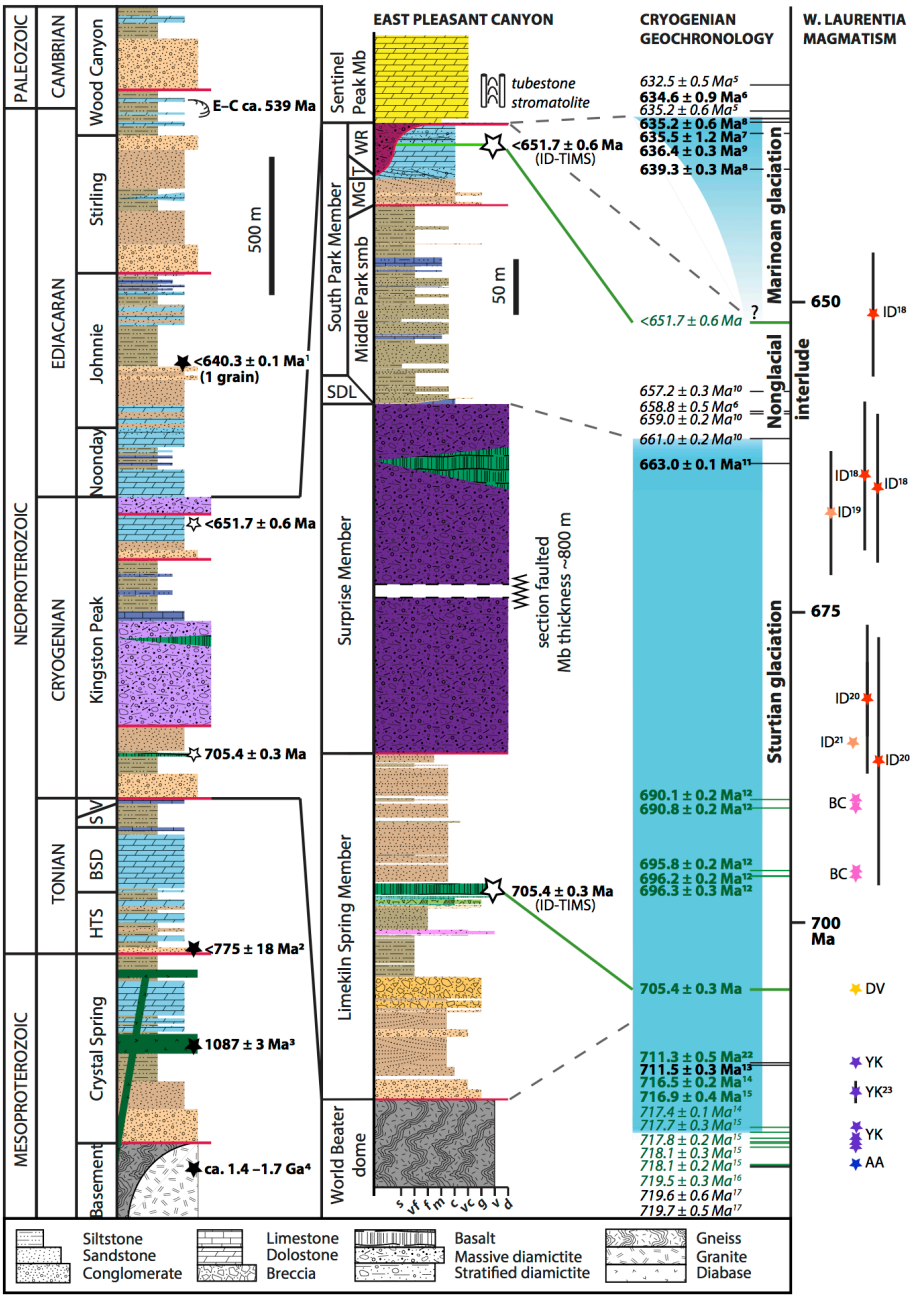

Figure 2.1. Regional and local stratigraphy of Death Valley, and compiled geochronology of the Cryogenian. Red lines are unconformities. Black stars are existing radioisotopic age constraints from Death Valley; white stars are new radioisotopic ages. Italicized ages are nonglacial; bold ages are synglacial. Green ages are from western Laurentia. Colored stars are compiled magmatic ages from western Laurentia and correspond to locations in Figure 2.2. All labelled uncertainties are internal. Mb—Member; smb—submember; HTS—Horse Thief Springs Formation; BSD—Beck Spring Dolomite; S—Saratoga sandstone; V—Virgin Spring Limestone; E-C—Ediacaran-Cambrian boundary; SDL—Sourdough Limestone Mb; MG—Mountain Girl smb; T—Thorndike smb; WR—Wildrose smb; s—siltstone; vf—very fine-grained; f—fine-grained; c—coarse-grained; vc—very coarse-grained; g—conglomerate; v—volcanic; d—diamictite; AA—Arctic Alaska; YK—Yukon; DV—Death Valley; BC—British Columbia, Canada; ID—Idaho. Numbered references are provided in Appendix A1 Table SM1.

2.2. Geological Background

In the Panamint Range, the Kingston Peak Formation is <2 km thick and is exposed for >60 km along both limbs of a doubly plunging anticline (Fig. 2.2; Labotka et al., 1980; Miller, 1985). The lowest unit, the Limekiln Spring Member, unconformably overlies Tonian units of the Pahrump Group and Mesoproterozoic basement. At Pleasant Canyon, it includes: 1) a basal unit, dominated by sedimentary breccia, conglomerate, and arkose, 2) a middle unit of siltstone to fine-grained sandstone with minor sedimentary breccia, rare lonestones, and volcanic and volcaniclastic horizons near the top, and 3) an upper unit composed of dominantly quartz arenite (Fig. 2.1; Labotka et al., 1980; Miller, 1985). The overlying Surprise Member has an erosive base and is composed primarily of massive diamictite with minor pillow basalt, volcaniclastic rocks, and stratified diamictite. It is sharply overlain by <35 m of finely laminated dark-blue limestone of the Sourdough Limestone Member, and a <1 km succession of mixed siliciclastic and carbonate strata of the South Park Member. In most sections, the Sourdough Limestone Member is gradationally overlain by the Middle Park submember of the South Park Member. The Middle Park submember primarily comprises siltstone to shale with minor thin beds of silty limestone and channelized bodies of arkose that locally erode the Sourdough Limestone Member. The Middle Park submember is overlain by the Mountain Girl submember, which is a conglomerate to arenite with an erosional base cutting down through units as low as the Surprise Member above an angular unconformity (Petterson et al., 2011a). Crossbedded arenite of the Mountain Girl submember grades into sandy carbonate and carbonate grainstone of the Thorndike submember. This is in turn unconformably overlain by diamictite of the Wildrose submember, which cuts stratigraphically as low as basement (Miller, 1985; Prave, 1999). The Limekiln Spring Member, Surprise Member,

and Wildrose submember all contain evidence of glacially influenced sedimentation, including massive diamictite with outsized and heterolithic clasts, lonestones, and faceted to striated clasts (e.g., Miller, 1985). The Wildrose submember is sharply overlain by finely laminated peloidal dolostone of the Sentinel Peak Member of the Noonday Formation.

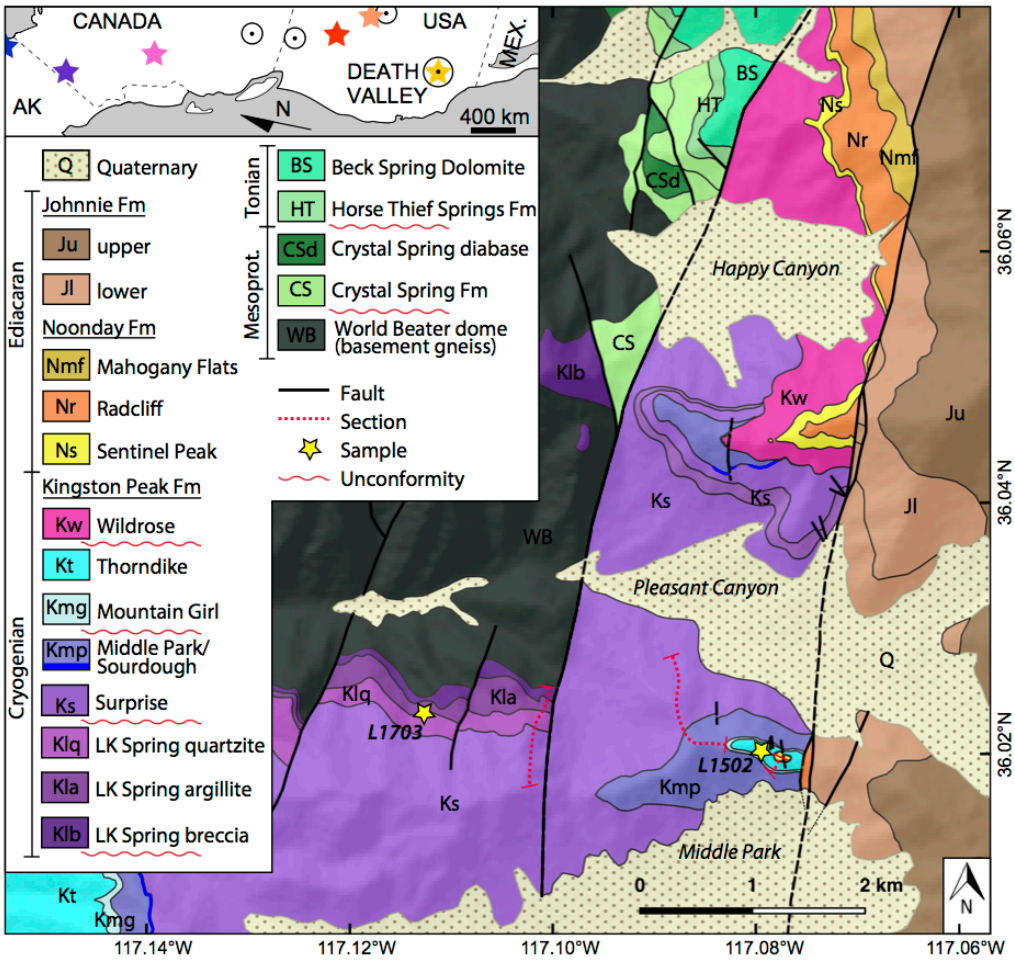

Figure 2.2. Geologic map of eastern Pleasant Canyon in the central Panamint Range, showing locations of measured sections and geochronology samples. Colored stars in inset map correspond to ages in Figure 2.1. Circles mark undated Cryogenian magmatic rocks.

2.3. Methods

2.3.1. Field Methods

Geologic mapping of Proterozoic strata throughout the central Panamint Range was conducted between 2015-2018 on 1:10,000 scale topographic maps, and three stratigraphic sections were

measured in the vicinity of Pleasant Canyon to create the composite section published here (Figs. 2.1, 2.2). Sample L1502 was collected from discontinuous lenses of a 0.2 m-thick light-gray fine-grained laminated siliciclastic unit in the Thorndike submember of the Kingston Peak Formation at 36.02063°N 117.08113°W (Figs. 2.2, 2.3C,F,G). Due to its very fine-grained character (mud to silt grain size), it is difficult to interpret petrographically if this is an epiclastic deposit or a reworked tuff bed. The single ID-TIMS age population of the Cryogenian grains from this sample may indicate an eruptive age (Fig. 2.4A), but it is conservatively interpreted as a maximum depositional age. Sample L1703B was collected from a milky intermediate to felsic horizon containing pillow lava fragment breccia within otherwise mafic volcanic flows in the Limekiln Spring Member of the Kingston Peak Formation at 36.02385°N 117.10602°W (Figs. 2.2, 2.3A,B,D,E).

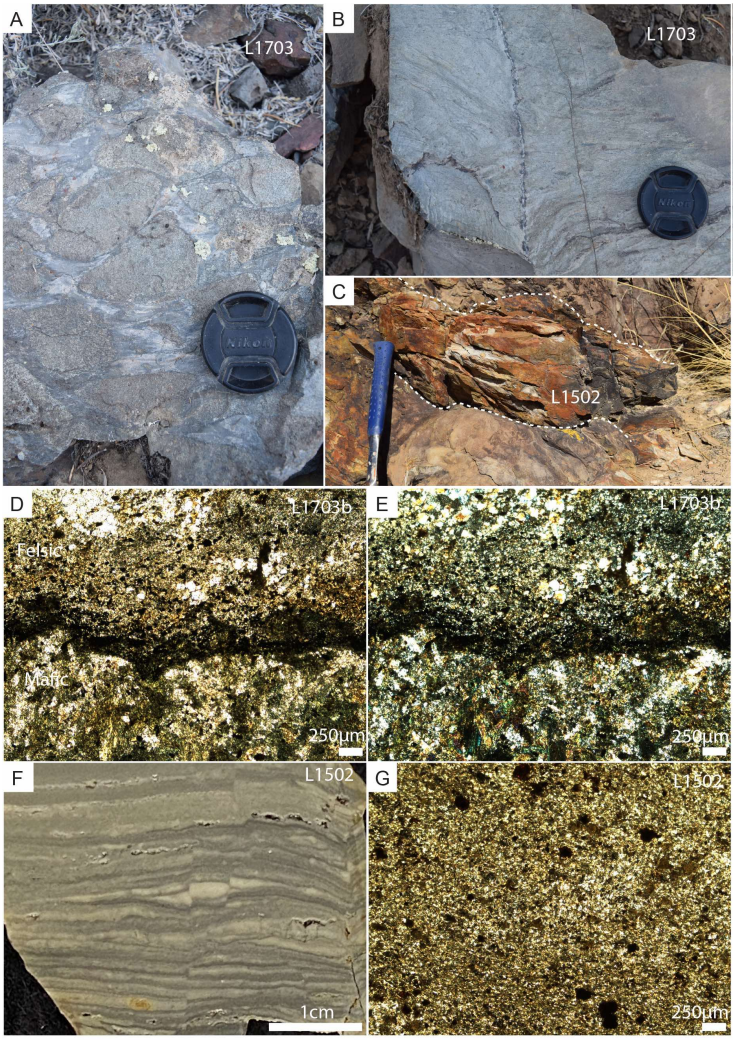

Figure 2.3. Photographs of sampled horizons. Lens cap is 5.2 cm in diameter. Hammer is 33 cm in length. A) Pillow lava fragment breccia within a dacitic flow in volcanic horizon of the Limekiln Spring Member (see Stevenson et al., 2009). B) Felsic zone in volcanic horizon of the Limekiln Spring Member with eutaxitic texture (sample L1703B). C) Siltstone or possible reworked tuff bed within dolomite grainstone of the Thorndike submember (sample L1502). D, E) Photomicrographs of L1703B from volcanic rocks in Limekiln Spring Member showing mafic and felsic zonation in (D) plain polarized light and (E) cross polarized light. F) Polished hand sample of L1502 showing fine laminations. G) Photomicrograph of L1502 showing silt-size grains.

2.3.2. Mineral Separation, Annealing, and Imaging

Sample L1502 from the Thorndike submember was collected three times due to low zircon yield (L1502, L1502B, L1502C). Weathering rinds were trimmed off of L1502A with a rock saw prior to crushing. Sample L1703B from the Limekiln Spring Member was collected once. For all four

samples, zircon grains were separated using a sledge, disc mill or shatterbox, 500 μm sieve, Wilfley shaker table, hand magnet, Frantz magnetic separator, and methylene iodide heavy liquid. Heavy mineral separates were annealed at 900ºC for >48 hours in a muffle furnace. Zircon grains were mounted in epoxy resin and polished. At Boise State University (BSU), zircon grains from all L1502 samples were imaged with a cathodoluminescence (CL) detector using a JEOL JSM-300 scanning electron microscope (SEM) in combination with a Gatan MiniCL. At University of California—Santa Barbara (UCSB), zircon grains from L1703B were imaged using a Centaurus CL detector attached to an FEI Quanta 400f field-emission SEM.

2.3.3. LA-ICPMS Analyses

At UCSB, zircon U-Pb geochronology LA-ICPMS analyses of sample L1703B were conducted with a Photon Machines Excite 193 nm Excimer laser coupled with a Nu Plasma 3D MC-ICPMS and Agilent 7700X quadrupole ICPMS, following the methods of Kylander-Clark et al. (2013). Zircons were ablated with a 25 μm laser spot using fluence and pulse rates of 1 J/cm^2 and 4 Hz, respectively, during a 35 second analysis (2 shots pre-ablation, 20 sec wash out, 15 sec ablation). The primary standards were 91500 (Wiedenbeck et al., 1995) and GJ-1 (Jackson et al., 2004) for calibration of age and trace element composition, respectively, and Plešovice was used as a secondary age standard (Sláma et al., 2008). Bias and drift in U-Pb ratios were corrected using *Iolite* (Paton et al., 2010), following procedures detailed in Kylander-Clark et al. (2013).

At BSU, zircon U-Pb geochronology laser ablation-inductively coupled mass spectrometry (LA-ICPMS) analyses of sample L1502 were conducted with a ThermoElectron X-Series II quadrupole ICPMS and New Wave Research UP-213 Nd:YAG UV laser ablation system. Zircons were ablated with a 25 μm (before August 2019) or 16 μm (starting August 2019) laser spot using fluence and pulse rates of 5 J/cm^2 and 10 Hz, respectively, during a 45 second analysis (15 sec gas

blank, 30 sec ablation) excavating a 25 μm deep pit. Ablated material was carried to the nebulizer flow of the plasma by a 1.2 L/min He gas stream. Total sweep duration is 950 ms, and quadrupole dwell times were 5 ms for Si and Zr, 40 ms for ^{202}Hg, ^{204}Pb, ^{208}Pb, ^{232}Th, and ^{238}U, 80 ms for ^{206}Pb, 200 ms for ^{49}Ti and ^{207}Pb, and 10 ms for all other HFSE and REE. Background count rates were obtained prior to each spot analysis and subtracted from the raw count rate. For concentration calculations, background-subtracted count rates were internally normalized to ^{29}Si and calibrated with the primary standards NIST SRM-610 and -612 glasses. Ablation pits that intersected mineral inclusions were identified based on Ti and P excursions, and associated sweeps were discarded. U-Pb dates from these analyses were retained if U-Pb ratios appeared to have been unaffected by the inclusions. Mass 204 signals were typically indistinguishable from zero following subtraction of Hg backgrounds, and dates are thus reported without common Pb correction.

For U-Pb and ^{207}Pb/^{206}Pb dates, instrumental fractionation of the background-subtracted ratios was corrected, and dates were calibrated with respect to interspersed measurements of standards and reference materials. Standards were used to monitor time-dependent instrumental fractionation based on 2 analyses every 10 analyses of unknown zircons. Radiogenic isotope ratio and age error propagation for all analyses includes uncertainty contributions from counting statistics and background subtraction. These uncertainties are the local standard deviations of the polynomial fits to the interspersed primary standard measurements versus time for the time-dependent, relatively larger U-Pb fractionation factor, and the standard errors of the means of the consistently time-invariant and smaller ^{207}Pb/^{206}Pb fractionation factor. These uncertainties are 0.7-1.7% (average of 1.1%) (2s) for ^{206}Pb/^{238}U and 0.2-0.8% (average of 0.6%) (2s) for ^{207}Pb/^{206}Pb. Errors on dates from individual analyses are given at 2s, and zircon LA-ICPMS metadata and data

are presented in Appendix A1 Table SM2. Kernel density estimation and Wetherill concordia plots (Fig. 2.4) were created using *IsoplotR* (Vermeesch, 2018).

2.3.4. CA-ID-TIMS Analyses

At BSU, single zircon U-Pb geochronology chemical abrasion-isotope dilution-thermal ionization mass spectrometry (CA-ID-TIMS) analyses were conducted on zircon grains from L1502 and L1703B based on LA-ICPMS screening, using methods modified after Mattinson (2005). Single annealed zircons were removed from epoxy mounts and transferred to 3 ml Teflon PFA beakers, loaded into 300 µl Teflon PFA microcapsules with 120 µl of 29 M HF, and partially dissolved for 12 hours at 190°C. Zircons were returned to 3 ml Teflon PFA beakers, rinsed in ultrapure H_2O, immersed in 3.5 M HNO_3, ultrasonically cleaned for one hour, and fluxed for 1 hour at 80°C. The HNO_3 was removed and zircons were rinsed twice in ultrapure H_2O, then reloaded into Teflon PFA beakers and spiked with BSU1B tracer solution with a calibration of $^{235}U/^{205}Pb = 77.93$ and $^{233}U/^{235}U = 1.007066$. Zircons were dissolved in 120 µl of 29 M HF for 48 hours at 220°C, dried to fluorides, and dissolved in 6 M HCl for 12 hours at 180°C. Uranium and Pb were separated using an HCl-based anion-exchange chromatographic procedure (Krogh, 1973), eluted together and dried with 2 µl of 0.05 N H_3PO_4.

Uranium and Pb were loaded on a single outgassed Re filament in 5 µl of a silica-gel/ H_3PO_4 mixture (Gerstenberger and Haase, 1997), and U and Pb isotopic measurements made on a GV IsotopX Phoenix multicollector thermal ionization mass spectrometers equipped with an ion-counting Daly detector. Lead isotopes for analyses with smaller amounts of radiogenic Pb were measured by peak- jumping all isotopes on the Daly detector for 150 cycles, and corrected for 0.16 ± 0.06%/a.m.u. (2s) mass fractionation. Lead isotopes for analyses with larger amounts of radiogenic Pb were measured by a Faraday-Daly routine that cycles 150-200 times between

placing mass 204 in the axial Daly collector and masses 205-208 on the H1-H4 Faraday detectors to placing mass 205 in the axial Daly and masses 206-208 in the H1-H3 Faradays, providing real-time Daly gain correction. These results were corrected for 0.10 ± 0.06%/a.m.u. (2s) mass fractionation. Transitory isobaric interferences due to high-molecular weight organics, particularly on ^{204}Pb and ^{207}Pb, disappeared within approximately 30 cycles. The ionization efficiency of each Pb isotope averaged 10^4 cps/pg. Linearity (to ≥1.4 x 10^6 cps) and the associated deadtime correction of the Daly detector were monitored by repeated analyses of NBS982. Uranium was analyzed as UO_2^+ ions in static Faraday mode on 10^{11} or 10^{12} ohm resistors for 200-300 cycles, and corrected for isobaric interference of $^{233}U^{18}O^{16}O$ on $^{235}U^{16}O^{16}O$ with an $^{18}O/^{16}O$ of 0.00206. Ionization efficiency averaged 20 mV/ng of each U isotope. Uranium mass fractionation was corrected using the known $^{233}U/^{235}U$ ratio of the tracer solutions.

CA-ID-TIMS U-Pb dates and uncertainties were calculated using the algorithms of Schmitz and Schoene (2007) and U decay constants recommended by Jaffey et al. (1971). $^{206}Pb/^{238}U$ ratios and dates were corrected for initial ^{230}Th disequilibrium using a Th/U[magma] = 3.0 ± 0.3, resulting in an increase in the $^{206}Pb/^{238}U$ dates of ~0.09 Ma. All common Pb in analyses was attributed to laboratory blank and subtracted based on the measured laboratory Pb isotopic composition and associated uncertainty. Uranium blanks were estimated at 0.013 pg. CA-ID-TIMS weighted mean $^{206}Pb/^{238}U$ dates were calculated from equivalent dates (pof >0.05) using *Isoplot 3.0* (Ludwig, 2003). Errors on the weighted mean dates are given as ± x / y / z, where x is the internal error based on analytical uncertainties only, including counting statistics, subtraction of tracer solution, and blank and initial common Pb subtraction, y includes the tracer calibration uncertainty propagated in quadrature, and z includes the ^{238}U decay constant uncertainty propagated in quadrature. Internal errors should be considered when comparing dates with

$^{206}Pb/^{238}U$ dates from other laboratories that used the same EARTHTIME tracer solution or a tracer solution that was cross-calibrated using EARTHTIME gravimetric standards. Errors including the uncertainty in the tracer calibration should be considered when comparing dates with those derived from other geochronological methods using the U-Pb decay scheme. Errors including uncertainties in the tracer calibration and ^{238}U decay constant (Jaffey et al., 1971) should be considered when comparing our dates with those derived from other geochronological decay schemes. Errors for weighted mean dates and dates from individual grains are given at 2s, and U-Pb CA-ID-TIMS data are presented in Appendix A1 Table SM3. Weighted mean plots (Fig. 2.4) were created using *IsoplotR* (Vermeesch, 2018).

2.4. Results

Sample L1502 was collected from a lenticular 0.2-m-thick bed of laminated light-gray siltstone within dolostone of the upper Thorndike submember, ~15 m below the base of the Wildrose submember (Fig. 2.3C,F,G). The first sample processed (L1502A) yielded a peak of late Neoproterozoic zircons, as well as late Paleoproterozoic to Mesoproterozoic zircons (Fig. 2.4A). Subsequent samples (L1502B and L1502C) were not trimmed prior to crushing, and also include Mesozoic and Cenozoic populations readily identified as from weathering rind and regolith contamination (common igneous ages within the Panamint Range; e.g., Andrew, 2002; Fig. 2.4A). ID-TIMS analyses of the late Neoproterozoic population resulted in four concordant analyses with a weighted mean $^{206}Pb/^{238}U$ age of 651.69 ± 0.64/0.73/0.99 Ma (internal/internal and tracer/internal, tracer, and decay constant 2*s* uncertainties) (mean square weighted deviation [MSWD] = 1.0; probability of fit [POF] = 0.40), and one slightly older analysis of 654.21 ± 0.47 Ma that was not included in the weighted mean (Fig. 2.4A).

Sample L1703B was collected from an intermediate to felsic horizon within otherwise mafic volcanic flows of the Limekiln Spring Member, interpreted as subaqueous flows rather than intrusions due to the presence of amygdules, pillow lava, and interfingering volcaniclastic breccia (Fig. 2.3A). This sample yielded a peak of Neoproterozoic grains, as well as peaks of late Paleoproterozoic to Mesoproterozoic grains, and a Mesozoic population that is interpreted as regolith contamination (Fig. 2.4B). ID-TIMS analyses of grains from the Neoproterozoic population yielded five concordant analyses with a weighted mean $^{206}Pb/^{238}U$ age of 705.44 ± 0.28/0.44/0.84 (MSWD = 0.5; POF = 0.76; Fig. 2.4B.

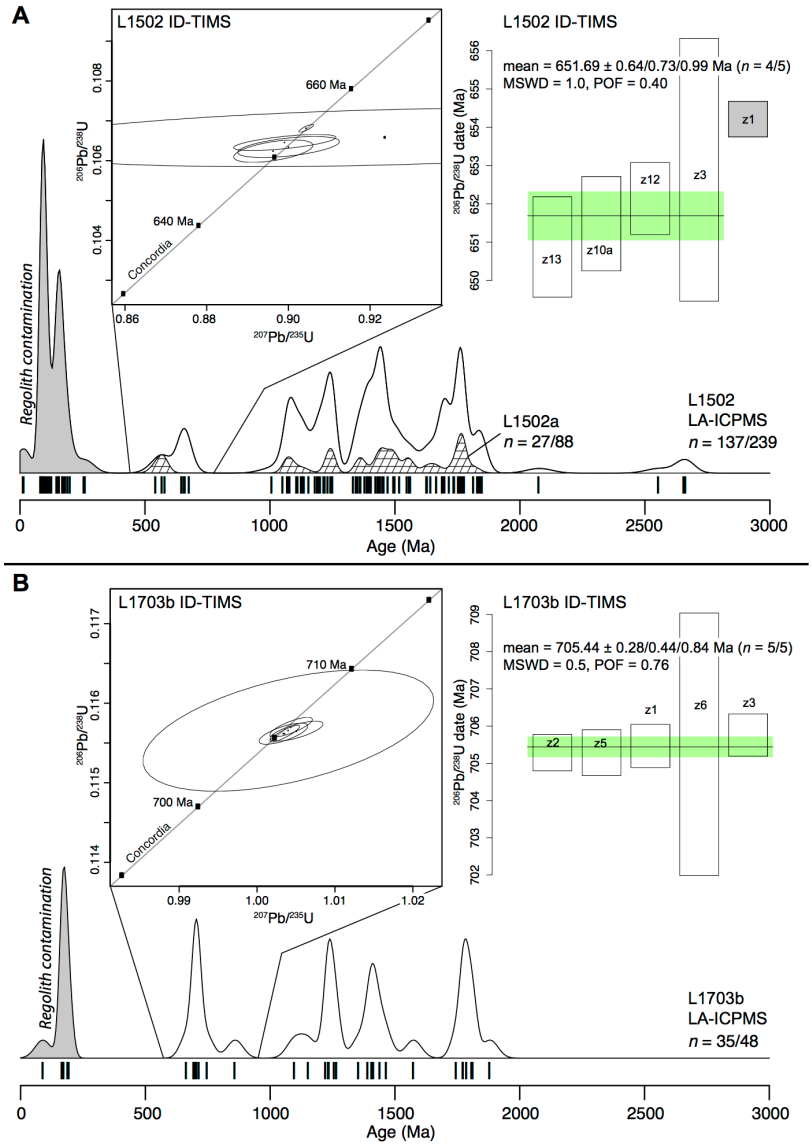

Figure 2.4. U-Pb geochronology of zircons separated from (A) L1502 and (B) L1703B. Reported uncertainties of 2s include internal/internal and tracer/internal, tracer, and decay constant uncertainties. Kernel density estimations (KDEs) use -10% to +15% discordance cutoffs, a smoothing bandwidth of 20 Ma, and a 900 Ma cutoff for $^{206}Pb/^{238}U$ to $^{207}Pb/^{206}Pb$ age calculations.

2.5. Discussion

2.5.1. Cryogenian Rifting

Following Tonian subsidence and deposition, basins in Death Valley were reactivated before 706 Ma with the development of an unconformity and deposition of breccia of the basal Limekiln Spring Member. The 705.44 ± 0.28 Ma age on volcanic rocks in the Limekiln Spring Member

could be conservatively interpreted as a maximum depositional age given the populations of basement-derived grains, but due to the lithology and tight agreement of grains analyzed with ID-TIMS, is likely a volcanic age (Figs. 2.3, 2.4B) with a component of magmatic inheritance or entrainment, and regolith contamination. The Limekiln Spring Member was deposited within actively forming grabens and contains sedimentary breccia, debris flows, and olistoliths derived from adjacent fault scarps and erosion of uplifted horsts of the underlying units (Figs. 2.2, 2.5A; Miller, 1985; Labotka et al., 1980). Additionally, it and the overlying Surprise Member both have basal unconformities and contain volcanic rocks that have tholeiitic whole-rock geochemical compositions consistent with within-plate basalts (Hammond, 1983). The Thorndike submember was deposited between the Mountain Girl and Wildrose submembers, both of which contain evidence for active syn-sedimentary faulting including basal angular unconformities, and fanglomerate and olistolith deposits (Figs. 2.2, 2.5B–D; Miller, 1985; Prave, 1999; Petterson et al., 2011a). Thus, we interpret the ages from the Limekiln Spring Member and Thorndike submember to constrain the tempo of active Cryogenian rifting in Death Valley, indicating a minimum duration of ~55 m.y. Furthermore, the development of four distinct angular unconformities during this interval suggests that rifting was punctuated rather than continuous.

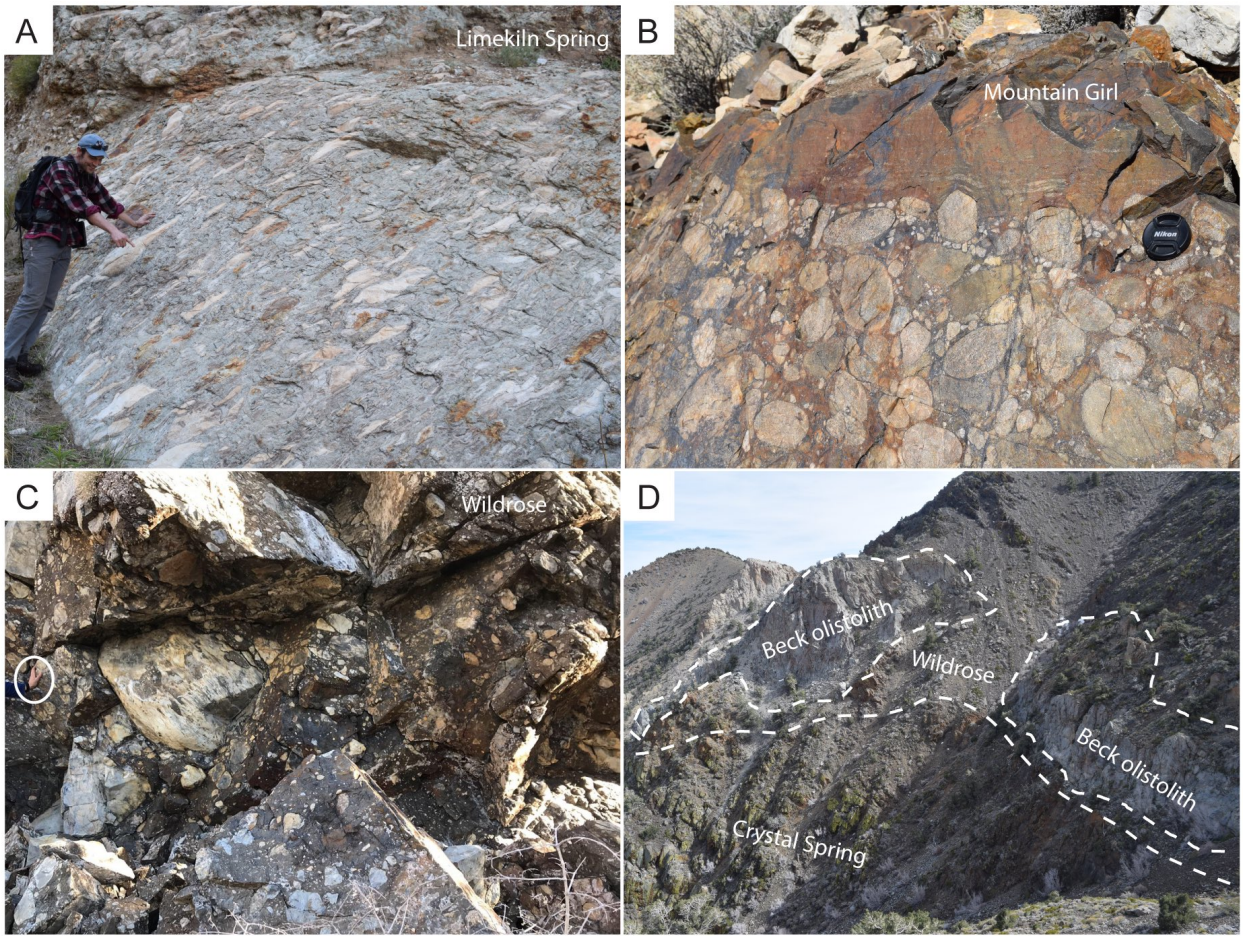

Figure 2.5. Field photographs of syn-rift sedimentary features. A) Sedimentary breccia within the lower Limekiln Spring Member composed primarily of clasts of Tonian Beck Spring Dolomite. Geologist for scale. B) Alluvial conglomerate within lower Mountain Girl submember composed of clasts of quartzite and basement gneiss. Lens cap is 5.2 cm in diameter. C) Fanglomerate within Wildrose submember composed primarily of clasts of Beck Spring Dolomite. Hand circled for scale. D) Olistostrome within the basal Wildrose submember containing olistoliths of Beck Spring Dolomite. Pinyons and junipers are ~1-3 meters tall.

When compiled with the growing record of magmatic and sedimentary age constraints along the entire western margin of Laurentia (Fig. 2.1; e.g., Lund et al., 2010), a picture emerges of episodic and laterally discontinuous subsidence and magmatism within geographically restricted fault-bound basins between 720 Ma and 635 Ma (Isakson, 2017). This episodic pattern of rifting, without clear synchroneity or directional diachroneity, is consistent with dynamics of younger, better-documented examples of continental rift systems, such as the East African Rift or

the opening of the Atlantic Ocean (e.g., Ebinger et al., 2013). However, the absence of classic passive-continental-margin strata in the early Ediacaran, combined with widespread evidence for subsequent late Ediacaran–early Cambrian rift-related subsidence and magmatism in western Laurentia prior to Cambrian passive-margin development (e.g., Bond et al., 1985; Levy and Christie-Blick, 1991; Karlstrom et al., 2018), is consistent with the idea that episodes of Cryogenian tectonism were part of a failed continental rift.

2.5.2 Cryogenian Chronology

The volcanic age from the Limekiln Spring Member demonstrates that this unit and the overlying Surprise Member were deposited during the ca. 717–661 Ma Sturtian glaciation, as first suggested by Prave (1999). Significant stratigraphic intervals of well-sorted quartz arenite and siltstone within the Limekiln Spring Member do not necessitate intervals of glacial retreat (c.f., Allen and Etienne, 2008; Le Heron et al., 2014), because such sediments are generated from subglacial discharge deposited below an ice shelf, outboard of the ice-grounding line (Domack et al., 1998), and/or from the recycling of weakly lithified preglacial sediments. The syn-Sturtian age on the Limekiln Spring Member and the maximum depositional age from the upper Thorndike submember suggest that the Sourdough Limestone Member is a Sturtian cap carbonate and that it and most of the South Park Member were deposited during the Cryogenian non-glacial interlude between ca. 661 and 651 Ma. Therefore, glacial diamictite of the overlying Wildrose submember was deposited during the Marinoan glaciation, and the Sentinel Peak Member of the Noonday Formation is a Marinoan cap carbonate (Fig. 2.1).

Although the base of the Wildrose submember is erosive and disconformable, the sampled bed from the Thorndike submember is near the top of the non-glacial interlude succession that is preserved in the Panamint Range. The weighted mean age of 651.69 ± 0.64 Ma is interpreted as a

maximum depositional age due to the significant population of detrital Mesoproterozoic grains, but, owing to the reproducibility of the ID-TIMS analyses (Fig. 2.4A), could be interpreted as a near-depositional age from a reworked ash-fall deposit. Regardless, this age provides the youngest precise constraint on the initiation of the Marinoan glaciation, which must have occurred after 652 Ma. When combined with the existing age constraints on the terminations of the Cryogenian glaciations (Condon et al., 2005; Prave et al., 2016; Rooney et al., 2020), this age indicates that the Marinoan glaciation lasted as long as 17 m.y., and the Cryogenian nonglacial interlude lasted at least 9 m.y. (Fig. 2.1). Provided there was not significant erosion or non-deposition of non-glacial strata above the Thorndike submember, this age is consistent with the 9.8 m.y. estimate for the duration of the nonglacial interlude based on cyclostratigraphy of the Datangpo Formation from drill-core magnetic susceptibility (Bao et al., 2018).

Following the Sturtian glaciation, enhanced silicate weathering and CO_2 drawdown in the post-snowball greenhouse would have resulted in a new steady-state CO_2 level on a million-year time scale (e.g., Higgins and Schrag, 2003). Mills et al. (2011) argued that the availability of weatherable rock and physical weathering transport could be the major limitations on silicate weathering rates, predicting a slower CO_2 drawdown and carbon cycle stabilization, potentially over 10 m.y. The >9 m.y. of nonglacial conditions between the Sturtian and Marinoan documented here is on the upper end of this timescale and suggests that post-snowball weathering alone cannot explain the subsequent onset of the Marinoan glaciation. Even if the background paleogeography was conducive to a cold climate (Kirschvink, 1992; Li et al., 2013), continued changes in paleogeography and weatherability (Park et al., 2020) or a more proximal trigger (Macdonald and Wordsworth, 2017) was needed to push the Earth to return to a snowball state.

2.6. Conclusions

New zircon U-Pb ID-TIMS ages from the Kingston Peak Formation in Death Valley include a volcanic age of 705.44 ± 0.28 Ma for the Limekiln Spring Member and a maximum depositional age of 651.69 ± 0.64 Ma for the Thorndike submember. These dates: (1) confirm that the Limekiln and Surprise members of the Kingston Peak Formation were deposited during the Sturtian glaciation, and the Wildrose submember was deposited during the Marinoan glaciation; (2) provide a minimum duration of 9 m.y. for the Cryogenian nonglacial interlude; and (3) are consistent with episodic subsidence and magmatism along the western Laurentian margin during active rifting throughout the Cryogenian (720–635 Ma), interpreted as part of a failed continental rift system prior to successful late Ediacaran–Cambrian rifting.

2.7. Acknowledgements

We thank the U.S. National Park Service at Death Valley for sampling permits. National Geographic Society grant CP-002ER-17, National Science Foundation Graduate Research Fellowship DGE- 1746891, the Harvard Booth Fellowship, the Smithsonian Buck Fellowship, and the Harvard University and Johns Hopkins University Earth and Planetary Sciences departments supported this research. We thank C. Wall, A. Kylander-Clark, J. Cottle, J. Pu, and T. Browne for laboratory assistance. Reviews from C. Dehler, J. Husson, and A. Prave improved this manuscript.

2.8. References

Allen, P.A., and Etienne, J.L., 2008, Sedimentary challenges to Snowball Earth: Nature Geoscience, v. 1, p. 817–825, doi:10.1038/ngeo355.

Andrew, J.E., 2002, The Mesozoic and Tertiary tectonic history of the Panamint Range and Quail Mountains, California [Ph. D. thesis]: Lawrence, Kansas, University of Kansas, 154 p.

Baldwin, G.J., Turner, E.C., and Kamber, B.S., 2016, Tectonic controls on distribution and stratigraphy of the Cryogenian Rapitan iron formation, northwestern Canada: Precambrian Research, v. 278, p. 303–322.

Bao, X., Zhang, S., Jiang, G., Wu, H., Li, H., Wang, X., An, Z., and Yang, T., 2018, Cyclostratigraphic constraints on the duration of the Datangpo Formation and the onset age of the Nantuo (Marinoan) glaciation in South China: Earth and Planetary Science Letters, v. 483, p. 52–63.

Barth, A.P., Wooden, J.L., and Coleman, D.S., 2001, SHRIMP-RG U-Pb zircon geochronology of Mesoproterozoic metamorphism and plutonism in the southwesternmost United States: Journal of Geology, v. 109, no. 3, p. 319–327.

Barth, A.P., Wooden, J.L., and Coleman, D.S., 2009, Assembling and disassembling California: a zircon and monazite geochronologic framework for Proterozoic crustal evolution in southern California: Journal of Geology, v. 117, p. 221–239.

Bond, G.C., Christie-Blick, N., Kominz, M.A., and Devlin, W.J., 1985, An Early Cambrian rift to post-rift transition in the Cordillera of western North America: Nature, v. 315, no. 6022, p. 742–746.

Bowring, S.A., Grotzinger, J.P., Condon, D.J., Ramezani, J., Newall, M.J. and Allen, P.A., 2007. Geochronologic constraints on the chronostratigraphic framework of the Neoproterozoic Huqf Supergroup, Sultanate of Oman. American Journal of Science, 307(10), pp.1097-1145.

Calver, C.R., Crowley, J.L., Wingate, M.T.D., Evans, D.A.D., Raub, T.D., and Schmitz, M.D., 2013, Globally synchronous Marinoan deglaciation indicated by U-Pb geochronology of the Cottons Breccia, Tasmania, Australia: Geology, v. 41, no. 10, p. 1127–1130.

Condon, D., Zhu, M., Bowring, S., Wang, W., Yang, A., and Jin, Y., 2005, U-Pb ages from the Neoproterozoic Doushantuo Formation, China: Science, v. 308, no. 5718, p. 95–98.

Cox, G.M., Strauss, J.V., Halverson, G.P., Schmitz, M.D., McClelland, W.C., Stevenson, R.S., and Macdonald, F.A., 2015, Kikiktat volcanics of Arctic Alaska—Melting of harzburgitic mantle associated with the Franklin large igneous province: Lithosphere, v. 7, no. 3, p. 275–295.

Cox, G.M., Isakson, V., Hoffman, P.F., Gernon, T.M., Schmitz, M.D., Shahin, S., Collins, A.S., Preiss, W., Blades, M.L., Mitchell, R.N., and Nordsvan, A., 2018a, South Australian U-Pb zircon (CA-ID-TIMS) age supports globally synchronous Sturtian deglaciation: Precambrian Research, v. 315, p. 257–263.

Cox, G.M., Halverson, G.P., Denyszyn, S., Foden, J., and Macdonald, F.A., 2018b, Cryogenian magmatism along the north-western margin of Laurentia: Plume or rift?: Precambrian Research, v. 319, p.144–157.

Crowley, J.L., Schoene, B., and Bowring, S.A., 2007, U-Pb dating of zircon in the Bishop Tuff at the millennial scale: Geology, v. 35, no. 12, p. 1123–1126.

Dickinson, W.R., and Gehrels, G.E., 2003, U–Pb ages of detrital zircons from Permian and Jurassic eolian sandstones of the Colorado Plateau, USA: paleogeographic implications: Sedimentary Geology, v. 163, no. 1–2, p. 29–66.

Domack, E.W., Jacobson, E.A., Shipp, S., and Anderson, J.B., 1999, Late Pleistocene–Holocene retreat of the West Antarctic Ice-Sheet system in the Ross Sea: Part 2—sedimentologic and stratigraphic signature: Geological Society of America Bulletin, v. 111, no. 10, p. 1517–1536.

Ebinger, C.J., van Wijk, J., and Keir, D., 2013, The time scales of continental rifting: Implications for global processes, *in* Bickford, M.E., ed., The Web of Geological Sciences: Advances, Impacts, and Interactions: Geological Society of America Special Paper 500, p. 1–26, doi:10.1130/2013.2500(11).

Eyster, A., Ferri, F., Schmitz, M.D., and Macdonald, F.A., 2018, One diamictite and two rifts: Stratigraphy and geochronology of the Gataga Mountain of northern British Columbia: American Journal of Science, v. 318, no. 2, p. 167–207.

Fanning, C.M., and Link, P.K., 2004, U-Pb SHRIMP ages of Neoproterozoic (Sturtian) glaciogenic Pocatello Formation, southeastern Idaho: Geology, v. 32, no. 10, p.881–884.

Gerstenberger, H., and Haase, G., 1997, A highly effective emitter substance for mass spectrometric Pb isotope ratio determinations: Chemical geology, v. 136, p. 309–312.

Hammond, J. G., 1983, Late Precambrian diabase intrusions in the southern Death Valley region, California: Their petrology, geochemistry, and tectonic implications [Ph.D. thesis]: Los Angeles, University of Southern California, 281 p.

Heaman, L.M., and Grotzinger, J.P., 1992, 1.08 Ga diabase sills in the Pahrump Group, California: Implications for development of the Cordilleran miogeocline: Geology, v. 20, no. 7, p. 637–640.

Higgins, J.A., and Schrag, D.P., 2003, Aftermath of a snowball Earth: Geochemistry, Geophysics, Geosystems, v. 4, no. 3, p. 1028.

Hoffman, P.F., et al., 2017, Snowball Earth climate dynamics and Cryogenian geology-geobiology: Science Advances, v. 3, p. e1600983.

Hoffmann, K.H., Condon, D.J., Bowring, S.A., and Crowley, J.L., 2004, U-Pb zircon date from the Neoproterozoic Ghaub Formation, Namibia: constraints on Marinoan glaciation: Geology, v. 32, no. 9, p. 817–820.

Isakson, V.H., 2017, Geochronology of the Tectonic, Stratigraphic, and Magmatic Evolution of Neoproterozoic to Early Paleozoic, North American Cordillera and Cryogenian Glaciation [Ph.D. thesis]: Boise, Boise State University, 657 p.

Jackson, S.E., Pearson, N.J., Griffin, W.L, and Belousova, E.A., 2004, The application of laser ablation-inductively coupled plasma-mass spectrometry to in situ U–Pb zircon geochronology: Chemical geology, v. 211, p. 47–69.

Jaffey, A.H., Flynn, K.F., Glendenin, L.E., Bentley, W.T., and Essling, A.M., 1971, Precision measurement of half-lives and specific activities of U 235 and U 238: Physical review C, v. 4, no. 1889.

Karlstrom, K., Hagadorn, J., Gehrels, G., Matthews, W., Schmitz, M., Madronich, L., Mulder, J., Pecha, M., Giesler, D., and Crossey, L., 2018, Cambrian Sauk transgression in the Grand Canyon region redefined by detrital zircons: Nature Geoscience, v. 11, no. 6, p. 438–443.

Keeley, J.A., Link, P.K., Fanning, C.M., and Schmitz, M.D., 2013, Pre-to synglacial rift-related volcanism in the Neoproterozoic (Cryogenian) Pocatello Formation, SE Idaho: New SHRIMP and CA-ID-TIMS constraints: Lithosphere, v. 5, no. 1, p. 128–150.

Kirschvink, J.L., 1992, Late Proterozoic low-latitude global glaciation: the snowball Earth, *in* Schopf, J.W., and Klein, C., eds., The Proterozoic Biosphere: Cambridge University Press, New York, p. 51–52.

Košler, J., Forst, L., and Sláma, J., 2008, Lamdate and Lamtool: Spreadsheet-based data reduction for laser ablation ICP-MS, *in* Sylvester, P., ed., Laser ablation ICP-MS in the Earth sciences: Current practices and outstanding issues: Mineralogical Association of Canada, Short Course Series, v. 40, p. 315–317.

Krogh, T.E., 1973, A low-contamination method for hydrothermal decomposition of zircon and extraction of U and Pb for isotopic age determinations: Geochimica et Cosmochimica Acta, v. 37, p. 485–494.

Kylander-Clark, A.R., Hacker, B.R., and Cottle, J.M., 2013, Laser-ablation split-stream ICP petrochronology: Chemical Geology, v. 345, p. 99–112.

Labotka, T.C., Albee, A.L., Lanphere, M.A., and McDowell, S.D., 1980, Stratigraphy, structure, and metamorphism in the central Panamint Mountains (Telescope Peak quadrangle), Death Valley area, California: Geological Society of America Bulletin, v. 91, p. 843–933.

Lanphere, M.A., Wasserburg, G.J.F., Albee, A.L., and Tilton, G.R., 1964, Redistribution of Strontium and Rubidium Isotopes during Metamorphism, World Beater Complex, Panamint Range, California, *in* Isotopic and Cosmic Chemistry: North Holland, Amsterdam, p. 269–320.

Le Heron, D.P., Busfield, M.E., and Prave, A.R., 2014, Neoproterozoic ice sheets and olistoliths: multiple glacial cycles in the Kingston Peak Formation, California: Journal of the Geological Society, v. 171, no. 4, p. 525–538.

Levy, M., and Christie-Blick, N., 1991, Tectonic subsidence of the early Paleozoic passive continental margin in eastern California and southern Nevada: Geological Society of America Bulletin, v. 103, no. 12, p. 1590–1606.

Li, Z.X., Evans, D.A., and Halverson, G.P., 2013, Neoproterozoic glaciations in a revised global palaeogeography from the breakup of Rodinia to the assembly of Gondwanaland: Sedimentary Geology, v. 294, p. 219–232.

Link, P.K., Corsetti, F.A., and Lorentz, N.J., 2005, Pocatello Formation and overlying strata, southeastern Idaho: snowball Earth diamictites, cap carbonates, and Neoproterozoic isotopic profiles, *in* Pederson, J., and Dehler, C.M., eds., Interior Western United States: Geological Society of America Field Guide, v. 6, p. 251–259.

Ludwig, K.R., 2003, User's manual for Isoplot 3.00, a geochronlogical toolkit for Microsoft Excel: Berkeley Geochronology Center Special Publications, v. 4, p. 25–32.

Lund, K., Aleinikoff, J.N., Evans, K.V., and Fanning, C.M., 2003, SHRIMP U-Pb geochronology of Neoproterozoic Windermere Supergroup, central Idaho: Implications for rifting of western Laurentia and synchroneity of Sturtian glacial deposits: Geological Society of America Bulletin, v. 115, no. 3, p. 349–372.

Lund, K., Aleinikoff, J.N., Evans, K.V., DuBray, E.A., Dewitt, E.H., and Unruh, D.M., 2010, SHRIMP U-Pb dating of recurrent Cryogenian and Late Cambrian–Early Ordovician alkalic magmatism in central Idaho: Implications for Rodinian rift tectonics: Geological Society of America Bulletin, v. 122, no. 3–4, p. 430–453.

Macdonald, F.A., and Wordsworth, R., 2017, Initiation of Snowball Earth with volcanic sulfur aerosol emissions: Geophysical Research Letters, v. 44, no. 4, p. 1938–1946.

Macdonald, F.A., Schmitz, M.D., Crowley, J.L., Roots, C.F., Jones, D.S., Maloof, A.C., Strauss, J.V., Cohen, P.A., Johnston, D.T., and Schrag, D.P., 2010, Calibrating the Cryogenian: Science, v. 327, no. 5970, p. 1241–1243.

Macdonald, F.A., Prave, A.R., Petterson, R., Smith, E.F., Pruss, S.B., Oates, K., Waechter, F., Trotzuk, D., and Fallick, A.E., 2013, The Laurentian record of Neoproterozoic glaciation,

tectonism, and eukaryotic evolution in Death Valley, California: Geological Society of America Bulletin, v. 125, no. 7–8, p. 1203–1223.

Macdonald, F.A., Schmitz, M.D., Strauss, J.V., Halverson, G.P., Gibson, T.M., Eyster, A., Cox, G., Mamrol, P., and Crowley, J.L., 2018, Cryogenian of Yukon: Precambrian Research, v. 319, p. 114–143.

MacLennan, S., Park, Y., Swanson-Hysell, N., Maloof, A., Schoene, B., Gebreslassie, M., Antilla, E., Tesema, T., Alene, M., and Haileab, B., 2018, The arc of the Snowball: U-Pb dates constrain the Islay anomaly and the initiation of the Sturtian glaciation: Geology, v. 46, no. 6, p. 539–542.

Mahon, R.C., Dehler, C.M., Link, P.K., Karlstrom, K.E., and Gehrels, G.E., 2014, Geochronologic and stratigraphic constraints on the Mesoproterozoic and Neoproterozoic Pahrump Group, Death Valley, California: A record of the assembly, stability, and breakup of Rodinia: Geological Society of America Bulletin, v. 126, no. 5–6, p. 652–664.

Mattinson, J.M., 2005, Zircon U–Pb chemical abrasion ("CA-TIMS") method: combined annealing and multi-step partial dissolution analysis for improved precision and accuracy of zircon ages: Chemical Geology, v. 220, p. 47–66.

Miller, J.M., 1985, Glacial and syntectonic sedimentation: The upper Proterozoic Kingston Peak Formation, southern Panamint Range, eastern California: Geological Society of America Bulletin, v. 96, no. 12, p. 1537–1553.

Mills, B., Watson, A.J., Goldblatt, C., Boyle, R., and Lenton, T.M., 2011, Timing of Neoproterozoic glaciations linked to transport-limited global weathering: Nature Geoscience, v. 4, no. 12, p. 861–864.

Park, Y., Swanson-Hysell, N.L., MacLennan, S.A., Maloof, A.C., Gebreslassie, M., Tremblay, M.M., Schoene, B., Alene, M., Anttila, E.S., Tesema, T., and Haileab, B., 2020, The lead-up to the Sturtian Snowball Earth: Neoproterozoic chemostratigraphy time-calibrated by the Tambien Group of Ethiopia. Geological Society of America Bulletin, v. 132, no. 5–6, p. 1119–1149.

Petterson, R., Prave, A.R., Wernicke, B.P., 2011a, Glaciogenic and related strata of the Neoproterozoic Kingston Peak Formation in the Panamint Range, Death Valley region, California, *in* Arnaud, E., Halverson, G.P., and Shields-Zhou, G., eds., The Geological Record of Neoproterozoic Glaciations: Geological Society Memoirs, London, v. 36, p. 459–465.

Paton, C., Woodhead, J.D., Hellstrom, J.C., Hergt, J.M., Greig, A., and Maas, R., 2010, Improved laser ablation U-Pb zircon geochronology through robust downhole fractionation correction: Geochemistry, Geophysics, Geosystems, v. 11, no. 3., p. Q0AA06.

Petterson, R., Prave, A.R., Wernicke, B.P., and Fallick, A.E., 2011b, The Neoproterozoic Noonday Formation, Death Valley region, California: Geological Society of America Bulletin, v. 123, no. 7–8, p. 1317–1336.

Prave, A.R., 1999, Two diamictites, two cap carbonates, two $\delta^{13}C$ excursions, two rifts: the Neoproterozoic Kingston Peak Formation, Death Valley, California: Geology, v. 27, no. 4, p. 339–342.

Prave, A.R., Condon, D.J., Hoffmann, K.H., Tapster, S., and Fallick, A.E., 2016, Duration and nature of the end-Cryogenian (Marinoan) glaciation: Geology, v. 44, no. 8, p. 631–634.

Rooney, A.D., Yang, C., Condon, D.J., Zhu, M., and Macdonald, F.A., 2020, U-Pb and Re-Os geochronology tracks stratigraphic condensation in the Sturtian Snowball aftermath: Geology, v. 48, no., 6, p. 625–629.

Schaltegger, U., Schmitt, A.K., and Horstwood, M.S.A., 2015, U–Th–Pb zircon geochronology by ID-TIMS, SIMS, and laser ablation ICP-MS: recipes, interpretations, and opportunities: Chemical Geology, v. 402, p. 89–110.

Schmitz, M.D., and Schoene, B., 2007, Derivation of isotope ratios, errors, and error correlations for U-Pb geochronology using ^{205}Pb-^{235}U-(^{233}U)-spiked isotope dilution thermal ionization mass spectrometric data: Geochemistry, Geophysics, Geosystems, v. 8, no. 8, p. Q08006.

Schoene, B., Crowley, J.L., Condon, D.J., Schmitz, M.D., and Bowring, S.A., 2006, Reassessing the uranium decay constants for geochronology using ID-TIMS U–Pb data: Geochimica et Cosmochimica Acta, v. 70, no. 2, p. 426–445.

Sláma, J., Košler, J., Condon, D.J., Crowley, J.L., Gerdes, A., Hanchar, J.M., Horstwood, M.S., Morris, G.A., Nasdala, L., Norberg, N., and Schaltegger, U., 2008, Plešovice zircon—a new natural reference material for U–Pb and Hf isotopic microanalysis: Chemical Geology, v. 249, p. 1–35.

Stevenson, J.A., Smellie, J.L., McGarvie, D.W., Gilbert, J.S., and Cameron, B.I., 2009, Subglacial intermediate volcanism at Kerlingarfjöll, Iceland: magma–water interactions beneath thick ice: Journal of Volcanology and Geothermal Research, v. 185, no. 4, p. 337–351.

Stewart, J.H., 1972, Initial deposits in the Cordilleran geosyncline: Evidence of a late Precambrian (< 850 my) continental separation: Geological Society of America Bulletin, v. 83, no. 5, p. 1345–1360.

Verdel, C., Wernicke, B.P., and Bowring, S.A., 2011, The Shuram and subsequent Ediacaran carbon isotope excursions from southwest Laurentia, and implications for environmental stability during the metazoan radiation: Geological Society of America Bulletin, v. 123, no. 7–8, p. 1539–1559.

Vermeesch, P., 2018, IsoplotR: a free and open toolbox for geochronology: Geoscience Frontiers, v. 9, p. 1479–1493.

Wiedenbeck, M., Allé, P., Corfu, F., Griffin, W.L., Meier, M., Oberli, F., von Quadt, A., Roddick, J.C., and Spiegel, W., 1995, Three natural zircon standards for U–Th–Pb, Lu–Hf, trace element and REE analyses: Geostandards Newsletter, v. 19, p. 1–23.

Wright, L.A., Troxel, B.W., Williams, E.G., Roberts, M.T., and Diehl, P.E., 1976, Precambrian sedimentary environments of the Death Valley region, eastern California, *in* Troxel, B.W., and Wright, L.A., eds., Death Valley Region, California and Nevada, Guidebook: Shoshone, California, Death Valley Publishing Co., p. 27–36.

Yonkee, W.A., Dehler, C.D., Link, P.K., Balgord, E.A., Keeley, J.A., Hayes, D.S., Wells, M.L., Fanning, C.M., and Johnston, S.M., 2014, Tectono-stratigraphic framework of Neoproterozoic to Cambrian strata, west-central US: Protracted rifting, glaciation, and evolution of the North American Cordilleran margin: Earth-Science Reviews, v. 136, p. 59–95.

Zhou, C., Huyskens, M.H., Lang, X., Xiao, S., and Yin, Q.-Z., 2019, Calibrating the terminations of Cryogenian global glaciations: Geology, v. 47, no. 3, p. 251–254.

CHAPTER 3. FINGERPRINTING LOCAL CONTROLS ON THE NEOPROTEROZOIC CARBON CYCLE WITH THE ISOTOPIC RECORD OF CRYOGENIAN CARBONATES IN THE PANAMINT RANGE, CALIFORNIA

A version of this chapter was published in:

[Nelson, L. L., Ahm, A. C., Macdonald, F. A., Higgins, J. A., & Smith, E. F. (2021). Fingerprinting local controls on the Neoproterozoic carbon cycle with the isotopic record of Cryogenian carbonates in the Panamint Range, California. *Earth and Planetary Science Letters*, *566*, *116956*]

Abstract

Neoproterozoic carbon isotope excursions are commonly attributed to changes in the global fraction of organic carbon burial associated with climate instability and/or oxygenation. Here we show that carbonate sediment deposited during the ca. 661 – <651 Ma Cryogenian non-glacial interlude between the Sturtian and Marinoan glaciations exhibit lateral offsets in carbonate-carbon isotope values from coeval units by as much as 10‰. Within the Thorndike submember of the Cryogenian succession in the Panamint Range, California, USA, carbonate-carbon isotope values can be linked to a laterally discontinuous dolomitization front: limestones exhibit $\delta^{13}C_{carb}$ values of ~+4 to +9‰, whereas values of stratigraphically equivalent dolostones are consistently lower, between ~-4 and +4‰. Field observations and analyses of clasts from the overlying Marinoan glacial diamictite show that the offset in $\delta^{13}C_{carb}$ values resulted from pre- to syn-Marinoan dolomitization. Further, $\delta^{44/40}Ca$ and $\delta^{26}Mg$ data indicate that this isotopic variability resulted from sediment-buffered diagenesis. We propose that extremely positive $\delta^{13}C_{carb}$ values record local primary productivity within restricted platform surface waters and/or oxygenated pore fluids and negative values reflect anaerobic remineralization of organic carbon within sediment pore waters. In this scenario, neither the original calcite/aragonite nor subsequent dolomite precipitates of the

Thorndike submember record $\delta^{13}C_{carb}$ values that are representative of global Cryogenian seawater, and instead they archive the evolution of local dissolved inorganic carbon pools.

3.1. Introduction

Carbon isotope ($\delta^{13}C$) data from shallow marine carbonate strata have long been used to reconstruct temporal shifts in the isotopic composition of seawater, correlate between stratigraphic sections regionally and globally, and construct chemostratigraphic age models (e.g., Saltzman and Thomas, 2012). The underlying assumption is that the $\delta^{13}C$ values of carbonate rocks reflect the composition of dissolved inorganic carbon (DIC) in seawater and are buffered from the effects of post-depositional diagenetic alteration (Banner and Hanson, 1990). This concept is substantiated by globally reproducible results in the Phanerozoic Eon, supported by both radiometric ages and biostratigraphy, and thus has been applied to the $\delta^{13}C$ record of the Proterozoic and Archean eons (e.g., Shields and Veizer, 2002; Halverson et al., 2005). Under this interpretation, and assuming the sampled carbonates are representative of the contemporaneous average global carbonate sink (Blättler and Higgins, 2017), $\delta^{13}C$ excursions through Earth history chronicle secular changes in the net global fluxes of organic carbon burial and oxidation, and can be linked to changes in the climate, environment, and biosphere.

Carbonate strata from the Neoproterozoic Era preserve highly variable $\delta^{13}C$ records, particularly those deposited before, in between, and after the Cryogenian snowball Earth glaciations (Hoffman and Schrag, 2002; Halverson et al., 2005). Carbonates for most of the Cryogenian non-glacial interlude – the >10 m.y. ice-free interval in between the end of the Sturtian glaciation and before the onset of the Marinoan glaciation (Rooney et al., 2020; Nelson et al.,

2020) – record ^{13}C-enriched $\delta^{13}C$ values (~+5 to +10‰) sometimes referred to as the Keele peak (e.g., Halverson et al., 2005). This and other protracted Neoproterozoic stratigraphic intervals recording positive $\delta^{13}C$ values have been interpreted as recording a high proportion of organic carbon burial, corresponding to high rates of oxidant accumulation within surface environments (e.g., Knoll et al., 1986). The Cryogenian non-glacial interlude is punctuated by what are thought to be three distinct large negative $\delta^{13}C$ excursions: the Rasthof (Hoffman and Schrag, 2002), Taishir (Johnston et al., 2012; Bold et al., 2016), and Trezona anomalies (Swanson-Hysell et al., 2010). When interpreted globally, these negative excursions both before and after the Cryogenian snowball Earth glaciations have been linked to a shutdown in biological productivity (Hoffman and Schrag, 2002), destabilization of methane hydrates following warming (Kennedy et al., 2001), oxidation of a methane greenhouse (Schrag et al., 2002), changes in anaerobic respiration due to an increase in organic carbon export (Tziperman et al., 2011), and the combined effect of a rapidly increasing global temperature and CO_2 drawdown (Higgins and Schrag, 2003).

Others have viewed the extreme fluctuations observed in the Neoproterozoic $\delta^{13}C$ record as difficult to interpret in a mass-balance framework due to the dramatic changes in oxidants that are implied, and have suggested alternative possibilities including: the existence of an unusually large pool of authigenic carbonate as a significant component of the global carbon cycle (Schrag et al., 2013), the existence of an unusually large reservoir of marine organic carbon to allow non-steady-state behavior (Rothman et al., 2003), and diagenetic origins for large excursions, related to either burial or meteoric fluids (Knauth and Kennedy, 2009; Derry, 2010). Additionally, studies on modern carbonate platforms have demonstrated that early marine diagenesis and aragonite production in platform top environments can result in variable $\delta^{13}C$ chemostratigraphic curves that are not accurate records of open-marine DIC fluctuations (Swart, 2008; Oehlert and Swart, 2014),

but rather records of the relative contributions of sediment-buffered versus fluid-buffered diagenetic precipitates (Ahm et al., 2018; Higgins et al., 2018). Using this framework, Ahm et al. (2019) invoked a diagenetic origin for $\delta^{13}C$ variability observed in Marinoan cap dolostones globally, known as the Maieberg anomaly. Along similar lines, by examining Neoproterozoic $\delta^{13}C$ records from the Otavi Platform in Namibia, Hoffman and Lamothe (2019) concluded that upper foreslope carbonates – strata that are most susceptible to seawater-buffered diagenesis – do not have the excursions of coeval platform and lower foreslope carbonates, and instead record DIC values akin to the modern ocean. Therefore, they speculate that nucleation kinetics were responsible for the large DIC variability observed on Proterozoic platforms. Bold et al. (2020) showed that early dolomitization fronts blunt the $\delta^{13}C$ variability preserved in Cryogenian carbonate successions in Mongolia, corroborating the potential for diagenetic fluids to affect the isotopic composition of carbonate minerals. Close covariation between organic carbon and carbonate $\delta^{13}C$ values has been documented for the Rasthof, Keele, Taishir, and Trezona carbon isotope anomalies during the Cryogenian non-glacial interlude, which may suggest primary perturbation to the surface carbon cycle (Swanson-Hysell et al., 2010; Johnston et al., 2012), although covariation between organic and carbonate $\delta^{13}C$ can be produced locally in platform and periplatform environments (Oehlert and Swart, 2014). Clearly, the origin, geographic variability, synchroneity, and significance of these large Cryogenian carbon isotope excursions remain uncertain.

Here, we present new $\delta^{13}C$, calcium isotope ($\delta^{44/40}Ca$) and magnesium isotope ($\delta^{26}Mg$) data from Cryogenian non-glacial interlude carbonate strata in the Panamint Range of Death Valley, California (Fig. 3.1). We observe significant $\delta^{13}C$ variability associated with a mapped dolomitization front and different sedimentary environments, and assess the origins of these trends

using geochemical tracers of diagenesis ($\delta^{44/40}Ca$ and $\delta^{26}Mg$) and interpretation of the evolving depositional setting. Our results suggest that observed variability can be explained by evolution of local DIC pools rather than global seawater, which may inform interpretations of Neoproterozoic carbonate platform geochemical records.

3.2. Geological Setting

The Panamint Range of southeastern California hosts a <2 km-thick Cryogenian succession, the Kingston Peak Formation (Fig. 3.1; Miller, 1985; Prave, 1999), which was deposited during multiple episodes of rifting on the southwestern margin of Laurentia related to the protracted breakup of Rodinia (Prave, 1999; Nelson et al., 2020) and outcrops for >60 km along both limbs of a doubly plunging anticline (Fig. 3.1D). The Kingston Peak Formation includes two distinct intervals of massive diamictite interpreted as glacial in origin, the Surprise Member and Wildrose submember (Miller, 1985), which have been correlated to the Sturtian (~717–661 Ma) and Marinoan (<651–635 Ma) snowball Earth glaciations based on the lithostratigraphy and $\delta^{13}C$ compositions of overlying cap carbonates, the Sourdough Limestone Member and Noonday Formation, respectively (Fig. 3.1B; Prave 1999; Petterson et al., 2011). More recently, these correlations were confirmed with high-precision geochronological constraints (Fig. 3.1; Nelson et al., 2020).

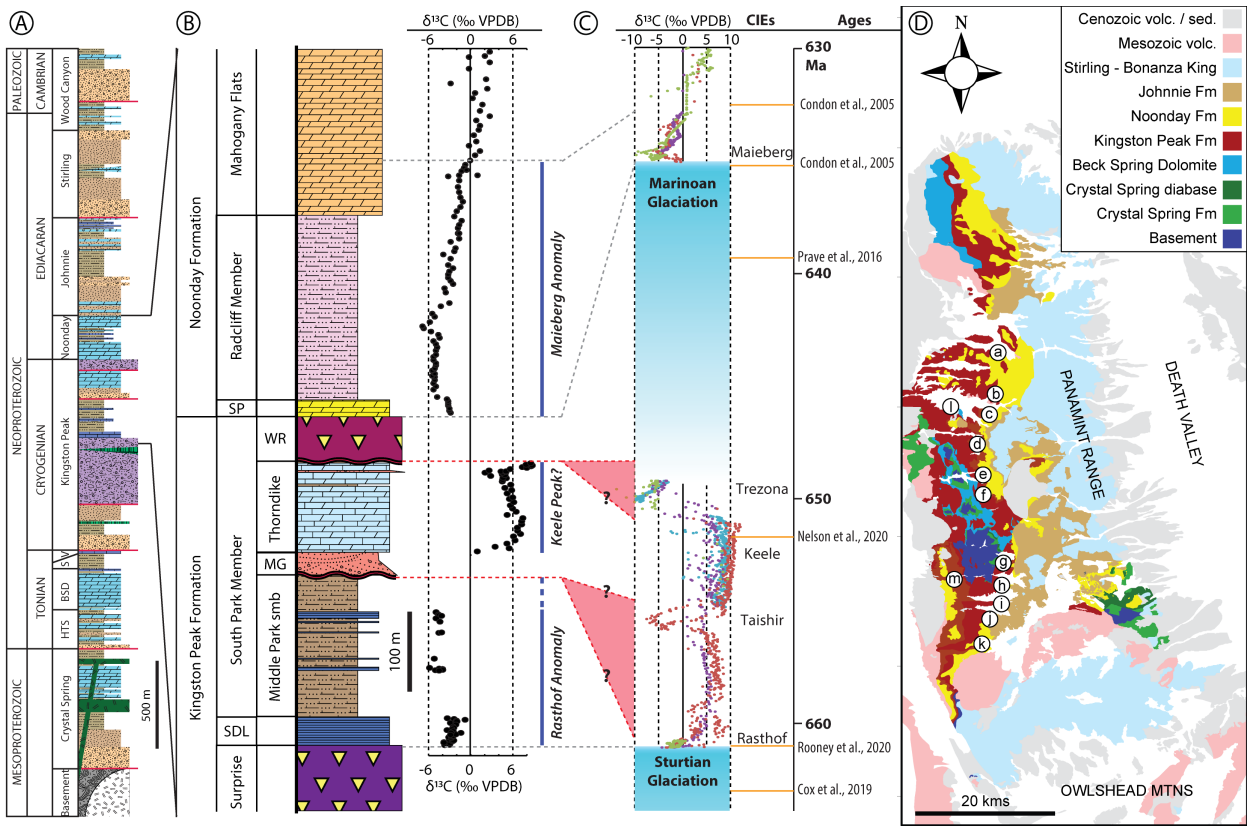

Figure 3.1. Geologic setting and generalized stratigraphy and chemostratigraphy of the Kingston Peak Formation, Death Valley (USA). A) Generalized stratigraphy of Death Valley. B) Composite chemostratigraphy of the Panamint Range. Sourdough data from South Park (L1509), Middle Park data from Pleasant Canyon (L1503), lower Thorndike data from Surprise Canyon (L1630), upper Thorndike data from Redlands Canyon (L1603), Sentinel Peak and Radcliffe data from Wildrose Canyon (L1803), Mahogany Flats data from Wildrose Canyon (Petterson et al., 2011). C) Composite carbon isotope profile of the Cryogenian. Green data points from NW Canada (Johnston et al., 2012); purple data points from Namibia (Halverson et al., 2005); Blue data points from Australia (Swanson-Hysell et al., 2010); red data points from Mongolia (Bold et al., 2016). Red lines are unconformities. D) Generalized map of Panamint Range with specific localities labeled to correspond to sections in Figures 3.3 and 3.4. Abbreviations: HTS—Horse Thief Springs Formation; BSD—Beck Spring Dolomite; S—Saratoga sandstone; V—Virgin Spring Limestone; SDL—Sourdough Limestone Member; SP—Sentinel Peak Member; MG—Mountain Girl submember; WR—Wildrose submember; VPDB—Vienna Peedee Belemnite; CIEs—Carbon Isotope Excursions.

The Sourdough Limestone Member and Middle Park, Mountain Girl, and Thorndike submembers of the South Park Member compose a <1 km succession of mixed siliciclastic and carbonate strata deposited during the Cryogenian non-glacial interlude. The Sourdough Limestone Member is a finely laminated dark blue limestone that sharply overlies the Surprise Member

diamictite, and is up to 35 m thick (Fig. 3.2A). In most sections, this is gradationally overlain by the Middle Park submember of the South Park Member, which reaches 180 m in thickness and comprises siltstone to shale with minor thin beds of finely laminated silty limestone (Fig. 3.2B) and arkosic turbidites. In some sections, arkosic grit channels in the basal Middle Park submember erosively remove much or all of the Sourdough Limestone Member. These post-Sturtian units are unconformably overlain by erosive conglomerate of the Mountain Girl submember, which grades into crossbedded quartz sandstone. Shoreface sandstone of the Mountain Girl submember grades into sandy carbonate and carbonate of the Thorndike submember, which is up to 100 m thick. Carbonate rocks of the Thorndike submember are largely recrystallized, but frequently preserve ripple cross-laminated and cross-bedded textures delineated by quartz grains (Fig. 3.2C,D), indicating they are primarily grainstone. Locally, microbialite structures occur (Fig. 3.2E,F). Near the top of the Thorndike submember, there are intraformational exposure surfaces, demarcated by thin layers of pebble conglomerate to sandstone underlain by sandstone- or breccia- filled karst pipes (Fig. 3.2G-J). A clastic bed ~15 m below the top contact of the Thorndike has a maximum depositional age of 651.7±0.6 Ma (Nelson et al., 2020). The Thorndike submember is unconformably overlain by diamictite of the Wildrose submember, which in some locations cuts as low as Mesoproterozoic basement (Miller, 1985; Prave, 1999).

Although other Neoproterozoic strata are exposed throughout the Death Valley region, units deposited during the Cryogenian non-glacial interlude are only exposed in the Panamint Range (along ~80 km of strike). Within Cryogenian strata, there are four angular unconformities, and evidence for active syn-sedimentary faulting, basement uplift, and structural generation of topographic highs at multiple stratigraphic levels (Miller, 1985; Prave, 1999). Sedimentary evidence for basin restriction during the Cryogenian includes abrupt lateral facies and thickness

variations within units, karst horizons, fine laminations that resemble seasonal varves, coarse debris flows, alluvial and fluvial depositional systems, and uranium-, sulfide-, and graphite-enrichments (Fig. 3.2; Carlisle et al., 1980; Miller, 1985). Taken together, these observations suggest sediment deposition was in locally formed basins generated by tectonic subsidence associated with the incipient rifting of this margin (Miller, 1985), which may have been partially-restricted from open marine environments.

Previous chemostratigraphic studies in the Death Valley region have documented negative $\delta^{13}C$ values in the Sourdough and Noonday, which have been correlated to the Rasthof and Maieberg negative $\delta^{13}C$ anomalies, respectively (Prave, 1999; Corsetti and Kaufman, 2003; Petterson et al., 2011). Additionally, there are some previously published $\delta^{13}C$ values from the Thorndike submember in the Panamint Range: Prave (1999) published three data points from Redlands Canyon with values of ~+6‰; Corsetti and Kaufman (2003) published values of ~+5‰ from Tucki Mountain; and Petterson et al. (2011) published scattered values ranging from ~-4 to +8‰ from sections in Wood Canyon and near the townsite of Skidoo in their Data Repository.

Metamorphic grade varies significantly across the Panamint Range. Rocks exposed along the western limb of the anticline and in the northern part of the range were subject to Mesozoic sillimanite-grade metamorphism and local marbleization (Labotka et al., 1985). However, rocks on the eastern limb – particularly in the central and southern Panamint Range – are greenschist-grade or lower. While this metamorphism and localized strain can locally change unit thicknesses, it has not significantly altered $\delta^{13}C$ within carbonate units as demonstrated by lateral $\delta^{13}C$ consistency in the Noonday Formation (Petterson et al., 2011).

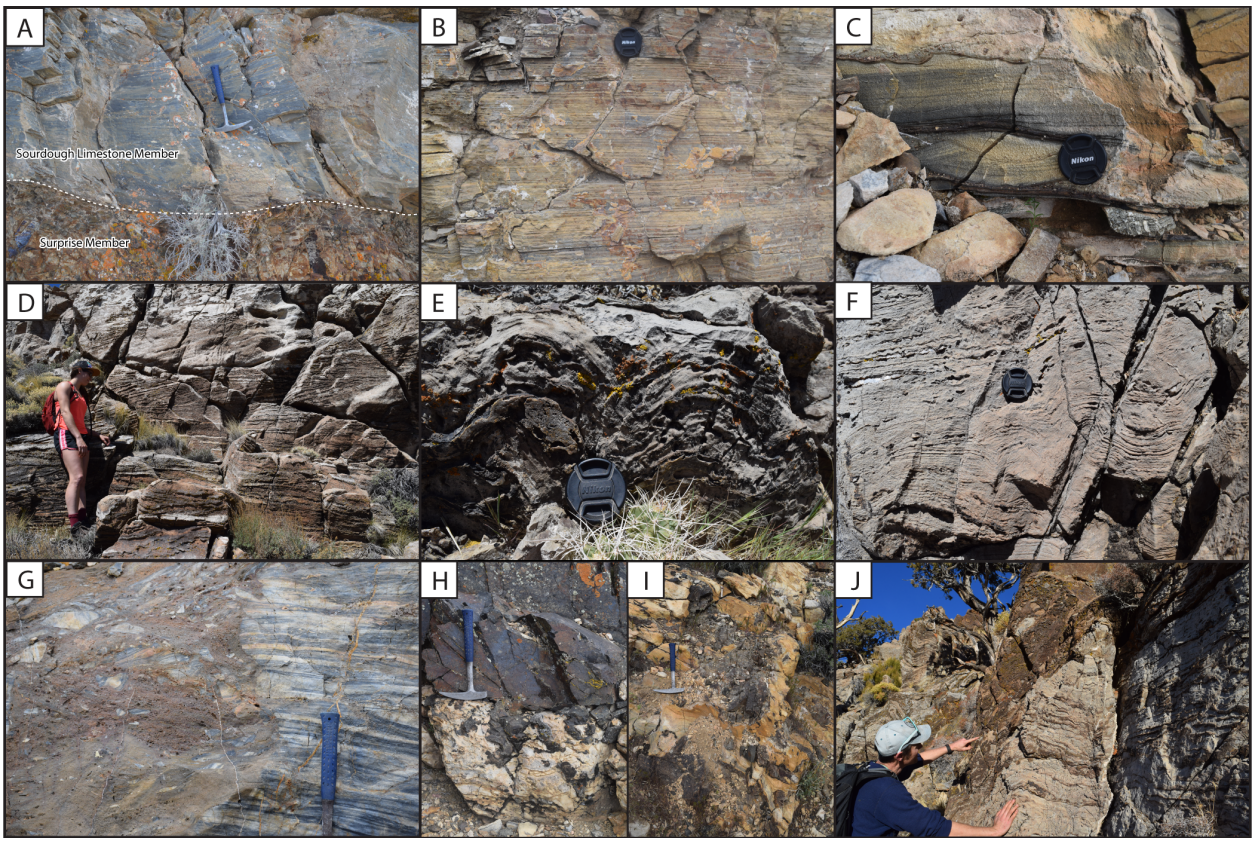

Figure 3.2. Field photographs of Sourdough Limestone Member, Middle Park submember, and Thorndike submember. Lens cap is 5.2 cm in diameter. Hammer is 33 cm long. A) Finely laminated dark blue limestone in basal Sourdough Limestone Member (Sturtian cap carbonate) sharply overlying Sturtian diamictite of the Surprise Member. B) Finely laminated limestone and siltstone of Middle Park submember. C) Ripple cross lamination in carbonate grainstone of the Thorndike submember. D) Large foresets in cross-bedded sandy carbonate grainstone of the Thorndike submember. E, F) Microbial carbonate with stromatolites within the Thorndike submember. G, H, I, J) Karst-related grikes infilled with sand and/or carbonate breccia within the upper Thorndike submember.

3.3. Methods

Mapping of Cryogenian strata throughout the Panamint Range was conducted between 2015-2018 at 1:10,000 scale. Twenty-six stratigraphic sections were measured in a north-south transect along ~50 km of strike, focusing on the lower-grade rocks within the eastern limb of the Panamint anticline. Within carbonate-bearing units, fist-sized carbonate samples were collected at 0.5 to 3-m resolution.

Fresh cut surfaces were microdrilled for powder along laminations, avoiding veins and siliciclastic grains. Samples were analyzed for carbonate carbon and oxygen isotopic compositions ($\delta^{13}C$ and $\delta^{18}O$) on a VG Optima dual inlet mass spectrometer at the Harvard University Laboratory for Geochemical Oceanography. Approximately 1 mg of powder was reacted in a common orthophosphoric acid bath at 90°C with a magnetic stirrer. Evolved CO_2 was collected cryogenically and analyzed using an in-house reference gas. Memory effects are estimated at <0.1‰ based on variability of standards. Isotopic results are reported in per mil (‰) notation relative V-PDB (Vienna-Pee Dee Belemnite) by using an in-house Cararra Marble standard that was calibrated against several NBS carbonate standards and cross-calibrated with other laboratories. Standard deviation (1σ) from standards was better than ±0.1‰ for $\delta^{13}C$ and $\delta^{18}O$.

Diamictite carbonate clast samples from the Wildrose submember, sampled between Redlands Canyon and South Park, were analyzed at the Johns Hopkins University Isotope Ratio Mass Spectrometer Laboratory. Samples were analyzed for $\delta^{13}C$ and $\delta^{18}O$ isotopic compositions using a GasBench II peripheral device coupled to a Thermo-Finnigan MAT253 isotope ratio mass spectrometer (IRMS) in continuous-flow mode. Approximately 0.3 mg of sample powder reacted with 100% phosphoric acid in helium-purged vials at 30 °C, overnight. Evolved CO_2 gas was then analyzed against tank CO_2 gas and isotopic results normalized to V-PDB ‰ scale using working in-house carbonate standards (ICM, Carrara Marble and IVA Analysentechnik, calcium carbonate) that are calibrated against international standards NBS-18 and IAEA-603. Standard deviation (1σ) of $\delta^{13}C$ and $\delta^{18}O$ values for in-house standards was <0.02‰ and <0.14‰, respectively.

The following sections were selected for analyses of trace element compositions and $\delta^{44/40}Ca$ and $\delta^{26}Mg$ isotopes: 1) one section of the Sourdough Limestone Member and Middle Park submember (L1509), 2) three sections of the Thorndike submember, including one limestone

section (L1509), one dolostone section (L1502), and one section of mixed carbonate mineralogy (L1603). At Princeton University, 5 mg of carbonate powder from each sample were dissolved in 5 mL 0.1N buffered acetic acid and allowed to react for 4 hours in order to dissolve the carbonate without leaching the less soluble siliciclastic components. Following dissolution, the supernatant was centrifuged and separated from the insoluble residue.

To purify Ca and Mg, samples were processed through an automated high-pressure ion chromatography system (Dionex UCS-5000+) following previously established methods (e.g., Higgins et al. 2018). The purified samples were analyzed for $\delta^{44/40}$Ca and δ^{26}Mg values on a Thermo Scientific Neptune Plus Multicollector-Inductively Coupled Plasma-Mass Spectrometer (MC-ICP-MS) at Princeton University, using standard sample-standard bracketing techniques to correct for instrumental mass bias. Calcium isotope measurements were carried out at medium resolution to avoid $ArHH^+$ interferences. All samples were diluted to match standard concentrations within 10% in order to ensure comparable levels of $ArHH^+$ based interference across samples and bracketing standards, and in order to minimize concentration-dependent isotope effects. Samples were measured twice within the same run, and some sample were re-measured over multiple runs.

All data are reported in delta notation relative to a known standard, and the reported delta value is the average of the repeated measurements. The 2σ uncertainty for each sample can be found in the supplementary data table. For Ca isotopes, the measured $\delta^{44/42}$Ca values are converted to $\delta^{44/40}$Ca values relative to modern seawater assuming mass dependent fractionation with a slope of 2.05. For Mg isotopes, measured δ^{26}Mg values are reported relative to DSM-3. Long-term external reproducibility for each isotope system is determined based on the standard deviation of known standards taken through the full chemical procedure with each batch of samples. For Ca

isotopes, the external reproducibility for SRM915b and SRM915a relative to modern seawater is -1.17±0.15‰ (2σ, N=41) and -1.86±0.16‰ (2σ, N=24), respectively. For Mg isotopes, the long-term reproducibility for Cambridge-1 and seawater (PSW) are -2.57±0.11‰ (2σ, N=11) and -0.81±0.13‰ (2σ, N=22), respectively.

The Sr/Ca, Mn/Ca, and Mg/Ca ratios were measured on aliquots of dissolved powders analyzed for $\delta^{44/40}$Ca and δ^{26}Mg. Measurements were performed using a Thermo Finnegan iCAP Q Inductively Coupled Plasma Mass Spectrometer (ICP-MS). The metal to Ca ratios were determined using a set of matrix-matched in-house standards spanning the sample concentration. The external reproducibility of the metal to calcium concentrations is estimated at >90% (N=29) from replicate measurements of the SRM-88b standard. All geochemical data tables from this study are available in Appendix A2.

3.4. Results

Carbon isotope values from the Sourdough Limestone Member and overlying Middle Park submember are all negative, ranging from -5.7 to -0.7‰ (Fig. 3.3). The majority of δ^{13}C values for the Sourdough Limestone Member are between -4 and -2‰, with a generally positive, but scattered, trend up-section. Data from the Middle Park submember are more scattered, but most values are between -5 and -2‰. There is no generalized trend, and significant scatter (>2‰) is also observed over short length scales and within individual beds (Fig. 3.3). Within these units, δ^{13}C and δ^{18}O values do not strongly covary (r^2<0.02; Fig. 3.3). The basal 3 m of the Sourdough Limestone have $\delta^{44/40}$Ca values between -1.6 and -1.3‰, expected values for neomorphosed aragonite precipitates (Ahm et al., 2018; Higgins et al., 2018), while samples from the rest of the Sourdough Limestone and from the Middle Park submember range from -1.3 to -0.9‰, within the

range of altered aragonite or of modern calcite precipitates from seawater (Gussone et al., 2005, 2020; Figs. 3.3, 3.8B,D). Ratios of Sr/Ca range from ~0 to ~4.3 mmol/mol with an average of 1.9 mmol/mol, and Mn/Ca ratios range from ~0 to ~4.1 mmol/mol with an average of 0.75 mmol/mol (Fig. 3.8D-F).

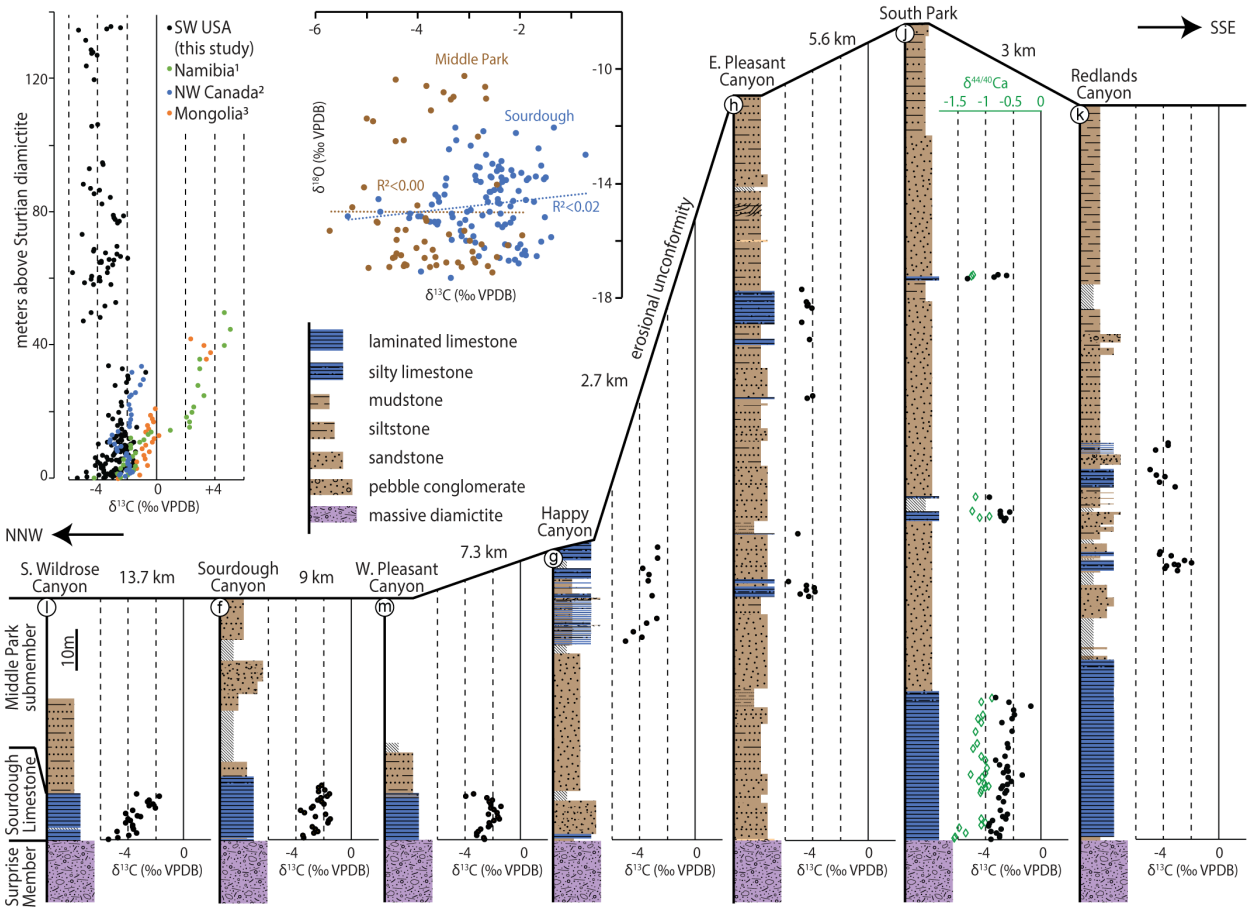

Figure 3.3. Lithostratigraphy and chemostratigraphy of the Sourdough Limestone Member and Middle Park submember. Sections correspond to labels in Fig. 3.1. Post-Sturtian $\delta^{13}C$ data from the Panamint Range are compared to corresponding data from Namibia (Halverson et al., 2005), NW Canada (Johnston et al., 2012), and Mongolia (Bold et al., 2016).

While carbonate rocks of the Sourdough Limestone Member and the Middle Park submember are exclusively limestone, those of the Thorndike submember vary in mineralogy along strike, with some sections preserved entirely as calcite, some as dolomite, and some with selective dolomitization interfingering with limestone (Figs. 3.4, 3.5). Dolomitization boundaries

are generally sharp, although within ~1 m of the adjacent limestone diffuse mm-scale veinlets of dolomite are common (Fig. 3.5C,D). The dolomitization boundaries generally follow bedding horizons, but are irregular and lobate on the outcrop scale (Fig 3.5A-C). Dolomitization fronts wedge in and out over relatively short lateral distances and occur within multiple stratigraphic horizons (Figs. 3.4, 3.5).

The Thorndike submember has large $\delta^{13}C$ variability that tracks mineralogy (Figs. 3.4-3.6). In limestone sections, $\delta^{13}C$ values range from ~+4 to +7‰, locally rising to +9‰ in the uppermost strata below the Wildrose diamictite. Limestone samples within 1-m of dolostone or siliciclastic beds are generally more negative (-2 to +4‰; Figs. 3.4-3.6). Dolomitized Thorndike beds have more $\delta^{13}C$ variability, ranging from -4 to +4‰. The correlation between $\delta^{13}C$ and mineralogy holds quantitatively with Mg/Ca data from select sections and qualitatively with 10% HCl field tests (Fig. 3.6A-B). Additionally, $\delta^{13}C$ values are more negative in thicker dolomitized intervals than in thinner ones (Fig. 3.6C). Measured $\delta^{13}C$ and $\delta^{18}O$ values in Thorndike samples do not covary (r^2=0.13/0.12), and $\delta^{18}O$ values range from -19.8 to -6.7‰, with a larger range and a lower average value among limestone samples (Fig. 3.6B).

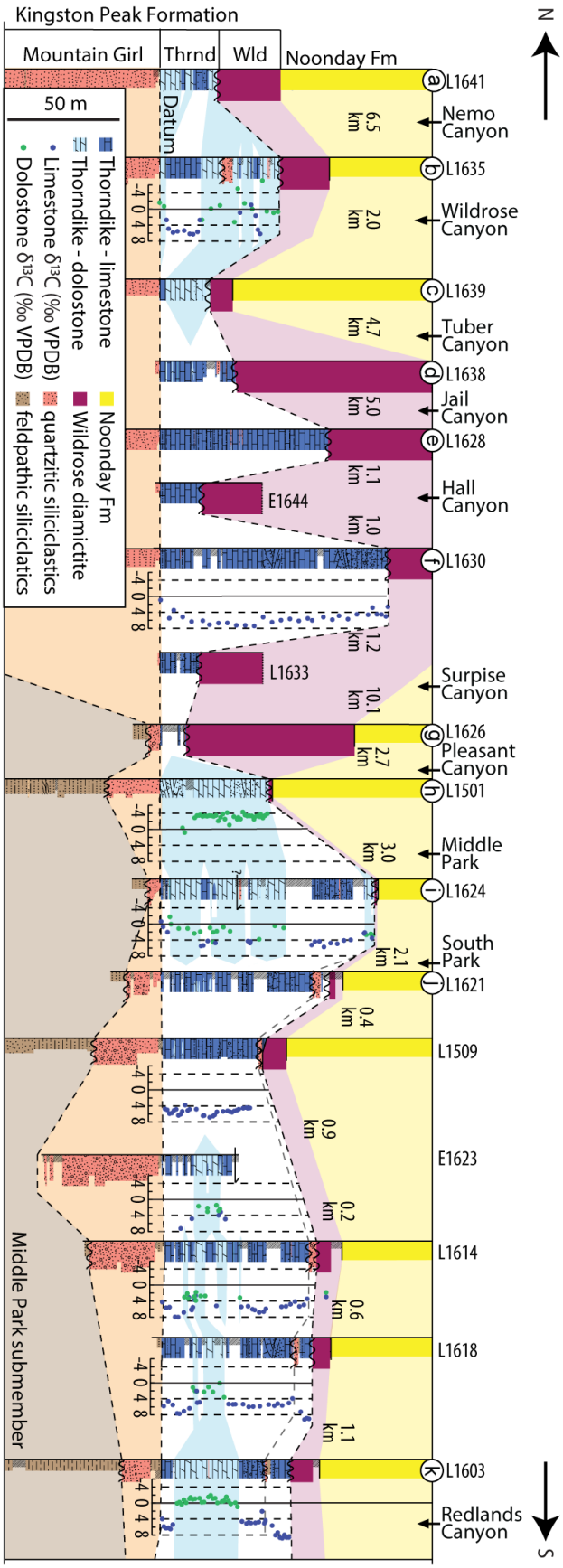
Kingston Peak Formation
Mountain Girl
Thrnd
Wld
Noonday Fm
N
S
50 m
Datum
Thorndike - limestone
Thorndike - dolostone
Wildrose diamictite
Noonday Fm
Limestone δ13C (‰ VPDB)
quartzitic siliciclastics
Dolostone δ13C (‰ VPDB)
feldpathic siliciclatics
a L1641
6.5 km
Nemo Canyon
b L1635
2.0 km
Wildrose Canyon
c L1639
4.7 km
Tuber Canyon
d L1638
5.0 km
Jail Canyon
e L1628
1.1 km
E1644
1.0 km
Hall Canyon
f L1630
1.2 km
L1633
10.1 km
Surpise Canyon
g L1626
2.7 km
Pleasant Canyon
h L1501
3.0 km
Middle Park
i L1624
2.1 km
South Park
j L1621
0.4 km
L1509
0.9 km
E1623
0.2 km
L1614
0.6 km
L1618
1.1 km
k L1603
Redlands Canyon
Middle Park submember
-4 0 4 8

Figure 3.4. Lithostratigraphy and $\delta^{13}C$ chemostratigraphy of the Thorndike submember. Sections correspond to labels in Fig. 3.1. Light blue shade represents dolomitization front. [Previous page]

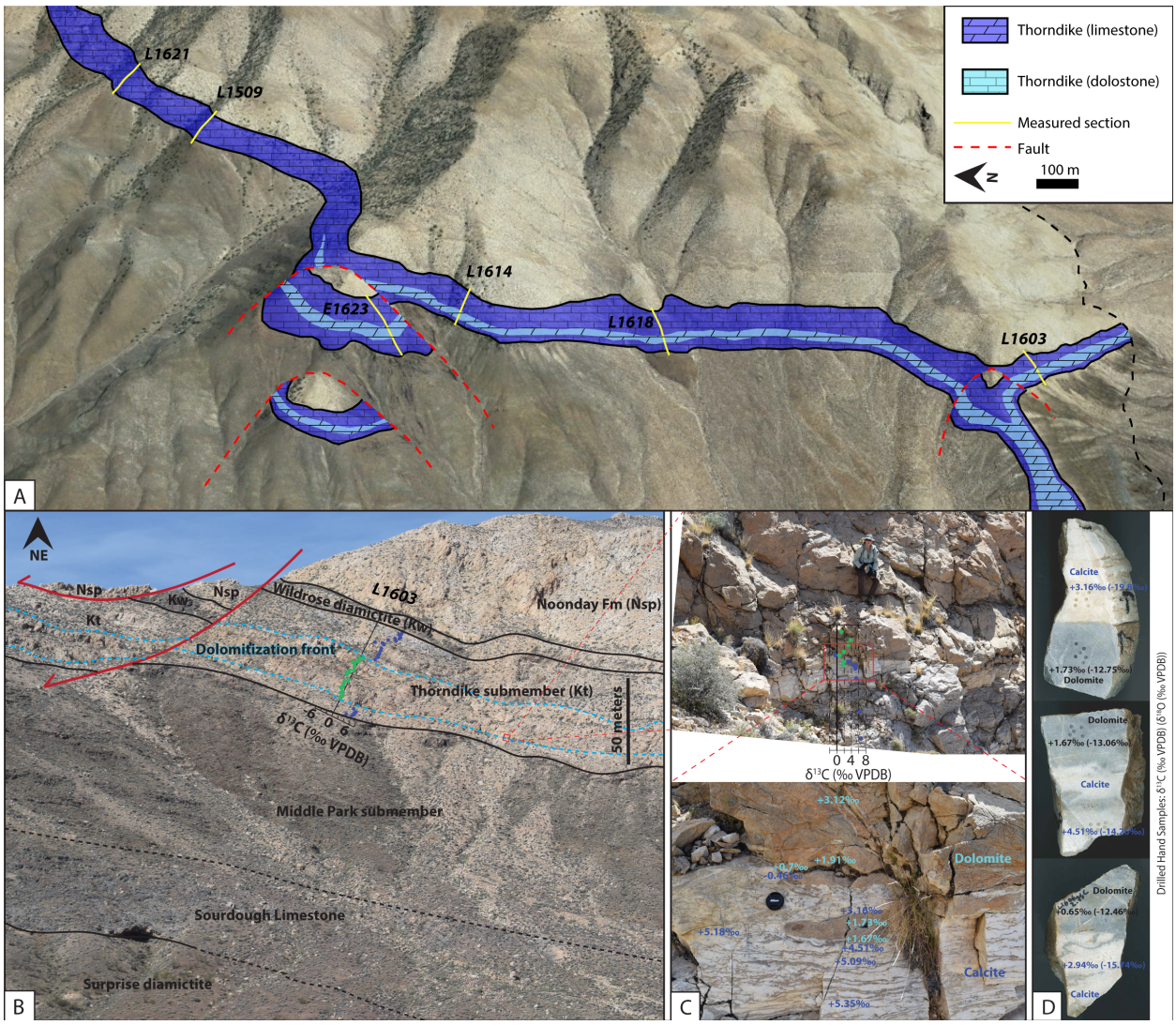

Figure 3.5. Alteration of carbon isotopes by dolomitization within the Thorndike submember in Redlands Canyon (section L1603). A) Annotated Google Earth image, demonstrating the spatial extent of laterally variable dolomitization within the Thorndike submember between South Park and Redlands Canyon. Section labels correspond to those in Fig. 3.4. B) Section-scale: Light blue lines outline the dolomitization front within the Thorndike submember. On the overlain $\delta^{13}C$ plot, points correspond to approximate stratigraphic position; blue points are limestone samples and green points are dolostone samples. C) Outcrop-scale: Images of the base of the dolomitized interval. Note the sharp, but irregular contact of the dolomitization, as well as the diffuse zone of dolomite veins proximal to the contact. On the overlain $\delta^{13}C$ plot, dark blue points are limestone and light blue points are dolomite. Values correspond to precise sample locations. D) Hand sample-scale: Drilled hand samples demonstrate high variability in $\delta^{13}C$ values on a cm-scale across the dolomitization front. $\delta^{18}O$ values are plotted in parentheses for comparison.

Between Redlands and South Park Canyon, clasts of the Wildrose diamictite are almost entirely carbonate and lithologically indistinguishable from the underlying Thorndike submember (Fig 3.7). Carbonate clasts include laminated light blue limestone, recrystallized white limestone, and orange to tan dolostone (Fig 3.7A-E). Limestone clasts have $\delta^{13}C$ values that range from -0.5 to +8.5‰, but most clasts are +4 to +8‰ (Fig. 3.7F,G). Dolostone clasts range from +0.3 to +3.2‰ and have lower values than most limestone samples (Fig. 3.7F,G). The majority of these values fall within the same ranges as the values of the underlying *in situ* limestone and dolostone beds of the Thorndike (Fig. 3.6C). Some dolostone clasts in the Wildrose diamictite are rimmed by calcite, and, in these samples, the rims generally have higher $\delta^{13}C$ values by up to 4‰ and lower and more consistent $\delta^{18}O$ values of ~-13‰ (Fig 3.7D,F).

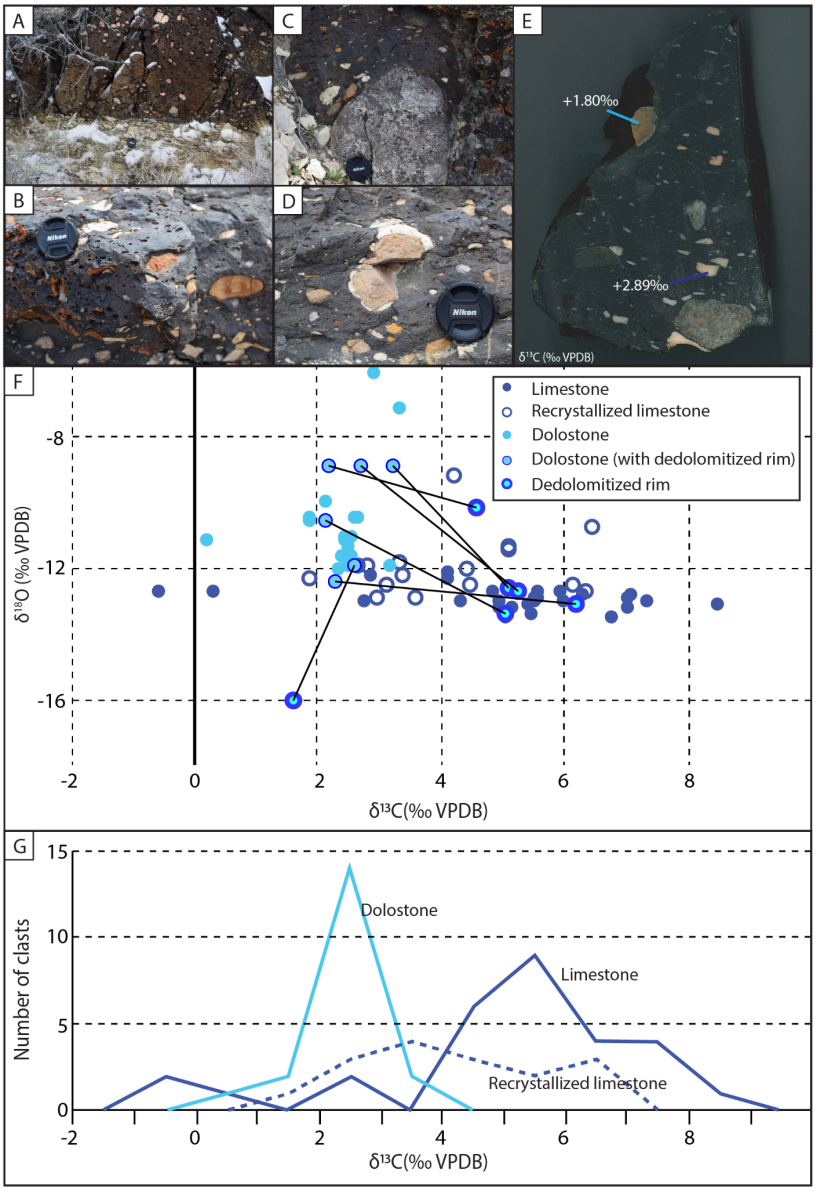

Figure 3.6. Field photographs and $\delta^{13}C$ data of the Wildrose submember. A) Wildrose diamictite erosively overlies the Thorndike submember, and basal portion is dominated by carbonate clasts of the Thorndike submember. B, C, E) There are both limestone and dolostone clasts within the basal Wildrose indicating dolomitization predated erosion of the Thorndike and deposition of the Wildrose—dolomite clasts are tan; limestone clasts are blue with lamination textures or white and recrystallized. D) Dolomite clast with dedolomitized rim. F) $\delta^{13}C$ values of various types of carbonate clasts within diamictite of the Wildrose submember sampled between South Park and Redlands Canyon suggest that dolomitization altered the carbon isotope values of the Thorndike prior to deposition of the Wildrose. Some dolostone clasts have dedolomitized reaction rims (pairs of rim and clast center are connected via lines), which show significant $\delta^{13}C$ alteration. G) Binned frequency of $\delta^{13}C$ clast composition by mineralogy. Coarsely recrystallized calcite clasts are distinguished from laminated limestone clasts that preserve sedimentary textures.

Within the three analyzed sections of the Thorndike submember, $\delta^{44/40}$Ca values for both dolostone and limestone samples are between -1.3 and -0.8‰ (Fig. 3.8), within the range of modern calcite precipitates from seawater (Gussone et al., 2005; 2020). There are no clear relationships between mineralogy and $\delta^{44/40}$Ca values, or between δ^{13}C and $\delta^{44/40}$Ca values (Fig. 3.8A,B). The δ^{26}Mg values of dolostone from these sections are between -1.8 and -1.2‰ (Fig. 3.8), which is ~1‰ higher than modern seawater-buffered dolomite (values ~-2.8‰, Higgins and Schrag, 2010). Dolostone $\delta^{44/40}$Ca and δ^{26}Mg values do not show a clear relationship (Fig. 3.8C). Limestone Sr/Ca ratios are scattered and range from ~0 to ~1.6 mmol/mol with an average of 0.4 mmol/mol. Dolostone Sr/Ca ratios range from ~0.1 to ~0.5 mmol/mol with an average of 0.3 mmol/mol and one outlier of 0.9 mmol/mol (Fig. 3.8D,E). Limestone Mn/Ca ratios range from ~0 to ~2.0 mmol/mol, with an average of 0.5 mmol/mol, and dolostone Mn/Ca ratios range from ~1.6 to ~9.4 mmol/mol with an average of 2.9 mmol/mol (Fig. 3.8F).

3.5. Discussion

3.5.1. Chemostratigraphy of the Sourdough and Middle Park

The Sourdough Limestone Member caps glaciogenic diamictite of the underlying Surprise Member and, together with the conformably overlying Middle Park submember, was deposited below wave base during post-Sturtian transgression (Nelson et al., 2020). We document lateral persistence of negative δ^{13}C values within the Sourdough Limestone Member and thin limestone beds of the Middle Park submember throughout the Panamint Range. Globally, in documented Sturtian cap carbonates, recovery of the Rasthof negative δ^{13}C excursion to positive values occurs over a short stratigraphic interval—typically within 10 m, and, even in the most expanded sections, within 20-40 m (Fig. 3.3; Bold et al., 2016; Hoffman and Schrag, 2002; Halverson et al., 2005)—

and presumably relatively rapidly (i.e. <100 kyrs, assuming sedimentation rate >0.1 mm/yr, Hoffman, 2011). Therefore, if the $\delta^{13}C$ values of the Sourdough Limestone Member and Middle Park submember record trends in the composition of global seawater DIC, the persistence of negative values for >130 m (Fig. 3.3) without a recovery to positive values would suggest rapid sedimentation rates within this basin, preserving an expanded stratigraphic record of the aftermath of the Sturtian glaciation. Such an interpretation is supported by sedimentological evidence consistent with fast sedimentation within the Middle Park submember, including channelized arkosic turbidites and soft-sediment deformation. Yet, the preservation of stratigraphically persistent negative $\delta^{13}C$ values within these units could have also resulted from local depositional conditions unrelated to trends in global seawater through processes which we discuss below.

The negative $\delta^{13}C$ values of the Sourdough Limestone and Middle Park are accompanied by low $\delta^{44/40}Ca$ values (as low as -1.6‰ with an average of -1.13‰; Fig. 3.3) and relatively high Sr/Ca values (average of 1.9 mmol/mol; Fig. 3.8), which are consistent with primary platform aragonite sediment for post-Sturtian cap carbonates—analogous to interpretations of aragonite precipitation accompanied by low $\delta^{13}C$ values for post-Marinoan cap carbonates (Ahm et al., 2019). In the Neoproterozoic, low $\delta^{13}C$ values of platform top aragonite have been linked to periods of sea-level rise, during which nutrient-rich and/or DIC-poor platform fluids were pushed to the surface (Ahm et al., 2019). Platform surface waters depleted in ^{13}C could have been generated by kinetic isotope effects due to CO_2 invasion driven by high primary productivity (Lazar and Erez, 1992) or upwelling of platform interior fluids that are out of equilibrium with the atmosphere (Clark et al., 1992). Allochems generated from such platformal carbonates and subsequently transported into more basinal environments could be preserved by sediment-buffered diagenesis (due to fast burial rates and/or minimal subsurface fluid flow in deeper water

environments) and therefore record negative $\delta^{13}C$ compositions, low $\delta^{44/40}Ca$ values, and high Sr/Ca values, comparable to those observed in the Sourdough Limestone Member and Middle Park submember.

In a variation from this model, the negative $\delta^{13}C$ values within limestone beds of the Middle Park could be the result of high local primary productivity and subsequent organic carbon remineralization and authigenic carbonate precipitation within pore space. This interpretation is consistent with $\delta^{13}C$ variability of >2‰ within relatively thin stratigraphic intervals (<5 m) or even single beds (Figs. 3.3, 3.9A). However, it is difficult to determine the original organic carbon concentrations in the unlithified sediment and coeval pore fluids of this unit, as organic matter could have been remobilized at a number of later stages including remineralization during early diagenesis, hydrocarbon migration, graphitization during burial metamorphism associated with Mesozoic orogenesis (Labotka et al., 1985), and oxidation by hydrothermal fluids associated with Miocene basin and range extension. Some of the other Cryogenian units in the Panamint Range (Limekiln Spring and Sourdough Limestone members) contain significant graphite enrichments (locally >1%), which have been interpreted as organic carbon in origin (Carlisle et al., 1980; Miller, 1985). Therefore, it is conceivable that this basin was a favorable environment for high productivity and that these mid-Cryogenian sediments, including those of the Middle Park, initially contained significant concentrations of organic carbon.

3.5.2. Chemostratigraphy of the Thorndike

The Thorndike submember is a carbonate platform deposit formed within shallow subaqueous environments of a partially restricted basin (see Geological Setting). Limestone of the Thorndike submember preserves highly ^{13}C-enriched $\delta^{13}C$ values (~+4 to +9‰), but dolostone samples within laterally equivalent strata preserve significantly lower $\delta^{13}C$ values (~-4 to +3‰) with $\delta^{13}C$

differences of up to 10‰. Since the isotopic alteration tracks mapped dolomitization fronts, which are irregular and occur at multiple stratigraphic levels, this range in $\delta^{13}C$ values cannot be explained by laterally diachronous deposition of the Thorndike submember or, consequentially, interpreted to reflect variation in primary seawater DIC values (Fig. 3.4).

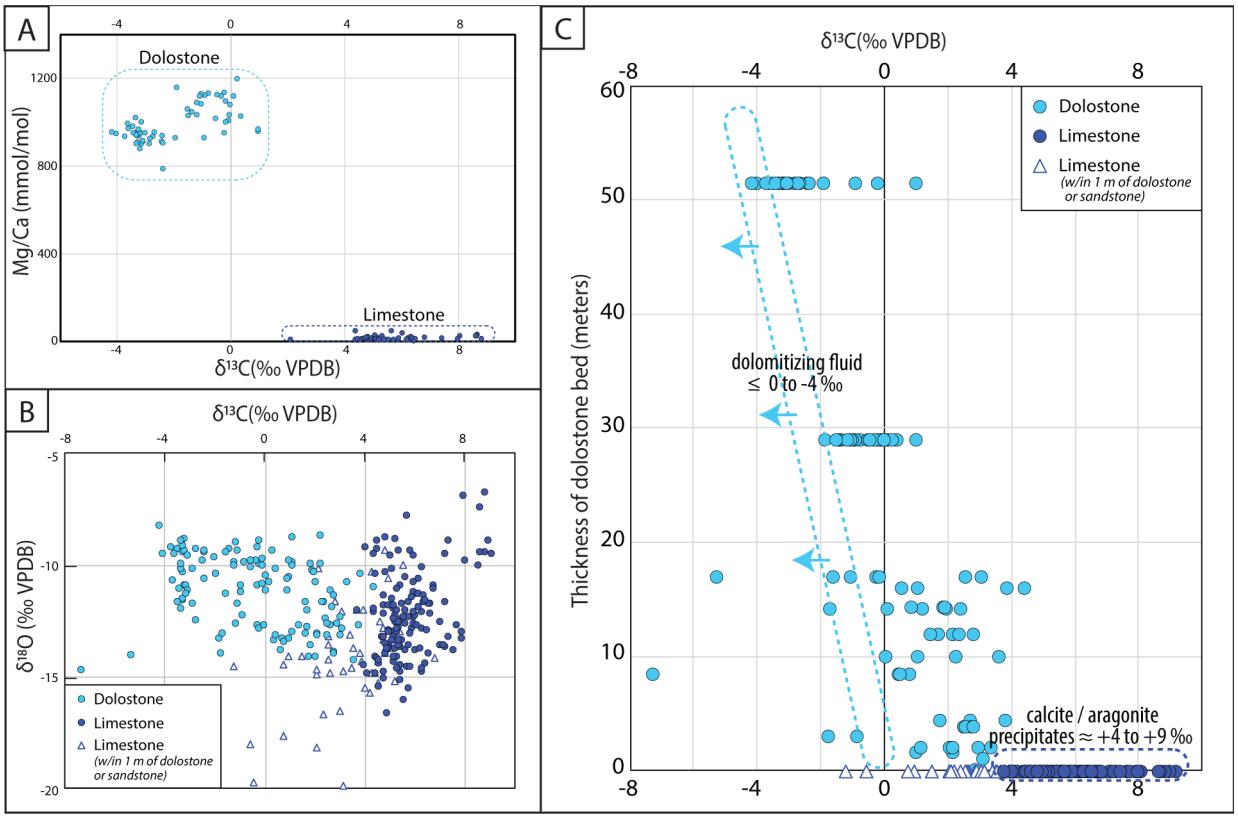

Figure 3.7. Cross plots showing mineralogy-dependent variability in $\delta^{13}C$ within Thorndike submember. A) Mg/Ca vs. $\delta^{13}C$ for sections L1502, L1509, and L1603 of Thorndike submember. B) $\delta^{18}O$ vs. $\delta^{13}C$ cross plot for samples from all sections of Thorndike submember. C) $\delta^{13}C$ values plotted against thickness of dolomitized interval they occur within, demonstrating that thicker zones of dolomitization have lower $\delta^{13}C$ values. Dolomite and limestone samples are in different colors. Limestone samples within 1-m of a dolostone or siliciclastic bed are plotted as triangles.

The timing of the dolomitization is critical to understanding the mechanism for isotopic alteration. The overlying Marinoan-age Wildrose diamictite contains abundant clasts of both dolostone and limestone that were clearly derived from the underlying Thorndike submember, which requires that dolomitization occurred during or prior to the Marinoan glaciation. Carbon isotope values of clasts within the Wildrose diamictite range from -1 to +9‰, with dolostone clasts

statistically lighter than limestone clasts (Fig. 3.7), comparable to the variability observed in the underlying Thorndike (Fig. 3.4). Curiously, some dolostone clasts are associated with recrystallized rims of calcite that have $\delta^{13}C$ values that are elevated by up to 4‰ compared to the clast interiors (N=6), and have lower and more consistent $\delta^{18}O$ values that trend towards ~-13‰ (Fig. 3.7F,G). The isotopic differences of these reaction rims are consistent with burial-related de-dolomitization of the clasts, possibly associated with the same stage of diagenesis as sediment-buffered neomorphism of aragonite to calcite within the underlying Thorndike submember. Fluids associated with this neomorphism would have been carbon buffered by ^{13}C-enriched limestone of the underlying Thorndike submember, and the recrystallized carbonates would have had relatively consistent and lower $\delta^{18}O$ composition associated with an elevated burial temperature (Fig. 3.6B). Under this scenario, the isotopic signatures on the de-dolomitized reaction rims of the Wildrose clasts are recording this later stage of burial-related neomorphism, while the dolomitization within the Thorndike submember and associated $\delta^{13}C$ alteration occurred prior to the deposition of the Wildrose submember.

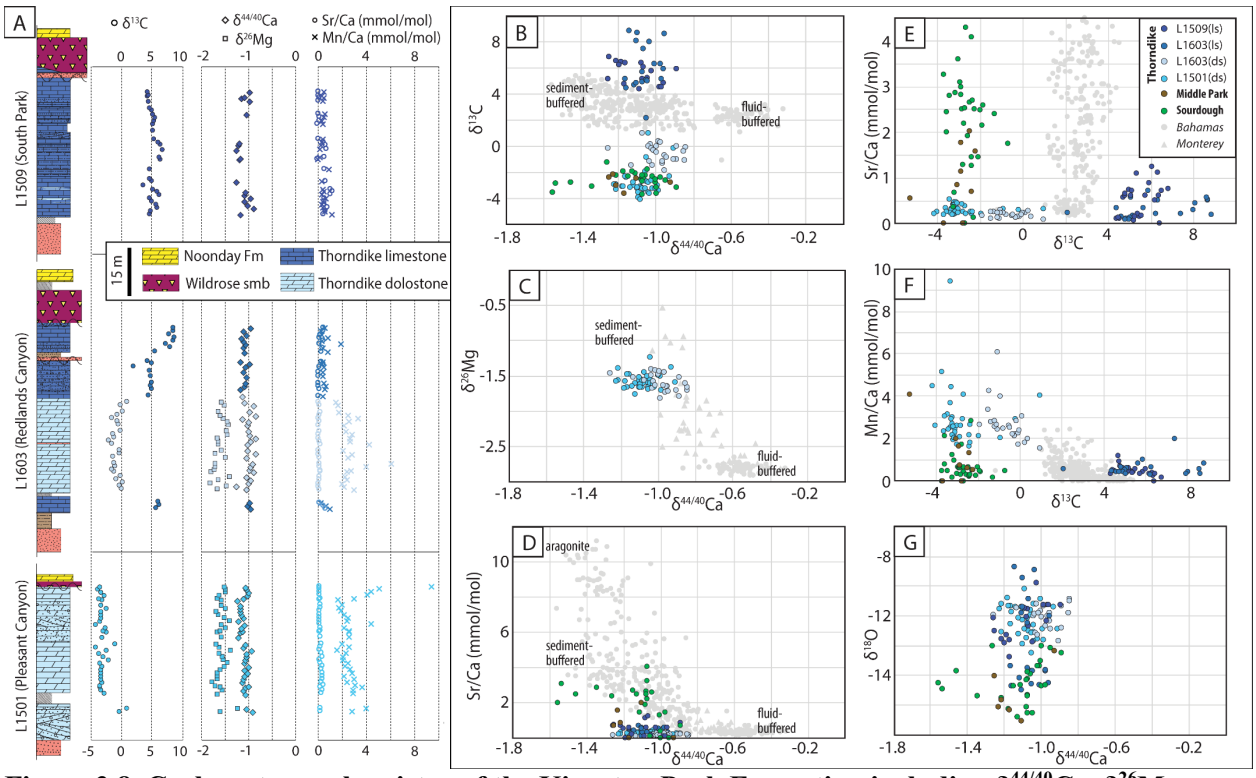

Figure 3.8. Carbonate geochemistry of the Kingston Peak Formation including $\delta^{44/40}Ca$, $\delta^{26}Mg$, Sr/Ca, and Mn/Ca data. A) Lithostratigraphy of Thorndike submember sections L1502, L1509, and L1603 with $\delta^{13}C$, $\delta^{44/40}Ca$, $\delta^{26}Mg$, Sr/Ca, and Mn/Ca data. Note dolostone and limestone samples are different colors and correspond to colors in cross plots. B-G) Cross plots comparing $\delta^{13}C$, $\delta^{18}O$, $\delta^{44/40}Ca$, $\delta^{26}Mg$, Sr/Ca, and Mn/Ca data from Sourdough Limestone Member, Middle Park submember, and Thorndike submember. Geochemical data from Miocene–Holocene carbonates from the Bahamas and authigenic dolomite from the Neogene Monterey Formation plotted for comparison (Blättler et al., 2015; Ahm et al., 2018; Higgins et al., 2018). ls—limestone; ds—dolostone.

Based on existing radiometric age constraints and the mineralogy and $\delta^{13}C$ values of carbonate clasts within the Wildrose, dolomitization and $\delta^{13}C$ alteration within the Thorndike must have occurred after deposition <652 Ma and before the end of the Marinoan glaciation at 635 Ma (Nelson et al., 2020). Since platform dolomitization is driven by subsurface fluid flow, which is enhanced by sea-level fluctuations (Kaufman, 1994), this relatively early dolomitization may have been related to either local, tectonically driven base level change or eustatic change forced by Cryogenian climate. The lateral variability of the dolomitization front may be explained by: 1) disparities in initial porosity of the carbonate; 2) proximity to basin faults active during times of

fluid migration; and/or 3) depositional position on the carbonate platform (platform interior, rim, foreslope). Given the high Mg^{2+} budget and fluid flow requirements for post-depositional dolomitization, modification of $\delta^{13}C$ values by dolomitizing fluids is conceptually reasonable. Similarly, $\delta^{13}C$ variability of up to 5‰ has been documented between limestone and dolostone in Cryogenian and Ediacaran sections from Mongolia (Bold et al., 2016, 2020). The observations from both the Thorndike and units in Mongolia demonstrate the ability of early-burial dolomitization to drastically alter $\delta^{13}C$ values. In the case of the Thorndike submember, the dolomitizing fluid must have been significantly ^{13}C-depleted, based on the directionality and extent of the alteration, which may help characterize the diagenetic processes operating within Neoproterozoic carbonate platforms.

Calcium and magnesium isotopes of carbonate rocks have been established as useful tracers of marine diagenesis and can be used to discriminate between seawater- and sediment-buffered diagenesis (Ahm et al., 2018; Higgins et al., 2018). Modern to recent dolomite that formed during early-marine diagenesis in a fluid-buffered setting tend to have high $\delta^{44/40}Ca$ values that approach modern seawater (0‰) and low $\delta^{26}Mg$ values that are 2‰ lighter than modern seawater (~-2.8‰, Higgins and Schrag, 2010). This offset of $\delta^{26}Mg$ values from seawater has been suggested to be the result of a Mg isotope fractionation factor of ~0.9980 associated with the recrystallization of low-Mg calcite and dolomite (Higgins and Schrag, 2010; Fantle and Higgins, 2014; Higgins et al., 2018), while the $\delta^{44/40}Ca$ values are similar to seawater because the Ca isotope fractionation factor associated with recrystallization approaches ~1.0000 (Fantle and DePaolo, 2007). In contrast, dolomites formed under sediment-buffered conditions have $\delta^{44/40}Ca$ values within the range of the precursor carbonate sediments (~-1.5 to -1.0‰, Gussone et al., 2005) and

δ^{26}Mg values that are variably enriched from -2.8‰ (due to Raleigh-type distillation, Fantle and Higgins, 2014; Blättler et al., 2015).

Calcium isotope values of the Thorndike limestone are within the range of modern calcite precipitates and bulk silicate Earth that, on average, are -1‰ depleted in $\delta^{44/40}$Ca relative to modern seawater (Fig. 3.8; Blättler and Higgins, 2017; Gussone et al., 2020). The $\delta^{44/40}$Ca values of the Thorndike dolomite samples are within the same range as the limestone samples, and the δ^{26}Mg values are ^{26}Mg-enriched (Fig. 3.8). These values indicate that the dolomitizing fluids were significantly evolved from coeval seawater (sediment-buffered dolomitization), since reactions with the surrounding sediment caused $\delta^{44/40}$Ca values to become lower and δ^{26}Mg values to become higher.

Previously, high δ^{13}C values of the Thorndike have been attributed to global processes that led to ^{13}C-enriched marine DIC, and thus correlated to highly positive values recorded in other Cryogenian carbonate strata globally termed the "Keele peak" (e.g., Halverson et al., 2005). Based on the regional stratigraphic and sedimentological evidence for partial restriction of the Thorndike carbonate platform, as well as the geochemical data presented herein, we suggest an alternative local explanation for these high δ^{13}C values that does not require extreme global seawater DIC composition. Below, we explore possible mechanisms for producing ^{13}C-enriched and ^{13}C-depleted δ^{13}C values within the limestone and dolostone, respectively, of the Thorndike submember.

High δ^{13}C values of Thorndike limestone may reflect intense local primary productivity on the platform top, which led to ^{13}C-enriched DIC in surface waters, as has been proposed to explain ^{13}C-enriched DIC on the Bahama Banks relative to modern marine DIC (Swart et al., 2009; Geyman and Maloof, 2019). Alternatively, rather than being produced within platform top waters,

^{13}C-enriched DIC could have been produced within pore fluids by high local oxygenic phototrophic productivity within oxic pore spaces of stromatolite reefs, microbial mats, or grainstones, adjacent to the sediment-water interface (Fig. 3.9A). Even though much of the Thorndike carbonate sediment is traction-bedded grainstone, the original precipitation of these carbonate minerals prior to transport may have occurred primarily within microbially influenced pore spaces. Another potential source of ^{13}C-enriched authigenic carbonate is within the methanogenesis zone, particularly if ^{13}C-depleted methane escapes as gas before remineralization (Hayes and Waldbauer, 2006; Birgel et al., 2015). While methanogenesis can decrease the carbonate saturation of pore waters, leading to carbonate dissolution rather than precipitation, carbonate can form where CO_2 production is offset by alkalinity production from phototrophic CO_2 fixation or anaerobic methane oxidation (Fig. 3.9A; Moore et al., 2004; Birgel et al., 2015). Although this type of balanced metabolic competition may be an implausible mechanism for production of the large volumes of authigenic carbonate necessary to lead to stratigraphically and laterally consistent $\delta^{13}C$ values at scale — such as those observed within limestone of the Thorndike submember for >80 m of strata across >50 km (Fig. 3.4) — it is possible this scale of carbonate precipitation could be supported during the Proterozoic by increased background carbonate supersaturation in ocean and/or pore fluids (Grotzinger and James, 2000; Higgins et al., 2009; Birgel et al., 2015).

The relatively low $\delta^{13}C$ values recorded in dolostone of the Thorndike submember (Figs. 3.4-3.6) indicate the DIC of dolomitizing fluids had a significantly lower $\delta^{13}C$ composition than the fluids from which the limestone precipitated. If dolomitization resulted from reflux circulation of platform waters, then ^{13}C-depleted fluids could have resulted from kinetic isotope effects related to CO_2 invasion in surface waters (e.g., Ahm et al., 2019), as conjectured above for the Sourdough

Limestone Member and Middle Park submember. Alternatively, the low $\delta^{13}C$ composition could be the product of organic carbon remineralization along the flow path of the dolomitizing fluid within platform waters and/or pore fluids, which is consistent with the sediment-buffered $\delta^{44/40}Ca$ and $\delta^{26}Mg$ values accompanying negatively altered $\delta^{13}C$ values. In this model, as fluids migrated across this partially restricted platform top and flushed through it, either through brine reflux or thermal convection (Fig. 3.9B; e.g., Kaufman, 1994), they became sediment-buffered with respect to Ca^{2+} and Mg^{2+} and diverged from the $\delta^{13}C$ composition of seawater DIC. However, rather than simply inheriting $\delta^{13}C$ values from the precursor carbonate sediments (which were ^{13}C-enriched), these dolomitizing fluids also incorporated remineralized organic carbon through aerobic respiration on the platform top and/or from zones of anaerobic organic carbon remineralization within the precursor sediment pore fluids, leading to ^{13}C-depleted DIC within the fluids relative to the sediment (Fig. 3.9; Malone et al., 2002; Meister and Reyes, 2019). We suggest that these fluids dolomitized portions of the platform, forming early-burial diagenetic dolomite with relatively ^{13}C-depleted $\delta^{13}C$ values. An organic carbon remineralization mechanism for the production of ^{13}C-depleted dolomite is supported by the high Mn/Ca ratios of the Thorndike dolostone relative to the precursor limestone (Fig. 3.8F; even accounting for differences in Mg/Ca), which suggest the dolomitizing fluids were reducing. This interpretation is further supported by a correlation between dolomite bed thickness and depletion of $\delta^{13}C$ (Fig. 3.6C). Within a reflux dolomitization scenario, dolomitizing fluids with a longer flow path had more opportunity to incorporate ^{13}C-depleted DIC through organic carbon remineralization (Fig. 3.9), and, moreover, larger volumes of fluid had higher oxidant loads and were less sediment-buffered by the ^{13}C-enriched precursor limestone.

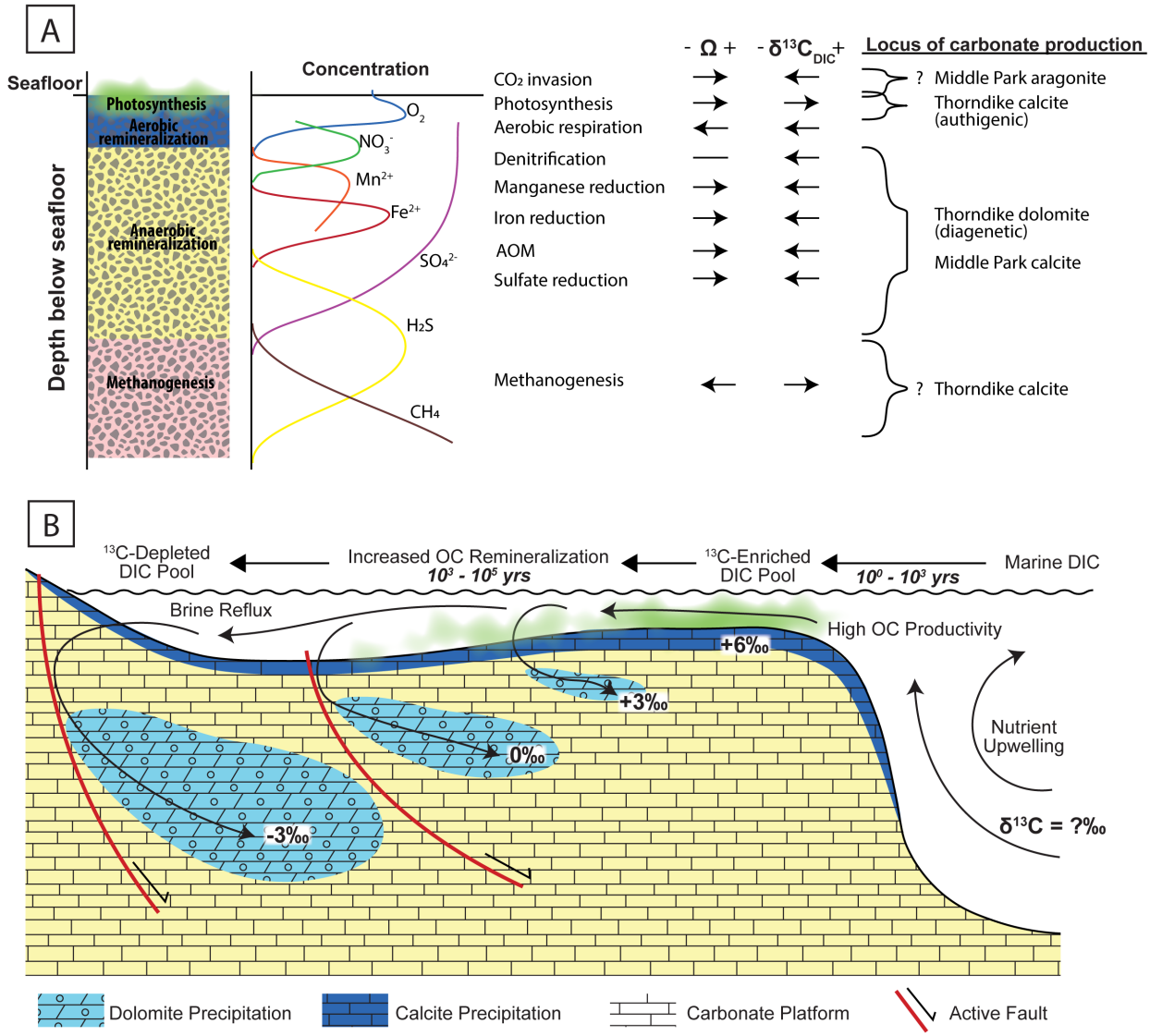

Figure 3.9. Schematic models of subsurface redox profiles and isotopic alteration by platformal dolomitization. A) Schematic subsurface redox profile beneath oxygenated bottom waters (Jorgensen and Kasten, 2006). The effects on pore water carbonate saturation (Ω) and DIC $\delta^{13}C$ composition of various subsurface organic carbon production and remineralization pathways (Ohmoto, 1972; Malone et al., 2002; Higgins et al., 2009; Bergmann et al., 2013; Meister and Reyes, 2019). Probable loci of authigenic carbonate production to produce observed $\delta^{13}C$ values of the Thorndike and Middle Park submembers. B) Schematic model for isotopic alteration by platformal dolomitization. Thicker intervals of dolomitization result from a longer fluid pathway, with more opportunity to incorporate isotopically light remineralized organic carbon, resulting in a relationship between dolomite thickness and $\delta^{13}C$ values. DIC—dissolved inorganic carbon; OC—organic carbon; AOM—anaerobic oxidation of methane.

We speculate that localized organic carbon production and remineralization could have been an important lever on $\delta^{13}C$ values of carbonates during the microbially dominated

Neoproterozoic. Since the $\delta^{13}C$ record is predominantly from carbonate rocks, it is fundamentally tied to carbonate sediment production, which is recognized to have varied significantly through Earth history (e.g., Grotzinger and James, 2000). Following the establishment of the skeletal carbonate factory in the late Cambrian, global carbonate production during the Phanerozoic was dominated by skeletal carbonate minerals produced by biomineralizing organisms (both metazoans and algae) within the water column and therefore in relative equilibrium with the DIC of seawater (assuming only minor kinetic effects). However, in the Proterozoic and Cambrian, carbonate production was likely restricted to shallow-water platforms dominated by microbial mats. In these settings, carbonate minerals were primarily produced within microbially influenced environments, such as beneath biofilms in inter-mat spaces or pore waters, and precipitated from fluids that were restricted from seawater and thus from the global DIC pool (Visscher and Stolz, 2005). If the bottom waters of these platform environments were oxygenated, the subsurface pore waters could have large redox gradients spanning fully aerobic to anaerobic and methanogenic redox zones (Fig 3.9A).

The redox zones of pore waters would control (1) the carbonate saturation state of the pore waters (Visscher and Stolz, 2005; Higgins et al., 2009; Bergmann et al., 2013), (2) the rates of organic carbon production and remineralization, and (3) the $\delta^{13}C$ composition of pore water DIC (Ohmoto, 1972; Malone et al., 2002; Meister and Reyes, 2019). Therefore, the $\delta^{13}C$ composition of authigenic carbonate precipitated below the sediment-water interface – the dominant space of carbonate precipitation in the Proterozoic microbial world – resulted from the relative locus of mineralization within the framework of this diagenetic redox profile (Fig. 3.9A). Moreover, both the locus of mineralization and structure of the redox profile would be controlled by local factors such as the amount of organic carbon within the unlithified sediments, sediment porosity, relative

openness of the system to fluid flow, and sedimentation rates. Large swings in the $\delta^{13}C$ record of platform carbonates formed under these microbially influenced conditions are consistent with local variations in sedimentary facies, rather than global changes to the surface carbon cycle.

For example, in carbonate platforms dominated by stromatolite reefs and grainstones with high porosities (relatively open-system), primary productivity could leave behind a ^{13}C-enriched pool of DIC from which to precipitate authigenic carbonate with positive $\delta^{13}C$ values, such as those seen in limestone of the Thorndike submember, which could be preserved if open-system behavior allowed organic carbon remineralization to be temporally or spatially separated from this precipitation. Conversely, in a depositional system of interbedded mudstone and carbonate (more closed-system settings), these siliciclastic layers could form seals on fluid migration after burial and compaction, preventing this open-system behavior during diagenesis. Anaerobic remineralization of organic carbon during diagenesis within such a closed system could produce a ^{13}C-depleted pool of DIC within the pore waters from which to precipitate authigenic carbonate with negative $\delta^{13}C$ values, such as those seen in limestone of the Middle Park submember. Depending on the specific conditions and fluid pathways, diagenetic dolomitization could introduce either marine DIC or fluids that are significantly evolved from marine DIC with altered isotopic compositions (such as those that dolomitized the Thorndike submember). If local sediment burial conditions and carbonate facies were the primary controls on $\delta^{13}C$ values, broadly correlative carbon isotope excursions, such as the Rasthof, Keele, and Trezona anomalies during the Cryogenian, can potentially be explained by regionally or globally consistent sedimentation and dolomitization patterns, controlled by factors such as margin-wide or global changes in sea level, climate, or tectonism.

If local carbonate platform processes contributed to the widespread, extreme variability in $\delta^{13}C$ values observed during the Neoproterozoic and early Cambrian, why is such variability not observed in microbially dominated carbonate platforms of the Mesoproterozoic (Fig. 3.10)? An implication of the outlined model is that a significant subsurface redox gradient was necessary to drive variation in carbon speciation, and thus $\delta^{13}C$ variability, within microbially mediated authigenic carbonates (Fig. 3.9). This suggests that the onset of large magnitude carbon isotope excursions in the Tonian (i.e. Bitter Spring anomaly) resulted from an increase in the oxygen levels of marine environments at this time (Fig. 3.10; Hoffman and Lamothe, 2019), which has been increasingly supported by other lines of evidence (e.g., Cole et al., 2016; Planavsky et al., 2018). Furthermore, this model may explain large $\delta^{13}C$ variability associated with the Great Oxidation Event and the subsequent Lomagundi excursion (e.g., Mayika et al., 2020). It has been suggested that after the Lomagundi excursion at ~2.05 Ga, oxygen levels decreased again (Bekker and Holland, 2012), perhaps associated with lower global primary productivity (Hodgskiss et al., 2019). Empirical evidence and models are consistent with the continuation of low oxygen (<1% present atmospheric level) and low marine primary productivity (<3% present level) throughout the mid-Proterozoic from ~2.05-0.81 Ga (e.g., Crockford et al., 2018; Planavsky et al., 2018). We suggest these environments lacked the requisite levels of surface productivity and subsurface redox gradients, even within microbially dominated carbonate platforms, to drive localized large carbon isotope variability within platform and pore waters.

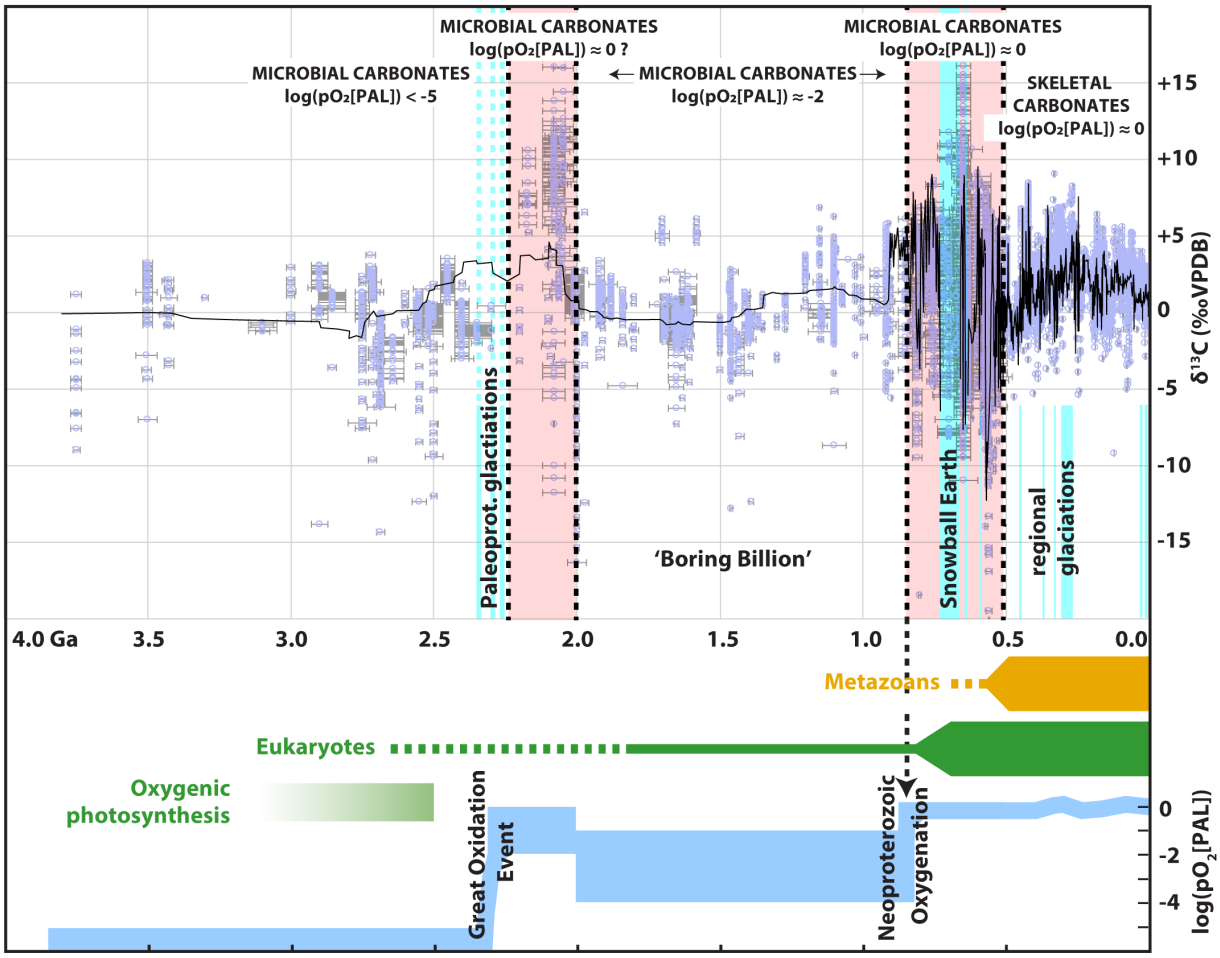

Figure 3.10. The carbon isotope record of Earth's carbonates. $\delta^{13}C_{carb}$ data points from Prokoph et al. (2008). Composite $\delta^{13}C$ curves from Shields and Veizer (2002) (Archean–Mesoproterozoic), modified from Halverson et al. (2005) (Neoproterozoic), and from Saltzman and Thomas (2012) (Cambrian–Quaternary). Atmospheric O_2 curve modified from Lyons et al. (2014). Pink shading indicates intervals of high $\delta^{13}C$ variability that is attributed to elevated subsurface pore water redox gradients.

3.6. Conclusions

We present $\delta^{13}C$, $\delta^{44/40}Ca$, and $\delta^{26}Mg$ geochemical data from carbonate strata deposited during the Cryogenian non-glacial interlude in the Panamint Range, California. Negative $\delta^{13}C$ values preserved for >100 m in the post-Sturtian Sourdough Limestone Member and Middle Park submember suggest an expanded record of the aftermath of the Sturtian glaciation. These are accompanied by relatively low $\delta^{44/40}Ca$ values and high Sr/Ca ratios, consistent with primary

aragonite sedimentation for Sturtian cap carbonates, which were sediment buffered in this environment due to high sedimentation rates. Persistent negative $\delta^{13}C$ values may have been produced through local anaerobic organic carbon remineralization and/or kinetic effects related to CO_2 invasion, both consistent with high platform primary productivity. Within the pre-Marinoan Thorndike submember, early-burial dolomitization drastically shifted $\delta^{13}C$ of carbonates, depleting values by up to 10‰ in comparison to stratigraphically equivalent limestone. Geochemical tracers of diagenesis ($\delta^{44/40}Ca$ and $\delta^{26}Mg$ values) suggest $\delta^{13}C$ variability in the Thorndike reflects the evolution of local dissolved inorganic carbon pools within a partially restricted carbonate platform: 1) Highly ^{13}C-enriched $\delta^{13}C$ values within limestone samples of the Thorndike resulted from local primary productivity on platform tops or within oxygenated pore waters; and 2) relatively ^{13}C-depleted $\delta^{13}C$ values within dolostone resulted from evolved dolomitizing fluids incorporating remineralized organic carbon from platform waters and/or sediment pore space. These results indicate sediment-buffered diagenesis, with respect to Ca and Mg isotopes, can lead to $\delta^{13}C$ alteration within carbonates through remineralization of platform top and sediment-hosted organic carbon within pore fluids. Therefore, in some cases, $\delta^{13}C$ variability in the Neoproterozoic could reflect variations in local organic carbon production and remineralization within platform top and pore waters, rather than perturbations to the global surface carbon cycle.

3.7. Acknowledgements

We thank the U.S. National Park Service at Death Valley National Park for a sampling permit. Field work was carried out on ancestral homelands of the Timbisha Shoshone Tribe. LLN was supported by the Harvard University Booth Postgraduate Fellowship, National Geographic

Society Early Career Grant CP-002ER-17, and National Science Foundation GRF DGE-1746891. EFS was supported by the National Science Foundation (NSF-1827715, NSF-2021064) and the Smithsonian Institution Buck Fellowship. ACA was supported by the Simons Foundation (SCOL 611878). The Harvard University Department of Earth and Planetary Sciences and Johns Hopkins University Department of Earth and Planetary Sciences provided additional support. We thank S. Goff and D. Schrag at Harvard University and D. Brenner at Johns Hopkins University for helping to analyze carbon and oxygen isotopes. We thank N. O'Connell and J. Haywood for enthusiastic assistance in the field, and C. Dwyer and S. Lobianco for assistance prepping samples for analyses. D. Johnston provided helpful comments on an early version of the discussion. We are grateful to A. Prave and N. Planavsky for thoughtful reviews that improved this manuscript, and to L. Derry for editorial feedback and support.

3.8. References

Ahm, A.S.C., Bjerrum, C.J., Blättler, C.L., Swart, P.K. and Higgins, J.A., 2018. Quantifying early marine diagenesis in shallow-water carbonate sediments. *Geochimica et Cosmochimica Acta*, *236*, pp.140-159.

Ahm, A.S.C., Maloof, A.C., Macdonald, F.A., Hoffman, P.F., Bjerrum, C.J., Bold, U., Rose, C.V., Strauss, J.V. and Higgins, J.A., 2019. An early diagenetic deglacial origin for basal Ediacaran "cap dolostones". *Earth and Planetary Science Letters*, *506*, pp.292-307.

Banner, J.L. and Hanson, G.N., 1990. Calculation of simultaneous isotopic and trace element variations during water-rock interaction with applications to carbonate diagenesis. *Geochimica et Cosmochimica Acta*, *54*(11), pp.3123-3137.

Beeler, S.R., Gomez, F.J. and Bradley, A.S., 2020. Controls of extreme isotopic enrichment in modern microbialites and associated abiogenic carbonates. *Geochimica et Cosmochimica Acta*, *269*, pp.136-149.

Bekker, A. and Holland, H.D., 2012. Oxygen overshoot and recovery during the early Paleoproterozoic. *Earth and Planetary Science Letters*, *317*, pp.295-304.

Bergmann, K.D., Grotzinger, J.P. and Fischer, W.W., 2013. Biological influences on seafloor carbonate precipitation. *Palaios*, *28*(2), pp.99-115.

Birgel, D., Meister, P., Lundberg, R., Horath, T.D., Bontognali, T.R., Bahniuk, A.M., de Rezende, C.E., Vásconcelos, C. and McKenzie, J.A., 2015. Methanogenesis produces strong 13C enrichment in stromatolites of Lagoa Salgada, Brazil: a modern analogue for Palaeo-/Neoproterozoic stromatolites? *Geobiology*, *13*(3), pp.245-266.

Blättler, C.L. and Higgins, J.A., 2017. Testing Urey's carbonate–silicate cycle using the calcium isotopic composition of sedimentary carbonates. *Earth and Planetary Science Letters*, *479*, pp.241-251.

Blättler, C.L., Miller, N.R. and Higgins, J.A., 2015. Mg and Ca isotope signatures of authigenic dolomite in siliceous deep-sea sediments. *Earth and Planetary Science Letters*, *419*, pp.32-42.

Bold, U., Smith, E.F., Rooney, A.D., Bowring, S.A., Buchwaldt, R., Dudás, F.Ő., Ramezani, J., Crowley, J.L., Schrag, D.P. and Macdonald, F.A., 2016. Neoproterozoic stratigraphy of the Zavkhan terrane of Mongolia: The backbone for Cryogenian and early Ediacaran chemostratigraphic records. *American Journal of Science*, *316*(1), pp.1-63.

Bold, U., Ahm, A.S.C., Schrag, D.P., Higgins, J.A., Jamsran, E. and Macdonald, F.A., 2020. Effect of dolomitization on isotopic records from Neoproterozoic carbonates in southwestern Mongolia. *Precambrian Research*, *350*, p.105902.

Carlisle, D., Kettler, R.M. and Swanson, S.C., 1980. Geological Study of uranium potential of the Kingston Peak Formation, Death Valley Region, California: U.S. Department of Energy Open File Report, Grand Junction, 109 p.

Clark, I.D., Fontes, J.C. and Fritz, P., 1992. Stable isotope disequilibria in travertine from high pH waters: laboratory investigations and field observations from Oman. *Geochimica et Cosmochimica Acta*, *56*(5), pp.2041-2050.

Cole, D.B., Reinhard, C.T., Wang, X., Gueguen, B., Halverson, G.P., Gibson, T., Hodgskiss, M.S., McKenzie, N.R., Lyons, T.W. and Planavsky, N.J., 2016. A shale-hosted Cr isotope record of low atmospheric oxygen during the Proterozoic. *Geology*, *44*(7), pp.555-558.

Corsetti, F.A. and Kaufman, A.J., 2003. Stratigraphic investigations of carbon isotope anomalies and Neoproterozoic ice ages in Death Valley, California. *Geological Society of America Bulletin*, *115*(8), pp.916-932.

Crockford, P.W., Hayles, J.A., Bao, H., Planavsky, N.J., Bekker, A., Fralick, P.W., Halverson, G.P., Bui, T.H., Peng, Y. and Wing, B.A., 2018. Triple oxygen isotope evidence for limited mid-Proterozoic primary productivity. *Nature*, *559*(7715), pp.613-616.

Derry, L.A., 2010. A burial diagenesis origin for the Ediacaran Shuram–Wonoka carbon isotope anomaly. *Earth and Planetary Science Letters*, *294*(1-2), pp.152-162.

Fantle, M.S. and DePaolo, D.J., 2007. Ca isotopes in carbonate sediment and pore fluid from ODP Site 807A: the Ca2+ (aq)–calcite equilibrium fractionation factor and calcite recrystallization rates in Pleistocene sediments. *Geochimica et Cosmochimica Acta*, *71*(10), pp.2524-2546.

Fantle, M.S. and Higgins, J., 2014. The effects of diagenesis and dolomitization on Ca and Mg isotopes in marine platform carbonates: implications for the geochemical cycles of Ca and Mg. *Geochimica et Cosmochimica Acta*, *142*, pp.458-481.

Geyman, E.C. and Maloof, A.C., 2019. A diurnal carbon engine explains 13C-enriched carbonates without increasing the global production of oxygen. *Proceedings of the National Academy of Sciences*, *116*(49), pp.24433-24439.

Grotzinger, J.P. and James, N.P., 2000. Precambrian carbonates: evolution of understanding, *in* Grotzinger, J.P. and James, N.P., eds. Carbonate Sedimentation and Diagenesis in the Evolving Precambrian World: SEPM, Special Publication 67, p. 3-20.

Gussone, N., Böhm, F., Eisenhauer, A., Dietzel, M., Heuser, A., Teichert, B.M., Reitner, J., Wörheide, G. and Dullo, W.C., 2005. Calcium isotope fractionation in calcite and aragonite. *Geochimica et Cosmochimica Acta*, *69*(18), pp.4485-4494.

Gussone, N., Ahm, A.S.C., Lau, K.V. and Bradbury, H.J., 2020. Calcium isotopes in deep time: Potential and limitations. *Chemical Geology*, p.119601.

Hayes, J.M. and Waldbauer, J.R., 2006. The carbon cycle and associated redox processes through time. *Philosophical Transactions of the Royal Society B: Biological Sciences*, *361*(1470), pp.931-950.

Halverson, G.P., Hoffman, P.F., Schrag, D.P., Maloof, A.C. and Rice, A.H.N., 2005. Toward a Neoproterozoic composite carbon-isotope record. *GSA bulletin*, *117*(9-10), pp.1181-1207.

Higgins, J.A. and Schrag, D.P., 2003. Aftermath of a snowball Earth. *Geochemistry, Geophysics, Geosystems*, *4*(3), 1028.

Higgins, J.A. and Schrag, D.P., 2010. Constraining magnesium cycling in marine sediments using magnesium isotopes. *Geochimica et Cosmochimica Acta*, *74*(17), pp.5039-5053.

Higgins, J.A., Fischer, W.W. and Schrag, D.P., 2009. Oxygenation of the ocean and sediments: consequences for the seafloor carbonate factory. *Earth and Planetary Science Letters*, *284*(1-2), pp.25-33.

Higgins, J.A., Blättler, C.L., Lundstrom, E.A., Santiago-Ramos, D.P., Akhtar, A.A., Ahm, A.C., Bialik, O., Holmden, C., Bradbury, H., Murray, S.T. and Swart, P.K., 2018. Mineralogy, early marine diagenesis, and the chemistry of shallow-water carbonate sediments. *Geochimica et Cosmochimica Acta*, *220*, pp.512-534.

Hodgskiss, M.S., Crockford, P.W., Peng, Y., Wing, B.A. and Horner, T.J., 2019. A productivity collapse to end Earth's Great Oxidation. *Proceedings of the National Academy of Sciences*, *116*(35), pp.17207-17212.

Hoffman, P.F., 2011. Strange bedfellows: glacial diamictite and cap carbonate from the Marinoan (635 Ma) glaciation in Namibia. *Sedimentology*, *58*(1), pp.57-119.

Hoffman, P.F. and Lamothe, K.G., 2019. Seawater-buffered diagenesis, destruction of carbon isotope excursions, and the composition of DIC in Neoproterozoic oceans. *Proceedings of the National Academy of Sciences*, *116*(38), pp.18874-18879.

Hoffman, P.F. and Schrag, D.P., 2002. The snowball Earth hypothesis: testing the limits of global change. *Terra Nova*, *14*(3), pp.129-155.

Johnston, D.T., Macdonald, F.A., Gill, B.C., Hoffman, P.F. and Schrag, D.P., 2012. Uncovering the Neoproterozoic carbon cycle. *Nature*, *483*(7389), pp.320-323.

Jørgensen, B.B. and Kasten, S., 2006. Sulfur cycling and methane oxidation. In *Marine geochemistry* (pp. 271-309). Springer, Berlin, Heidelberg.

Kaufman, J., 1994. Numerical models of fluid flow in carbonate platforms; implications for dolomitization. *Journal of Sedimentary Research*, *64*(1a), pp.128-139.

Kennedy, M.J., Christie-Blick, N. and Sohl, L.E., 2001. Are Proterozoic cap carbonates and

isotopic excursions a record of gas hydrate destabilization following Earth's coldest intervals? *Geology*, *29*(5), pp.443-446.

Knauth, L.P. and Kennedy, M.J., 2009. The late Precambrian greening of the Earth. *Nature*, *460*(7256), pp.728-732.

Knoll, A.H., Hayes, J.M., Kaufman, A.J., Swett, K. and Lambert, I.B., 1986. Secular variation in carbon isotope ratios from Upper Proterozoic successions of Svalbard and East Greenland. *Nature*, *321*(6073), pp.832-838.

Labotka, T.C., Warasila, R.L. and Spangler, R.R., 1985. Polymetamorphism in the Panamint Mountains, California: A 39AR-40AR study. *Journal of Geophysical Research: Solid Earth*, *90*(B12), pp.10359-10371.

Lazar, B. and Erez, J., 1992. Carbon geochemistry of marine-derived brines: I. 13C depletions due to intense photosynthesis. *Geochimica et Cosmochimica Acta*, *56*(1), pp.335-345.

Malone, M.J., Claypool, G., Martin, J.B. and Dickens, G.R., 2002. Variable methane fluxes in shallow marine systems over geologic time: The composition and origin of pore waters and authigenic carbonates on the New Jersey shelf. *Marine Geology*, *189*(3-4), pp.175-196.

Mayika, K.B., Moussavou, M., Prave, A.R., Lepland, A., Mbina, M. and Kirsimäe, K., 2020. The Paleoproterozoic Francevillian succession of Gabon and the Lomagundi-Jatuli event. *Geology*, *48*(11), pp.1099-1104.

Meister, P. and Reyes, C., 2019. The carbon-isotope record of the sub-seafloor biosphere. *Geosciences*, *9*(12), p.507.

Miller, J.M., 1985. Glacial and syntectonic sedimentation: The upper Proterozoic Kingston Peak Formation, southern Panamint Range, eastern California. *Geological Society of America Bulletin*, *96*(12), pp.1537-1553.

Moore, T.S., Murray, R.W., Kurtz, A.C. and Schrag, D.P., 2004. Anaerobic methane oxidation and the formation of dolomite. *Earth and Planetary Science Letters*, *229*(1-2), pp.141-154.

Nelson, L.L., Smith, E.F., Hodgin, E.B., Crowley, J.L., Schmitz, M.D. and Macdonald, F.A., 2020. Geochronological constraints on Neoproterozoic rifting and onset of the Marinoan glaciation from the Kingston Peak Formation in Death Valley, California (USA). *Geology*, *48*(11), p. 1083-1087.

Oehlert, A.M. and Swart, P.K., 2014. Interpreting carbonate and organic carbon isotope covariance in the sedimentary record. *Nature Communications*, *5*(1), pp.1-7.

Ohmoto, H., 1972. Systematics of sulfur and carbon isotopes in hydrothermal ore deposits. *Economic Geology*, *67*(5), pp.551-578.

Petterson, R., Prave, A.R., Wernicke, B.P. and Fallick, A.E., 2011. The Neoproterozoic Noonday Formation, Death Valley region, California. *Bulletin*, *123*(7-8), pp.1317-1336.

Planavsky, N.J., Cole, D.B., Isson, T.T., Reinhard, C.T., Crockford, P.W., Sheldon, N.D. and Lyons, T.W., 2018. A case for low atmospheric oxygen levels during Earth's middle history. *Emerging Topics in Life Sciences*, *2*(2), pp.149-159.

Prave, A.R., 1999. Two diamictites, two cap carbonates, two δ13C excursions, two rifts: the Neoproterozoic Kingston Peak Formation, Death Valley, California. *Geology*, *27*(4), pp.339-342.

Prokoph, A., Shields, G.A. and Veizer, J., 2008. Compilation and time-series analysis of a marine carbonate $\delta^{18}O$, $\delta^{13}C$, $^{87}Sr/^{86}Sr$ and $\delta^{34}S$ database through Earth history. *Earth-Science Reviews*, *87*(3-4), pp.113-133.

Rooney, A.D., Yang, C., Condon, D.J., Zhu, M. and Macdonald, F.A., 2020. U-Pb and Re-Os geochronology tracks stratigraphic condensation in the Sturtian snowball Earth aftermath. *Geology*, *48*(6), pp.625-629.

Rothman, D.H., Hayes, J.M. and Summons, R.E., 2003. Dynamics of the Neoproterozoic carbon cycle. *Proceedings of the National Academy of Sciences*, *100*(14), pp.8124-8129.

Saltzman, M.R. and Thomas, E., 2012. Carbon isotope stratigraphy. *In* The Geologic Time Scale, eds. Gradstein, F.M., Ogg, J.G., Schmitz, M.D., and Ogg, G., pp. 207-232.

Schrag, D.P., Berner, R.A., Hoffman, P.F. and Halverson, G.P., 2002. On the initiation of a snowball Earth. *Geochemistry, Geophysics, Geosystems*, *3*(6), pp.1-21.

Schrag, D.P., Higgins, J.A., Macdonald, F.A. and Johnston, D.T., 2013. Authigenic carbonate and the history of the global carbon cycle. *Science*, *339*(6119), pp.540-543.

Shields, G. and Veizer, J., 2002. Precambrian marine carbonate isotope database: Version 1.1. *Geochemistry, Geophysics, Geosystems*, *3*(6), pp.1-12.

Swanson-Hysell, N.L., Rose, C.V., Calmet, C.C., Halverson, G.P., Hurtgen, M.T. and Maloof, A.C., 2010. Cryogenian glaciation and the onset of carbon-isotope decoupling. *Science*, *328*(5978), pp.608-611.

Swart, P.K., 2008. Global synchronous changes in the carbon isotopic composition of carbonate sediments unrelated to changes in the global carbon cycle. *Proceedings of the National Academy of Sciences*, *105*(37), pp.13741-13745.

Swart, P.K., Reijmer, J.J. and Otto, R., 2009. A reevaluation of facies on Great Bahama Bank II: Variations in the δ13C, δ18O and mineralogy of surface sediments. *Int. Assoc. Sedimentol. Spec. Publ 41*, pp.47-59.

Tziperman, E., Halevy, I., Johnston, D.T., Knoll, A.H. and Schrag, D.P., 2011. Biologically induced initiation of Neoproterozoic snowball-Earth events. *Proceedings of the National academy of Sciences*, *108*(37), pp.15091-15096.

Visscher, P.T. and Stolz, J.F., 2005. Microbial mats as bioreactors: populations, processes, and products. *Palaeogeography, Palaeoclimatology, Palaeoecology*, *219*, pp.87-100.

CHAPTER 4. TUBEY OR NOT TUBEY: DEATH BEDS OF EDIACARAN MACROFOSSILS OR MICROBIALLY INDUCED SEDIMENTARY STRUCTURES?

A version of this chapter was published in:

[Nelson, L. L., & Smith, E. F. (2019). Tubey or not tubey: Death beds of Ediacaran macrofossils or microbially induced sedimentary structures? *Geology*, *47, 10*, *909-913*.]

Abstract

Within the upper Ediacaran Esmeralda Member of the Deep Spring Formation in south- eastern California, USA, an ~3 m stratigraphic interval contains multiple clastic bedding surfaces with enigmatic, three-dimensionally preserved corrugated tubes (<60 cm in length and <6 cm in width). When viewed as fragments and *in situ* on bedding planes, these resemble larger versions of annulated, tubular soft-bodied macrofossils that are common in late Ediacaran biotic assemblages regionally and globally. Despite superficial similarities to casts and molds of body fossils preserved in correlative strata, we suggest these tubes are instead previously undescribed organosedimentary structures that developed through differential compaction of rippled heterolithic interbeds bound by pyritized microbial mat layers. These distinctive structures formed within peritidal settings in the latest Ediacaran Period as the result of specific ecological and environmental conditions marked by flourishing microbial mat communities and dysoxic sediments. This interpretation may inform the biogenicity of other structures previously reported as macroscopic body or trace fossils.

4.1. Introduction

The Ediacaran Period hosts evidence of the first macroscopic organisms and the first metazoan fossils (Conway Morris, 1993; Bobrovskiy et al., 2018), which are often preserved as casts and

molds within siliciclastic facies (e.g., Gehling, 1999). Accompanying many of these fossils are textured organic surfaces, preserving evidence of microbial mat communities (e.g., Hagadorn and Bottjer, 1997; Gehling and Droser, 2009). Distinguishing between macrofossils, microbial textures, and abiotic sedimentary features in Ediacaran strata is critical to recognizing and interpreting early macroscopic life in the fossil record and to understanding evolutionary patterns and taphonomic windows, yet is often challenging due to the enigmatic morphologies of Ediacaran organisms and mat textures. Here, we report problematic casts and molds of macroscopic annulated tubular structures from terminal Ediacaran siliciclastic strata in southeastern California, USA. These structures morphologically resemble tubular Ediacaran body fossils that occur within coeval strata regionally and globally, but are up to an order of magnitude larger in size. We explore the origins of these forms to determine if they are true fossilized Ediacaran metazoans or previously undescribed sedimentary structures that developed through unusual local environmental and ecological conditions.

4.2. Geological Background

The upper Ediacaran to lower Cambrian Esmeralda Member of the Deep Spring Formation, which is the focus of this study, is 200–400-m-thick in the White-Inyo Mountains (Fig. 4.1A,B) and records deposition in shoreface to outer shelf environments (Stewart, 1970; Nelson, 1978). The age of the Esmeralda Member of the Deep Spring Formation is constrained by biostratigraphy and chemostratigraphy from this unit and correlative units across the Great Basin (Fig. 4.1B). Late Ediacaran body fossils—including cloudinids, erniettomorphs, and a range of other tubular forms preserved as casts and molds or as pyrite pseudomorphs—have been reported from the underlying Reed Dolomite, the Dunfee and Esmeralda members of the Deep Spring Formation, and the

correlative lower member of the Wood Canyon Formation in the Death Valley region (Taylor, 1966; Signor et al., 1987; Grant, 1990; Horodyski et al., 1994; Hagadorn et al., 2000; Smith et al., 2016, 2017). Regionally, the first appearance datum of *Treptichnus pedum*, which is currently used to define the base of the Cambrian Period (Landing, 1994), occurs within the Esmeralda Member of the Deep Spring Formation above a negative $\delta^{13}C_{carb}$ excursion that is considered an informal marker of the Ediacaran–Cambrian boundary (Corsetti and Kaufman, 1994; Corsetti and Hagadorn, 2000).

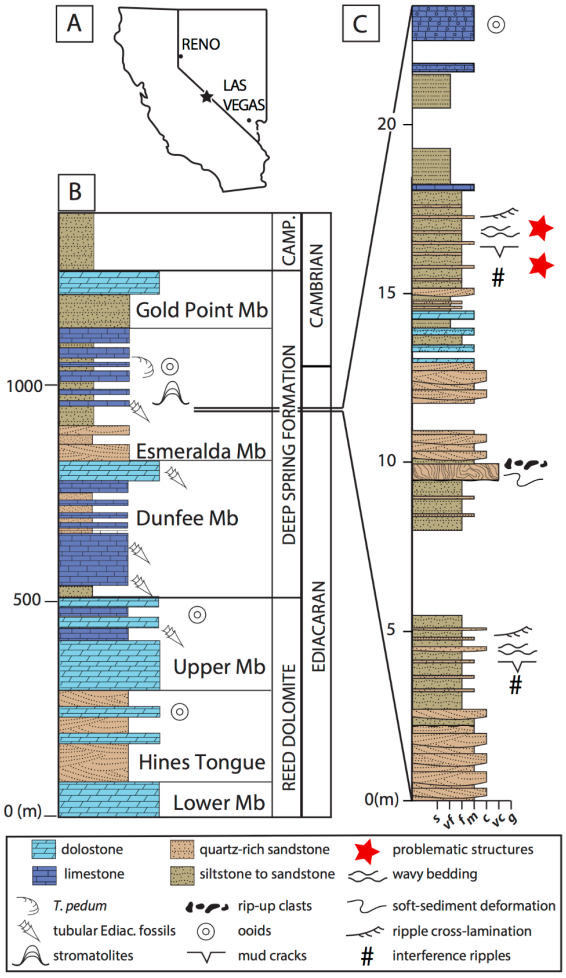

Figure 4.1. Regional and local stratigraphy. A) Locality map with star marking study site in California. B) Generalized stratigraphy and biostratigraphy of Ediacaran–Cambrian units in the White and Inyo Mountains, California and Esmeralda County, Nevada. Adapted from Stewart, 1970 and Nelson, 1978. C) Detailed stratigraphic section of interval within the Esmeralda Member of the Deep Springs Formation containing the problematic tubular structures. See Fig. 4.2 for location (L1649) and Fig. 4.3 for additional detailed sections.

In addition to a record of body and trace fossils, late Ediacaran–early Cambrian siliciclastic strata of the Great Basin host microbially induced sedimentary structures (e.g., Hagadorn and Bottjer, 1997). More broadly, problematic sedimentary structures with a diverse range of morphologies—some of which were originally identified as body or trace fossils—are widely recognized in Ediacaran–Cambrian siliciclastic facies, and many of these are attributed to microbial influence (e.g., Hagadorn and Bottjer 1999; Seilacher et al., 2005; Schieber et al., 2007; Porada et al., 2008). Although the significance of microbial mats in forming these structures is now commonly recognized, the geneses of many of them are not fully understood, and physical production mechanisms such as current waning, wind-induced shear, sediment loading, or wave action have all been invoked (e.g., Dzulynski and Simpson, 1966; Teichert, 1970; Thomas et al., 2013; Mariotti et al., 2014). Regardless of precise formational mechanisms, these structures provide insight into the environmental and ecological functions of microbial communities in these early metazoan ecosystems.

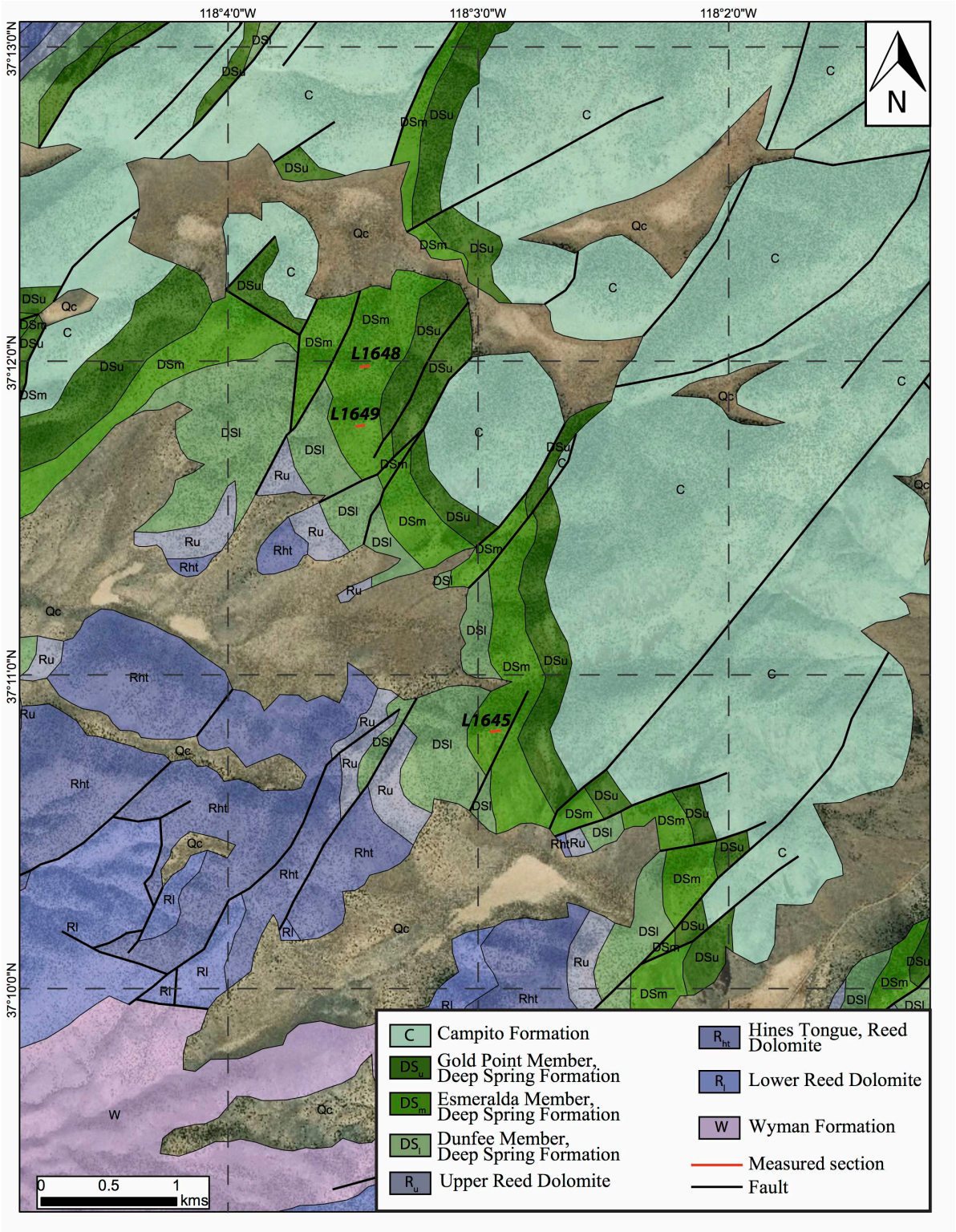

Figure 4.2. Geologic map of study area in the Wacouba Mountain Quadrangle, California, USA showing locations of three measured sections (see Fig. 4.3). Adapted from Nelson (1966).

4.3. Methods

Field work conducted in the Waucoba Mountain Quadrangle (Inyo County, California; Fig. 4.2) included the measurement of three detailed stratigraphic sections (Fig. 4.1, 4.3) and the documentation and collection of hundreds of tubular structures both *in situ* and from talus. Distinctive marker beds and carbon isotope chemostratigraphy allowed for precise correlation to other sections regionally in Inyo and Esmeralda counties (e.g. Smith et al., 2016). More than 300 specimens were brought back to the laboratory at Johns Hopkins University for sample preparation and photography. Collected specimens were photographed with low angle light sources and sometimes coated in WD-40. A table saw was used to cut specimens—both perpendicular and parallel to the long axis of the tubes—to observe morphologies in cross section. Thin sections were made of cross sections of select specimens for detailed petrographic observation. Cuts parallel to the long axes of the tubes allowed for measurements of the tube thicknesses and the wavelengths of the corrugations. These measurements were made using a dial caliper with uncertainty defined by variability of the measured features across a single specimen. These measurements were used to understand the relationship between the thicknesses of the tubular structures and the wavelengths of the corrugations.

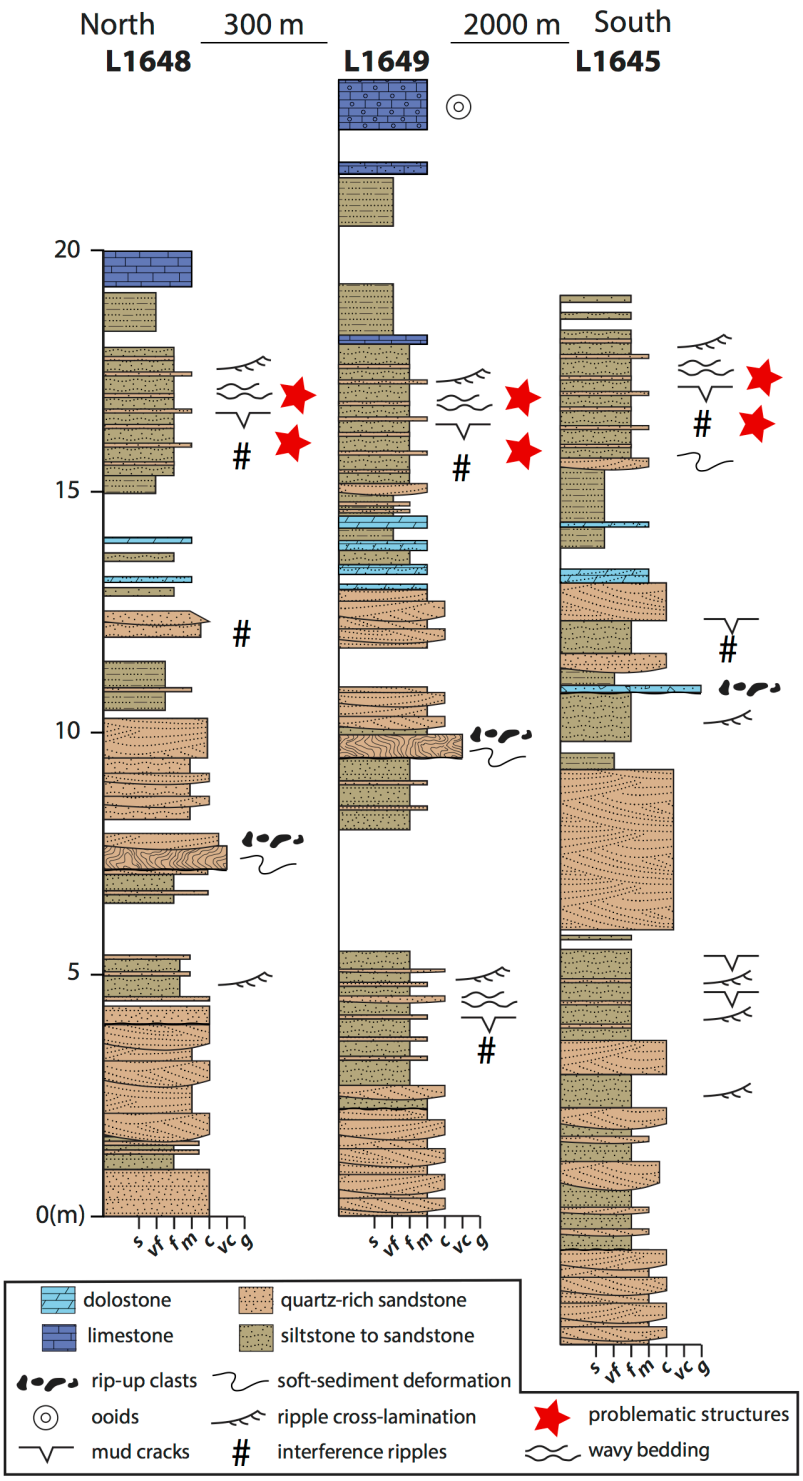

Figure 4.3. Detailed stratigraphic sections of interval within the Esmeralda Member of the Deep Springs Formation containing the problematic tubular structures.

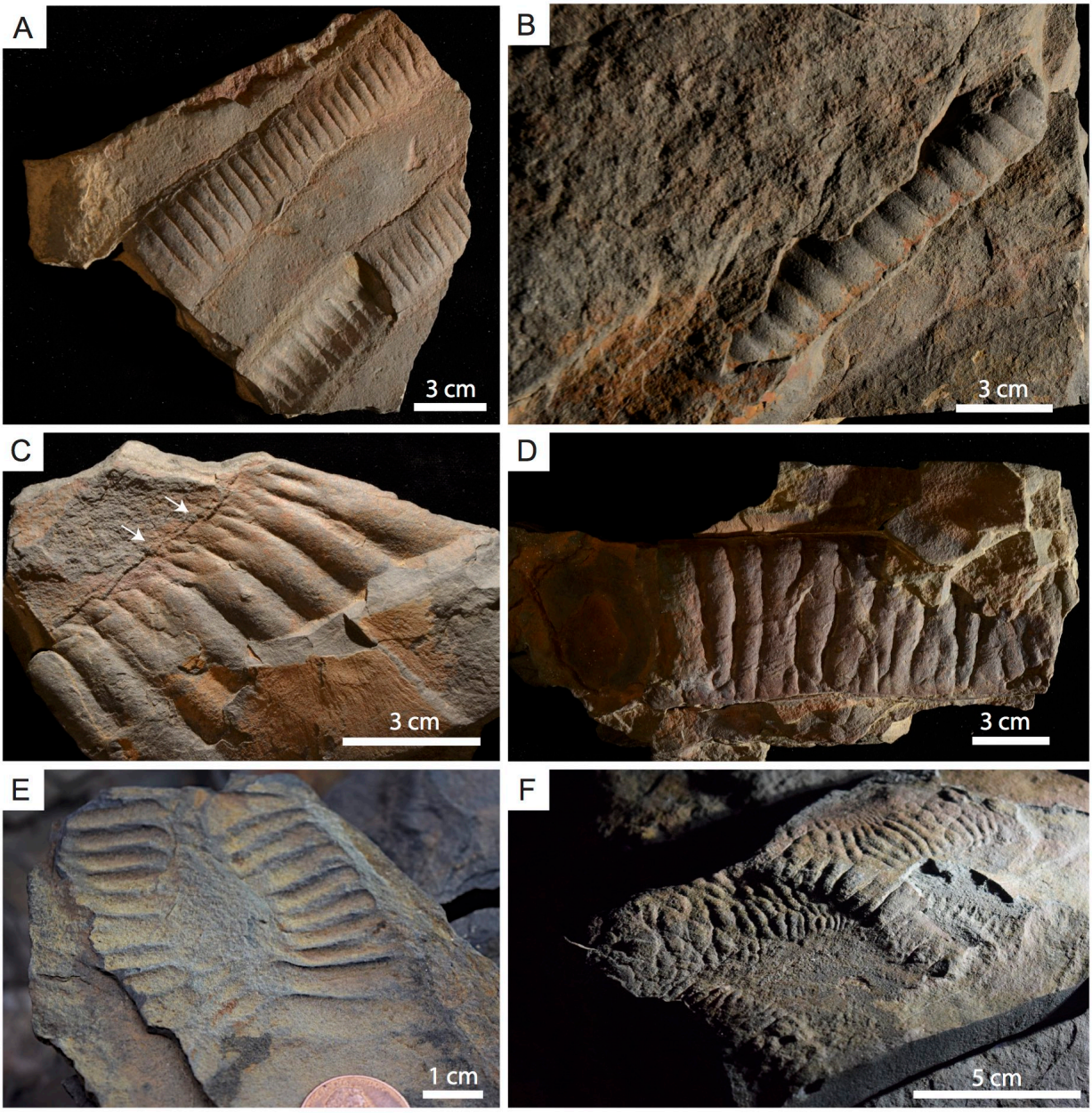

Figure 4.4. Photographs of problematic structures. A) Two approximately parallel tubular structures on bedding surface illustrating cast and mold preservation and corrugation concavity. B) Single tubular structure with regular corrugations protruding from a bedding surface. C) Tubular structure with apparent sharp boundary and pinching at the edge (highlighted with arrows). D) Large tubular structure with sharply defined boundaries, but more irregular corrugations. View is looking down onto bedding surface. E) Intersecting molds of two curved, corrugated tubular structures. F) Apparent overlapping tubular structures on a complex textured organic surface.

4.4. Results

4.4.1. Stratigraphic Context and Depositional Environment of Problematic Structures

Problematic macroscopic tubular structures are found within ~3 m of the Esmeralda Member of the Deep Spring Formation in the White-Inyo Mountains of southeastern California (Fig. 4.1C, 4.4A-F). This interval is below the nadir of a large negative $\delta^{13}C_{carb}$ excursion and correlative with the stratigraphic interval that contains tubular body fossils preserved as pyrite pseudomorphs in the Esmeralda Member of the Deep Spring Formation at Mount Dunfee, Nevada (Smith et al., 2016). The three-dimensional corrugated tubular structures described in this study are preserved on multiple bedding surfaces within wavy-bedded (see Reineck and Wunderlich, 1968) sandstone, siltstone, and mudstone (Fig. 4.5A,C). More than 400 specimens were observed across ~6 km along strike.

The stratigraphic interval preserving these enigmatic structures is within a broad transgressive sequence above ~75 m of cross-bedded quartz sandstone of the lower Esmeralda Member (Fig. 4.1B,C). Above these shoreface sandstone beds are finely laminated mudstone and siltstone containing white, quartz-rich sandstone channels and very minor sandy dolostone interbeds. This interval includes a storm deposit bed, containing cobble-sized sandstone to mudstone rip-up clasts and intense soft sediment deformation structures, that is traceable along strike for kilometers (Fig. 4.5B). The ~3 m of strata containing the tubular structures described here are above this event bed, and composed of wavy-bedded dark-gray to black mudstone to fine-grained sandstone with thin, light-gray medium-grained quartz sandstone interbeds (Fig. 4.5C). Sedimentary structures found interbedded with and on the same bedding surfaces as the problematic tubular forms include mud cracks, interference ripples, long crested wave ripples, starved ripples, and microbially induced wrinkle structures (Fig. 4.5). This dominantly siliciclastic

peritidal stratigraphic interval is overlain by mixed oolitic grainstone, stromatolitic limestone, and siltstone to medium-grained sandstone, deposited as the result of continued transgression to a shallow-marine, inner-shelf environment.

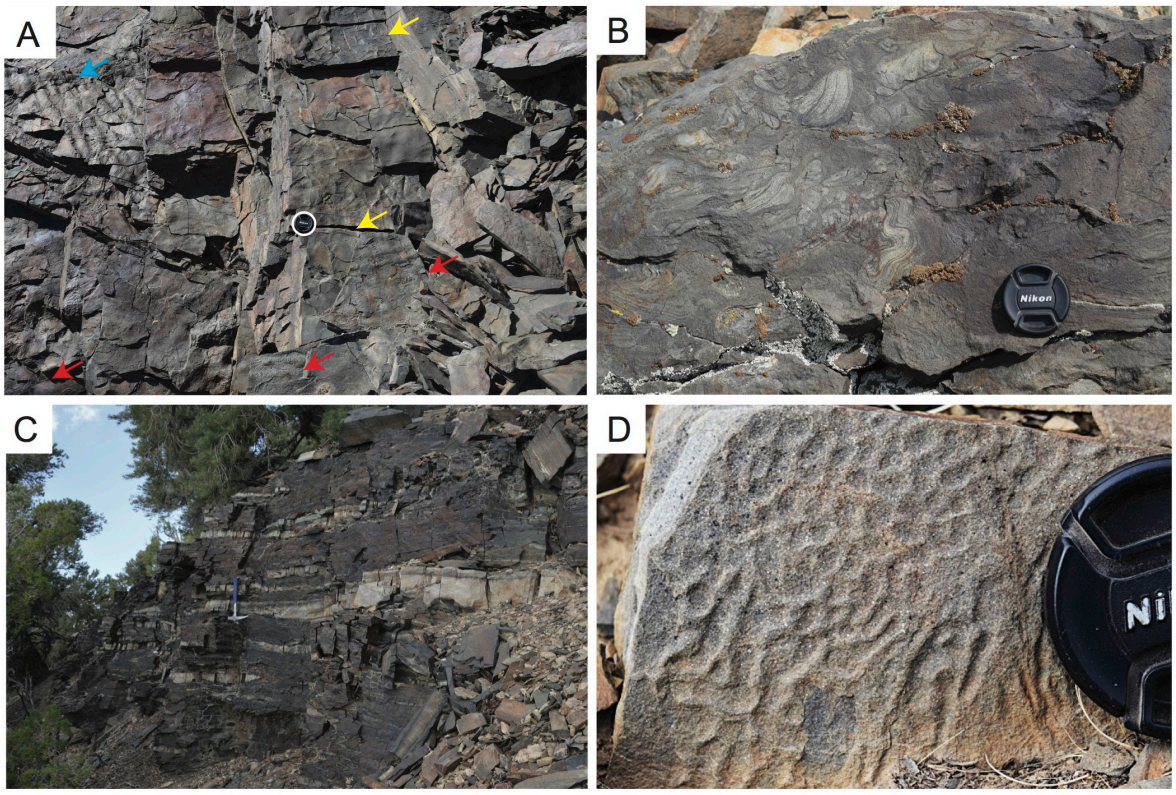

Figure 4.5. Photographs of associated sedimentary facies and structures. In A, B, and D, lens cap is 5.2 cm in diameter. A) Plan view of multiple bedding planes with ripple marks (blue arrow), mud cracks (yellow arrows), and tubular structures (red arrows). Lens cap is circled. B) Rip-up clasts of slumped sandstone and siltstone, interpreted as a storm deposit and laterally traceable event bed below pseudofossil interval. C) Interval of wavy-bedded sediments preserving problematic structures. Hammer is 33 cm in length. D) Microbially induced wrinkle marks.

4.4.2. Morphological Descriptions

The tubular structures are preserved as casts and molds that are infilled with medium to coarse grained light grey quartz-rich sandstone, and surrounded by dark-gray to black, iron-rich mudstone to fine sandstone. The lengths of the tubes range from 3 to 62 cm, although no terminations were ever observed in our study (>400 examples), and the widths range from 2 to 6 cm. The wavelengths of the corrugations (crest to crest) range from 0.2 to 2 cm (Fig. 4.4). A linear regression of the

wavelengths of the corrugations plotted against the thicknesses of the tubular structures has an R^2 value of 0.798, suggestive of a linear scaling relationship (Fig. 4.6). The corrugations of the tubes are oriented approximately perpendicular to the long axes, and are concave down along the top surfaces and concave up along the bottom surfaces (Fig. 4.4A-E). Along a single bedding surface, the tubes are often oriented roughly parallel to one another (Fig. 4.4A,E), but between bedding surfaces, the orientations change (Fig. 4.5A). Additionally, there are examples of tubes that bifurcate (Fig. 4.4E and 4.7A). Some of tubes appear to have sharp and straight boundaries in plan view (Fig. 4.4A-D), while some specimens show evidence for pinching or shrinking along the edge (Fig. 4.4C,E). Although many of the specimens appear as compressed tubes or cylinders in plan view due to these sharp boundaries (Fig. 4.4), sectioning of specimens reveals that, in most cases, the apparent tube structures are actually sheets that continue laterally, and the abrupt edges are controlled by onlapping of fine grained sediments or by boudinage (Fig. 4.7A-C).

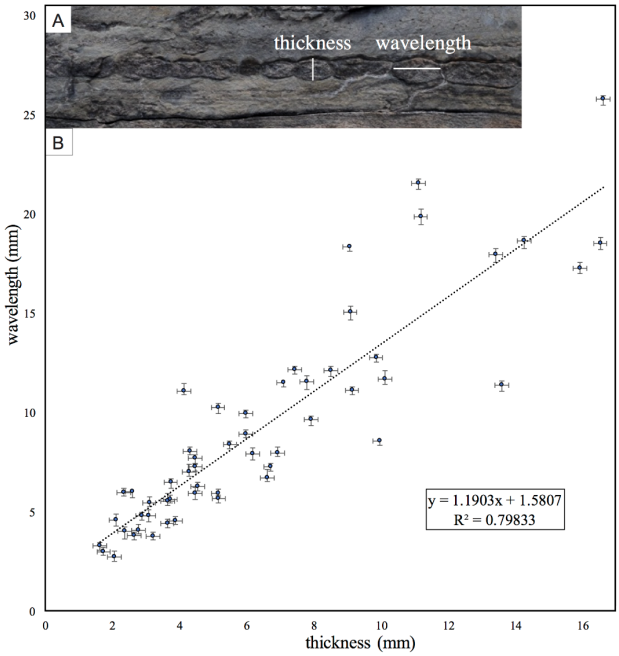

Figure 4.6. Aspect ratios of tubular structures. A) Photograph showing examples of the thickness and corrugation wavelength measurements on a tubular structure. B) Cross plot of the thickness of tubular structures and the wavelength of the corrugations, demonstrating a linear scaling relationship.

In cross section, all of the tubes have sharp boundaries between the quartz-rich infilling sandstone and the surrounding dark mudstone to fine sandstone (Fig 4.7C,E). In some specimens, injection structures of the quartz sand into the surrounding finer sediments were observed in thin section at these boundaries (Fig. 4.7D). Some of the structures appear to have a regular, corrugated morphology that resembles biological annulations (Fig. 4.4A-C,E), while others have more complex and irregular forms of corrugations and three-dimensional relief with splaying and overlapping ridges (Fig. 4.4D,F). Sometimes on single bedding planes there are overlaps and intersections between corrugations and classic examples of microbially induced wrinkle structures (Fig. 4.4F).

The bedding surfaces that preserve the structures often have a veneer of iron oxide, and the grey to black siltstone to sandstone contains abundant grains of pyrite pseudomorphs (Fig. 4.7D,E). In many cases, pyrite pseudomorphs are concentrated along the boundaries of the tubular structures (Fig. 4.7E).

4.5. Discussion

These unusual Ediacaran tubular structures pose a problem: are these body fossils or previously undescribed sedimentary structures? We interpret them as mechanically formed structures rather than body fossil casts and molds, based on the following observations: (1) In the hundreds of specimens found, longitudinal terminations to the structures were never observed; (2) the corrugations of the tubes are always oriented perpendicular to the long axes of these forms, even when they bend and bifurcate (Fig. 4.7A); (3) there are clear examples of bifurcations of the tubes

that resemble wave ripple imperfections (Fig. 4.7A); (4) while some tubes appear to have discrete edges (Fig. 4.4A-D), when sectioned it is evident that these are wavy, sheeted structures with only apparent tubular morphology due to infilling sediment (Fig. 4.7B); and (5) the structure thicknesses are linearly related to the wavelengths of the corrugations—even within a single specimen, where the thickness changes laterally across centimeters, the wavelengths also change (Figs. 4.6, 4.7C). Such a scaling relationship is characteristic of natural boudinage (e.g., Marques et al., 2012), and many of the other characteristics listed here would not be expected of tubular body fossils. Instead, we suggest that the apparent tubular morphology formed because the crests of ripples on the tops of sandstone beds were differentially compacted into the surrounding mudstone to siltstone, forming loaded ripples that attained near symmetrical, biconvex forms within the sandstone beds. During burial, extension due to gravitational compaction was localized within the competent quartz sand layers, leading to the mechanical formation of boudins parallel to the biconvex ripple crests, and creating apparent annulations (Fig. 4.8).

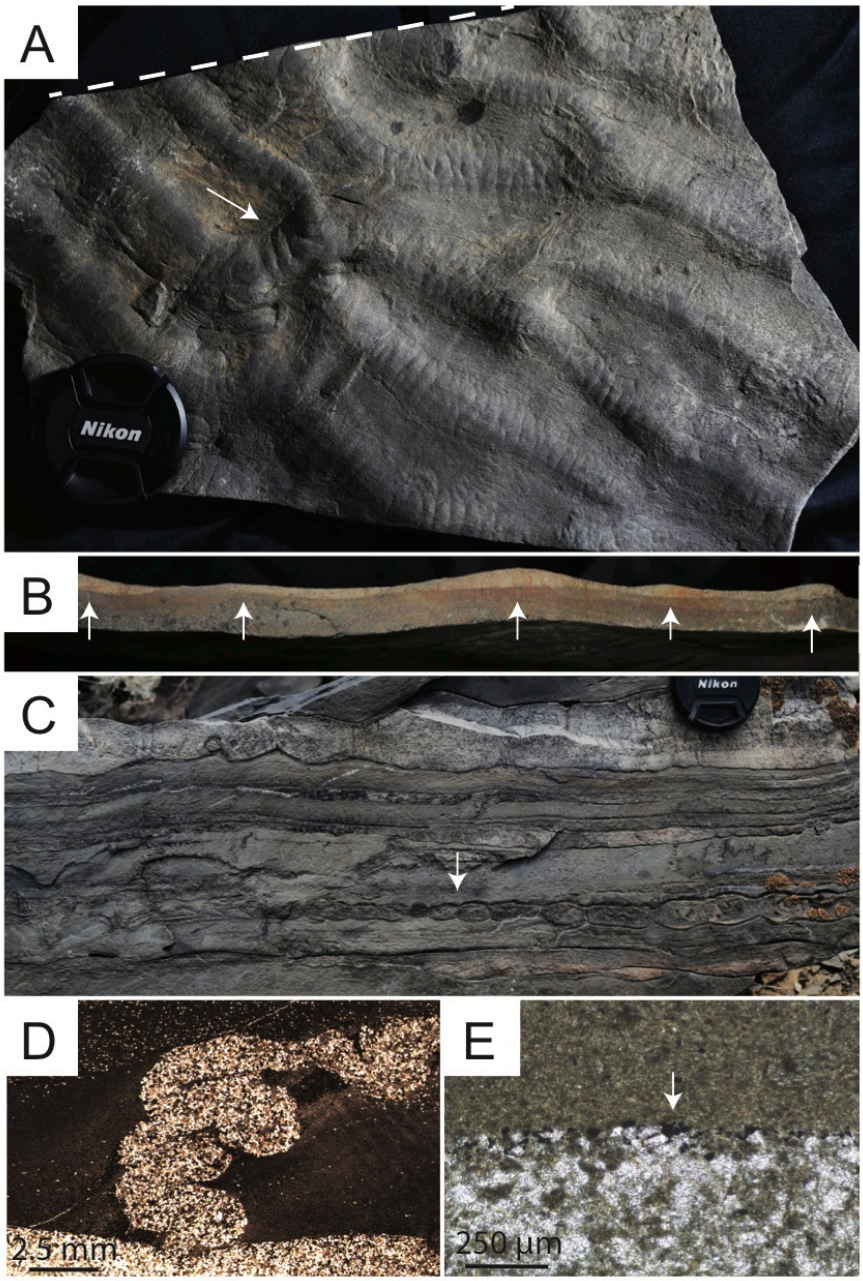

Figure 4.7. Photographs showing sedimentary clues of origin. A) Bifurcating ripples with corrugations oriented perpendicular to ripple crest. Arrow points to corrugations bending around ripple crest at bifurcation. Lens cap is 6.8 cm in diameter. Dashed white line is section shown in Fig. 4.7B. B) Cross section of slab in Fig. 4.7A. Arrows point to individual ribbed tube structures. C) Photograph of cross section of structure in outcrop. Arrow points to corrugations along a tube in which the wavelength of these structures scales with the thickness of the sandstone bed across centimeters. Lens cap is 5.2 cm in diameter. D) Photomicrograph of the sharp boundary along a tube edge with an injection of quartz sand into the surrounding mud and silt at a defect. E) Photomicrograph of the sharp boundary of a tube edge with concentrated pyrite pseudomorphs marked by arrow.

However, this interpretation begs the following question: if these are sedimentary structures, why are they not more common in the geologic record? The sharp boundaries between the different lithologies, marked by concentrated iron oxides and containing injection structures at defects (Fig. 4.7D,E), are critical to interpreting the genesis of these structures. These features are evidence for an impermeable layer between the heterolithic layers that allowed the coarser sand to deform as coherent bodies during burial. We suggest these boundaries resulted from precipitation of iron sulfides during diagenetic mineralization of decaying microbial mats (Gehling et al., 2005; Droser et al., 2006). Therefore, a biotic, microbial component was required for this formational process, as were redox conditions conducive to early diagenetic precipitation of pyrite in peritidal environments—unusual environmental conditions that could explain the paucity of the structures in the sedimentary record.

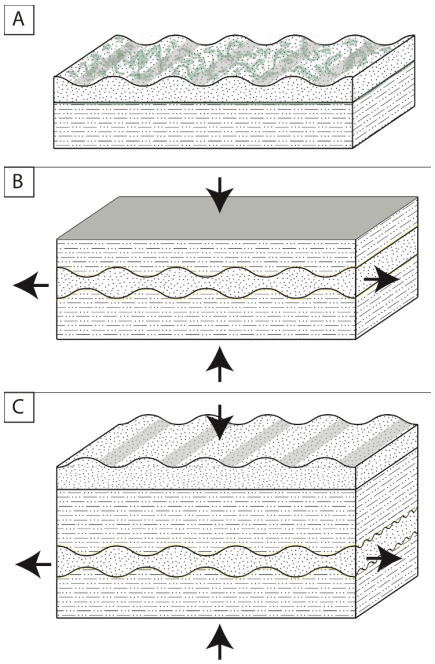

Figure 4.8. Schematic model for genesis of structures. A) Development of widespread microbial mats on rippled bedding planes in heterolithic sediments. B) In response to the vertical stress of burial, load structures develop beneath ripple crests within thin, wave rippled sand layers that are bound by silt and mud. C) As a result of continued compaction and horizontal extension parallel to ripple crests, corrugated tubular structures form through mechanical boudinage of the loaded ripples. Sand layers deform cohesively due to diagenetic mineralization of decaying microbial mats.

These structures could easily be mistaken for macroscopic Ediacaran tubular or ribbed body fossils, analogous to the original misidentification of the microbially induced sedimentary structure Kinneyia as an algal fossil (Walcott, 1914; Pflüger, 1995) or of Mawsonites as a medusoid (Glaessner and Wade, 1966; Seilacher et al., 2005). In fact, Cloud and Nelson (1966) and Nelson and Durham (1966) reported c.f. *Pteridinium* from the Esmeralda Member of the Deep Spring Formation at the Mollie Gibson Mine section, which we suggest are equivalent structures, based on observations at this locality and the figured specimen. Additionally, the purported 2.1 Ga colonial macrofossils from Francevillian series of Gabon (El Albani et al., 2010, 2014) may instead be similar microbially induced pseudofossils. The strata preserving these putative macrofossils contain textured organic surfaces and are formed of black pyrite-rich heterolithic muds, silts, and sands with abundant evidence for soft-sediment deformation (Reynaud et al., 2018), similar to the sedimentary facies of the Deep Spring Formation that host the problematic structures discussed herein. The structures are similarly characterized as flexible sheets coated with iron oxide pseudomorphs of pyrite that formed during early diagenesis, and demonstrate comparable radial and wrinkled fabrics. El Albani et al. (2010, 2014) suggested that these internal fabrics do not resemble microbial structures and instead represent coordinated growth, and thus the earliest fossilized colonial organisms; however, here, we demonstrate that similarly complex structures can be produced by the interaction of microbial mats with specific sedimentary facies and dispute this classification.

4.6. Conclusion

In summary, these problematic specimens from the Deep Spring Formation are not late Ediacaran body fossils, but examples of a previously undescribed microbially induced sedimentary structure that formed during early diagenesis through the mechanical boudinage of wavy-bedded sediments bound by mineralizing microbial mats. Load structures developed beneath ripple crests in thin, wave rippled sand layers that were deposited within silt and mud, and corrugated lenses formed in response to vertical loading pressure and horizontal extension during burial of these microbially bound layers. In this model, there are a number of environmental requirements for the formation of these sedimentary structures, but the only ones that have changed through geologic time are the abundance and role of microbial mats, as well as their diagenetic mineralization pathways. The narrow stratigraphic range of these structures supports a microbial proliferation coupled with dysoxic conditions in peritidal sediments immediately prior to the Ediacaran–Cambrian boundary.

4.7. Acknowledgements

We acknowledge the Harvard University Alex G. Booth Fellowship, the National Geographic Society Early Career Grant CP-002ER-17, the Lewis and Clark Fund for Exploration and Field Research, Palaeontological Association Research Grant #PA-RG201703, and the Smithsonian Institution Peter Buck Fellowship for financial support. We acknowledge the Inyo National Forest for a research permit. We thank J. Bennet for laboratory assistance and D. Erwin, M. Droser, and P. Myrow for useful discussions. We thank J. Schiffbauer, S. Pruss, T. Gibson, and J. Schmitt for thoughtful and constructive comments that greatly improved this manuscript.

4.8. References

Bobrovskiy, I., Hope, J. M., Ivantsov, A., Nettersheim, B. J., Hallmann, C., and Brocks, J. J., 2018, Ancient steroids establish the Ediacaran fossil Dickinsonia as one of the earliest animals: Science, v. 361, no. 6408, p. 1246–1249.

Cloud Jr, P.E., and Nelson, C.A., 1966, Phanerozoic-Cryptozoic and related transitions: New evidence: Science, v. 154, no. 3750, p. 766–770.

Conway Morris, S., 1993, The fossil record and the early evolution of the Metazoa: Nature, v. 361, no. 6409, p. 219.

Corsetti, F. A., and Hagadorn, J. W., 2000, Precambrian-Cambrian transition: Death Valley, United States: Geology, v. 28, no. 4, p. 299–302.

Corsetti, F. A., and Kaufman, A. J., 1994, Chemostratigraphy of Neoproterozoic-Cambrian units, White-Inyo Region, eastern California and western Nevada: implications for global correlation and faunal distribution: Palaios, p. 211–219.

Droser, M. L., Gehling, J. G., and Jensen, S. R., 2006, Assemblage palaeoecology of the Ediacara biota: the unabridged edition?: Palaeogeography, Palaeoclimatology, Palaeoecology, v. 232, no. 2-4, p. 131–147.

Dzulynski, S., and Simpson, F., 1966, Experiments on interfacial current markings: Geologica Romana, v. 5, p. 197–214.

El Albani, A., Bengtson, S., Canfield, D. E., Bekker, A., Macchiarelli, R., Mazurier, A., Hammarlund, E. U., Boulvais, P., Dupuy, J.-J., and Fontaine, C., 2010, Large colonial organisms with coordinated growth in oxygenated environments 2.1 Gyr ago: Nature, v. 466, no. 7302, p. 100.

El Albani, A., Bengtson, S., Canfield, D.E., Riboulleau, A., Bard, C.R., Macchiarelli, R., Pemba, L.N., Hammarlund, E., Meunier, A., Mouélé, I.M. and Benzerara, K., 2014, The 2.1 Ga old Francevillian biota: biogenicity, taphonomy and biodiversity: PLoS One, v. 9, no. 6, p.e99438 *PLoS One*, *9*(6), p.e99438.

Gehling, J., Droser, M., Jensen, S., Runnegar, B., and Briggs, D., 2005, Ediacara organisms: relating form to function: Evolving form and function: fossils and development, p. 43-66.

Gehling, J. G., 1999, Microbial mats in terminal Proterozoic siliciclastics; Ediacaran death masks: Palaios, v. 14, no. 1, p. 40–57.

Gehling, J. G., and Droser, M. L., 2009, Textured organic surfaces associated with the Ediacara biota in South Australia: Earth-Science Reviews, v. 96, no. 3, p. 196–206.

Glaessner, M.F. and Wade, M., 1966, The late Precambrian fossils from Ediacara, South Australia: Palaeontology, v. 9, no. 4, p. 599–628.

Grant, S. W., 1990, Shell structure and distribution of Cloudina, a potential index fossil for the terminal Proterozoic: American Journal of Science, v. 290, p. 261–294.

Hagadorn, J. W., and Bottjer, D. J., 1997, Wrinkle structures: Microbially mediated sedimentary structures common in subtidal siliciclastic settings at the Proterozoic-Phanerozoic transition: Geology, v. 25, no. 11, p. 1047–1050.

Hagadorn, J.W. and Bottjer, D.J., 1999, Restriction of a late Neoproterozoic biotope; suspect-microbial structures and trace fossils at the Vendian-Cambrian transition: Palaios, v. 14, no. 1, p. 73–85.

Hagadorn, J. W., Fedo, C. M., and Waggoner, B. M., 2000, Early Cambrian Ediacaran-type fossils from California: Journal of Paleontology, v. 74, no. 04, p. 731–740.

Horodyski, R., Gehling, J., Jensen, S., and Runnegar, B., 1994, Ediacara fauna and earliest Cambrian trace fossils in a single parasequence set, southern Nevada, *in* Geological Society of America Abstracts with Programs, v. 26, p. 60.

Landing, E., 1994, Precambrian-Cambrian boundary global stratotype ratified and a new perspective of Cambrian time: Geology, v. 22, no. 2, p. 179–182.

Marques, F.O., Fonseca, P.D., Lechmann, S., Burg, J.P., Marques, A.S., Andrade, A.J. and Alves, C., 2012, Boudinage in nature and experiment: Tectonophysics, v. 526, p. 88-96.

Mariotti, G., Pruss, S., Perron, J., and Bosak, T., 2014, Microbial shaping of sedimentary wrinkle structures: Nature Geoscience, v. 7, no. 10, p. 736.

Nelson, C. A., 1966, Geologic map of the Waucoba Mountain quadrangle, Inyo County, California. USGS Geologic Quadrangle 528.

Nelson, C. A., 1978, Late Precambrian–Early Cambrian stratigraphic and faunal succession of eastern California and the Precambrian–Cambrian boundary: Geological Magazine, v. 115, p. 121–126.

Nelson, C., and Durham, J., 1966, Guidebook for field trip to Precambrian–Cambrian succession White-Inyo Mountains: California: Los Angeles, University of California.

Pflüger, F., 1995, Morphodynamik, aktualismus und sedimentstrukturen neues jahrbuch für geologie und paläontologie: Abhandlungen v. 195, p. 75–83.

Porada, H., Ghergut, J., and Bouougri, E. H., 2008, Kinneyia-type wrinkle structures—critical review and model of formation: Palaios, v. 23, no. 2, p. 65–77.

Reineck, H.E. and Wunderlich, F., 1968, Classification and origin of flaser and lenticular bedding: Sedimentology, v. 11 no. 1-2, p. 99–104.

Reynaud, J. Y., Trentesaux, A., El Albani, A., Aubineau, J., Ngombi-Pemba, L., Guiyeligou, G., Bouton, P., Gauthier-Lafaye, F., and Weber, F., 2018, Depositional setting of the 2· 1 Ga Francevillian macrobiota (Gabon): Rapid mud settling in a shallow basin swept by high-density sand flows: Sedimentology, v. 65, no. 3, p. 670–701.

Schieber, J., Bose, P. K., Eriksson, P., Banerjee, S., Sarkar, S., Altermann, W., and Catuneanu, O., 2007, Atlas of microbial mat features preserved within the siliciclastic rock record, Elsevier.

Seilacher, A., Buatois, L.A. and Mángano, M.G., 2005, Trace fossils in the Ediacaran–Cambrian transition: behavioral diversification, ecological turnover and environmental shift: Palaeogeography, Palaeoclimatology, Palaeoecology, v. 227, no. 4, p. 323–356.

Signor, P. W., Mount, J. F., and Onken, B. R., 1987, A pre-trilobite shelly fauna from the White-Inyo region of eastern California and western Nevada: Journal of Paleontology, v. 67, no. 3, p. 425–438.

Smith, E., Nelson, L., Tweedt, S., Zeng, H., and Workman, J. B., 2017, A cosmopolitan late Ediacaran biotic assemblage: new fossils from Nevada and Namibia support a global biostratigraphic link: Proc. R. Soc. B, v. 284, no. 1858, p. 20170934.

Smith, E. F., Nelson, L. L., Strange, M. A., Eyster, A. E., Rowland, S. M., Schrag, D. P., and Macdonald, F. A., 2016, The end of the Ediacaran: Two new exceptionally preserved body fossil assemblages from Mount Dunfee, Nevada, USA: Geology, v. 44, no. 11, p. 911-914.

Stewart, J. H., 1970, Upper Precambrian and lower Cambrian strata in the southern Great Basin, California and Nevada: US Geological Survey Professional Paper 620.

Taylor, M. E., 1966, Precambrian mollusc-like fossils from Inyo County, California: Science, v. 153, no. 3732, p. 198–201.

Teichert, C., 1970, Runzelmarken (wrinkle marks): Journal of Sedimentary Research, v. 40, no. 3.

Thomas, K., Herminghaus, S., Porada, H., and Goehring, L., 2013, Formation of Kinneyia via shear-induced instabilities in microbial mats: Phil. Trans. R. Soc. A, v. 371, no. 2004, p. 20120362.

Walcott, C. D., 1914, Pre-Cambrian Algonkian algal flora: Smithsonian Miscellaneus Collections, v. 64, no. 2, 77–156.

CHAPTER 5. A LINK BETWEEN RIFT-RELATED VOLCANISM AND END-EDIACARAN EXTINCTION? INTEGRATED CHEMOSTRATIGRAPHY, BIOSTRATIGRAPHY, AND U-PB GEOCHRONOLOGY FROM SONORA, MEXICO

A version of this chapter was published in:

[Hodgin, E. B.†, Nelson, L. L.†, Wall, C. J., Barrón-Díaz, A. J., Webb, L. C., Schmitz, M. D., Fike, D. A., Hagadorn, J. W., & Smith, E. F. (2021). A link between rift-related volcanism and end-Ediacaran extinction? Integrated chemostratigraphy, biostratigraphy, and U-Pb geochronology from Sonora, Mexico. *Geology*, *49, 2*, *115-119*.] †Co-first authors.

Abstract

We present chemostratigraphy, biostratigraphy, and geochronology from a succession that spans the Ediacaran–Cambrian boundary in Sonora, Mexico. A sandy hematite-rich dolostone bed, which occurs 20 m above carbonates that record the nadir of the basal Cambrian carbon isotope excursion within the La Ciénega Formation, yielded a maximum depositional age of 539.40 ± 0.23 Ma using U-Pb chemical abrasion–isotope dilution–thermal ionization mass spectrometry on a population of sharply faceted volcanic zircon crystals. This bed, interpreted to contain reworked tuffaceous material, is above the last occurrences of late Ediacaran body fossils and below the first occurrence of the Cambrian trace fossil *Treptichnus pedum*, and so the age calibrates key markers of the Ediacaran–Cambrian boundary. The temporal coincidence of rift-related flood basalt volcanism in southern Laurentia (>250,000 km^3 of basalt), a negative carbon isotope excursion, and biological turnover is consistent with a mechanistic link between the eruption of a large igneous province and end-Ediacaran extinction.

5.1. Introduction

The Ediacaran–Cambrian boundary is one of the critical biological transitions in Earth history, marking the disappearance of Ediacaran organisms, a diverse assemblage of early macroscopic life forms, and the subsequent radiation of modern clades of metazoans. Continued efforts to understand the timing and extent of environmental and geochemical change across this boundary—and its potential role in driving extinction and evolution—are hampered by challenges in correlating and integrating records regionally and globally.

A large negative carbon isotope ($\delta^{13}C$) excursion, termed the basal Cambrian carbon isotope excursion (BACE), coincides with the Ediacaran–Cambrian boundary in a number of regions globally (Magaritz et al., 1986; Narbonne et al., 1994; Brasier et al., 1996; Kimura et al., 1997; Zhang et al., 1997; Corsetti and Hagadorn, 2000; Amthor et al., 2003; Loyd et al., 2012). The BACE has been suggested as a formal marker of the Ediacaran–Cambrian boundary (Zhu et al., 2019) and to be mechanistically linked to extinction (Kimura et al., 1997; Amthor et al., 2003). Currently, the best age constraint on this excursion is from the Ara Group of Oman, where an ash bed below the onset of a negative $\delta^{13}C$ excursion has been dated at 541.00 ± 0.13 Ma with U-Pb chemical abrasion–isotope dilution–thermal ionization mass spectrometry (CA-ID-TIMS) on zircon (Bowring et al., 2007). Correlation of these $\delta^{13}C$ excursions from localities around the world remains uncertain, and assessing the synchrony or duration of the BACE—necessary steps in considering its possible origins and consequences—requires improved radioisotopic age constraints.

5.2. Geological Background

The Caborca block in NW Mexico consists of Mesoproterozoic basement (Anderson and Silver, 1981) and contains a well-exposed succession of Neoproterozoic–early Paleozoic shallow-marine strata (Fig. 5.1; Stewart et al., 1984) that record the Ediacaran–Cambrian transition within the La Ciénega and Cerro Rajón formations (Sour-Tovar et al., 2007; Loyd et al., 2012; Barrón-Díaz et al., 2019a). The La Ciénega Formation consists of four units. Unit 1 is composed of mixed dolostone, sandy dolostone, and siltstone to medium sandstone, and it contains 6 m of basalt at Cerro Rajón (Stewart et al., 1984). *Cloudina hartmannae* fossils occur within wackestone to packstone dolostone beds in the middle of Unit 1 (Stewart et al., 1984; Sour-Tovar et al., 2007). The uppermost part of Unit 1 is micaceous siltstone to fine sandstone with minor channels of medium quartz sandstone, and it is overlain by blue-weathering dolostone and minor sandy dolostone of Unit 2. Thin-bedded sandy dolostone and sandstone at the base of Unit 3 mark a conformable transition into micaceous siltstone to fine sandstone with minor beds of quartz sandstone, dolomite, sandy dolomite, and basalt. Unit 4 is massive buff-weathering dolostone with poorly developed stromatolites and oolite at the base. A previous report of *Cloudina* from Unit 4 (Sour-Tovar et al., 2007) has since been refuted (Loyd et al., 2012; Barrón-Díaz et al., 2019b). Loyd et al. (2012) identified a negative $\delta^{13}C$ anomaly in Units 2–4 with a nadir of -6.2‰ and correlated this with the BACE.

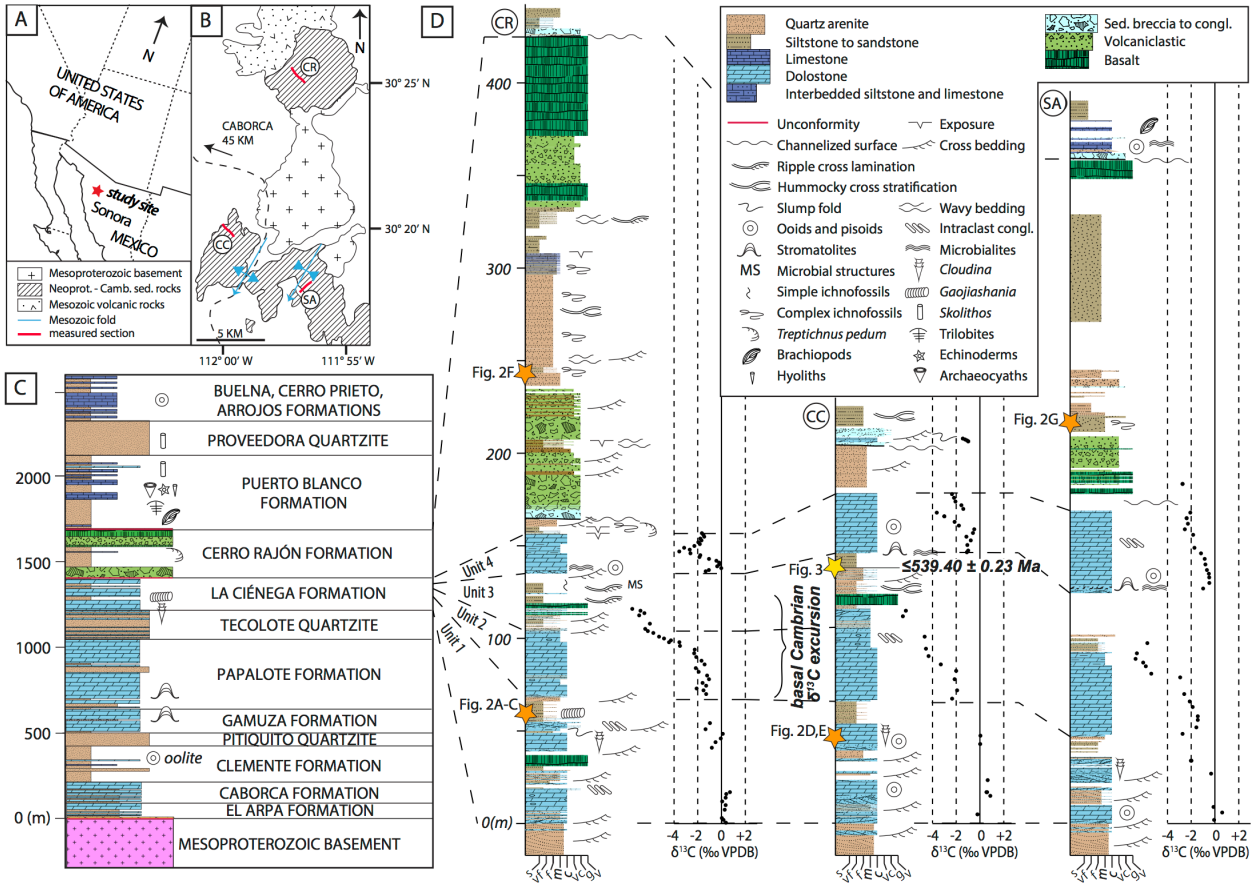

Figure 5.1. Locality map and integrated stratigraphy of the Ediacaran–Cambrian boundary near Caborca, northwestern Mexico. (A) Locality map with star marking study site. (B) Geologic map showing distribution of Neoproterozoic–Cambrian strata and locations of measured sections; modified from Barrón-Díaz et al. (2019a). (C) Generalized Neoproterozoic–Cambrian lithostratigraphy and biostratigraphy, including data compiled from Stewart et al. (1984) and Barrón-Díaz et al. (2019a). (D) Integrated lithostratigraphy, biostratigraphy, $\delta^{13}C$ chemostratigraphy, and geochronology from measured sections, corresponding to Fig. 5.1B. Neoprot.—Neoproterozoic; Camb.—Cambrian; CR—Cerro Rajón; CC—Cerro Clemente; SA—Cerro San Agustín; s—siltstone; vf—very fine-grained; f—fine-grained; m—medium-grained; c—coarse-grained; v—very coarse-grained; g—conglomerate; v—volcanic; VPDB—Vienna-Pee Dee Belemnite; sed.—sedimentary; congl.—conglomerate.

The La Ciénega Formation is overlain by the Cerro Rajón Formation, and the contact is a thin, locally preserved interval of siltstone to sandstone containing mud cracks and complex ichnofossils, including *Treptichnus pedum* (Loyd et al., 2012; Barrón-Díaz et al., 2019a, 2019b). A boulder conglomerate disconformably overlies this sequence, erosively cutting down into Unit 4 of the La Ciénega Formation, and it contains dolostone, quartzite, and basalt clasts. The Cerro

Rajón Formation contains variable proportions of siliciclastic, volcaniclastic, and volcanic rocks with minor silty to sandy limestone. The volcanic and volcaniclastic rocks are ocean-island basalt-type enriched alkaline basalts characteristic of intraplate volcanism (Barrón-Díaz et al., 2019b). Abundant bed-parallel and more complex bed-penetrating ichnofossils occur within clastic facies throughout the Cerro Rajón Formation (Stewart et al., 1984; Sour-Tovar et al., 2007; Barrón-Díaz et al., 2019a), which is disconformably overlain by erosive conglomerate at the base of the Puerto Blanco Formation Unit 2 that, in turn, contains Cambrian Series 2 trilobites and brachiopods (Stewart et al., 1984; Sour-Tovar et al., 2007; Barrón-Díaz et al., 2019a).

5.3. Methods

Field work conducted near Caborca, Mexico included the measurement of stratigraphic sections of the La Ciénega and Cerro Rajón formations at three localities (Figs. 5.1A-B). Carbonate samples were collected at 1-3 m resolution for carbon and oxygen stable isotope analyses. Zircon grains were separated from a sandy dolostone bed, imaged by cathodoluminescence (CL), and dated by laser ablation inductively coupled plasma mass spectrometry (LA-ICPMS) and CA-ID-TIMS. See the supplemental materials in Appendix A3 for detailed methods.

5.4. Results

5.4.1. Chemostratigraphy

Carbonate $\delta^{13}C$ values are ~0‰ in the lower dolostone of Unit 1 of the La Ciénega Formation, and decrease to below -6‰ within Unit 2 and to values as low as -7.5‰ in thin dolostone beds of Unit 3 interbedded with fine-grained siliciclastic rocks, before recovering to ~0‰ near the base of Unit 4 (Fig. 5.1D). Unit 4 contains a second negative $\delta^{13}C$ excursion with values down to -3.6‰. These

results were reproduced in three sections of the La Ciénega Formation (Fig. 5.1D and Appendix A3 Table S1), and closely resemble documented trends in coeval successions from Nevada (Corsetti and Hagadorn, 2003; Smith et al., 2016, 2017) and California (Corsetti and Hagadorn, 2000), demonstrating local to regional reproducibility of this $\delta^{13}C$ excursion.

Although the most negative $\delta^{13}C$ values at the nadir of the excursion correspond to a siliciclastic-rich interval, much of the excursion, including the decrease to ~-6‰, occurs within bedded dolo-grainstone. Isotopic values do not coherently vary with noticeable changes in lithology, depositional environment, or sequence boundaries, and $\delta^{13}C$ and $\delta^{18}O$ isotopes do not covary (R^2=0.0025; Fig. 5.2). Taken together, this suggests carbon isotopes were not reset by fluid-rock interactions related to meteoric diagenesis (Lohmann, 1988).

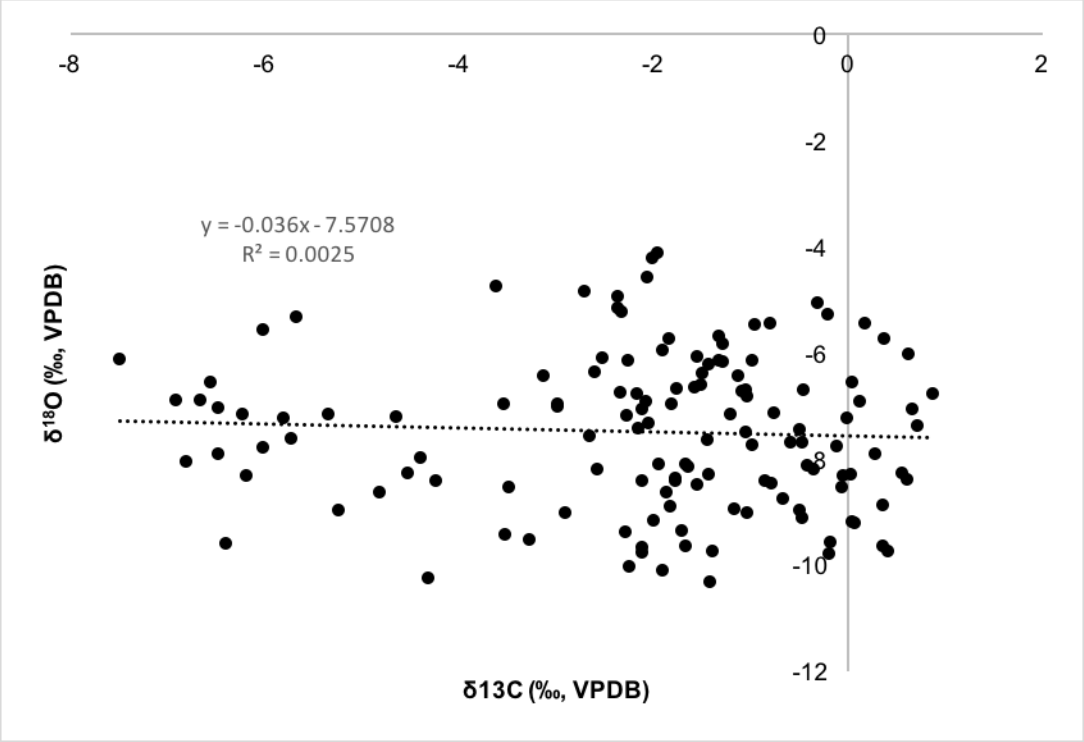

Figure 5.2. Carbon-oxygen isotope cross plot from the La Ciénega Fm. Dotted black line is a linear regression fitted to the data (Fig. 5.1 and Appendix A3 Table S1) with an R^2 value of 0.0025.

5.4.2. Paleontology

Cloudina shell beds or coquina—preserved with varying degrees of silicification—occur at all three localities within dolostone beds of Unit 1 of the La Ciénega Formation and include examples of nested funnel structures (Fig. 5.3D-E; Sour-Tovar et al., 2007). Annulated tubular fossils preserved as casts and molds in siltstone of the upper part of Unit 1 of the La Ciénega Formation were tentatively identified as *Gaojiashania* based on the presence of densely spaced transverse rings, lack of tapering, and similarity in size and morphology to specimens documented in Nevada (Fig. 5.3A-C; Smith et al., 2016, 2017). In one specimen, the rings are lightly replaced by iron oxides, likely pyrite pseudomorphs (Fig. 5.3C). Small, bed-planar ichnofossils occur in siliciclastic intervals of Unit 3 of the La Ciénega Formation, and more complex, bed-penetrating ichnofossils occur in siliciclastic horizons of the Cerro Rajón Formation (Fig. 5.3F-G; Stewart et al., 1984; Sour-Tovar et al., 2007; Barrón-Díaz et al., 2019a).

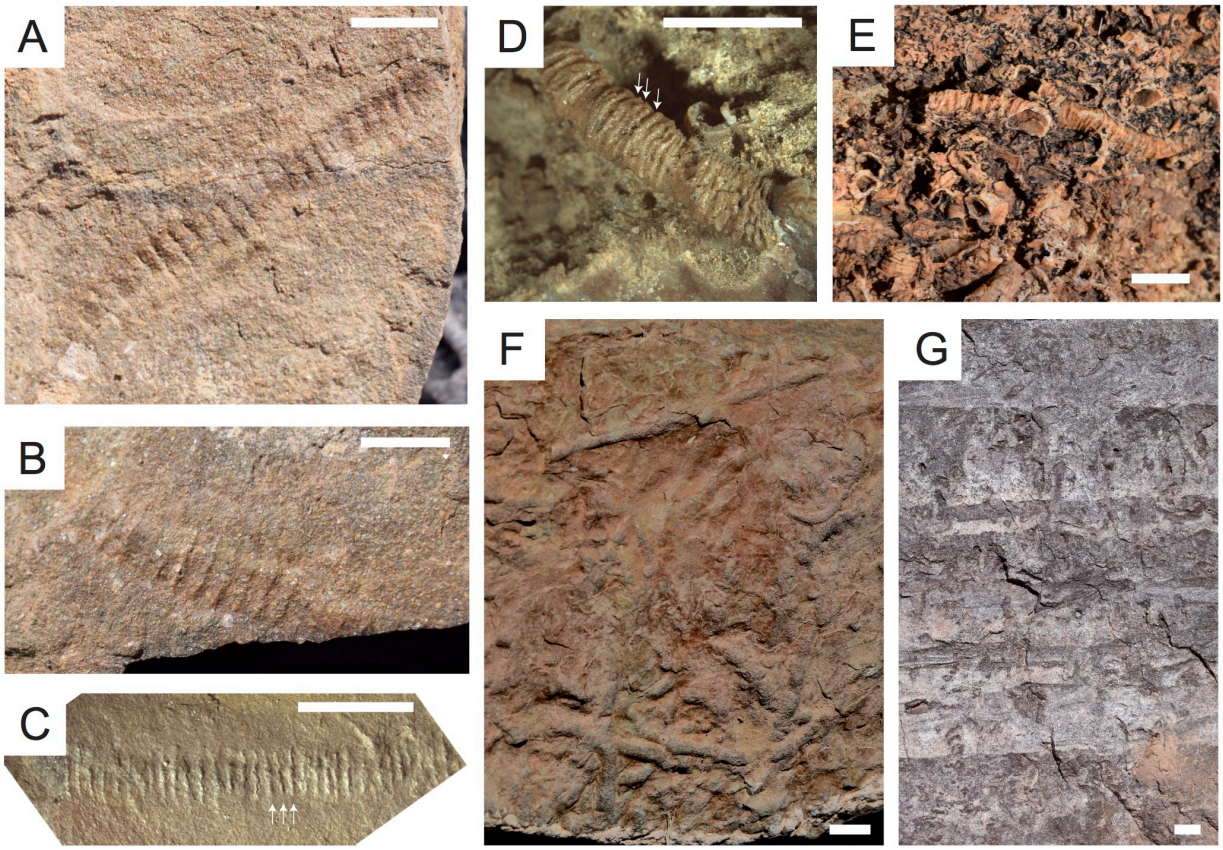

Figure 5.3. Photographs of fossils from La Ciénega and Cerro Rajón formations, northwestern Mexico. Scale bars are 1 cm. Stratigraphic positions of specimens are shown in Fig. 5.1D. (A) Cast of an annulated tubular body fossil in micaceous siltstone of La Ciénega Formation, tentatively identified as *Gaojiashania* sp. (B) Mold of specimen in Fig. 5.3A. (C) Annulated tubular body fossil with rings lightly replaced by iron oxides in micaceous siltstone of La Ciénega Formation, tentatively identified as *Gaojiashania* sp. Arrows highlight rings. (D) Silicified *Cloudina* in dolostone of La Ciénega Formation; arrows highlight nested funnel structure. (E) Silicified *Cloudina* coquina in dolostone of La Ciénega Formation. (F) Complex bed-penetrating ichnofossils preserved on bed sole within sandstone of lower Cerro Rajón Formation. (G) Cross section view of vertical to subvertical bed-penetrating ichnofossils within sandstone of lower Cerro Rajón Formation.

5.4.3. Geochronology

U-Pb geochronological analyses were obtained from a 10-cm-thick bed of sandy hematite-rich dolostone near the top of Unit 3 of the La Ciénega Formation at Cerro Clemente (Fig. 5.1D; Appendix A3 Fig. S2). The bed is well laminated with a matrix consisting of fine-grained peloidal dolomicrite containing subordinate hematite, secondary silica, and clay (Appendix A3 Fig. S2). Secondary mineral infilling of original porosity and hematization of clay minerals may be related

to similar features observed in diagenetically altered tuffaceous horizons in marine carbonates (e.g., Kiipli et al., 2000; see supplementary material in Appendix A3). Redeposited material within the bed includes rounded grains of holoclastic quartz and accidental lithics of basement-derived metamorphic rock fragments (Appendix A3 Fig. S2).

Screening of zircons by LA-ICPMS (130 analyses) yielded age populations at 540, 1000–1100, 1400–1500, and 1700–1800 Ma (Appendix A3 Fig. S3A and Table S2), each defining discordia lines toward a Pb loss event at ca. 60 Ma, the timing of metasomatism and greenschist facies metamorphism related to Laramide orogenesis (Appendix A3 Fig. S3B-D; Barrón-Díaz et al., 2019c). The ca. 540 Ma crystals have characteristics of a rift-related volcanic source, including consistent temperature-correlated differentiation trends in trace element geochemistry (Appendix A3 Fig. S4), inclusions of apatite and glass, and subdued internal oscillatory and sector zoning in an overall intense CL response (Fig. 5.4; Appendix A3 Fig. S5). Six sharply faceted zircon grains were selected for CA-ID-TIMS (Fig. 5.4D), with four grains split in half, yielding 10 zircon analyses. Six fragments with reproducible $^{206}Pb/^{238}U$ dates yield a weighted mean date of 539.40 ± 0.23/0.35/0.66 Ma (2σ internal/2σ internal and tracer/2σ internal, tracer, and decay constant uncertainties) (Fig. 5.4A-C; Appendix A3 Table S3; mean square weighted deviation = 1.05; probability of fit = 0.34), which we report conservatively as a maximum depositional age, but with a high probability of deposition close to eruption.

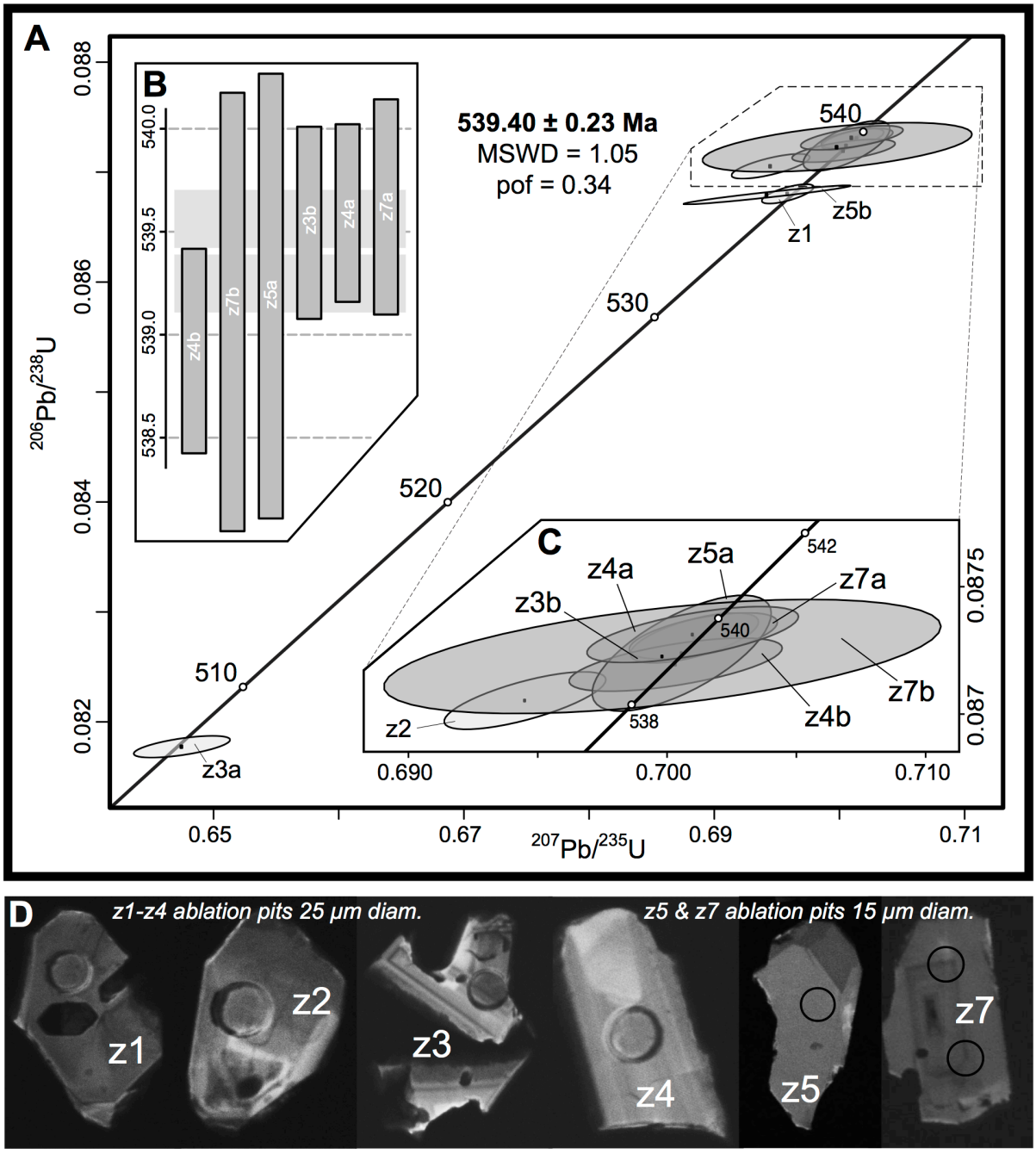

Figure 5.4. U-Pb zircon geochronology from sample CC1801-138 reported with 2σ internal uncertainty. Stratigraphic position is shown in Fig. 5.1D. (A) CA-ID-TIMS U-Pb Concordia plot. (B) Age-rank plot of zircon fractions used to calculate weighted mean. (C) Concordia inset of zircon fractions used to calculate weighted mean. (D) Cathodoluminescence images of zircons analyzed by CA-ID-TIMS. MSWD—mean square weighted deviation; pof—probability of fit.

5.5. Discussion and Conclusions

The 539.40 ± 0.23 Ma dated horizon occurs ~20 m above the nadir and below the recovery from a negative $\delta^{13}C$ excursion that is reproduced across three sections of the La Ciénega Formation (Fig. 5.1D), providing a maximum age constraint on the nadir of the BACE. Minimal evidence for facies dependence of $\delta^{13}C$ values or alteration by meteoric diagenesis, in combination with the reproducibility of the BACE along the southwestern Laurentian margin through variable lithologies and across stratigraphic sequence boundaries (Corsetti and Hagadorn, 2000, 2003; Smith et al., 2016, 2017), suggest a marine carbon cycle perturbation at the Ediacaran–Cambrian boundary, rather than a diagenetic origin. By contrast, at Farm Swartpunt in Namibia, there is an ~140 m section of strata with dated ash beds (Linnemann et al., 2019) that overlap with the 539.40 ± 0.23 Ma age of the dated horizon in Sonora, and yet, there, the $\delta^{13}C$ values of carbonates remain stable at ~1‰ (Saylor et al., 1998). If the date reported here is a near-depositional age, as we suggest, then on some margins the BACE was not recorded, which could be explained by the existence of local, isotopically distinct pools of dissolved inorganic carbon (Swart et al., 2009; Geyman and Maloof, 2019). While the 541.00 ± 0.13 Ma age below the $\delta^{13}C$ excursion in Oman is ~1.5 m.y. older, this may not directly date the onset of the BACE because the Ara Group was deposited in an evaporitic basin with probably depositional hiatuses (e.g., Zhu et al., 2019). Additional geochronology from strata containing this excursion will thus be necessary to test its global synchrony, duration, and synoptic variability, and to evaluate possible regional controls (Fig. 5.5).

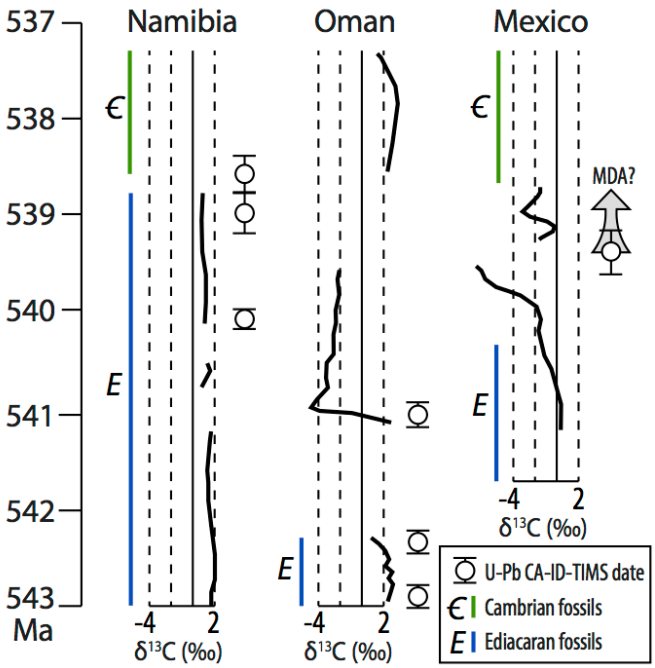

Figure 5.5. Compiled age constraints on the Ediacaran–Cambrian boundary from Namibia (Saylor et al., 1998; Linnemann et al., 2019), Oman (Amthor et al., 2003; Bowring et al., 2007), and Mexico. MDA—maximum depositional age.

In addition to calibrating the chemostratigraphic record in Sonora, the dated horizon occurs above the last stratigraphic occurrences of the Ediacaran fossils *Cloudina* and *Gaojiashania* and below the first occurrence of *Treptichnus pedum* in this region. This new date from Sonora is within error of the age range (539.20-538.39 Ma) recently proposed for the Ediacaran–Cambrian boundary at Swartpunt, Namibia based on the last occurrences of Ediacaran body fossils and the first occurrences of *Treptichnus pedum* and other complex trace fossils (Fig. 5.5; Linnemann et al., 2019). Although biostratigraphic overlap between cloudinids and clades classically interpreted as Cambrian have been documented in Siberia and Mongolia (Zhu et al., 2017; Yang et al., 2020), confirmation of biostratigraphic correlation between Namibia and Mexico with U-Pb geochronology is consistent with hypotheses of globally synchronous biotic turnover and extinction of Ediacaran clades at the Ediacaran–Cambrian boundary.

The dated horizon in Sonora occurs among basaltic rocks with an enriched mantle source that have been linked to rift-related volcanism within the Caborca block (Stewart et al., 1984; Barrón-Díaz et al., 2019b). Trace element geochemistry from the ca. 540 Ma zircon population is consistent with a mantle-derived source (Appendix A3 Fig. S4; Grimes et al., 2015). The 539.40 ± 0.23 Ma age of this zircon population coincides with bimodal rift-related volcanism in southwestern Oklahoma (USA) that evolved from a magma source of similar composition and mineralogy (Barrón-Díaz et al., 2019b), and spanned from 539–530 Ma (Thomas et al., 2012), with an initial magmatic pulse resolved by CA-ID-TIMS at ca. 539.5 to 539.0 Ma (Wall et al., 2020). The volume of these early Cambrian basaltic lavas has been estimated at >250,000 km^3 and interpreted as a flood basalt province associated with the rifting of the southern margin of Laurentia (Hanson et al., 2013; Brueseke et al., 2016).

In southwestern North America, the last appearance of Ediacaran fossils consistently occurs beneath the nadir of the BACE (Smith et al., 2016, 2017). Here, new geochronology demonstrates temporal coincidence between this biotic turnover, the BACE, and a pulse of volumetrically significant rift-related flood basalt volcanism. We suggest that there is a mechanistic link between this magmatism, environmentally driven extinction at the Ediacaran–Cambrian boundary through alteration of marine chemistry and/or climate and a perturbation to the carbon cycle through isotopically light carbon inputs from volcanic outgassing and combusted organic carbon—perhaps analogous to links between the Central Atlantic Magmatic Province and the Triassic–Jurassic mass extinction during the breakup of Pangaea (Schoene et al., 2010; Ruhl et al., 2011).

5.6. Acknowledgements

We are grateful to A. Lizarraga for property access; J. Ramezani and I. Bennett (Massachusetts Institute of Technology, USA) and R. Mundil (Berkeley Geochronology Center, California, USA) for mineral separation assistance; J. Crowley (Boise State University, Idaho, USA) and G. Seward, F. Apen, A. Kylander-Clark, and F. Macdonald (University of California–Santa Barbara, USA) for U-Pb geochronology assistance; D. Brenner (Johns Hopkins University [JHU], Maryland, USA) and S. Moore (Washington University, St. Louis, Missouri, USA) for stable isotope analysis assistance; and Beck for field assistance. Our funding sources included U.S. National Science Foundation (NSF) Graduate Research Fellowship Program grant DGE-1746891 and National Geographic Early Career grant CP-002ER-17 to L.L. Nelson; NSF EAR-1827669 and support from the JHU Department of Earth and Planetary Sciences to E.F. Smith; and support from Harvard University to E.B. Hodgin. Constructive reviews from F. Bowyer, M. Zhu, and A. Prave improved this manuscript.

5.6. References

Amthor, J.E., Grotzinger, J.P., Schröder, S., Bowring, S.A., Ramezani, J., Martin, M.W., and Matter, A., 2003, Extinction of Cloudina and Namacalathus at the Precambrian-Cambrian boundary in Oman: Geology, v. 31, p. 431–434. doi:10.1130/0091-7613(2003)031<0431:EOCANA>2.0.CO;2.

Anderson, T., and Silver, L., 1981, An overview of Precambrian rocks in Sonora: Revista Mexicana de Ciencias Geológicas, v. 5, p. 131–139.

Barrón-Díaz, A.J., Paz-Moreno, F.A., and Hagadorn, J.W., 2019a, The Cerro Rajón Formation—a new lithostratigraphic unit proposed for a Cambrian (Terreneuvian) volcano-sedimentary succession from the Caborca region, northwest Mexico: Journal of South American Earth Sciences, v.89, p. 197–210. doi:10.1016/j.jsames.2018.11.003.

Barrón-Díaz, A.J., Paz-Moreno, F.A., Lozano-Santa Cruz, R., Herrera-Urbina, S., Centeno-García, E., and López-Martínez, M., 2019b, Early Cambrian alkaline volcanism on the southern margin of Laurentia: evidence in the volcaniclastic units from the Puerto Blanco Formation in the Caborca block, NW Mexico: International Geology Review, v. 61, p. 1189–1206. doi:10.1080/00206814.2018.1501619.

Barrón-Díaz, A.J., Paz Moreno, F.A., Miggins, D.P., and Iriondo, A., 2019c, Geochronology and geothermometry of the Laramide metamorphism in the Cambrian metabasalts from the Cerro Rajón Formation, Caborca region, northwest Mexico: Journal of South American Earth Sciences, v. 91, p. 47–56. doi:10.1016/j.jsames.2019.01.005.

Bowring, S.A., Grotzinger, J.P., Condon, D.J., Ramezani, J., Newall, M.J., and Allen, P.A., 2007, Geochronologic constraints on the chronostratigraphic framework of the neoproterozoic Huqf Supergroup, Sultanate of Oman: American Journal of Science, v. 307, p. 1097–1145. doi:10.2475/10.2007.01.

Brasier, M.D., Shields, G., Kuleshov, V.N., and Zhegallo, E.A., 1996, Integrated chemo- and biostratigraphic calibration of early animal evolution: Neoproterozoic–early Cambrian of southwest Mongolia: Geological Magazine, v. 133, p. 445–485. doi:10.1017/S0016756800007603.

Brueseke, M.E., Hobbs, J.M., Bulen, C.L., Mertzman, S.A., Puckett, R.E., Walker, J.D., and Feldman, J., 2016, Cambrian intermediate-mafic magmatism along the Laurentian margin: Evidence for flood basalt volcanism from well cuttings in the Southern Oklahoma Aulacogen (U.S.A.): Lithos, v. 260, p. 164–177. doi:10.1016/j.lithos.2016.05.016.

Corsetti, F.A., and Hagadorn, J.W., 2000, Precambrian-Cambrian transition: Death Valley, United States: Geology, v. 28, p. 299–302. doi:10.1130/0091-7613(2000)028<0299:PCTDVU>2.3.CO;2.

Corsetti, F.A., and Hagadorn, J.W., 2003, The Precambrian–Cambrian Transition in the Southern

Great Basin: The Sedimentary Record, v. 1, p. 4–8. doi:10.2110/sedred.2003.1.4.

Geyman, E.C., and Maloof, A.C., 2019, A diurnal carbon engine explains 13C-enriched carbonates without increasing the global production of oxygen: Proceedings of the National Academy of Sciences of the United States of America, v. 116, p. 24433-24439. doi:10.1073/pnas.1908783116.

Grimes, C.B., Wooden, J.L., Cheadle, M.J., and John, B.E., 2015, "Fingerprinting" tectono-magmatic provenance using trace elements in igneous zircon: Contributions to Mineralogy and Petrology, v. 170, p. 1–26, doi:10.1007/s00410-015-1199-3.

Hanson, R.E., Puckett, R.E., Keller, G.R., Brueseke, M.E., Bulen, C.L., Mertzman, S.A., Finegan, S.A., and McCleery, D.A., 2013, Intraplate magmatism related to opening of the southern Iapetus Ocean: Cambrian Wichita igneous province in the Southern Oklahoma rift zone: Lithos, v. 174, p. 57–70. doi:10.1016/j.lithos.2012.06.003.

Kiipli, E., Kallaste, T., and Kiipli, T., 2000, Hematite and goethite in Telychian marine red beds of the East Baltic: GFF, v. 122, p. 281–286.

Kimura, H., Matsumoto, R., Kakuwa, Y., Hamdi, B., and Zibaseresht, H., 1997, The Vendian-Cambrian δ13C record, North Iran: Evidence for overturning of the ocean before the Cambrian Explosion: Earth and Planetary Science Letters, v. 147, E1–E7. doi:10.1016/s0012-821x(97)00014-9.

Linnemann, U., Ovtcharova, M., Schaltegger, U., Gärtner, A., Hautmann, M., Geyer, G., Vickers-Rich, P., Rich, T., Plessen, B., Hofmann, M., and Zieger, J., 2019, New high-resolution age data from the Ediacaran–Cambrian boundary indicate rapid, ecologically driven onset of the Cambrian explosion: Terra Nova, v. 31, p. 49–58. doi:10.1111/ter.12368.

Lohmann, K.C., 1988, Geochemical Patterns of Meteoric Diagenetic Systems and Their Application to Studies of Paleokarst, *in* Paleokarst, p. 58–80. doi:10.1007/978-1-4612-3748-8_3.

Loyd, S.J., Marenco, P.J., Hagadorn, J.W., Lyons, T.W., Kaufman, A.J., Sour-Tovar, F., and Corsetti, F.A., 2012, Sustained low marine sulfate concentrations from the Neoproterozoic to the Cambrian: Insights from carbonates of northwestern Mexico and eastern California: Earth and Planetary Science Letters, v. 339, p. 79–94. doi:10.1016/j.epsl.2012.05.032.

Magaritz, M., Holser, W.T., and Kirschvink, J.L., 1986, Carbon-isotope events across the Precambrian/Cambrian boundary on the Siberian Platform: Nature, v. 320, p. 258–259. doi:10.1038/320258a0.

Narbonne, G.M., Kaufman, A.J., and Knoll, A.H., 1994, Integrated chemostratigraphy and biostratigraphy of the Windermere Supergroup, northwestern Canada: implications for Neoproterozoic correlations and the early evolution of animals: Geological Society of America Bulletin, v. 106, p. 1281–1292. doi:10.1130/0016-

7606(1994)106<1281:ICABOT>2.3.CO;2.

Ruhl, M., Bonis, N.R., Reichart, G.J., Sinninghe Damsté, J.S., and Kürschner, W.M., 2011, Atmospheric carbon injection linked to end-Triassic mass extinction: Science, v. 333, p. 430–434. doi:10.1126/science.1204255.

Saylor, B.Z., Kaufman, A.J., Grotzinger, J.P., and Urban, F., 1998, A composite reference section for terminal Proterozoic strata of southern Namibia: Journal of Sedimentary Research, v. 68, no. 6, p.1223–1235.

Schoene, B., Guex, J., Bartolini, A., Schaltegger, U., and Blackburn, T.J., 2010, Correlating the end-Triassic mass extinction and flood basalt volcanism at the 100 ka level: Geology, v. 38, p. 387–390. doi:10.1130/G30683.1.

Smith, E.F., Nelson, L.L., Strange, M.A., Eyster, A.E., Rowland, S.M., Schrag, D.P., and Macdonald, F.A., 2016, The end of the Ediacaran: Two new exceptionally preserved body fossil assemblages from Mount Dunfee, Nevada, USA: Geology, v. 44, p. 911–914. doi:10.1130/G38157.1.

Smith, E.F., Nelson, L.L., Tweedt, S.M., Zeng, H., and Workman, J.B., 2017, A cosmopolitan late ediacaran biotic assemblage: New fossils from Nevada and Namibia support a global biostratigraphic link: Proceedings of the Royal Society B: Biological Sciences, v. 284, p. 1–10. doi:10.1098/rspb.2017.0934.

Sour-Tovar, F., Hagadorn, J.W., and Huitrón-Rubio, T., 2007, Ediacaran and Cambrian index fossils from Sonora, Mexico: Palaeontology, v. 50, p. 169–175. doi:10.1111/j.1475-4983.2006.00619.x.

Stewart, J.H., McMenamin, M.A.S., and Morales-Ramirez, J.M., 1984, Upper Proterozoic and Cambrian rocks in the Caborca region, Sonora, Mexico - physical stratigraphy, biostratigraphy, paleocurrent studies and regional relations.: US Geological Survey Professional Paper, v. 1309, p. 1–36. doi:10.3133/pp1309.

Swart, P.K., Reijmer, J.J.G., and Otto, R., 2009, A re-evaluation of facies on Great Bahama Bank II: variations in the δ13C, δ18O and mineralogy of surface sediments: Int. Assoc. Sedimentol. Spec. Publ., v. 41, p. 47–59.

Thomas, W.A., Tucker, R.D., Astini, R.A., and Denison, R.E., 2012, Ages of pre-rift basement and synrift rocks along the conjugate rift and transform margins of the argentine precordillera and laurentia: Geosphere, v. 8, p. 1366–1383. doi:10.1130/GES00800.1.

Wall, C.J., Hanson, R.E., Schmitz, M., Price, J.D., Donovan, R.N., Boro, J.R., Eschberger, A.M., and Toews, C.E., 2021, Integrating zircon trace-element geochemistry and high-precision U-Pb zircon geochronology to resolve the timing and petrogenesis of the late Ediacaran–Cambrian Wichita igneous province, Southern Oklahoma Aulacogen, USA: Geology, v. 49, no. 3, p. 268–272.

Yang, B., Steiner, M., Schiffbauer, J.D., Selly, T., Wu, X., Zhang, C., and Liu, P., 2020, Ultrastructure of Ediacaran cloudinids suggests diverse taphonomic histories and affinities with non-biomineralized annelids: Scientific Reports, v. 8, p. 1–10. doi:10.1038/s41598-019-56317-x.

Zhang, J., Li, G., Zhou, C., Zhu, M., and Yu, Z., 1997, Carbon isotope profiles and their correlation across the Neoproterozoic–Cambrian boundary interval on the Yangtze Platform, China: Bulletin of the National Museum of Natural Science, v. 10, p. 107–116.

Zhu, M., Zhuravlev, A.Y., Wood, R.A., Zhao, F., and Sukhov, S.S., 2017, A deep root for the Cambrian explosion: Implications of new bioand chemostratigraphy from the Siberian Platform: Geology, v. 45, p. 459–462. doi:10.1130/G38865.1.

Zhu, M., Yang, A., Yuan, J., Li, G., Zhang, J., Zhao, F., Ahn, S.Y., and Miao, L., 2019, Cambrian integrative stratigraphy and timescale of China: Science China Earth Sciences, v. 62, p. 25–60. doi:10.1007/s11430-017-9291-0.

CHAPTER 6. PUSHING THE BOUNDARY: A CALIBRATED EDIACARAN–CAMBRIAN STRATIGRAPHIC RECORD FROM THE NAMA GROUP IN NORTHWESTERN REPUBLIC OF SOUTH AFRICA

A version of this chapter was published in:

[Nelson, L. L., Ramezani, J., Almond, J. E., Darroch, S. A. F., Taylor, W. L., Brenner, D. C., Furey, R. P., Turner, M., & Smith, E. F. (2022). Pushing the boundary: A calibrated Ediacaran–Cambrian stratigraphic record from the Nama Group in northwestern Republic of South Africa. *Earth and Planetary Science Letters*, *580, 117396*.]

Abstract

The Nama Group exposed on the Neint Nababeep Plateau along the Orange River in northwestern Republic of South Africa is now recognized as an expanded record of the Ediacaran–Cambrian transition that provides opportunity for an integrated stratigraphic approach in examining the geochemical and biologic evolution across this fundamental geologic boundary at unprecedented resolution. U-Pb zircon geochronology by the CA-ID-TIMS method on six intercalated volcanic ash beds in the Nama Group (from the Huns Member to the Nomtsas Formation) at this locality is used to construct a high-resolution, Bayesian, age-stratigraphic model, which allows a direct temporal calibration of the biostratigraphy and carbon isotope record from 539.63±0.15 Ma to 537.95±0.28 Ma (2σ internal errors). Across the border in the Witputs subbasin of southern Namibia, ash beds at the base of Nudaus Formation and within the Nasep Member yielded new U-Pb ages of 545.27±0.11 Ma and 542.65±0.15 Ma, respectively. Our combined geochronology reveals the detailed depositional history of the Nama Group at a regional scale, suggesting that a relatively low sediment accumulation rate in the Kuibis Subgroup and the lower Schwarzrand Subgroup was followed by accelerated sedimentation in the upper Schwarzrand Subgroup. This is

consistent with a pattern of exponential increase in subsidence typical of foreland basins. Some of the observed chemostratigraphic trends throughout the Nama Group could relate to a shift from a seawater-buffered to a sediment-buffered regime of early marine diagenesis driven by this increase in sedimentation rate.

Occurrences of soft-bodied erniettomorphs, calcified body fossils, and trace fossils within the Neint Nababeep Plateau are broadly consistent with known global biostratigraphic ranges. However, we document the youngest radioisotopically calibrated occurrences of Ediacaran-type fossils, which stratigraphically overlap with large and complex bilaterian ichnofossils, between 539.18+0.17/−0.26 Ma and 538.30+0.14/−0.14 Ma. Yet, the index fossil *Treptichnus pedum* remains undocumented from this section, and we suggest that its first regional occurrence may be younger than these strata. Despite relatively continuous and high rates of carbonate sedimentation across the Ediacaran–Cambrian boundary (as currently recognized), the upper Nama Group of the Neint Nababeep Plateau does not preserve the characteristic negative carbon isotope excursion observed within other basal Cambrian successions. One possible explanation for its absence is that this chemostratigraphic marker is not ubiquitous in all carbonate depositional environments. Alternatively, the basal Cambrian carbon isotope excursion, and perhaps the Ediacaran–Cambrian boundary as defined by the first appearance of *Treptichnus pedum*, might be >1 m.y. younger than currently recognized, postdating 538 Ma and, thus, suggesting a more condensed early Cambrian radiation. Difficulties in determining with confidence the first appearance datum of the index fossil *Treptichnus pedum* in the Nama Group highlight the challenge of a global biostratigraphic definition for the base of Cambrian and underscore the necessity of an integrated stratigraphic and radioisotope geochronologic approach to understand the tempo and patterns of environmental and biologic evolution across the Ediacaran–Cambrian boundary.

6.1. Introduction

The Ediacaran–Cambrian boundary marks a critical biological transition in Earth history: the disappearance of the Ediacaran biota from the fossil record—potentially the first mass extinction of complex life—and the subsequent appearance of many metazoan clades during the Cambrian Period, including the majority of currently recognized modern phyla. The base of the Cambrian Period is defined by the first appearance of the trace fossil *Treptichnus pedum* (Brasier et al., 1994). Secondary informal markers include the first occurrences of small shelly fossils, the last occurrences of Ediacaran-type body fossils, and a large negative carbon isotope excursion, termed the BAsal Cambrian carbon isotope Excursion (BACE) (e.g., Darroch et al., 2018). As few Ediacaran–Cambrian sections have all of these markers, robust and precise correlations remain a significant problem in determining rates and global synchroneity of geochemical change and biotic turnover across this boundary. An additional potential problem is that mounting evidence demonstrates that carbon isotope excursions are not always reliable global stratigraphic markers within shallow water carbonate rocks (e.g., Higgins et al., 2018).

Currently, the Ediacaran–Cambrian boundary is temporally constrained by radioisotopic geochronology from the Nama Group near Witputs, Namibia where an ash bed below the first appearance of *Treptichnus pedum* in the Nomtsas Formation has been dated at 538.58±0.19 Ma, and strata containing fossils of erniettomorphs and *Cloudina* are constrained to <538.99±0.21 Ma (Linnemann et al., 2019). Geochronological constraints on the BACE come from the Ara Group of Oman, where an ash bed that coincides with the onset of a negative carbon isotope ($\delta^{13}C$) excursion has been dated at 541.00±0.13 Ma (Bowring et al., 2007), and from the La Ciénega Formation of Sonora, Mexico, where a bed 20 m above the nadir of a large negative $\delta^{13}C$ excursion has a maximum depositional age of 539.40±0.23 Ma (Hodgin et al., 2021).

Here, we present a high-resolution age-stratigraphic model based on U-Pb zircon geochronology by the chemical abrasion isotope dilution thermal ionization mass spectrometry (CA-ID-TIMS) method from eight Nama Group ash beds from southern Namibia and northwestern Republic of South Africa, which range from c. 545 to 538 Ma. Within this framework, we present calibrated high-resolution biostratigraphic and chemostratigraphic datasets from the Nama Group of the Neint Nababeep Plateau along the Orange River, allowing for examination of global biostratigraphic and chemostratigraphic correlations and trends across the Ediacaran–Cambrian transition.

6.2. Geological background

The Nama Group is a >1 km-thick succession of predominantly marine siliciclastic and carbonate rocks that were deposited within a late Ediacaran–early Cambrian foreland on the western margin (present-day coordinates) of the Kalahari craton. Basin formation resulted from continental flexure related to pending collision with the Rio de Plata craton to the west—the Gariep Orogen—and with the Congo craton to the north—the Damara Orogen (Fig. 6.1; Germs, 1983; Germs and Gresse, 1991). Two distinct subbasins of the Nama Group have been recognized in Namibia south of Windhoek: the Zaris subbasin (north), and the Witputs subbasin (south). These are separated by the Osis arch—a paleo-high of Mesoproterozoic basement, interpreted as a peripheral bulge (Fig. 6.1; Germs, 1983; Germs and Gresse, 1991). The Kuibis Subgroup thins out over the Osis arch, suggesting that the basins were at least partially segmented by an east-northeast trending topographic high during the deposition of the basal Nama Group (Germs, 1983) with greater early subsidence in the northern subbasin. The early Cambrian Fish River Subgroup unconformably overlies the Schwarzrand Subgroup in both

subbasins and was deposited as a molasse in fluvial-deltaic settings during the final stages of orogenic collision (e.g., Geyer, 2005).

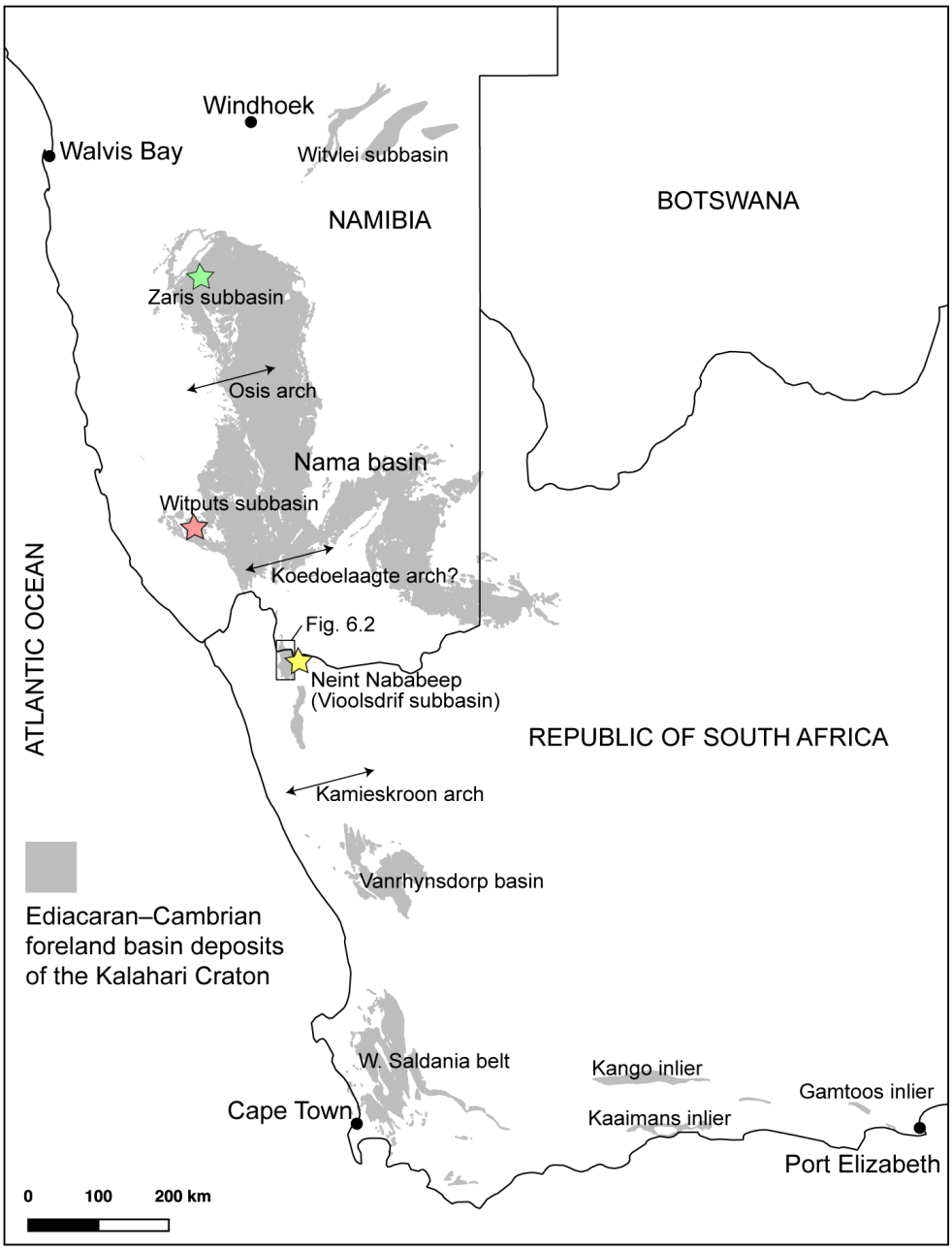

Figure 6.1. Regional outcrop extent of late Ediacaran to early Cambrian foreland basin strata on the Kalahari Craton in southern Africa. Yellow star marks study area on the Neint Nababeep Plateau; red and green stars mark sections in Figure 6.10. Compiled from geologic maps of the Geological Survey of Namibia and the Republic of South Africa Council for Geoscience.

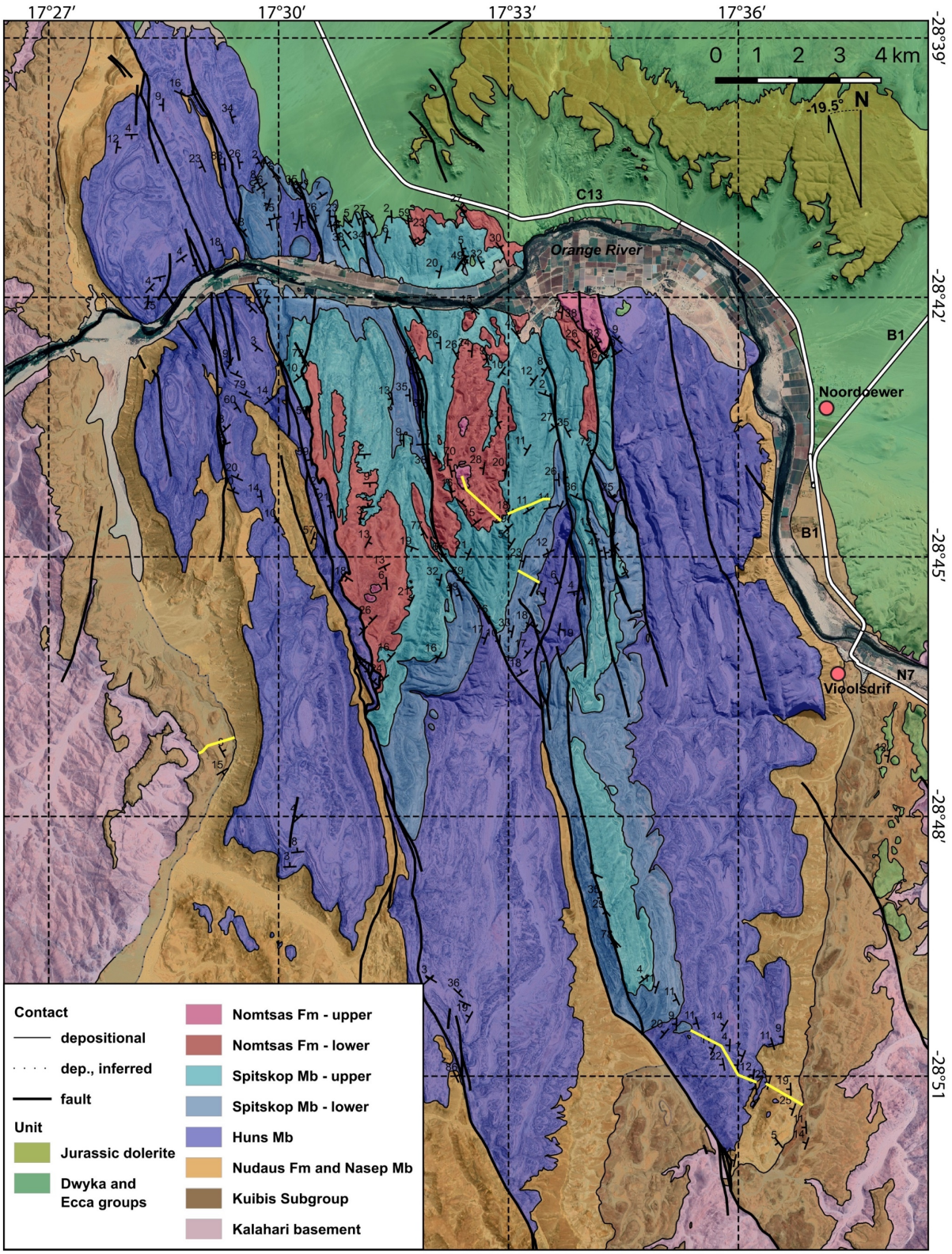

Figure 6.2. Geologic map of the Neint Nababeep Plateau in northwestern Republic of South Africa and southwestern Namibia. The Orange River marks the international boundary. Yellow lines are measured sections corresponding to the composite stratigraphic column in Figure 6.3.

Exposures of the Nama Group have also been recognized east of Windhoek in the Witvlei subbasin and in southernmost Namibia along the Orange River near the towns of Noordoewer and Aussenkehr, respectively. The exposures of the Nama Group near Noordoewer continue into the Republic of South Africa on the Neint Nababeep Plateau (Almond, 2009), and additional inliers occur to the south near the towns of Steinkopf and Springbok (Germs and Gresse, 1991; Gresse et al., 2006). Germs and Gresse (1991) interpreted all of these southernmost Nama Group exposures as part of the Vioolsdrif subbasin, separated from the Witputs subbasin by the Koedoelaagte arch, a possible east-northeast trending forebulge that was active during deposition of parts of the Schwarzrand Subgroup and the Fish River Subgroup. Alternatively, all of these exposures could be considered a southern extension of the Witputs subbasin (Germs et al., 2009). This study focuses on the Nama Group of the Neint Nababeep Plateau (Figs. 1, 2). Additional Ediacaran–Cambrian foreland basin deposits that likely correlate or partially correlate to the Nama Group occur further south in the Republic of South Africa, extending along the margin of the Kalahari craton from the Vanrhynsdorp basin along the Saldania belt to Port Elizabeth (Fig. 6.1; Germs and Gresse, 1991; Gresse and Germs, 1993).

Carbon isotope chemostratigraphy of carbonate strata in the Nama Group has been one tool used for correlation regionally and globally (e.g., Saylor et al., 1998). It has been suggested that negative $\delta^{13}C$ values within carbonates of the Dabis Formation of the basal Kuibis Subgroup correlate to the end of the global Shuram carbon isotope excursion (Wood et al., 2015), which is thought to have terminated by >564.3 Ma based on Re-Os geochronology (Rooney et al., 2020). However, in South China, an ash bed U-Pb ID-TIMS date of 551.09±1.02 Ma records the recovery of a large negative excursion (Condon et al., 2005), and therefore it is possible that there are multiple distinct negative carbon isotope excursions >551 Ma (Yang et al., 2021). Regardless of

whether this excursion is associated with the Shuram or with a separate, younger perturbation, the negative excursion in the Dabis Formation correlates basal carbonate strata between the Witputs and Zaris subbasins (Saylor et al., 1998; Wood et al., 2015). The overlying Zaris Formation records a recovery to positive $\delta^{13}C$ values, peaking at +5‰ before decreasing to ~ -1‰ near the top of the unit (Saylor et al., 1998). Carbonates of the Schwarzrand Subgroup record positive $\delta^{13}C$ values ranging from ~ 0 to +3‰ that have been correlated to the late Ediacaran positive carbon isotope plateau (Saylor et al., 1998).

In the Zaris subbasin, the Hoogland Member of the Zaris Formation of the upper Kuibis Subgroup contains an ash bed with a U-Pb CA-ID-TIMS age of 547.36±0.23 Ma (Grotzinger et al., 1995; Bowring et al., 2007). In the Witputs subbasin, the Spitskop Member of the upper Schwarzrand Subgroup contains five ash beds dated with U-Pb CA-ID-TIMS on zircon between 540.10±0.10 Ma and 538.99±0.21 Ma, and the overlying Nomtsas Formation contains an ash bed dated at 538.58±0.19 Ma (Grotzinger et al., 1995; Linnemann et al., 2019), as well as the Cambrian index fossil *Treptichnus pedum* (Germs, 1972; Wilson et al., 2012). The Fish River Subgroup also preserves *Treptichnus pedum* (Germs, 1972; Geyer, 2005) and contains c. 540-530 Ma detrital zircon populations (Newstead, 2010; Blanco et al., 2011). A radioisotopic age gap has existed for the lower and middle Schwarzrand Subgroup.

The Nama Group preserves soft-bodied Ediacara biota of the late Ediacaran 'Nama Assemblage' (Laflamme et al., 2013) in the upper part of the Kuibis Subgroup (Kliphoek and Urikos members), including rangeomorphs and erniettomorphs (e.g., Pflug, 1970, 1972). Erniettomorphs are also found in the Nudaus, Nasep, and Spitskop members of the Schwarzrand Subgroup, with the youngest occurrences in the upper Spitskop Member in the Witputs subbasin (above the c. 538.99 Ma date of Linnemann et al. (2019)), and in the Schwarzrand Subgroup of

the Zaris subbasin (Grotzinger et al., 1995). Poorly preserved casts and molds of macroscopic tubular and annulated body fossils have been identified in both the Witputs and Zaris subbasins, and likely belong to multiple metazoan taxa, but are not readily classifiable (e.g., Germs, 1972; Darroch et al., 2016; Smith et al., 2017; Darroch et al., 2021). Carbonaceous ribbon-like compressional fossils assigned to *Vendotaenia* are preserved in the Feldshuhhorn Member of the Schwarzrand Subgroup in the Witputs subbasin (Cohen et al., 2009). Similar tubular compression fossils also occur in the lower Nudaus Formation, but have not been taxonomically assigned, as they lack branching, longitudinal creases, and organic walls that are preserved in the Feldshuhhorn population (Cohen et al., 2009).

Calcified body fossils, including *Cloudina* and *Namacalathus*, are preserved in the Omkyk Member in the Zaris subbasin (below the c. 547.36 Ma ash bed), and in the Mooifontein, Huns, and Spitskop members of the Witputs subbasin, with the last occurrence above the c. 538.99 Ma ash bed at Swartpunt (Grotzinger et al., 1995). *Cloudina* also have also been reported, but not figured, from the Mara Member of the Witputs subbasin (Germs, 1972). The calcified fossil *Namapoikia*, which occurs in the Omkyk Member in the Zaris subbasin, was first interpreted as a metazoan (Wood et al., 2002), but subsequently has been reinterpreted as a microbially formed buildup (Mehra et al., 2020).

Trace fossils in the Nama Group are thoroughly reviewed by Darroch et al. (2021). Their compiled ichnostratigraphy suggests the appearance of simple, vertical plug-shaped ichnofossils in the Kuibis Subgroup and the appearance of simple horizontal trace trails, such as *Helminthopsis*, *Helminthoidichnites*, and *Archaeonassa* in the lower Schwarzrand Subgroup (Nasep Member and Vingerbreek Member of the Witputs and Zaris subbasins, respectively). The more complex horizontal burrow *Parapsammichnites pretziliformis* was reported in the basal Spitskop Member

of the Witputs subbasin (Fish River Canyon) and demonstrates complex bulldozing and active backfilling behavior (Buatois et al., 2018). *Streptichnus narbonnnei* was reported from the uppermost Spitskop Member of the Witputs subbasin (Farm Swartpunt) and is another complex trace fossil composed of clusters of radiating burrows extending from a central point (Jensen and Runnegar, 2005). Treptichnids occur as low as the basal Huns Member in the Witputs subbasin, and their small discontinuous burrows demonstrate relatively complex probing behavior (Jensen et al., 2000; Darroch et al., 2021). The first appearance of the more complex *Treptichnus pedum* (the index fossil marking the base of the Cambrian Period) occurs much higher in the strata within the Nomtsas Formation and the overlying Fish River Subgroup (Germs, 1972; Wilson et al., 2012). Scratch circles, formed by rotation of tethered organisms, have been reported from the Nudaus Formation at the Neint Nababeep Plateau and from the Spitskop Member at Farm Swartpunt (Jensen et al., 2018).

Stromatolitic and thrombolitic bioherms that form high-relief patch reefs and pinnacle reefs have been described at a number of levels within the Nama Group, including the Omkyk and Hoogland members in the Zaris subbasin and the Huns, Feldshuhhorn and Spitskop members of the Witputs subbasin (e.g., Saylor et al., 1995; Grotzinger, 2000; Grotzinger et al, 2005). These buildups are generally interpreted to have formed during flooding events and are onlapped by siltstone or silty limestone deposited during transgressive sequences. These carbonate reefs often host packstone and wackestone of *Cloudina* and *Namacalathus* fossils deposited within and between stromatolites, thrombolites, and neptunian dikes (Grotzinger et al., 2005). Bioherms are often selectively dolomitized (Saylor et al., 1995). Exhumed pinnacle reefs at Farm Swartpunt are interpreted to occur at the contact between the Huns Member and overlying Feldshuhhorn Member and reach 50 m in vertical relief (Saylor et al., 1995).

6.3. Methods

Fieldwork conducted throughout the Neint Nababeep Plateau in northwestern Republic of South Africa and southern Namibia included geologic mapping at variable scales using the Midland Valley FieldMove digital mapping application and the measurement of detailed stratigraphic sections with a folding meter stick (Fig. 6.2). The results were integrated into a composite stratigraphic section of the Nama Group (Fig. 6.3). Fist-sized carbonate samples were collected at 0.5–2 m resolution for carbon and oxygen stable isotope analyses, and all identified volcanic ash beds were sampled (3 to 7 kg each) for zircon separation and U-Pb geochronology. Body and trace fossils were identified and photographed in the field, and select specimens were collected for further study and reposition at the University of Cape Town. Two additional ash beds were collected in Namibia (Witputs subbasin) from the basal Vingerbreek Member of the Nudaus Formation and from the lower Nasep Member of the Urusis Formation, respectively, on the D727 road, ~30 km NNE of the well documented stratigraphic section at Farm Swartpunt and ~180 km NNW of the Neint Nababeep Plateau. The Nasep ash bed was originally identified, but not dated, by Saylor et al. (2005). U-Pb geochronology by the CA-ID-TIMS method was carried out on single, chemically abraded zircons from the sampled ash beds. Weighted mean $^{206}Pb/^{238}U$ ages are reported at 95% confidence interval and in the format ± *X*/*Y*/*Z* Ma, where *X* is the internal error based on analytical uncertainties only, *Y* includes the tracer calibration uncertainty, and *Z* includes y plus the ^{238}U decay constant uncertainty (Jaffey et al., 1971). Carbon and oxygen isotope ratios are reported in per mil notation relative to Vienna-Pee Dee Belemnite (VPDB).

6.3.1. Carbon and oxygen isotopes

Most carbonate samples were analyzed at the Johns Hopkins University Department of Earth and Planetary Sciences Isotope Ratio Mass Spectrometer Laboratory. Samples were analyzed for carbon and oxygen isotopic compositions ($\delta^{13}C$ and $\delta^{18}O$) using a GasBench II peripheral device coupled to a Thermo-Finnigan MAT253 isotope ratio mass spectrometer (IRMS) in continuous-flow mode. Approximately 0.3 mg of sample carbonate powder reacted with 0.1 mL of 100% phosphoric acid in helium-purged vials at 30 °C, overnight. Evolved CO_2 gas was then analyzed against tank CO_2 gas and isotopic results normalized to VPDB per mil (‰) scale using working in house carbonate standards (ICM, Carrara Marble and IVA Analysentechnik, calcium carbonate) that are calibrated against international standards NBS-18 and IAEA-603. Standard deviations (1σ) of $\delta^{13}C$ and $\delta^{18}O$ values for in house standards were <0.05‰ and <0.34‰, respectively.

Samples from section L1651 and E1680 (Mooifontein Member) were measured at the Harvard University Laboratory for Geochemical Oceanography. Approximately 1 mg of carbonate powder reacted in a common phosphoric acid bath at 90°C with a magnetic stirrer, and evolved CO_2 gas was collected cryogenically and analyzed against an in-house reference gas on a VG Optima dual inlet IRMS. Isotopic results were normalized to V-PDB using an in house Cararra Marble standard calibrated against several NBS carbonate standards. Memory effects from the common acid bath are estimated at <0.1‰ based on variability of standards run directly after samples, and standard deviations (1σ) of $\delta^{13}C$ and $\delta^{18}O$ values for in house standards were <0.1‰ and <0.1‰, respectively. All data are presented in Fig. 6.3, Fig. 6.4, and Appendix A4 Table SM1.

6.3.2. U-Pb zircon geochronology

Volcanic ash beds within the Nama Group are typically 5 to 50 cm-thick, strongly silicified, and are distinguished by their pinkish-white to orange colors in outcrop. Zircon grains from eight samples were separated and analyzed for U-Pb geochronology at the Massachusetts Institute of Technology (MIT) Isotope Laboratory by the chemical abrasion-isotope dilution-thermal ionization mass spectrometry (CA-ID-TIMS) method, following the procedures outlined in Ramezani et al. (2011). Zircons were separated by standard crushing, magnetic susceptibility and high-density liquid techniques and handpicked under a binocular microscope based on their aspect ratios and morphologic characteristics, with preference given to multi-faceted prisms that contain glass (melt) inclusions parallel to their long axis. Selected zircons for analysis were annealed at 900ºC for 60 hours in a muffle furnace, followed by partial dissolution in purified 29 M HF at 210ºC for 12 to 14 hours inside a high-pressure vessel, using methods modified after Mattinson (2005). Chemically abraded grains were fluxed successively in 3.5 M HNO_3 and 6 M HCl on a hot plate and in an ultrasonic bath and thoroughly rinsed after each step with MQ water to remove the leachates, before being loaded individually into PFA microcapsules, spiked with a U-Pb isotopic tracer solution and completely dissolved in 29 M HF at 210ºC for 48 hours. Either the EARTHTIME ET535 or ET2535 mixed ^{205}Pb-^{233}U-^{235}U±^{202}Pb tracer (Condon et al., 2015; McLean et al., 2015) was used in the analyses. Following an HCl-based anion exchange column chemistry procedure (Krogh, 1973), the purified U and Pb were loaded together onto an outgassed Re filament in a silica gel/phosphoric acid mixture, and ratios of U and Pb isotopes were measured on an IsotopX X62 multi-collector thermal ionization mass spectrometer equipped with a Daly photomultiplier ion counting system at MIT. Pb isotopes were measured as mono-atomic ions in a peak hopping mode on the ion counter and were corrected for mass-dependent isotope

fractionation either by using the $^{205}Pb/^{202}Pb$ ratio of the tracer (ET2535), or by applying an independently determined fractionation correction of 0.18% ± 0.05% per atomic mass unit (2σ). U isotopes were measured as dioxide ions in a static mode using three Faraday collectors, while subjected to a within-run mass fractionation correction using the $^{233}U/^{235}U$ ratio of the spike and a sample $^{238}U/^{235}U$ ratio of 137.818 ± 0.045 (Hiess et al., 2012), as well as an oxide correction based on an $^{18}O/^{16}O$ ratio of 0.00205 ± 0.00005.

A total of 52 single zircons from eight volcanic ash samples were analyzed. Complete Pb and U isotopic data are given in Appendix A4 Table SM2 and the age results are summarized in Table 6.1 and Figure 6.6. Data reduction, calculation of dates and propagation of uncertainties used the Tripoli and ET_Redux applications and algorithms (Bowring et al., 2011; McLean et al., 2011). The measured $^{206}Pb/^{238}U$ dates were corrected for initial ^{230}Th disequilibrium based on a magma Th/U ratio of 2.8 ± 1.0 (2σ). Ages for each volcanic ash bed were calculated based on the weighted mean of a statistically coherent cluster of $^{206}Pb/^{238}U$ dates, after excluding older analyses representing detrital or xenocrystic zircons and resulting in MSWD values of significantly larger than 2. Only in one case (sample L1835-0), younger outliers indicating persistent Pb loss were excluded. Uncertainties on the weighted mean dates are given at 95% confidence level (2σ) and in the ± x / y / z Ma format, where x is the internal error based on analytical uncertainties only, y includes the tracer calibration uncertainty, and z includes y plus the ^{238}U decay constant uncertainty of Jaffey et al. (1971). y should be considered when comparing dates with those derived from other U-Pb geochronological methods or with those using a different isotopic tracer.

The Bchron R software package (Haslett and Parnell, 2008; Parnell et al., 2008) was implemented to create a probabilistic age-depth model for the entire stratigraphic section using

Bayesian interpolation. This model assumes a normal distribution for input $^{206}Pb/^{238}U$ dates, assumes the principle of stratigraphic superposition, requiring any stratigraphic position to be younger than underlying positions, and is based on random variability in sediment accumulation rates. Ages and uncertainties of key stratigraphic levels from the Bayesian age-depth model are presented in Table 6.2.

6.4. Results

6.4.1. Stratigraphy

The Nama Group is exposed on the Neint Nababeep Plateau along the Orange River within a north-plunging syncline (Fig. 6.2). To the north, the Nama Group is overlain by strata of the Carboniferous–Jurassic Karoo Supergroup, and to the west, south, and east, it is surrounded by underlying exposures of Mesoproterozoic basement rocks of the Kalahari craton. The Nama Group is cut by NNW-SSE trending steeply dipping faults, which are primarily reverse faults with the WSW side-up (Fig. 6.2). While much of the strata across the Plateau are gently dipping within broad folds, there are isoclinal folds, as well as intense cleavage and calcite veining, proximal to the major reverse faults. Lower portions of the Nama Group, including the Kuibis Subgroup, Nudaus Formation, and Nasep and Huns members are well exposed along the eastern and western edges of the Plateau, while the overlying Spitskop Member and Nomtsas Formation are only exposed in the central area, at the core of the syncline.

Lithostratigraphic divisions of the Nama Group exposed on the Neint Nababeep Plateau broadly correspond to those of the Witputs subbasin as defined by Germs (1983), Saylor et al. (1995), and Saylor (2003) (e.g., Almond, 2009). Sequences correlative to the Kanies and Mara members of the Kuibis Subgroup are not present. A basal conglomerate and overlying cross bedded

sandstones are correlated to the Kliphoek Member, which grades into siltstone that is sharply overlain by limestone of the Mooifontein Member, defining an overall transgressive sequence from fluvial to shallow marine that onlaps onto granitic basement of the Richtersveld Terrane. The lower Mooifontein Member is orange weathering limestone with ripple cross lamination and beds of intraclast breccia that grades into an interval of interbedded siltstone and silty limestone, which is then overlain by ~3 m of black weathering limestone grainstone.

The Kuibis Subgroup is overlain by a sequence boundary defined by laterally variable incision into the upper Mooifontein Member by the overlying Niederhagen Member of the Nudaus Formation. Carbonate sedimentary breccia and silicified coarse quartz sandstone to pebble conglomerate occur as channel fill (Germs and Gaucher, 2012). The basal Niederhagen Member is overlain by interbedded siltstone and sandstone that contains cross bedding, interference ripples, mud cracks, and wavy bedding indicative of a peritidal setting, which grades into trough cross bedded coarse to very coarse quartz sandstone. The Niederhagen Member is sharply overlain by mudstone, siltstone, and sandstone of the Vingerbreek Member of the Nudaus Formation. Much of the Vingerbreek Member is mud to siltstone that was deposited below wave base, although a few intervals of sandstone have low angle cross stratification or ripple cross stratification indicative of traction currents. At the top of the Vingerbreek Member, siltstone grades into sandstone and then a distinctive marker bed of black weathering oolitic limestone, which is overlain by siltstone. In western parts of the Witputs subbasin in Namibia (e.g., our L1941 sample location), the Niederhagen Member of the Nudaus Formation is absent and instead the Vingerbreek Member directly overlies the Mooifontein Member (Saylor et al., 1995).

Siltstone of the uppermost Nudaus Formation of the lower Schwarzrand Subgroup is overlain by quartz sandstone that marks the base of the Nasep Member of the basal Urusis

Formation. In sections on the west side of the plateau, this sandstone is overlain by a thin interval of limestone, but this carbonate does not occur on the east side of the plateau, due to a marginally more proximal setting (c.f. Saylor, 2003). The sandstone (or limestone) of the basal Nasep Member is overlain by siltstone that grades into interbedded siltstone and cross bedded quartz sandstone, and then grades into sandy limestone grainstone of the basal Huns Member.

The Huns Member, which is composed of ~220 m of cliff-forming dark blue to dark-grey weathering limestone. Much of it is cross bedded grainstone, some of which is oolitic; however, there are also thin intervals of siltstone, which are interpreted as flooding surfaces, some of which contain kinneyia-type wrinkle structures that are interpreted to be microbially mediated sedimentary forms. These flooding surfaces often preserve ~5 to 50 cm silicified volcanic ash beds, which form prominent orange weathering horizons. At least twenty ash beds were identified in the upper Schwarzrand Subgroup (Huns Member-Nomtsas Formation), some of which are laterally discontinuous. In the lower Huns Member, there are several horizons of microbial limestone including microbialites and low-relief stromatolites. The Huns Member is overlain by the Feldshuhhorn Member with the contact defined at the base of an interval of siltstone that marks a prominent flooding surface. Siltstone grades into fine to medium micaceous sandstone containing low angle cross stratification and channelized sandstone beds with slump folding. This is overlain by limestone of the basal Spitskop Member which contains ooids as well as a distinctive marker bed of columnar stromatolites. For mapping purposes, we informally divided the Spitskop Member into a lower and an upper submember. The lower submember of the Spitskop Member is composed of mixed limestone and siliciclastic rocks. Limestone intervals dominantly comprise grainstone, some of which is oolitic. Siliciclastic intervals are interpreted as flooding surfaces with siltstone at the base associated with maximum transgression, broadly coarsening (and shallowing) upward

into micaceous sandstone. Sedimentary structures include low angle cross-stratification and slump folding within channelized sandstone beds, as well as microbially mediated kinneyia-type structures. The upper submember of the Spitskop Member is cross stratified limestone grainstone with subordinate intervals of silty limestone packstone to wackestone and a few horizons with stromatolite mounds. In sections within the eastern part of the plateau, the upper submember reaches >150 m (measured section in Fig. 6.3), while in the western part of the plateau it is ~85 m thick and dominantly comprised of stromatolitic reefs rather than grainstone.

The top of the Spitskop Member is defined by a transgressive surface and large stromatolite reefs that form high relief pinnacles and mounds (up to 10s of meters in height). These reefs are onlapped by silty limestone and siltstone, which have preferentially weathered away such that at some localities the outcrops resemble primary seafloor topographic relief (Fig. 6.5A,B). Reefs are formed of amalgamations of stromatolites that have morphologies ranging from large domes to conical structure, and commonly have thrombolitic cores. Siltstone, sandstone, and silty limestone of the Nomtsas Formation overlie the reefs and host carbonate clast debrites and carbonate olistoliths (up to 20 m in diameter) that are interpreted as submarine mass transport deposits (Fig. 6.5C). The base of some channelized sandstone beds within this unit contain flute marks (Fig. 6.5D,E), and no sedimentary structures indicative of traction currents were observed. Overall, the Nomtsas Formation is interpreted to have been deposited during a transgression related to flexure of continental crust underlying the Nama foreland basin that drowned out the carbonate platform by increasing the flux of siliciclastic material. High-relief pinnacle reefs formed in the basal Nomtsas Formation as microbial stromatolites initially kept pace with increasing subsidence, but were eventually drowned out by the siliciclastic sediment and/or increasing water depth. Steep slope gradients generated from the flexure of the continental margin led to the deposition of

submarine mass flow deposits, including olistostromes and sedimentary breccias. The Nomtsas Formation is the stratigraphically highest exposed unit of the Nama Group on the Neint Nababeep Plateau.

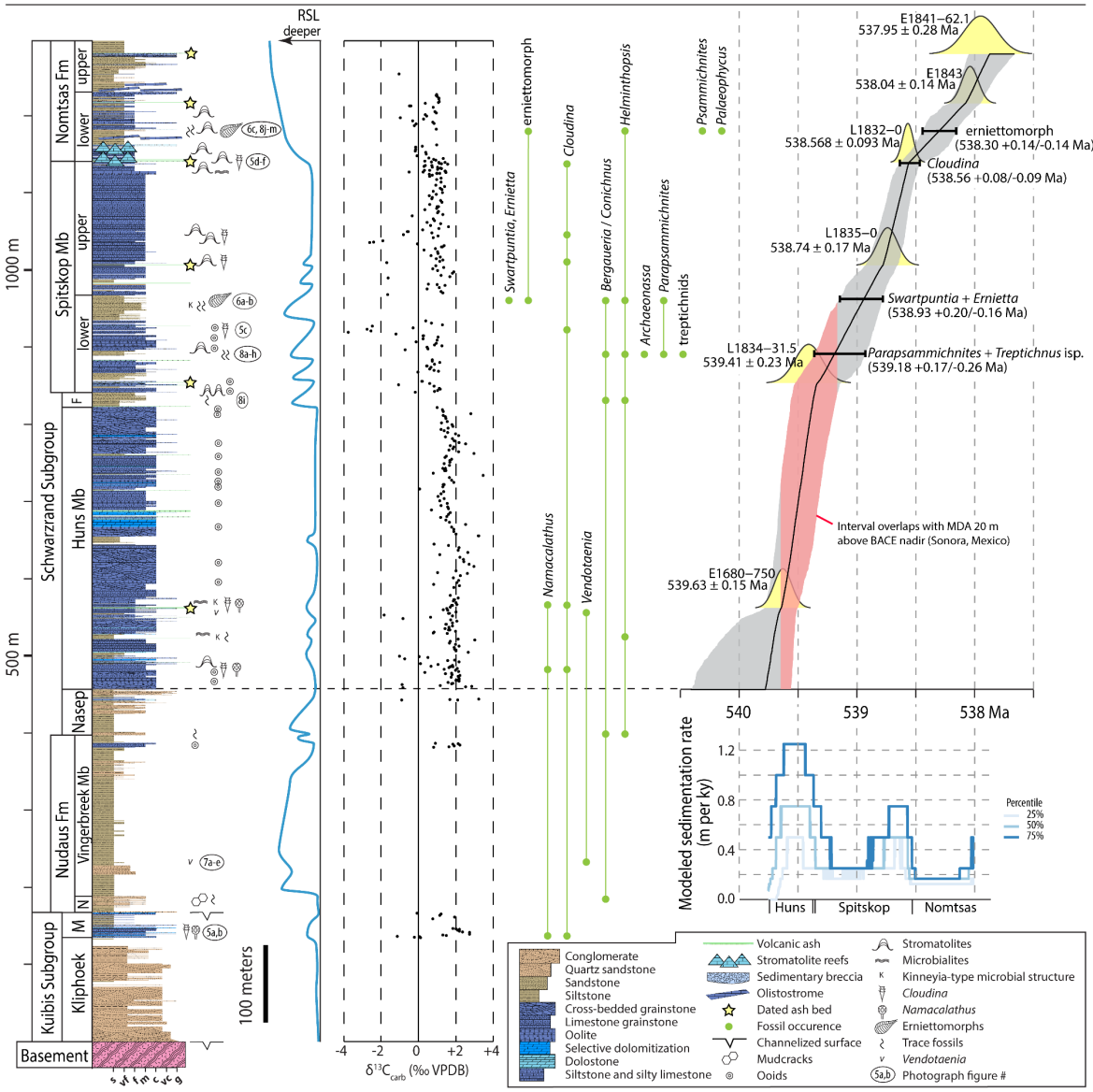

Figure 6.3. Lithostratigraphy, biostratigraphy, carbon isotope chemostratigraphy, and Bayesian age-depth model of the Nama Group in the Neint Nababeep Plateau (section localities shown in Fig. 6.2). Volcanic ash bed dates are weighted mean $^{206}Pb/^{238}U$ dates with internal 2σ uncertainties. The Bchron Bayesian age-depth model is presented with its median (black line) and its 95% confidence interval (grey area). Red shaded area represents overlap with maximum depositional age (MDA) for BACE from Hodgin et al. (2021). Predicted dates for fossil occurrences are calculated with their associated uncertainty using the Bchron Bayesian age-depth model. Modeled sedimentation rate does not account for delithification. M—Mooifontein; N—Niederhagen; F—Feldshuhhorn; RSL—Relative Sea Level; VPDB—Vienna-Pee Dee Belemnite.

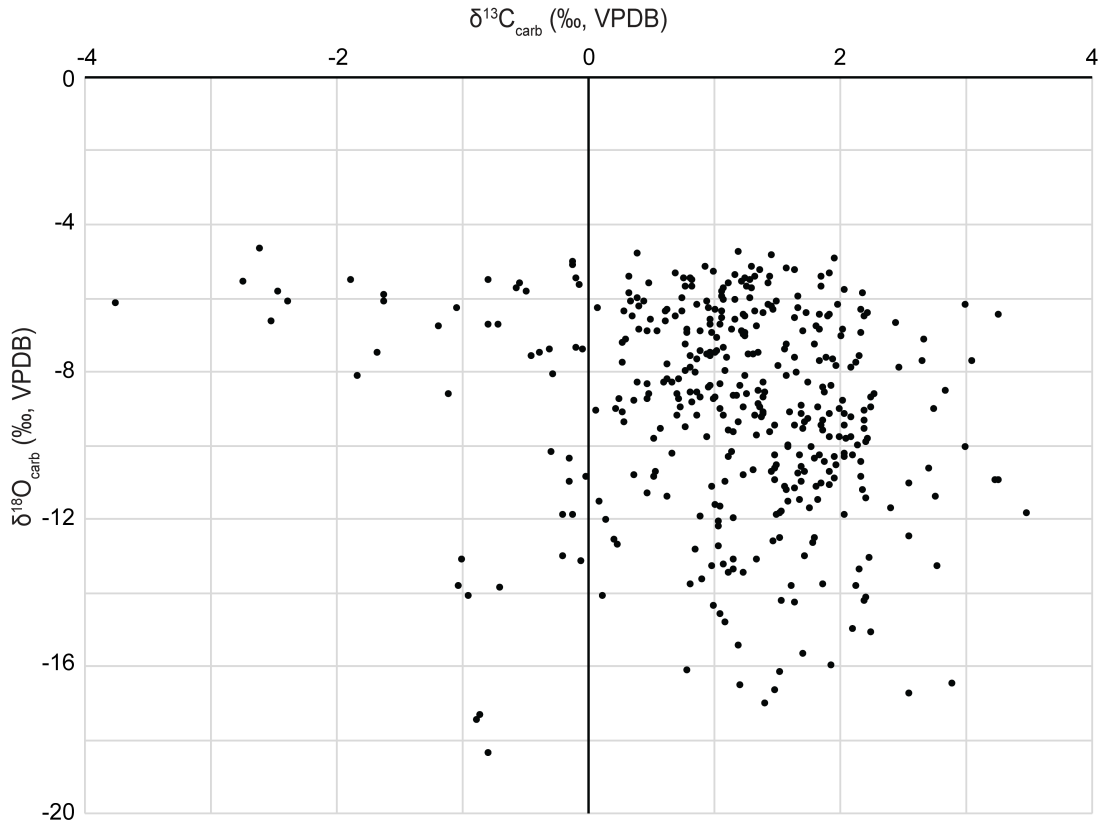

Figure 6.4. Carbon and oxygen isotope cross plot. VPDB—Vienna-Pee Dee Belemnite.

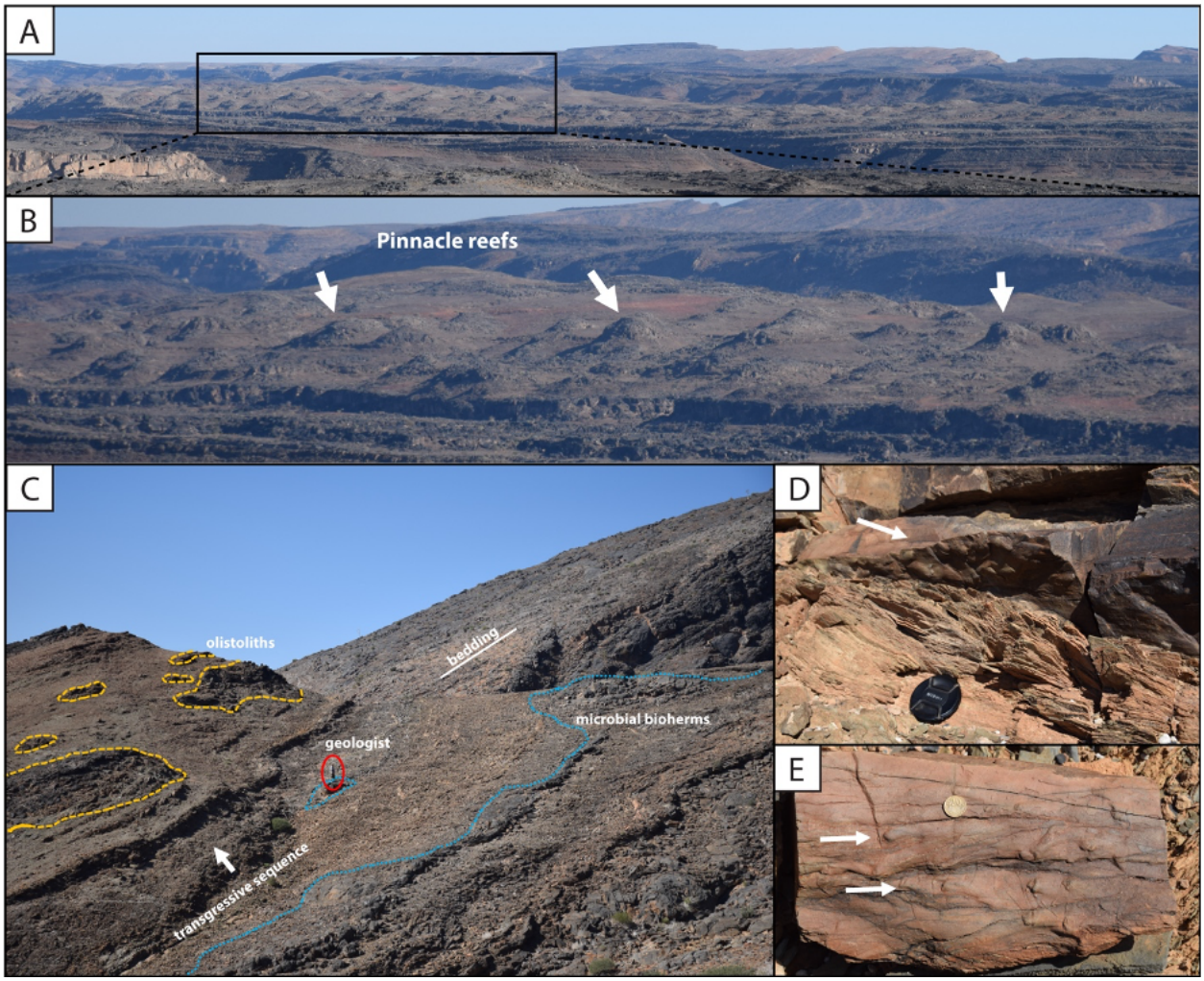

Figure 6.5. Field photographs of the Nomtsas Formation. A, B) Pinnacle reefs of stromatolitic and thrombolitic bioherms weathering out of onlapping siltstone and silty limestone at the base of the Nomtsas Formation. Field of view in 3B is ~1 km. C) Contact between Spitskop Member and Nomtsas Formation. Bioherm build ups denoted with dashed blue line and olistoliths of limestone denoted with orange dashed line D, E) Flute marks on the base of turbidite beds within the Nomtsas Formation. Lens cap is 5.2 cm in diameter. Coin is 1.9 cm in diameter.

6.4.2. Geochronology

Our new U-Pb geochronology based on eight interstratified ash bed ages, integrated into a Bayesian age model, presents the first high-resolution chronostratigraphic framework for the entire Nama Group across southern Namibia and northwestern Republic of South Africa. Six of these ash beds are from the Schwarzrand Subgroup at the Neint Nababeep Plateau, spanning the lower Huns Member to the Nomtsas Formation, which encompasses the Ediacaran–Cambrian transition. Another two are from the lower Schwarzrand Subgroup, basal contact of the Nudaus Formation

and lower Nasep Member of the Urusis Formation, in the Witputs subbasin (Figs. 2, 4, 9; Appendix A4 Table SM2). Table 6.1 summarizes the age results, which range from 545.27±0.11/0.18/0.61 Ma (Nudaus Formation) to 537.95±0.28/0.36/0.68 Ma (Nomtsas Member). The average analytical uncertainty of individual zircons analyses was ±400 kyr (0.7‰), which enabled calculation of weighted mean ages with internal uncertainties as low as ±100 kyr (0.2‰) in order to resolve age differences among closely spaced ash beds (Fig. 6.6).

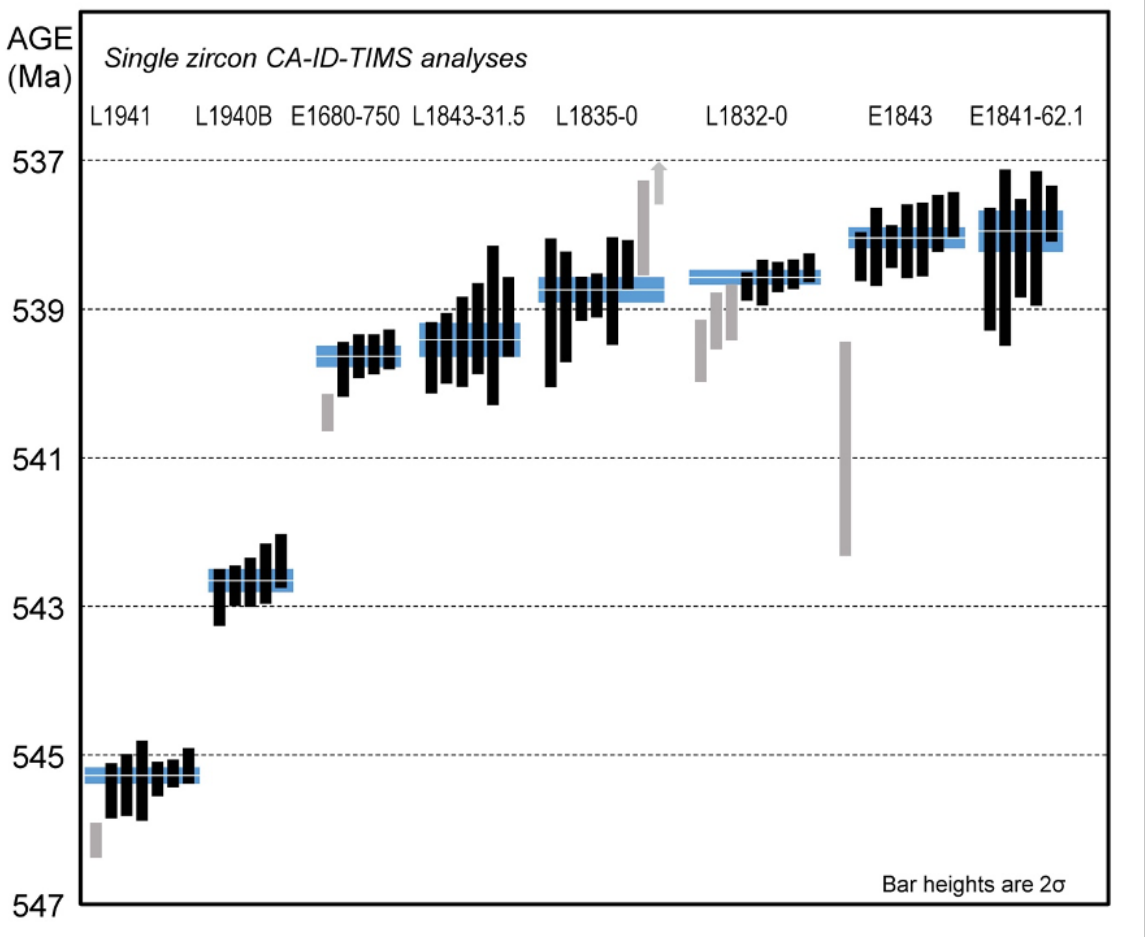

Figure 6.6. Ranked age plot of the analyzed zircons from the interstratified ash beds of the Nama Group. Vertical bars are individual zircon analyses with their 2σ analytical uncertainty; black bars are analyses used in age calculation. Arrow represents the analysis plotting outside the diagram. Blue band signifies the 95% confidence level (2σ) internal uncertainty of the weighted mean age.

Our Bayesian age-depth model suggests that ~820 m of strata of the upper Schwarzrand Subgroup (Huns Member–Nomtsas Formation) were deposited in 1.90+0.84/−0.39 m.y. with an average sediment accumulation rate of 43.2+11.3/−13.2 cm/kyr (Fig. 6.3). This age-depth model does not incorporate delithification; taking into account expected sediment compaction by using carbonate parameters from Kim et al. (2018) and a 1.5–3 km range for burial depth would increase this rate by 42–66%. Our age model reveals that siliciclastic-dominated intervals (Feldshuhhorn and lower Spitskop members and Nomtsas Formation) had resolvably lower average sediment accumulation rates than carbonate-dominated intervals (Huns and upper Spitskop members) (Fig. 6.3). Some of this disparity may be attributed to ~40–70% more post-depositional sediment compaction in shale compared to carbonate (with parameters from Kim et al. (2018) and 1.5–3 km burial depths), but this does not account for the entire difference in modeled stratigraphic accumulation rates. Our age model incorporates a previously reported CA-ID-TIMS U-Pb date of 547.36±0.23 Ma from an ash bed in the Hoogland Member of the Zaris subbasin in Namibia (Bowring et al., 2007), which is correlative to the middle of the Mooifontein Member to the south (e.g., Germs, 1983; Grotzinger et al., 1995; Saylor et al., 1998). Along with two new ash bed dates from the Witputs subbasin in Namibia, this establishes a temporal framework for the entire Nama Group. Based on the composite age-stratigraphic model, average sediment accumulation rates for the lower Schwarzrand subgroup (Nudaus Formation and Nasep Member) are significantly lower than the upper Schwarzrand subgroup (4.3+1.0/−0.3 cm/kyr vs. 43.2+11.3/−13.2 cm/kyr), and, again, only a fraction of this difference can be attributed to lithologically variable compaction.

TABLE 6.1. SUMMARY OF CALCULATED U-Pb DATES AND THEIR UNCERTAINTIES.

Sample	Latitude (N)	Longitude (E)	Unit	$^{206}Pb/^{238}U$ Age (Ma)	error (2σ)*			MSWD†	n§	No.
					X	*Y*	*Z*			
Neint Nababeep Plateau, Republic of South Africa										
E1841-62.1	-28.72461°	17.53997°	Nomtsas Formation	537.95	0.28	0.36	0.68	0.98	5	5
E1843	-28.72706°	17.54244°	Nomtsas Formation	538.04	0.14	0.27	0.63	1.4	7	8
L1832-0	-28.74472°	17.54450°	Nomtsas Formation	538.568	0.093	0.17	0.60	0.95	5	8
L1835-0	-28.75117°	17.55109°	Spitskop Member	538.74	0.17	0.25	0.63	1.1	6	8
L1834-31.5	-28.75965°	17.55480°	Spitskop Member	539.41	0.23	0.33	0.66	0.60	6	6
E1680-750	-28.79168°	17.50051°	Huns Member	539.63	0.15	0.27	0.64	0.47	4	5
Witputs subbasin, Namibia										
L1940B	-27.33969°	16.69826°	Nasep Member	542.65	0.15	0.21	0.62	1.0	5	5
L1941	-27.22152°	16.79246°	Nudaus Formation	545.27	0.11	0.18	0.61	0.63	6	7

**X*—internal (analytical) uncertainty in the absence of all external or systematic errors; *Y*—incorporates the U-Pb tracer calibration error; *Z*—includes X and Y, as well as the uranium decay constant errors (Jaffey et al., 1971).

†MSWD—mean square of weighted deviates.

§*n*—number of analyses included in the calculated weighted mean date out of the total number of analyses (No.).

A noteworthy outcome of the new Nama Group chronostratigraphy is the absence of hiatuses in the upper Schwarzrand subgroup, even at the high resolution of our age model. This is particularly significant for the Spitskop Member–Nomtsas Formation boundary, which has been traditionally described as unconformable valley incisions in the Witputs subbasin (e.g., Grotzinger et al., 1995; Saylor et al., 1995). Our Bayesian age-depth model based on tightly bracketing U-Pb ages does not indicate any detectable changes in the sediment accumulation rate across the latter boundary, when compared to that of other lithologically similar stratigraphic intervals of the upper Nama Group (see Figs. 2, 4). This finding has important implications for the interpretation and placement of the Ediacaran–Cambrian boundary (see Discussion below).

TABLE 6.2. AGES OF KEY STRATIGRAPHIC LEVELS WITHIN THE NAMA GROUP

Lithostratigraphic or biostratigraphic horizon	Stratigraphic depth (meters)	Model age (Ma)
Top of section	0	537.87 +0.18/−0.21
Uppermost limestone of Nomtsas Formation	54	538.04 +0.14/−0.12
Erniettomorph	99.5	538.30 +0.14/−0.14
Pinnacle reef interval	140	538.55 +0.08/−0.10
Highest occurrence of cloudinids	141	538.56 +0.08/−0.09
Base of Nomtsas Formation	143	538.56 +0.08/−0.09
Swartpuntia / Ernietta	315	538.93 +0.20/−0.16
Parapsammichnites / Treptichnus isp.	386	539.18 +0.17/−0.26
Base of Spitskop Member	438.5	539.36 +0.19/−0.19
Base of Feldschuhhorn Member	456.5	539.38 +0.19/−0.19
Namacalathus	708	539.63 +0.14/−0.14
Base of Huns Member	821	539.78 +0.63/−0.22
Base of Nasep Member	880	542.70 +0.48/−0.16
Base of Schwarzrand Subgroup	1116	546.72 +0.34/−0.71

6.4.3. Carbon and oxygen isotope chemostratigraphy

Carbon isotope ($\delta^{13}C$) values of carbonates of the Mooifontein Member are scattered between ~ -1‰ and ~ +3‰. Within the Huns Member the $\delta^{13}C$ values are ~ +2‰, decreasing to ~ +1‰ near the top and staying at ~ +1‰ throughout the Spitskop Member and lower Nomtsas Formation (Fig. 6.3). Throughout much of the section, there is significant scatter, and the more negative values (>-4‰) are associated with more siliciclastic-rich intervals (silty to sandy limestone or proximity to siltstone and sandstone), but these individual data points do not form consistent trends and are lithology dependent (Fig. 6.3), and therefore may be the result of very localized and stratigraphically confined organic carbon remineralization rather than reflecting any basin-wide negative $\delta^{13}C$ excursion. The few samples with negative $\delta^{13}C$ values have relatively enriched or

depleted $\delta^{18}O$ values, which is also consistent with localized diagenetic influence, while the majority of samples show no consistent trends among $\delta^{13}C$ and $\delta^{18}O$ values (Fig. 6.4).

6.4.4. Biostratigraphy

In the Nama Group outcrops of the Neint Nababeep Plateau, calcified fossils of *Cloudina* and *Namacalathus* occur in the lower limestone of the Mooifontein Member and the lower Huns Member (Fig. 6.7A,B; Gresse et al., 2006; Almond, 2009). Calcified tubular fossils also occur in the Spitskop Member and in the basal Nomtsas Formation, which are likely cloudinids as well, but are mostly preserved as recrystallized tubes without readily identifiable cone-in-cone structure (Fig. 6.7C–F). However, some of the tubular fossils in this interval are replaced by iron oxide and preserve characteristic cone-in-cone structure (Fig. 6.7D,F), and therefore are identified as *Cloudina*.

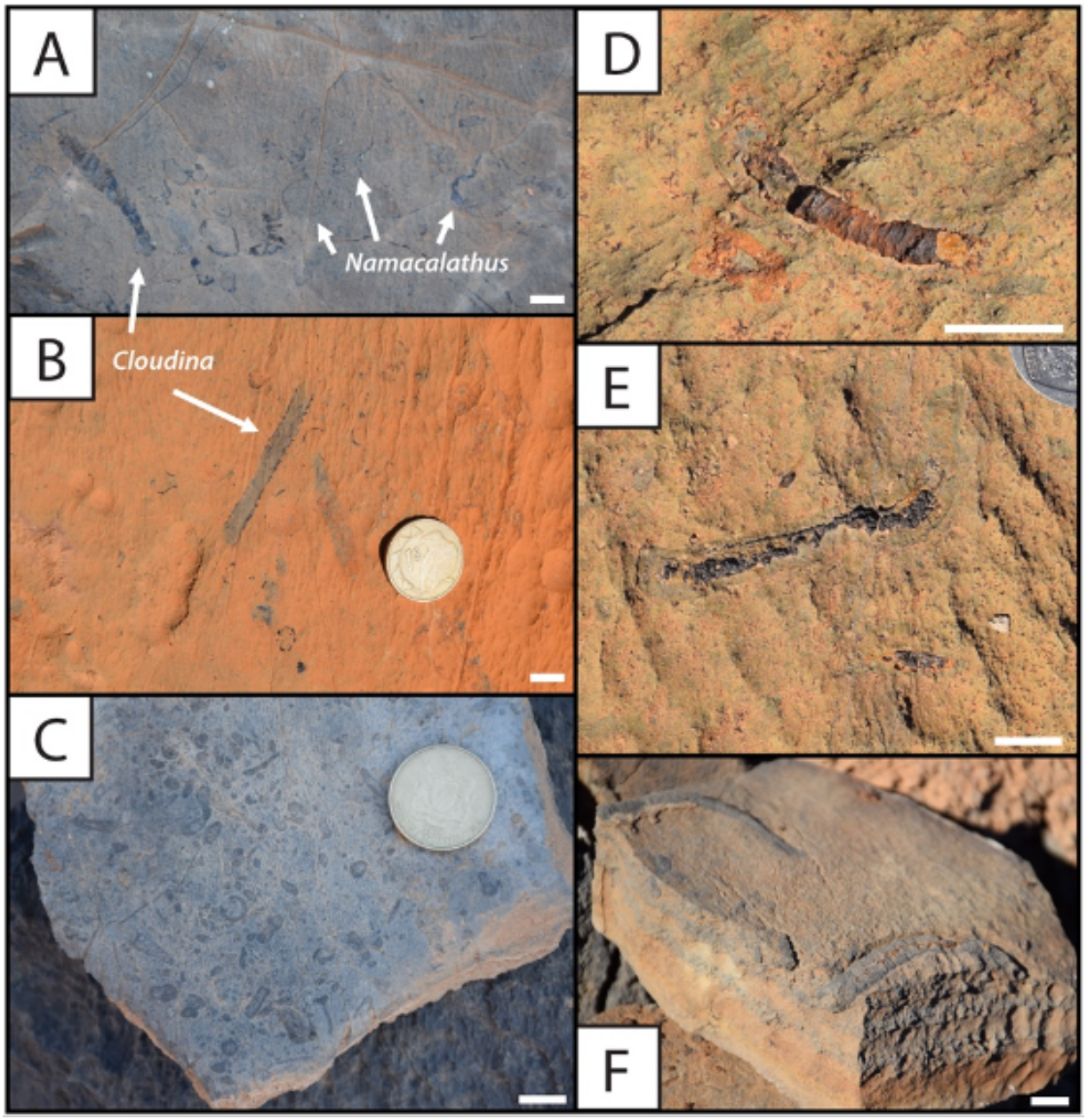

Figure 6.7. Calcified body fossils from the Neint Nababeep Plateau. A, B) *Cloudina* and *Namacalathus* in the Mooifontein Member. C) Shell hash in limestone wackestone in the lower Spitskop Member with circular cross sections of broken cloudinid fossils. D–F) Cloudinid fossils in the basal Nomtsas Formation that are selectively replaced by iron oxides (likely oxidized pyrite). Specimens in (D) and (F) show characteristic cone-in-cone structure of cloudinomorphs. Scale bars are 1 cm.

Body fossils of erniettomorphs, including *Swartpuntia germsi* and probable *Ernietta plateauensis*, are preserved in sandstone beds within the lower Spitskop Member (Fig. 6.8A,B) and are the first soft-bodied Ediacaran fossils to be reported in the Republic of South Africa. Erniettomorphs occur in approximately correlative strata of the Spitskop Member at Farm Swartpunt (Witputs subbasin) in Namibia (e.g., Grotzinger et al., 1995; Narbonne et al., 1997). An additional partial erniettomorph body fossil resembling *Ernietta* was found in the lower Nomtsas Formation, above the 538.568±0.093 Ma and below the 538.04±0.14 Ma ash beds, but is not definitively identifiable (Fig. 6.8C). Ribbon-like, filamentous compressional body fossils are preserved on bedding planes within siltstone to fine sandstone of the lower Nudaus Formation, as well as within the lower Huns Member (Fig. 6.9; Almond, 2009). These are morphologically similar to tubular fossils within the lower Nudaus Formation of the Witputs subbasin in Namibia described by Cohen et al. (2009), and we tentatively assign them to *Vendotaenia*, although this identification will require reassessment as the taxonomic framework for Ediacaran tubular fossils improves. These filamentous fossils are associated with scratch circles (Jensen et al., 2018), and so they may have been tethered organisms. Poorly preserved casts and molds of annulated or ribbed tubular body fossils that are <1 cm in diameter occur in siliciclastic intervals of the lower Spitskop Member, but do not preserve the morphological detail for confident identification.

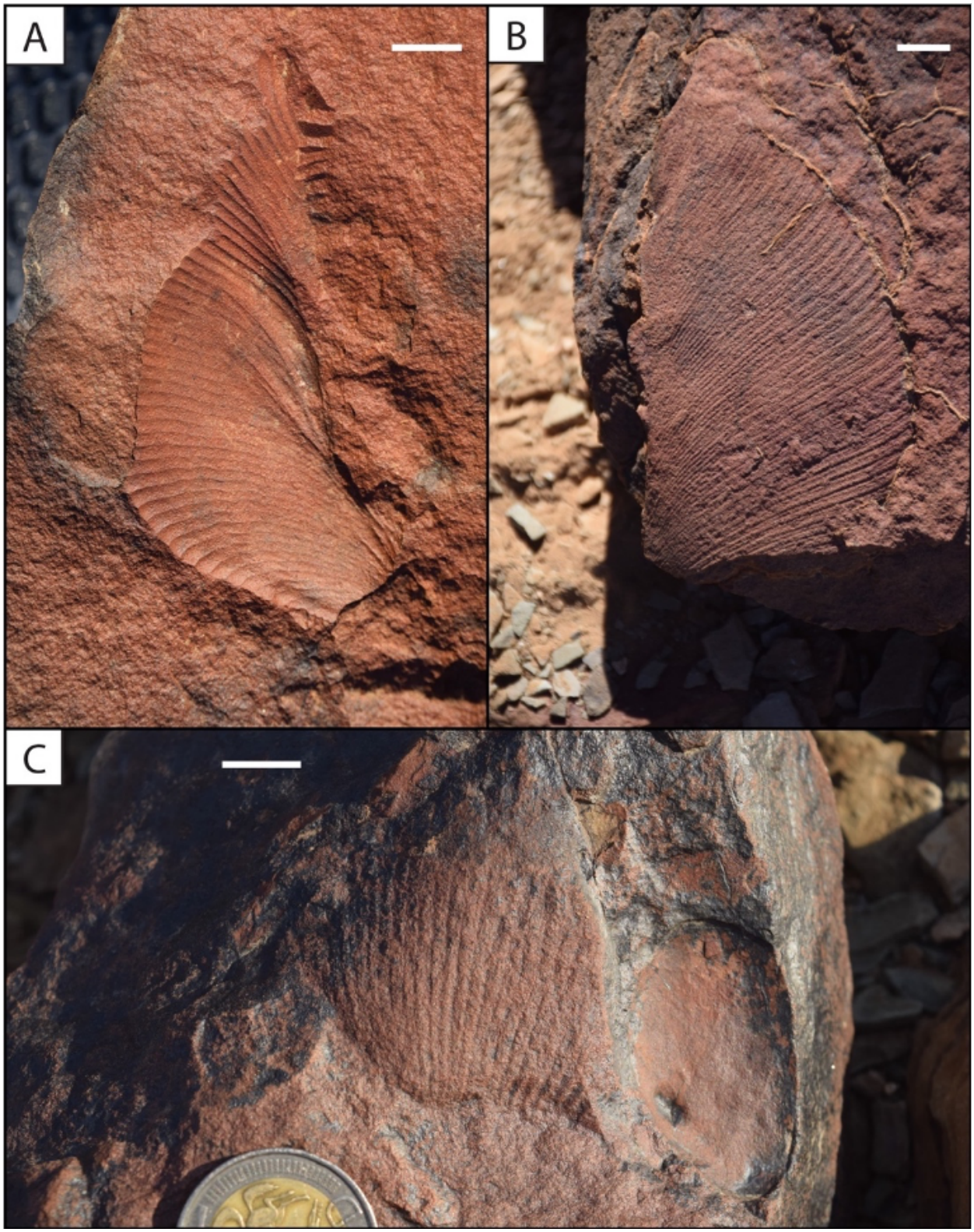

Figure 6.8. Erniettomorph body fossils from the Neint Nababeep Plateau. A) Probable *Ernietta plateauensis* in the lower Spitskop Member. B) *Swartpuntia germsi* in the lower Spitskop Member. C) Indeterminate erniettomorph in the Nomtsas Formation. Scale bars are 1 cm.

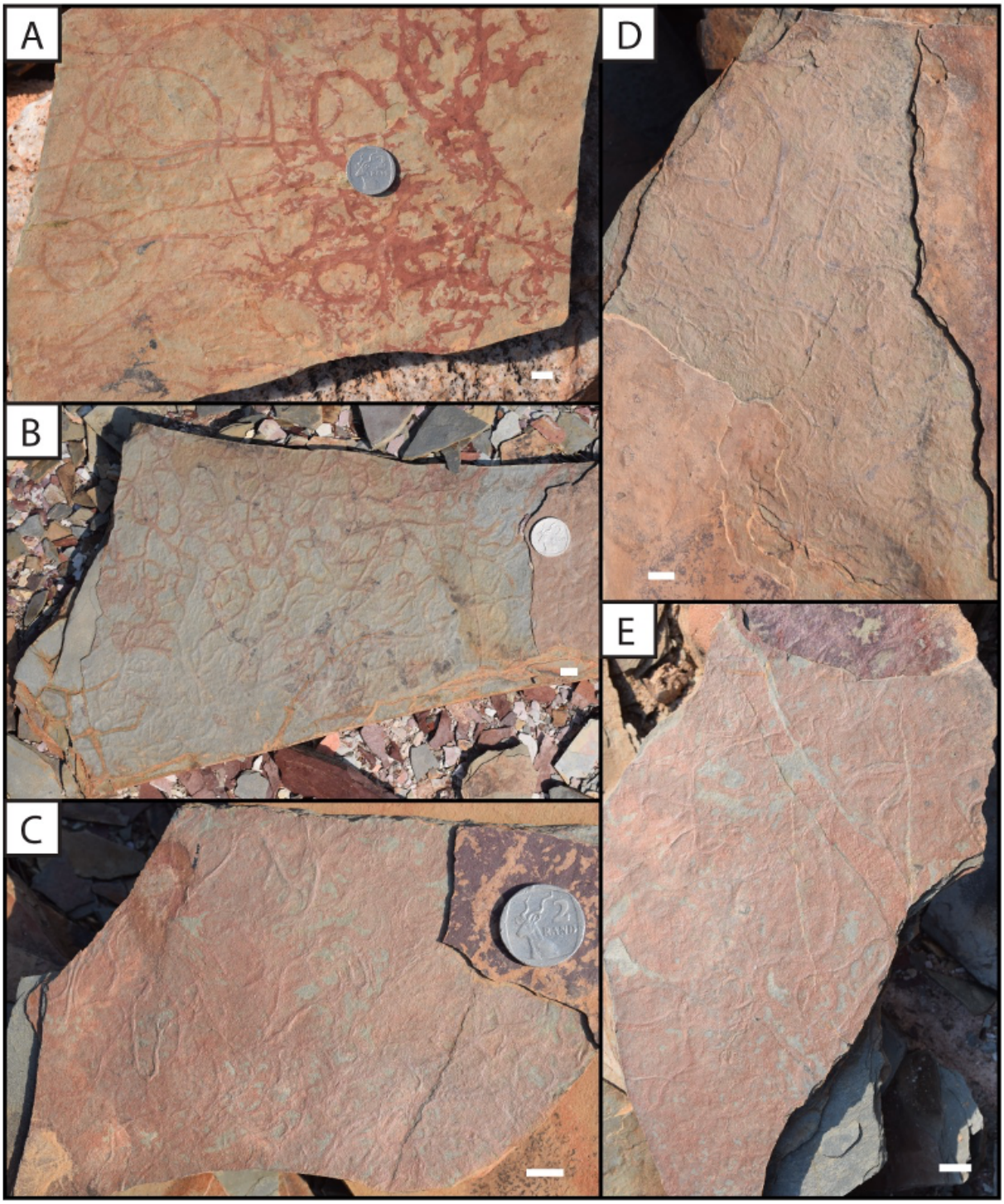

Figure 6.9. Compression fossils of *Vendotaenia* in the Nudaus Formation from the Neint Nababeep Plateau. Scale bars are 1 cm.

Ichnofossils were identified within several stratigraphic horizons, and identification follows classifications of Darroch et al. (2021). Vertical plug-shaped fossils that are assigned to either *Bergaueria* or *Conichnus* occur in the Niederhagen Member of the Nudaus Formation, the basal Nasep Member, the Feldshuhhorn Member, and siliciclastic intervals of the lower Spitskop Member. Simple bed planar trace fossils, assigned to *Helminthopsis* (on the basis that there is little evidence of overcrossing), occur in the Nasep, lower Huns, Feldshuhhorn, and lower Spitskop members of the Urusis Formation, and in the Nomtsas Formation (see also Gresse et al., 2006; Almond, 2009). In the lower Nomtsas Formation, densely spaced and overlapping bed-planar burrows are particularly large with widths >1 cm and lengths >10 cm (Fig. 6.10L,M); the lack of branching and structureless infill in these trace fossils allow tentative identification as *Palaeophycus*. More complex horizontal burrows that demonstrate bulldozing and active backfilling behavior are identified as *Parapsammichnites pretziliformis* (Buatois et al., 2018) and occur in the lower Spitskop Member in high abundance within a <5 m interval at the top of the second major siliciclastic interval (Fig. 6.10A–F). Dense, cross-cutting meshworks of horizontal to oblique burrows in these same slabs possessing irregularly-spaced constrictions may be attributable to *Torrowangea* (Fig. 6.10A). *Archaeonassa*, a sinuous horizontal trail with a wide central furrow and lateral ridges, occurs within this same interval (Fig. 6.10H). Larger, bilobed and unbranched trace fossils with pronounced medial grooves also occur within the Nomtsas Formation (Fig. 6.10J–K); however, the higher relief and the possible presence of poorly-preserved arcuate backfill (see Fig. 6.10K) instead suggest that these may represent *Psammichnites*. Recent work (e.g., MacNaughton et al., 2021) suggests that *Psammichnites* may be a useful biostratigraphic marker for the early Cambrian, however, we note that in the Neint-Nabeeb Plateau this ichnotaxon apparently predates the first appearance of *Treptichnus pedum* (see Section 5.1).

One trace fossil specimen recovered from the lower Spitskop Member exhibits strings of almond-shaped probes (strongly resembling those described by Darroch et al. (2021) from the base of the Spitskop Member in Namibia; their Fig. 13F–G), which likely represent discontinuous horizontal to vertical branching off of a single concealed master burrow (Fig. 6.10G). Given that these burrows lack the diagnostic features of *Treptichnus* while representing a broadly similar (albeit less complex) behavior, these are best identified as treptichnids (see e.g., Jensen et al., 2000). Finally, one enigmatic fossil found in the Feldshuhhorn Member possesses a helical, corkscrew-type structure (Fig. 6.10I) and thus resembles an isolated probe belonging to the latest Ediacaran trace fossil *Streptichnus narboneii* (Jensen and Runnegar, 2005). However, given that the fossil exhibits sinistral twisting (rather than dextral, which is more typical of *Streptichnus*), the lack of any other associated burrows radiating from a single entryway, and the observation that both the tightness and angle of coiling appear to change along the length of the structure, we instead tentatively assign this fossil to *Harlaniella*, which is a problematic body fossil best known from late Ediacaran sections in Russia and Ukraine (Ivantsov, 2013).

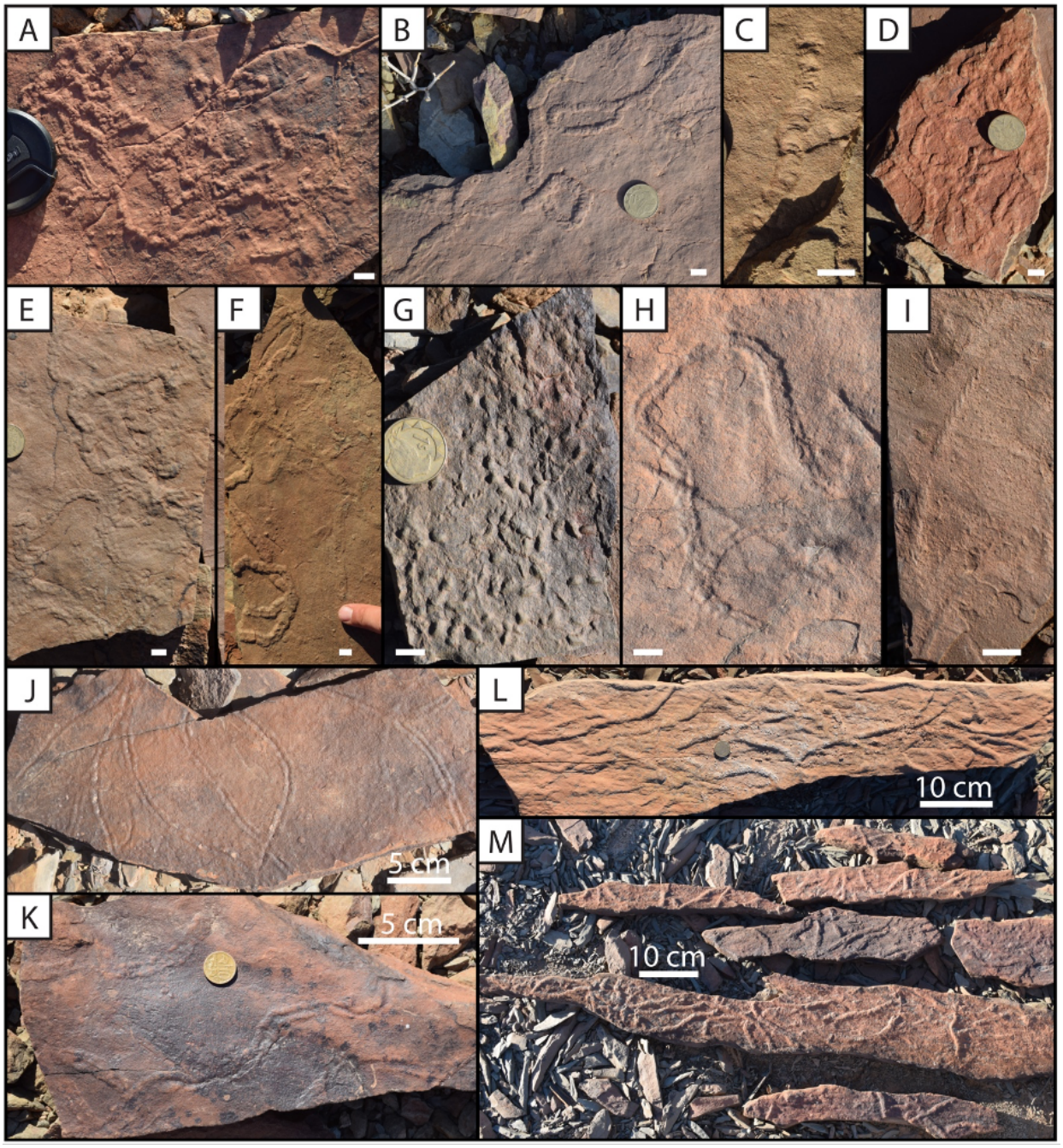

Figure 6.10. Trace fossils in the lower Spitskop Member and lower Nomtsas Formation from the Neint Nababeep Plateau. Scale bars are 1 cm unless otherwise noted. A–F) *Parapsammichnites pretziliformis* in the lower Spitskop Member exhibiting characteristic overcrossing behavior, and arcuate active backfill. Irregular meshwork of horizontal burrows in the center of A exhibiting irregular constrictions is potentially attributable to *Torrowangea*. G) Probable treptichnids in the lower Spitskop Member, preserved as strings and arcs of individual almond-shaped 'probes'. H) *Archaeonassa* in the lower Spitskop Member. I) Unidentified helical structure in the Feldshuhhorn Member potentially attributable to the body fossil *Harlaniella*. J–K) Probable *Psammichnites* in the Nomtsas Formation. L–M) Large, planar, unbranched and crosscutting trace fossils in the Nomtsas Formation with structureless infill, identified as *Palaeophycus*.

6.5. Discussion

6.5.1. Placement of the Ediacaran–Cambrian boundary in the Nama Group

For decades, the Nama Group of Namibia has been recognized as a critical record of the Ediacaran–Cambrian boundary, and the ash bed ages from the Spitskop Member and Nomtsas Formation at Farm Swartpunt (Grotzinger et al., 1995; Linnemann et al., 2019) have been used for the calibration of the Geologic Time Scale (Peng et al., 2020). The consensus view has been that the base of the incised valleys of the basal Nomtsas Formation is the stratigraphic position of the Ediacaran–Cambrian boundary in Namibia (e.g., Germs, 1972,1983; Grotzinger et al., 1995; Saylor et al., 1995). This notion is influenced by incomplete and discontinuous exposures of the lithostratigraphic boundary, as well as documentation of *Treptichnus pedum* (or *Phycodes pedum* based on previous nomenclature) in units identified as the Nomtsas Formation at Farm Swartkloofberg by Germs (1972) and at Farm Sonntagsbrunn (Grotzinger et al., 1995; Wilson et al., 2012). However, the specimens identified as "closely related to or identical with *Phycodes pedum*" at Swartkloofberg by Germs (1972) (their Plate 2, Fig. 5) lack clear systematic branching patterns of straight to slightly curved segments diagnostic of *Treptichnus pedum* (Seilacher, 2007). There has been no subsequent documentation of this fossil from the Nomtsas Formation at Swartkloofberg (e.g., Saylor and Grotzinger, 1996). *Treptichnus pedum* has, however, been extensively documented from the Nomtsas Formation at Farm Sonntagsbrunn by Wilson et al. (2012). These specimens are in a unit they identify as 'Valley Fill 2', which they interpret as lower shoreface facies that occur within an incised valley and below a capping sheet deposit of upper shoreface sandstone. Above the Nomtsas Formation, within the Fish River Subgroup, *Treptichnus pedum* has been well documented within the Rosenhof Member of the Gross Aub Formation (e.g., Germs, 1972; Crimes and Germs, 1982; Geyer and Uchman, 1995; Geyer, 2005). Beyond the

ichnofossil record, the placement of the Ediacaran–Cambrian boundary at the base of the Nomtsas valley incision has been justified based on the last occurrences of Ediacaran-type fossils in the underlying Spitskop Member, and by the absence of the BACE in the upper Nama Group, which has been attributed to the hiatus at the unconformity (e.g., Grotzinger et al., 1995).

This study demonstrates that the Nomtsas Formation on the Neint Nababeep Plateau is associated with marine transgression rather than valley incision, and at this locality there is no demonstrable unconformity at the contact between the Spitskop Member and the Nomtsas Formation. Instead, there is continuous deposition, transitioning from carbonate shelf environment to a deeper marine environment dominated by siliciclastic sedimentation. This is supported by a number of lines of evidence including: 1) development of large pinnacle microbial reefs at this contact; 2) the absence of any paleo-relief or evidence of incision; 3) the presence of mass transport deposits and turbidites along with the absence of sedimentary structures indicative of traction currents in the Nomtsas Formation; and 4) the high-resolution U-Pb geochronology that demonstrates no resolvable hiatus. While valley incision clearly occurs at the base of the Nomtsas Formation at both Farm Swartkloofberg and in the 'Valley Fill 1' unit at Farm Sonntagsbrunn, in both cases, valley fill sediments were deposited below wave base and are dominated by suspension sedimentation of mud and silt accompanied by gravity-driven flows of sand and carbonate-clast conglomerate and diamictite (Saylor and Grotzinger, 1996; Wilson et al., 2012). Thus, it is reasonable that these were localized submarine channels formed by mass wasting during margin flexure and marine transgression (Saylor and Grotzinger, 1996; Wilson et al., 2012), rather than by a fluvial system related to a regional unconformity. This is consistent with our interpretations of the Neint Nababeep Plateau, as well as recent geochronology at Swartpunt and Swartkloofberg (Linnemann et al., 2019).

Since no definitive specimens of *Treptichnus pedum* have been found in the Nomtsas Formation at Swartkloofberg or the Neint Nababeep Plateau, it may be argued that the biostratigraphically defined Ediacaran–Cambrian boundary occurs still higher in the section, younger than 537.87+0.18/−0.21 Ma. While there are clear occurrences of *Treptichnus pedum* within the 'Valley Fill 2' unit at Farm Sonntagsbrunn, given the stratigraphic interpretation of the Nomtsas as part of a transgressive systems tract, it is possible that the shoreface 'Valley Fill 2' and 'Upper Nomtsas Member' units of Wilson et al. (2012) are not directly correlative to the dated Nomtsas Formation at Farm Swartkloofberg or the Neint Nababeep Plateau, and instead are younger than 537.9 Ma, and genetically related to the orogenic molasse of the Fish River Subgroup. This interpretation is further supported by the presence of a probable erniettomorph in the sandstones of the Nomtsas Formation and *Cloudina* in the limestones of the basal Nomtsas Formation at the Neint Nababeep Plateau, which indicate these Ediacaran-type fossils continue into the Nomtsas Formation. On the other hand, it has been documented that cloudinids may overlap in their stratigraphic range with the earliest Cambrian fossil assemblages (e.g., small shelly fossil zone I) without a sharp biotic turnover (Yang et al., 2016; Zhu et al., 2017). Globally, outside of the Nama Group, the first appearance datum of *Treptichnus pedum* is not well constrained by radioisotopic age constraints, and a biostratigraphically defined boundary younger than 537.9 Ma is compatible with current data. Alternatively, since the first appearance of *Treptichnus pedum* was originally chosen to mark the base of the Cambrian Period in an attempt to place the boundary close to the earliest occurrence of the first unquestionable bilaterian fossil, perhaps the boundary should be placed much lower in the Nama Group where other complex, bilaterian ichnofossils occur, as suggested by Geyer (2005). If the occurrence of *Parapsammichnites pretziliformis* in the lower Spitskop Member, or the stratigraphically lower occurrence of *Treptichnus* isp. in the lower

Huns of the Witputs subbasin (Jensen et al., 2000), is taken as such earliest occurrence, then the interval between 539.18+0.17/−0.26 Ma and 538.30+0.14/−0.14 Ma—the last occurrence of an erniettomorph—may be hypothesized as an Ediacaran–Cambrian 'transition interval'. Overall, the age-calibrated fossil assemblages of the upper Nama Group at the Neint Nababeep Plateau further underscore the difficulties in arriving at a unified, global, biostratigraphic definition of the Ediacaran–Cambrian boundary.

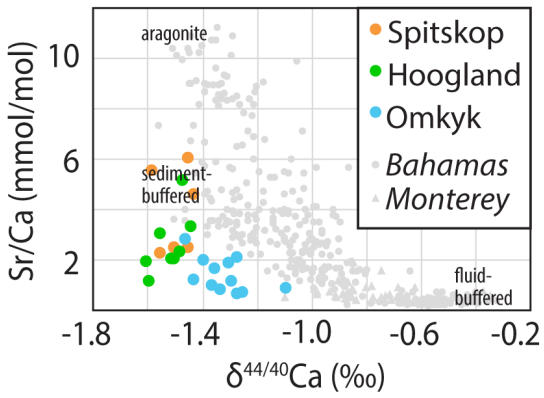

Figure 6.11. Cross plot compares published Sr/Ca and $\delta^{44/40}$Ca data from the Omkyk, Hoogland, and Spitskop members; data from Tostevin et al. (2019*a*) and Wood et al. (2015). Geochemical data from Miocene–Holocene carbonates from the Bahamas and authigenic dolomite from the Neogene Monterey Formation plotted for comparison (Blättler et al., 2015; Ahm et al., 2018; Higgins et al., 2018)

Figure 6.12. Composite geochronology and chemostratigraphy of the Nama Group. A) Witputs and Zaris subbasin stratigraphy adapted from Saylor et al. (1995) and Grotzinger et al. (1995). Volcanic ash bed dates are weighted mean ^{206}Pb/^{238}U dates with internal 2σ uncertainties; *date from Bowring et al., 2007; **date from Linnemann et al., 2019; other geochronology data are from this paper. δ^{13}C data from Zaris subbasin from Wood et al. (2015); $\delta^{44/40}$Ca data from Tostevin et al. (2019*a*); δ^{238}U data from Tostevin et al. (2019*b*); δ^{13}C data from Witputs subbasin from Saylor et al. (1998), Ries et al. (2009), and Wood et al. (2015); δ^{13}C data from Neint Nababeep Plateau from this study. The Bchron Bayesian age-depth model is presented with its median (black line) and its 95% confidence interval (grey area). Modeled sedimentation rate does not account for delithification. Mb—Member; Fm—Formation; D—Dabis Formation; S—Subgroup; Ka—Kanies; Ma—Mara; Kl—Kliphoek; M—Mooifontein; Fe/F—Feldshuhhorn; Na—Nasep; MDA—Maximum Depositional Age. [Next page]

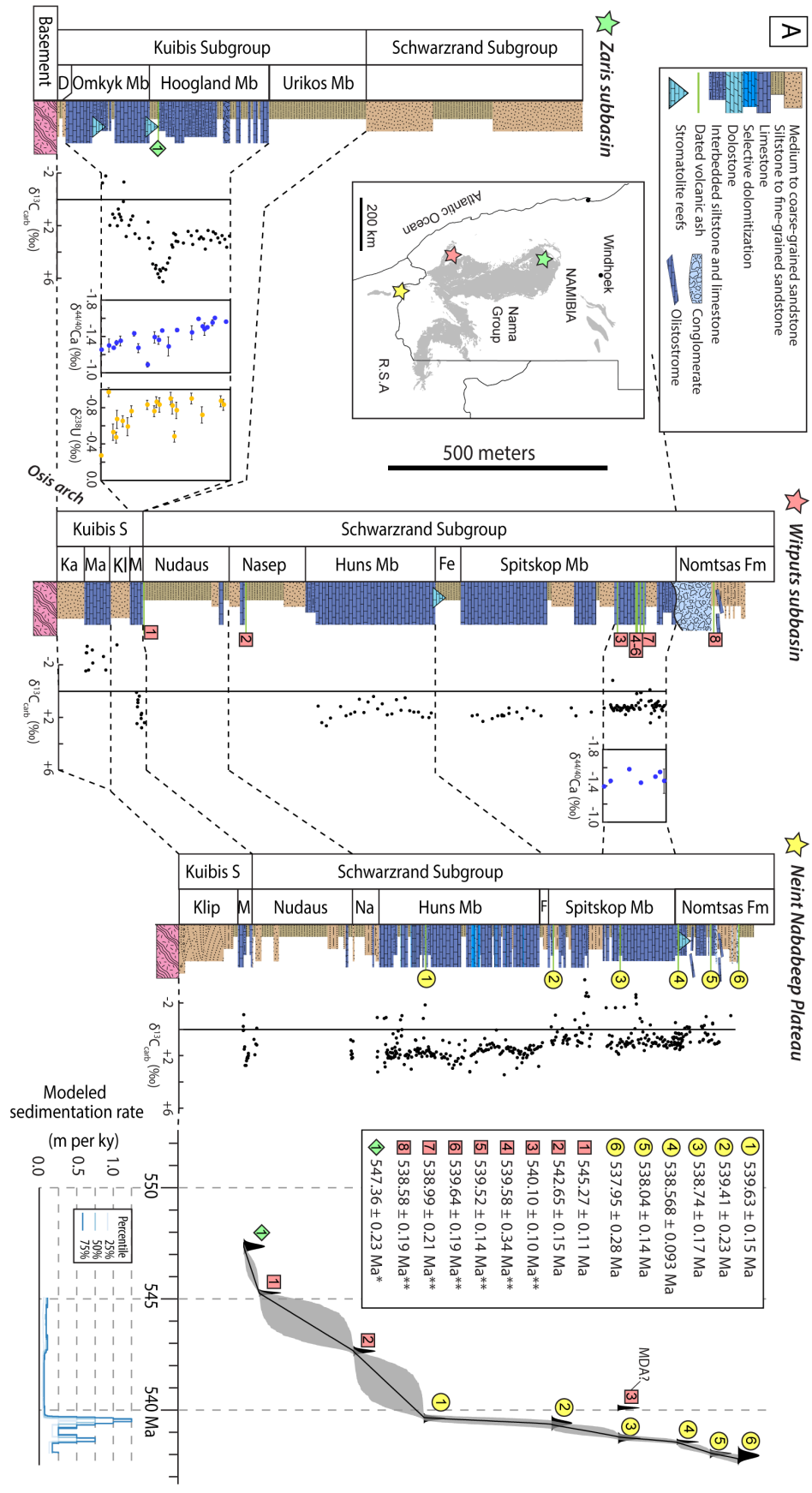
A
Medium to coarse-grained sandstone
Siltstone to fine-grained sandstone
Limestone
Selective dolomitization
Dolostone
Interbedded siltstone and limestone
Dated volcanic ash
Conglomerate
Stromatolite reefs
Olistostrome
Zaris subbasin
Basement
Kuibis Subgroup
Schwarzrand Subgroup
D
Omkyk Mb
Hoogland Mb
Urikos Mb
Atlantic Ocean
200 km
Windhoek
NAMIBIA
Nama Group
R.S.A
500 meters
Osis arch
Witputs subbasin
Kuibis S
Schwarzrand Subgroup
Ka
Ma
Kl
M
Nudaus
Nasep
Huns Mb
Fe
Spitskop Mb
Nomtsas Fm
Neint Nababeep Plateau
Kuibis S
Schwarzrand Subgroup
Klip
M
Nudaus
Na
Huns Mb
F
Spitskop Mb
Nomtsas Fm
Modeled sedimentation rate
(m per ky)
0.0
0.5
1.0
Percentile
25%
50%
75%
550
545
540 Ma
MDA?
① 539.63 ± 0.15 Ma
② 539.41 ± 0.23 Ma
③ 538.74 ± 0.17 Ma
④ 538.568 ± 0.093 Ma
⑤ 538.04 ± 0.14 Ma
⑥ 537.95 ± 0.28 Ma
1 545.27 ± 0.11 Ma
2 542.65 ± 0.15 Ma
3 540.10 ± 0.10 Ma**
4 539.58 ± 0.34 Ma**
5 539.52 ± 0.14 Ma**
6 539.64 ± 0.19 Ma**
7 538.99 ± 0.21 Ma**
8 538.58 ± 0.19 Ma**
◇ 547.36 ± 0.23 Ma*

6.5.2. Chemostratigraphy of the Nama Group

At a number of localities globally, a large negative carbon isotope excursion, the BACE, has been shown to immediately predate the first appearance of *Treptichnus pedum* and/or postdate the last occurrence of Ediacaran-type fossils (e.g., Narbonne et al., 1994; Brasier et al., 1996; Zhang et al., 1997; Corsetti and Hagadorn, 2000; Smith et al., 2016). Therefore, the BACE is thought to mark the Ediacaran–Cambrian boundary and has been linked to environmental perturbation and, possibly, extinction (e.g., Amthor et al., 2003; Smith et al., 2016; Darroch et al, 2018; Hodgin et al., 2021), even though its absolute age has not been independently well constrained. While a negative carbon isotope excursion occurs in carbonates of the basal Kuibis Subgroup (e.g., Saylor et al., 1998; Wood et al., 2015), there is no negative carbon isotope excursion preserved within ~780 m of carbonate deposits of the upper Schwarzrand Subgroup that spans 1.74 m.y. from c. 539.8 to 538.0 Ma, despite a high average sedimentation rate of ~44 cm/kyr (apparently higher in carbonate-dominated intervals) and no clear hiatuses (Fig. 6.3).

Two possible explanations for the absence of the BACE in the upper Nama Group are: 1) this excursion is younger than carbonates of the Schwarzrand Subgroup, or, 2) Schwarzrand Subgroup carbonates record the composition of local platform water or porewater dissolved inorganic carbon that is not representative of the composition of seawater. The simplest explanation is that the BACE is younger than 538.04±0.14 Ma—the age of the ash bed at the top of the lower Nomtsas Formation that marks the end of carbonate sedimentation in the Nama Group. This is consistent with a younger age for the Ediacaran–Cambrian boundary than currently recognized, which, as suggested in Section 5.1., is also consistent with the absence of *Treptichnus pedum* in these units. Such an interpretation would imply that the 539.40±0.23 Ma U-Pb CA-ID-TIMS date from the horizon in the La Ciénega Formation of Sonora, Mexico just above the nadir

of the BACE should be considered a maximum, rather than syn-, depositional age (Hodgin et al., 2021), that is >1 m.y. older than deposition of this unit. This would also imply that either the ash bed with the U-Pb CA-ID-TIMS date of 541.00±0.13 Ma from the Ara Group of Oman (Bowring et al., 2007) is >3 m.y. older than the negative carbon isotope excursion just above it preserved in the A4 carbonate stringer, or that this is an older excursion, distinct from the BACE. This could be comparable to the recent interpretation of two stratigraphically discrete carbon isotope excursions in the Ediacaran successions of South China that were previously attributed to the single Shuram excursion (Yang et al., 2021).

If the BACE is in fact older than 538.04±0.14 Ma, as suggested by the dates from the La Ciénega Formation and/or the Ara Group, and contemporaneous with the deposition of the upper Nama Group, then a second possible explanation for the absence of a negative $\delta^{13}C$ excursion in the Huns or Spitskop members is that some or all of these carbonate rocks do not faithfully record secular changes in the $\delta^{13}C$ composition of coeval seawater. When unlithified carbonate sediment is transformed to limestone through neomorphism and diagenesis, this diagenetic system can range from fluid-buffered, whereby the compositions of diagenetic mineral phases resemble the diagenetic fluid, to sediment-buffered, whereby the compositions of the diagenetic mineral phases resemble the primary carbonate sediment (Higgins et al., 2018). A sediment-buffered diagenetic regime for the upper Nama Group is consistent with existing Ca isotope ($\delta^{44/40}Ca$) and Sr concentration data for the Spitskop Member (Figs. 6.11, 6.12; Tostevin et al., 2019*a*), because sediment-buffered limestone preserves high Sr/Ca and low $\delta^{44/40}Ca$ of primary aragonite (Higgins et al., 2018). This mode of diagenetic influence, in which sediment pore fluids were more isolated from seawater, may have resulted from the extremely high sediment accumulation rates (~40 to 120 cm/kyr; Fig. 6.3)—for comparison, sediment accumulation rates for carbonates of the

Ediacaran Ara Group of Oman are estimated at only 4 to 9 cm/kyr (Bowring et al., 2007). Sediment-buffered diagenesis would have promoted the preservation of primary sediment $\delta^{13}C$ signatures during neomorphism and lithification (Higgins et al., 2018). Therefore, if the $\delta^{13}C$ values of the Schwarzrand Subgroup are decoupled from primary marine values, these are unlikely to have resulted from diagenesis, but instead may have responded to local controls on the composition of dissolved inorganic carbon within restricted platform top waters or platform pore fluids, such as primary productivity and microbial metabolic effects (e.g., Geyman and Maloof, 2019; Nelson et al., 2021). Such an interpretation remains speculative, and, hence the bulk of evidence presently suggest that the BACE postdated deposition of carbonates of the Nama Group.

A decrease in $\delta^{44/40}Ca$ values from the lower carbonate units of the Nama Group (Omkyk Member of the Kuibis Subgroup) to the upper carbonate units of the Nama Group (Spitskop Member of the Schwarzrand Subgroup) was previously interpreted as representing a global change in the marine Ca isotope composition, potentially related to increased evaporate deposition or increased global weathering (Tostevin et al., 2019*a*). The Bayesian age-depth model for the Nama Group presented herein establishes a significant increase in sediment accumulation rate from the Kuibis Subgroup to the upper Schwarzrand Subgroup (Fig. 6.12), which is consistent with typical subsidence of foreland basins that is classically thought to accelerate with time (e.g., DeCelles and Giles, 1996). Therefore, we suggest the decrease in $\delta^{44/40}Ca$ values and corresponding increase in Sr/Ca values resulted from a change in diagenetic regime from fluid-buffered to sediment-buffered marine diagenesis due to the increase in sedimentation rate, rather than any global change (Figs. 6.11, 6.12). A decrease in $\delta^{238/235}U$ values from carbonates of the Omkyk Member to the overlying Hoogland Member of the Zaris subbasin has been documented and interpreted as a global expansion of anoxia (Tostevin et al., 2019*b*). Similar to the change in $\delta^{44/40}Ca$ values, this decrease

may instead have been caused by a change in diagenetic regime, driven by the acceleration of sediment accumulation within the Nama basin (Fig. 6.12). This is because $\delta^{238/235}U$ values higher than seawater can be produced by pore water reduction of uranium in fluid-buffered diagenetic regimes with a plentiful uranium supply from seawater (Chen et al., 2018), while sediment-buffered carbonate minerals are more likely to preserve primary seawater $\delta^{238/235}U$ values (Chen et al., 2018; Tostevin et al., 2019*b*). As Tostevin et al. (2019*b*) recognize, the higher $\delta^{238/235}U$ values correspond to the highest $\delta^{44/40}Ca$ values within the lower Omkyk Member, consistent with this process (Fig. 6.12). Therefore, these higher $\delta^{238/235}U$ values were caused by seawater-buffered diagenesis, while the lower $\delta^{238/235}U$ values of the upper Omkyk and Hoogland members are the more faithful record of late Ediacaran marine oxygen levels, consistent with globally widespread seafloor anoxia (Tostevin et al., 2019*a*).

6.6. Conclusions

The base of the Cambrian was one of the first recognized stratigraphic boundaries (originally thought to mark the end of an 'azoic' Precambrian epoch) and marks a particularly significant juncture in Earth history with the start of the Phanerozoic Eon. Nevertheless, the Ediacaran–Cambrian boundary remains a poorly understood geological transition, in terms of the tempo and relationships among environmental, evolutionary, and ecological change. This is largely because radioisotope geochronologic data for this interval remain scarce and correlating stratigraphic sections among, and even within, paleo-continents remains challenging.

New ash bed U-Pb CA-ID-TIMS geochronology from the Nama Group of the Neint Nababeep Plateau in the Republic of South Africa and the Witputs subbasin in Namibia allow for construction of, to date, the highest resolution age-stratigraphic model for global strata spanning

c. 548 to 538 Ma. Limestones of the upper Schwarzrand Subgroup were deposited with relatively continuous and high rates of sedimentation from 539.78+0.63/−0.22 Ma to 538.04+0.14/−0.12 Ma, but do not preserve a negative $\delta^{13}C$ excursion that can be correlated to the BACE. This could be because of local controls on the dissolved inorganic carbon composition of surface waters and/or porewaters of this carbonate platform, or because the BACE is younger than currently recognized and occurred after 538.04+0.14/-0.12 Ma. Ediacaran-type fossils including erniettomorphs and cloudinomorphs occur in the Nomtsas Formation, after 538.56+0.08/-0.09 Ma, stratigraphically overlapping with relatively complex bilaterian trace fossils, such as *Parapsammichnites*, *Archaeonassa*, *Psammichnites*, and treptichnids. However, we cannot discount at this time the possibility that the first occurrence of the index fossil *Treptichnus pedum* and thus the biostratigraphically defined Ediacaran–Cambrian boundary could postdate 537.9 Ma, condensing the duration of the early Cambrian. When placed in a global stratigraphic context, our results reveal the challenges of a purely biostratigraphic definition of the Ediacaran–Cambrian boundary and highlight the necessity of an integrated approach (chemostratigraphy, biostratigraphy, and radioisotopic geochronology) in reconstructing the tempo and patterns of evolution across this key interval of Earth history. The new age-stratigraphic model for the Nama Group provides a foundation for further temporal calibration of the terminal Ediacaran biostratigraphic and geochemical records.

6.7. Acknowledgements

This project was funded by the National Science Foundation (NSF) grant EAR-1827715 to EFS and JR. LLN was supported by NSF Graduate Research Fellowship DGE-1746891 and the American Philosophical Society Lewis and Clark Fund for Exploration and Field Research. We

thank the Johns Hopkins University (JHU) Department of Earth and Planetary Sciences for additional financial and logistical support. We thank the South African Heritage Resources Agency and the Geological Survey of Namibia for research and collection permits. We thank H. Mocke for permitting support. I. Bennett and R. Frazer are acknowledged for assistance in processing and analyzing samples in the MIT Isotope Lab, and A. Lindsay-Kaufman, L. Webb, and J. Thompson for assistance in processing and analyzing samples in the stable isotope laboratory at JHU. We are grateful to F. Macdonald and D. Schrag for supporting stable isotope analyses at Harvard University. R. Nel is acknowledged for field assistance. We are extremely grateful to R. Swart for logistical support, hospitality, and countless discussions about the geology of southern Africa. We are thankful to J. Grotzinger for discussions about the Nama Group and for leading a field trip to the Zaris subbasin in Namibia, and to K.-H. Hoffmann for discussions and logistical support. EFS and LLN thank P. Hoffman for generously loaning us his bakkie in 2016 to commence this study. We thank P. Hoffman and D. Erwin for comments on an earlier draft, two anonymous reviewers for critical feedback that improved this manuscript, and B. Wing for editorial assistance.

6.8. References

Ahm, A. C., Bjerrum, C. J., Blättler, C. L., Swart, P. K., and Higgins, J. A., 2018, Quantifying early marine diagenesis in shallow-water carbonate sediments: Geochimica et Cosmochimica Acta, v. 236, p. 140-159.

Almond, J. E., 2009, Contributions to the palaeontology and stratigraphy of the Alexander Bay sheet area (1: 250.000 geological sheet 2816), Unpublished report for the Council for Geoscience: Natura Viva cc, Cape Town, 117 p.

Amthor, J. E., Grotzinger, J. P., Schröder, S., Bowring, S. A., Ramezani, J., Martin, M. W., and Matter, A., 2003, Extinction of Cloudina and Namacalathus at the Precambrian-Cambrian boundary in Oman: Geology, v. 31, no. 5, p. 431-434.

Blanco, G., Germs, G. J. B., Rajesh, H. M., Chemale Jr, F., Dussin, I. A., and Justino, D., 2011, Provenance and paleogeography of the Nama Group (Ediacaran to early Palaeozoic, Namibia): petrography, geochemistry and U–Pb detrital zircon geochronology: Precambrian Research, v. 187, no. 1-2, p. 15-32.

Blättler, C. L., Miller, N. R., and Higgins, J. A., 2015, Mg and Ca isotope signatures of authigenic dolomite in siliceous deep-sea sediments: Earth and Planetary Science Letters, v. 419, p. 32-42.

Bowring, J. F., McLean, N. M., and Bowring, S. A., 2011, Engineering cyber infrastructure for U-Pb geochronology: Tripoli and U-Pb_Redux: Geochemistry Geophysics Geosystems, v. 12.

Bowring, S.A., Grotzinger, J. P., Condon, D. J., Ramezani, J., Newall, M. J., and Allen, P. A., 2007, Geochronologic constraints on the chronostratigraphic framework of the Neoproterozoic Huqf Supergroup, Sultanate of Oman: American Journal of Science, v. 307, no. 10, p. 1097-1145.

Brasier, M., Cowie, J., and Taylor, M., 1994, Decision on the Precambrian-Cambrian boundary stratotype: Episodes Journal of International Geoscience, v. 17, no. 1, p. 3-8.

Brasier, M. D., Shields, G., Kuleshov, V. N., and Zhegallo, E. A., 1996, Integrated chemo- and biostratigraphic calibration of early animal evolution: Neoproterozoic–early Cambrian of southwest Mongolia: Geological Magazine, v. 133, p. 445-485, https://doi.org/10.1017/S0016756800007603.

Buatois, L. A., Almond, J., Mángano, M. G., Jensen, S., and Germs, G. J., 2018, Sediment disturbance by Ediacaran bulldozers and the roots of the Cambrian explosion: Scientific reports, v. 8, no. 1, p. 1-9.

Chen, X., Romaniello, S. J., Herrmann, A. D., Hardisty, D., Gill, B. C., and Anbar, A. D., 2018, Diagenetic effects on uranium isotope fractionation in carbonate sediments from the

Bahamas: Geochimica et Cosmochimica Acta, v. 237, p. 294-311. https://doi.org/10.1016/j.gca. 2018.06.026.

Cohen, P. A., Bradley, A., Knoll, A. H., Grotzinger, J. P., Jensen, S., Abelson, J., Hand, K., Love, G., Metz, J., McLoughlin, N., and Meister, P., 2009, Tubular compression fossils from the Ediacaran Nama group, Namibia: Journal of Paleontology, v. 83, no. 1, p. 110-122.

Condon, D., Zhu, M., Bowring, S., Wang, W., Yang, A., and Jin, Y., 2005, U-Pb ages from the neoproterozoic Doushantuo Formation, China: Science, v. 308, no. 5718, p. 95-98.

Condon, D. J., Schoene, B., McLean, N. M., Bowring, S. A., and Parrish, R. R., 2015, Metrology and traceability of U-Pb isotope dilution geochronology (EARTHTIME Tracer Calibration Part I): Geochimica Et Cosmochimica Acta, v. 164, p. 464-480.

Corsetti, F. A., and Hagadorn, J. W., 2000, Precambrian-Cambrian transition: Death Valley, United States: Geology, v. 28, p. 299-302.

Crimes, T. P., and Germs, G. J., 1982, Trace fossils from the Nama Group (Precambrian-Cambrian) of Southwest Africa (Namibia): Journal of Paleontology, v. 56, no., 4, p. 890-907.

Darroch, S. A., Boag, T. H., Racicot, R. A., Tweedt, S., Mason, S. J., Erwin, D. H., and Laflamme, M., 2016, A mixed Ediacaran-metazoan assemblage from the Zaris Sub-basin, Namibia: Palaeogeography, Palaeoclimatology, Palaeoecology, v. 459, p. 198-208.

Darroch, S. A., Smith, E. F., Laflamme, M., and Erwin, D. H., 2018, Ediacaran extinction and Cambrian explosion: Trends in ecology & evolution, v. 33, no. 9, p. 653-663.

Darroch, S. A., Cribb, A. T., Buatois, L. A., Germs, G. J., Kenchington, C. G., Smith, E. F., Mocke, H., O'Neil, G. R., Schiffbauer, J. D., Maloney, K. M., Racicot, R. A., Turk, K. A., Gibson, B. M., Almond, J., Koester, B., Boag, T. H., Tweedt, S. M., and Laflamme, M., 2021, The trace fossil record of the Nama Group, Namibia: Exploring the terminal Ediacaran roots of the Cambrian explosion: Earth-Science Reviews, v. 212, p. 103435.

DeCelles, P. G., and Giles, K. A., 1996, Foreland basin systems: Basin research, v. 8, no. 2, p. 105-123.

Germs, G. J. B., and Gresse, P. G., 1991, The foreland basin of the Damara and Gariep orogens in Namaqualand and southern Namibia: stratigraphic correlations and basin dynamics: South African Journal of Geology, v. 94, no. 2, p. 159-169.

Germs, G. J. B., 1972, Trace fossils from the Nama Group, South-West Africa: Journal of Paleontology, v. 46, no. 6, p. 864-870.

Germs, G. J. B., 1983, Implications of a sedimentary facies and depositional environmental analysis of the Nama Group in Southwest Africa/Namibia, *in* Miller, R. McG., ed., Evolution of the Damara Orogen: Geological Society of South Africa, Special Publication 11, p. 89-114.

Germs, G. J. B., and Gresse, P. G., 1991, The foreland basin of the Damara and Gariep orogens in Namaqualand and southern Namibia: stratigraphic correlations and basin dynamics: South African Journal of Geology, v. 94, no. 2, p. 159-169.

Germs, G. J. B., Miller, R. McG., Frimmel, H. E., and Gaucher, C., 2009, Syn- to Late-Orogenic Sedimentary Basins of Southwestern Africa, *in* Gaucher, C., Sial, A. N., Halverson, G. P., and Frimmel, H. E., eds., Neoproterozoic-Cambrian Tectonics, global change and evolution: a focus on Southwestern Gondwana: Elsevier.

Geyer, G., 2005, The Fish River Subgroup in Namibia: stratigraphy, depositional environments and the Proterozoic–Cambrian boundary problem revisited: Geological Magazine, v. 142, no. 5, p. 465-498.

Geyer, G., and Uchman, A., 1995, Ichnofossil assemblages from the Nama Group (Neoproterozoic-Lower Cambrian) in Namibia and the Proterozoic-Cambrian boundary problem revisited, *in* Geyer, G., and Landing, E., eds., Morocco '95 – the Lower–Middle Cambrian standard of western Gondwana: Beringeria Special Issue 2, p. 175-202.

Geyman, E. C., and Maloof, A. C., 2019, A diurnal carbon engine explains ^{13}C-enriched carbonates without increasing the global production of oxygen: Proceedings of the National Academy of Sciences, v. 116, no. 49, p. 24433-24439.

Gresse, P. G., and Germs, G. J. B., 1993, The Nama foreland basin: sedimentation, major unconformity bounded sequences and multisided active margin advance: Precambrian Research, v. 63, no. 3-4, p. 247-272.

Gresse, P. G., Veh, M. W. von, and Frimmel, H. E, 2006, Namibian (Neoproterozoic) to Early Cambrian successions, *in* Johnson, M. R., Anhaeusser, C. R., and Thomas, R. J., eds., The Geology of South Africa: Geological Society of South Africa, Johannesburg/Council for Geoscience, Pretoria, p. 395-420.

Grotzinger, J. P., 2000, Facies and paleoenvironmental setting of thrombolite-stromatolite reefs, terminal Proterozoic Nama Group (ca. 550–543 Ma), central and southern Namibia: Communications of the Geological Survey of Namibia, v. 12, p. 221-233.

Grotzinger, J. P., Bowring, S. A., Saylor, B. Z., and Kaufman, A. J., 1995, Biostratigraphic and geochronologic constraints on early animal evolution: Science, v. 270, no. 5236, p. 598-604.

Grotzinger, J., Adams, E. W., and Schröder, S., 2005, Microbial–metazoan reefs of the terminal Proterozoic Nama Group (c. 550–543 Ma), Namibia: Geological Magazine, v. 142, no. 5, p. 499-517.

Haslett, J., and Parnell, A., 2008, A simple monotone process with application to radiocarbon-dated depth chronologies: Journal of the Royal Statistical Society: Series C (Applied Statistics), v. 57, no. 4, p. 399-418.

Hiess, J., Condon, D. J., McLean, N., and Noble, S. R., 2012, $^{238}U/^{235}U$ Systematics in Terrestrial Uranium-Bearing Minerals: Science, v. 335, no. 6076, p. 1610-1614, https://doi.org/10.1126/science.1215507.

Higgins, J. A., Blättler, C. L., Lundstrom, E. A., Santiago-Ramos, D. P., Akhtar, A. A., Ahm, A. C., Bialik, O., Holmden, C., Bradbury, H., Murray, S. T., and Swart, P. K., 2018, Mineralogy, early marine diagenesis, and the chemistry of shallow-water carbonate sediments: Geochimica et Cosmochimica Acta, v. 220, p. 512-534.

Hodgin, E. B., Nelson, L. L., Wall, C. J., Barrón-Díaz, A. J., Webb, L. C., Schmitz, M. D., Fike, D. A., Hagadorn, J. W. and Smith, E. F., 2021, A link between rift-related volcanism and end-Ediacaran extinction? Integrated chemostratigraphy, biostratigraphy, and U-Pb geochronology from Sonora, Mexico: Geology, v. 49, no. 2, p. 115-119.

Ivantsov, A. Y., 2013, New data on Late Vendian problematic fossils from the genus *Harlaniella*: Stratigraphy and Geological Correlation, v. 21, p. 592-600.

Jaffey, A. H., Flynn, K. F., Glendenin, L. E., Bentley, W. C., and Essling, A. M., 1971, Precision Measurement of Half-Lives and Specific Activities of ^{235}U and ^{238}U: Physical Review C, v. 4, no. 5, p. 1889-1906.

Jensen, S., and Runnegar, B. N., 2005, A complex trace fossil from the Spitskop Member (terminal Ediacaran–? Lower Cambrian) of southern Namibia: Geological Magazine, v. 142, no. 5, p. 561-569.

Jensen, S., Saylor, B. Z., Gehling, J. G., and Germs, G. J., 2000, Complex trace fossils from the terminal Proterozoic of Namibia: Geology, v. 28, no. 2, p. 143-146.

Jensen, S., Högström, A. E. S., Almond, J., Taylor, W. L., Meinhold, G., Høyberget, M., Ebbestad, J. O., R., Agić, H., and Palacios, T., 2018, Scratch circles from the Ediacaran and Cambrian of Arctic Norway and southern Africa, with a review of scratch circle occurrences: Bulletin of Geosciences, v. 93, no. 3, p. 287-304.

Krogh, T. E., 1973, Low-Contamination Method for Hydrothermal Decomposition of Zircon and Extraction of U and Pb for Isotopic Age Determinations: Geochimica Et Cosmochimica Acta, v. 37, no. 3, p. 485-494, https://doi.org/10.1016/0016-7037(73)90213-5.

Laflamme, M., Darroch, S. A., Tweedt, S. M., Peterson, K. J., and Erwin, D. H., 2013, The end of the Ediacara biota: Extinction, biotic replacement, or Cheshire Cat?: Gondwana Research, v. 23, no. 2, p. 558-573.

Linnemann, U., Ovtcharova, M., Schaltegger, U., Gärtner, A., Hautmann, M., Geyer, G., Vickers-Rich, P., Rich, T., Plessen, B., Hofmann, M., and Zieger, J., 2019, New high-resolution age data from the Ediacaran–Cambrian boundary indicate rapid, ecologically driven onset of the Cambrian explosion: Terra Nova, v. 31, no. 1, p. 49-58.

Mattinson, J. M., 2005, Zircon U/Pb chemical abrasion (CA-TIMS) method; combined annealing and multi-step partial dissolution analysis for improved precision and accuracy of zircon ages: Chemical Geology, v. 220, no. 1-2, p. 47-66.

McLean, N. M., Bowring, J. F., and Bowring, S. A., 2011, An algorithm for U-Pb isotope dilution data reduction and uncertainty propagation: Geochemistry Geophysics Geosystems, v. 12.

McLean, N. M., Condon, D. J., Schoene, B., and Bowring, S. A., 2015, Evaluating uncertainties in the calibration of isotopic reference materials and multi-element isotopic tracers (EARTHTIME Tracer Calibration Part II): Geochimica Et Cosmochimica Acta, v. 164, p. 481-501.

Mehra, A., Watters, W. A., Grotzinger, J. P., and Maloof, A.C., 2020, Three-dimensional reconstructions of the putative metazoan Namapoikia show that it was a microbial construction: Proceedings of the National Academy of Sciences, v. 117, no. 33, p. 19760-19766.

Narbonne, G. M., Kaufman, A. J., and Knoll, A. H., 1994, Integrated chemostratigraphy and biostratigraphy of the Windermere Supergroup, northwestern Canada: Implications for Neoproterozoic correlations and the early evolution of animals: Geological Society of America Bulletin, v. 106, p. 1281-1292.

Narbonne, G. M., Saylor, B. Z., and Grotzinger, J. P., 1997, The youngest Ediacaran fossils from Southern Africa: Journal of Paleontology, v. 71, p. 953-967.

Nelson, L. L., Ahm, A. S. C., Macdonald, F. A., Higgins, J. A., and Smith, E. F., 2021, Fingerprinting local controls on the Neoproterozoic carbon cycle with the isotopic record of Cryogenian carbonates in the Panamint Range, California: Earth and Planetary Science Letters, v. 566, p.116956.

Newstead, B. L., 2010, The Congo-Kalahari cratonic relationship: from Rodinia to Gondwana: M.S. Thesis, University of Florida, Gainesville, 234 p.

Parnell, A. C., Haslett, J., Allen, J. R., Buck, C. E., and Huntley, B., 2008, A flexible approach to assessing synchroneity of past events using Bayesian reconstructions of sedimentation history: Quaternary Science Reviews, v. 27, no. 19-20, p. 1872-1885.

Peng, S. C., Babcock, L. E., and Ahlberg, P., 2020, Chapter 19 - The Cambrian Period, *in* Gradstein, F. M., Ogg, J. G., Schmitz, M. D., and Ogg, G. M., eds., Geologic Time Scale 2020, Elsevier, p. 565-629, https://doi.org/10.1016/B978-0-12-824360-2.00019-X.

Pflug, H. D., 1970, Zur Fauna der Nama-Schichten in Südwest Afrika I. Pteridinia, Bau und Systematische Zugehörigkeit: Palaeontographica A134, p. 226-262.

Pflug, H. D., 1972, Zur Fauna der Nama-Schichten in Südwest-Afrika. III. Erniettomorpha, Bau und Systematik: Palaeontographica A139, p. 134-170.

Ramezani, J., Hoke, G. D., Fastovsky, D. E., Bowring, S. A., Therrien, F., Dworkin, S. I., Atchley, S. C., and Nordt, L. C., 2011, High-precision U-Pb zircon geochronology of the Late Triassic Chinle Formation, Petrified Forest National Park (Arizona, USA): Temporal constraints on the early evolution of dinosaurs: Geological Society of America Bulletin, v. 123, no. 11-12, p. 2142-2159, https://doi.org/10.1130/b30433.1.

Rooney, A. D., Cantine, M. D., Bergmann, K. D., Gómez-Pérez, I., Al Baloushi, B., Boag, T. H., Busch, J. F., Sperling, E. A., and Strauss, J. V., 2020, Calibrating the coevolution of Ediacaran life and environment: Proceedings of the National Academy of Sciences, v. 117, no. 29, p. 16824-16830.

Saylor, B. Z., 2003, Sequence stratigraphy and carbonate-siliciclastic mixing in a terminal Proterozoic foreland basin, Urusis Formation, Nama Group, Namibia: Journal of Sedimentary Research, v. 73, no. 2, p. 264-279.

Saylor, B. Z., and Grotzinger, J. P., 1996, Reconstruction of important Proterozoic-Cambrian boundary exposures through the recognition of thrust deformation in the Nama Group of southern Namibia: Communications of the Geological Survey of Namibia, v. 11, p. 1-12.

Saylor, B. Z., Grotzinger, J. P., and Germs, G. J. B., 1995, Sequence stratigraphy and sedimentology of the Neoproterozoic Kuibis and Schwarzrand subgroups (Nama Group), southwestern Namibia: Precambrian Research, v. 73, no. 1-4, p. 153-171.

Saylor, B. Z., Kaufman, A. J., Grotzinger, J. P., and Urban, F., 1998, A composite reference section for terminal Proterozoic strata of southern Namibia: Journal of Sedimentary Research, v. 68, no. 6, p. 1223-1235.

Saylor, B. Z., Poling, J. M., and Huff, W. D., 2005, Stratigraphic and chemical correlation of volcanic ash beds in the terminal Proterozoic Nama Group, Namibia: Geological Magazine, v. 142, no. 5, p. 519-538.

Seilacher, A., 2007, Trace Fossil Analysis: Springer, Heidelberg.

Smith, E. F., Nelson, L. L., Strange, M. A., Eyster, A. E., Rowland, S. M., Schrag, D. P., and Macdonald, F. A., 2016, The end of the Ediacaran: Two new exceptionally preserved

body fossil assemblages from Mount Dunfee, Nevada, USA: Geology, v. 44, no. 11, p. 911-914.

Smith, E. F., Nelson, L. L., Tweedt, S. M., Zeng, H., and Workman, J. B., 2017, A cosmopolitan late Ediacaran biotic assemblage: new fossils from Nevada and Namibia support a global biostratigraphic link: Proceedings of the Royal Society B: Biological Sciences, v. 284, no. 1858, p. 20170934.

Tostevin, R., Bradbury, H. J., Shields, G. A., Wood, R. A., Bowyer, F., Penny, A. M., and Turchyn, A. V., 2019*a*, Calcium isotopes as a record of the marine calcium cycle versus carbonate diagenesis during the late Ediacaran: Chemical Geology, v. 529, p.119319.

Tostevin, R., Clarkson, M. O., Gangl, S., Shields, G. A., Wood, R. A., Bowyer, F., Penny, A. M., and Stirling, C. H., 2019*b*, Uranium isotope evidence for an expansion of anoxia in terminal Ediacaran oceans: Earth and Planetary Science Letters, v. 506, p. 104-112.

Wilson, J. P., Grotzinger, J. P., Fischer, W. W., Hand, K. P., Jensen, S., Knoll, A. H., Abelson, J., Metz, J. M., McLoughlin, N., Cohen, P. A., and Tice, M. M., 2012, Deep-water incised valley deposits at the Ediacaran–Cambrian boundary in southern Namibia contain abundant Treptichnus pedum: Palaios, v. 27, no. 4, p. 252-273.

Wood, R. A., Grotzinger, J. P., and Dickson, J. A. D., 2002, Proterozoic modular biomineralized metazoan from the Nama Group, Namibia: Science, v. 296, no. 5577, p. 2383-2386.

Wood, R. A., Poulton, S. W., Prave, A. R., Hoffmann, K. H., Clarkson, M. O., Guilbaud, R., Lyne, J. W., Tostevin, R., Bowyer, F., Penny, A. M., and Curtis, A., 2015, Dynamic redox conditions control late Ediacaran metazoan ecosystems in the Nama Group, Namibia: Precambrian Research, v. 261, p. 252-271.

Yang, B., Steiner, M., Zhu, M., Li, G., Liu, J., and Liu, P., 2016, Transitional Ediacaran–Cambrian small skeletal fossil assemblages from South China and Kazakhstan: Implications for chronostratigraphy and metazoan evolution: Precambrian Research, v. 285, p. 202-215.

Zhang, J., Li, G., Zhou, C., Zhu, M., and Yu, Z., 1997, Carbon isotope profiles and their correlation across the Neoproterozoic-Cambrian boundary interval on the Yangtze Platform, China: Bulletin of the National Museum of Natural Science, v. 10, p. 107-116.

Zhu, M., Zhuravlev, A. Y., Wood, R. A., Zhao, F., and Sukhov, S. S., 2017, A deep root for the Cambrian explosion: Implications of new bio- and chemostratigraphy from the Siberian Platform: Geology, v. 45, no. 5, p. 459-462, https://doi.org/10.1130/g38865.1.

CHAPTER 7. PATHS FORWARD

The studies in this thesis make inroads into resolving some of the stratigraphic complexities of the late Neoproterozoic Era–early Cambrian Period, but many outstanding questions remain. Though I have helped to resolve the timing of Cryogenian glaciations, future work may be able to identify and test potential proximal triggers for the onset of the Marinoan glaciation and explain why its duration was >40 m.y. shorter than that of the Sturtian glaciation. Improved understanding of the carbon isotope record of carbonate rocks before and after Cryogenian glaciations is critical to better understanding both initiation and deglaciation processes. It is clear that the mechanistic origins and chemostratigraphic utilities of Neoproterozoic carbon isotope excursions remain highly uncertain. High precision geochronology data are necessary to test the correlations of Neoproterozoic carbon isotope excursions, and these excursions must be considered within the framework of their associated carbonate depositional and diagenetic systems. The proposed role of pore water redox evolution in generating carbon isotope excursions requires evaluation with local and global redox proxies.

This thesis provides calibrated bio- and chemo-stratigraphic records for the terminal Ediacaran that compel future evaluation against correlative records. Defining and calibrating the eon-scale stratigraphic boundary for the base of the Cambrian is a clear priority for geobiologists and Earth historians. It is increasingly apparent that the current global stratotype is inadequate and that there are currently insufficient data to constrain the synchronicity and relative timing of biological and geochemical change in the terminal Ediacaran and early Cambrian, or to tie these records to an absolute timescale. Should *Treptichnus pedum* define the boundary? If so, when did this behavior first appear? Is the BAsal Cambrian carbon isotope Excursion (BACE) a global phenomenon, and, if so, what caused this dramatic shift in seawater composition? There is

increasing promise of resolving these open questions in the next decade through the production of integrated stratigraphic data sets akin to those provided within this body of work.

APPENDICES

APPENDIX A1. Supplement to Chapter 2

Please visit https://doi.org/10.1130/GEOL.S.12510476 for tables that include compiled geochronology data from the Cryogenian Period, L1502 and L1703B LA-ICPMS U-Pb isotopic data, and L1502 and L1703B CA-ID-TIMS U-Pb isotopic data.

APPENDIX A2. Supplement to Chapter 3

Please visit https://www.sciencedirect.com/science/article/pii/S0012821X21002156#ec0010 for tables that include stratigraphic section coordinates, section and sample labels, and geochemical data for all samples presented in this chapter.

APPENDIX A3. Supplement to Chapter 5

Please visit https://doi.org/10.1130/GEOL.S.12915629 for supplemental materials and tables that include carbon and oxygen isotope data, LA-ICPMS U-Pb data, and CA-ID-TIMS U-Pb isotopic data.

APPENDIX A4. Supplement to Chapter 6

Please visit https://www.sciencedirect.com/science/article/pii/S0012821X22000322#se0140 for tables that include carbon and oxygen isotopic data and U-Pb isotopic data.